

WARSAW UNIVERSITY OF TECHNOLOGY

DISCIPLINE OF SCIENCE - PHYSICAL SCIENCES

FIELD OF SCIENCE - NATURAL SCIENCES

Ph.D. THESIS

Wioleta Rzęsa, M.Sc.

**Non-identical particle femtoscopy of pairs containing
deuteron and interaction studies of nucleons with strange
matter**

Supervisors:

Professor Adam Kisiel, Ph.D., D.Sc.

Georgy Kornakov, Ph.D., D.Sc.

Warsaw 2024



Streszczenie

Femtoscopia par nieidentycznych zawierających deuteron i badania oddziaływań nukleonów z materią dziwną

Niniejsza rozprawa koncentruje się na trzech głównych tematach badawczych. Po pierwsze, badania dotyczą właściwości czasoprzestrzennych źródeł i mechanizmu produkcji lekkich jonów produkowanych w relatywistycznych zderzeniach ciężkich jonów, w których obecna jest plazma kwarkowo-gluonowa. Po drugie, bada dynamikę i oddziaływanie cząstek prostych (pion, kaon, proton) i złożonych (deuteron). Po trzecie, mierzy parametry oddziaływania silnego między najprostszymi mezonami dziwnymi a pojedynczymi i związanymi nukleonami.

Metoda badawcza zastosowana w tej rozprawie do analizy wyżej wymienionych zagadnień jest znana jako femtoscopia, która bada korelacje dwóch cząstek w przestrzeni pędu. Niniejsza praca przedstawia korelacje pędów zmierzone za pomocą detektora ALICE w zderzeniach Pb–Pb przy energii zderzenia $\sqrt{s_{NN}} = 5.02$ TeV. Analiza skupia się na pomiarze i interpretacji femtoskopowych korelacji pomiędzy różnymi parami cząstek, w tym pionami i deuteronami, protonami i deuteronami, kaonami i protonami, a także kaonami i deuteronami. Wszystkie te pary można odpowiednio opisać za pomocą oddziaływań obejmujących zarówno siły Coulombowskie, jak i oddziaływania silne. Oddziaływania te są zdefiniowane przy użyciu różnych technik, takich jak rozwiązania oparte na równaniu Schrödingera, parametryzacji numerycznej, podejścia dwu- i trójciałowego, i uwzględniając funkcje falowe wyższych pędów orbitalnych. Badanie określa femtoskopowe rozmiary źródeł nieidentycznych par dwóch cząstek przy różnych centralnościach zderzeń. W szczególności, analizy pion–deuteron i proton–deuteron dostarczają pierwszych pomiarów femtoskopowych rozmiarów źródeł deuteronów w zderzeniach Pb–Pb. Pomiar ten nie był wcześniej możliwy w bezpośrednich badaniach deuteron–deuteron ze względu na niewystarczającą statystykę zebranych danych. W rezultacie niniejsza rozprawa oferuje unikalny pomiar wartości źródeł cząstek złożonych z więcej

niż jednego nukleonu. Wartości te są następnie porównywane z wartościami cząstek prostych, takich jak piony i protony, w celu zbadania ich kolektywnego zachowania, które jest efektem napędzającym dynamikę femtoskopowych źródeł. Przeprowadzona analiza proton–deuteron wskazuje na ograniczony wpływ dynamiki trójciałowej, ponieważ dane eksperymentalne mogą być dobrze opisane zarówno przez oddziaływania dwu-, jak i trójciałowe. Z kolei badanie kaon–proton pokazuje, że w źródłach zderzeń ciężkich jonów efekty sprzężonych kanałów odgrywają znikomą rolę w określaniu funkcji korelacji. Co więcej, badania kaon–proton i kaon–deuteron przedstawiają pierwsze pomiary parametrów rozpraszania oddziaływania silnego dla analizowanych systemów przy użyciu femtoskopii, dostarczając wartości, które są unikalne w skali globalnej. Pomiar długości rozpraszania kaon–deuteron dla oddziaływania silnego jest pierwszym tego rodzaju pomiarem dotychczas wykonanym. Badanie to umożliwia wyznaczenie parametrów zależnych od izospinu dla najprostszych cząstek dziwnych, co daje również wgląd w oddziaływanie kaon–neutron — oddziaływanie trudne do zbadania bezpośrednio ze względu na brak ładunku neutronu. Wszystkie zmierzone parametry zostały porównane z oczekiwaniami i dostępnymi pomiarami. Niniejsza praca dostarcza także kilku spostrzeżeń dotyczących zależności wielkości źródeł w funkcji masy poprzecznej nieidentycznych cząstek oraz przyszłych kierunków badań.

Słowa kluczowe: chromodynamika kwantowa, zderzenia ciężkich jonów, femtoskopia, oddziaływania, deuterony, sektor dziwny.

Abstract

Non-identical particle femtoscopy of pairs containing deuteron and interaction studies of nucleons with strange matter

This thesis focuses on three main research topics. First, it investigates the space-time properties and production mechanism of light nuclei in relativistic heavy ion collisions where quark-gluon plasma is present. Second, it studies the dynamics and interaction of simple hadrons with composite objects (deuterons). Third, it measures the scattering parameters of the strong interaction between the lightest strange meson and single and bound nucleons.

The method used in this thesis to investigate the aforementioned topics is known as femtoscopy, which examines two-particle correlations in momentum space. This work presents the momentum correlations measured with the ALICE detector in Pb–Pb collisions at a collision energy of $\sqrt{s_{\text{NN}}} = 5.02$ TeV. It focuses on the measurement and interpretation of femtoscopic correlations between various particle pairs, including pions and deuterons, protons and deuterons, kaons and protons, and kaons and deuterons. All of these pairs can be adequately described by interactions involving both Coulomb and strong forces which are determined using various techniques such as resolving Schrödinger equations, numerical parametrization, two- and three-body approaches, including higher order partial waves. The study determines the femtoscopic source sizes of non-identical two-particle pairs across different collision centralities. Notably, the pion–deuteron and proton–deuteron studies provide the first measurements of deuteron femtoscopic source sizes in Pb–Pb collisions. This measurement has not been previously possible in direct deuteron–deuteron studies due to insufficient data. As a result, this thesis offers unique values for the homogeneity lengths of composite objects. These values are further compared with those of simpler particles, such as pions and protons, to investigate their collective flow behavior, which is the driving force behind femtoscopic source dynamics. The

proton–deuteron and kaon–proton studies provide the first experimental evidence of effects expected in large femtoscopic sources. Specifically, the proton–deuteron study indicates a reduced impact of three-body dynamics, as the data can be well described by both two- and three-body interactions involving the underlying nucleons of the pair. In contrast, the kaon–proton study demonstrates that, in heavy-ion collision sources, coupled channel effects play a negligible role in determining the correlation functions. Furthermore, the kaon–proton and kaon–deuteron studies present the first measurements of their scattering parameters using femtoscopic techniques. The measurement of the kaon–deuteron scattering length for the strong interaction is the first of its kind. This study opens the door to determining isospin-dependent parameters in the fundamental strangeness sector, which also enables insights into the kaon–neutron interaction—an interaction that is difficult to investigate experimentally due to the neutron’s lack of charge. All the measured parameters are compared with expectations and previous measurements when available. This thesis provides also several insights into m_T scaling of non-identical particles and future directions in studies using the femtoscopy technique.

Keywords: quantum chromodynamics, heavy-ion collisions, femtoscopy, interactions, deuterons, strangeness sector.

Acknowledgements

During my Ph.D. journey, I met many people. People who made this period easier and filled it with unforgettable memories. People who are unique, inspiring, and endlessly supportive. People that I consider my own **scientific family**.

Georgy Kornakov, a simple "thank you" could never fully express how deeply grateful I am for how much I have grown, both in science and in life, thanks to you. I have lost count of how many times you have helped me go through scientific crises. In this challenging journey of endless studies, you've always been my first aid. Thank you for your amazing ideas, broad knowledge, patience, empathy, unwavering support and positive attitude. You were not only my supervisor but also a good friend. I am so lucky to have had you as my supervisor. This Ph.D. journey would not have been the same without you - 'in fact', it wouldn't have happened at all.

Adam Kisiel, I will always remember that I chose nuclear physics because I was inspired by you. You were always present at critical points and many times provided accurate explanations to difficult questions. Also, I really appreciate the way how you shared your opinion and knowledge. Very clearly and patiently. I can only confirm what I've heard many times before: that you are an expert in my research field. I am really happy that my thesis was supervised by you.

I would like to thank all the members of the Heavy Ion Reaction Group (HIRG) at the Faculty of Physics, Warsaw University of Technology, for the perfect working atmosphere and for so many years of cooperation. I cannot list all of you here because it would take a long paragraph of names, but believe me, you all make me feel that I simply like the whole Warsaw group very much. Below I list only those of you who have spent the most time with me, either in the office or working in the same ALICE team.

Daniela Ruggiano, I may say a hundred times that social activities exhaust me, but honestly, this Ph.D. journey would have been quite lonely without you. Thank you

for listening to all my dramas, for the many discussions and even our fights. And of course for all the trips and conferences we've shared together. You're the next one to defend - good luck Dany!

Małgosia Janik, for me you are like an angel. You solve all problems incredibly fast. You took care of me and offered to help me many times, even when I didn't openly ask for it. You've also given me a lot of good advice, and I will never forget that.

Łukasz Graczykowski, I think you are the best psychologist in the team. You have often reassured me about the technical aspects of my life as a Ph.D. student. Apart from that, you have been very supportive and have given me many good comments on my studies. Thank you for that.

Jakub, Kasia, Zuzia, Shirajum, Marta, Maja and Pritam, my WUT siblings. Thank you for *Star Wars* evenings, for dancing at CERN, for sharing trivialities about animals, for support, for those moments of laughter and just simple scientific (and not) conversations, for coffee, for little trips, for sarcasm, and for time. For good time.

I would like to thank people from my favorite Femtoscopy Physics Analysis Group at CERN, for listening to my updates, many inspiring discussions, friendly environment and many checks of my studies. Once again, I cannot list you all, so I will name only those who directly helped with some of the studies. I am very grateful to Dongfang Wang, for our fight with the proton–deuteron study. Also direct thanks should go to Bhawani Singh, Laura Fabbietti, Dimitar Michailov for their help with proton–deuteron/kaon–proton study.

Scott Pratt and Marysia Stefaniak, thank you for numerous discussions, emails, and messages, especially regarding the theoretical study of the proton–deuteron system. I truly appreciate our little collaboration, and I am grateful for all the supporting words that I heard from you.

Yuri Sinyukov and Volodymyr Shapoval, thank you for our collaboration on pion–pion study. For exchanged knowledge and many discussions resulting in effectively written paper.

Mermaid Team (Gabi Moryc, Aga Borucka and Jakub Kopyciński), Ania Kawęcka and Asia Latusek, you have been showing me the light of life outside science since the beginning of my university studies. Thank you for remembering me even though I was always busy during my Ph.D. life.

Finally, I would like to thank my brother Sylwek. You have always been truly happy about my successes and made an effort to be a part of my life. Having someone who understands me both, in science and in life, is just priceless. I will always be grateful for that.

Contents

Streszczenie	III
Abstract	V
1 Preface	1
2 Introduction	3
2.1 Standard Model	3
2.2 Quantum Chromodynamics	5
2.3 Mass of particles	7
2.4 Hadron–hadron interactions	9
2.5 Relativistic heavy-ion collisions	14
2.5.1 The quark-gluon plasma	14
2.5.2 Collectivity	18
2.6 Femtoscopy	20
2.6.1 Source function	22
2.6.2 Two-particle wave function	25
2.7 Particle production and formation of light-ions	31
2.7.1 Particles’ yield	32
2.7.2 Elliptic flow	35
2.7.3 Event-by-event fluctuations	36
2.7.4 Femtoscopy – a tool revealing the production mechanism of light ions	38
3 Experimental data	39
3.1 CERN accelerator complex	39
3.2 ALICE Experiment	41
3.2.1 Trigger system	42
3.2.2 The Inner Tracking System	43

3.2.3	The Time Projection Chamber	44
3.2.4	The Time-Of-Flight detector	49
3.2.5	Other sub-detectors of the ALICE experiment	49
3.3	Data overview	52
4	Analysis technique	55
4.1	Experimental correlation function	55
4.2	Data selection criteria	56
4.3	Corrections	63
4.3.1	PID purity	64
4.3.2	Primary fraction	65
4.3.3	Gaussianity fraction	67
4.3.4	Momentum resolution	73
4.3.5	Non-femtoscopic effects	76
4.4	Numerical fitting	82
5	Results	85
5.1	Pion–deuteron	86
5.1.1	Introduction and model description	87
5.1.2	Results	89
5.2	Proton–deuteron	98
5.2.1	Introduction and model description	99
5.2.2	Results	107
5.3	Kaon–proton	113
5.3.1	Introduction and model description	114
5.3.2	Results	118
5.4	Kaon–deuteron	126
5.4.1	Introduction and model description	127
5.4.2	Results	130
5.5	Non-identical sources and m_T scaling	134
6	Uncertainties	139
6.1	Particle and event selection uncertainties	139
6.2	Systematic uncertainties of corrections and the fit	142
6.3	Statistical uncertainties of the fit	146

<i>Contents</i>	XIII
7 Summary	147
Bibliography	157

List of Figures

2.1	The Standard Model of Particle Physics. Picture from [2].	4
2.2	Right: the first order diagram of a gluon exchange between two quarks. Left: diagrams of leading order quark–gluon and gluon–gluon loop. . .	6
2.3	Summary of measurements of α_s as a function of the energy scale Q . Figure from [6].	7
2.4	The masses of the six quark flavors (red circles) gained through the interaction with the Higgs field alone and with additional spontaneous chiral symmetry breaking in QCD shown in y-axis and x-axis, respectively. Picture from [8].	8
2.5	Schematic representation of experimental techniques used for interaction measurements among pairs of hadrons. From left to right: scattering experiments, exotic atom experiments, femtoscopy. . . .	10
2.6	Schematic illustration of typical nucleon–nucleon potential together with characteristic interaction regions of short-, medium- and long-range effects.	12
2.7	Schematic views of heavy-ion collision evolution (from bottom to top). The left and right sides represent the evolution without and with the QGP state. Picture from [30].	15
2.8	A phase diagram of nuclear matter as a function of temperature and baryon chemical potential μ_B . Figure from [38].	16
2.9	Geometrical illustration of first order Fourier decomposition of flow patterns. From left to right: directed, radial and elliptic flow.	19
2.10	Schematic representation of the interplay between the radial and elliptic flows. Picture from [53].	20

2.11	Illustration of the femtoscopy technique. Two particles/ions collide creating a particle-emitting source. The drawing shows a schematic measurements of the emitted correlated pair that contribute to certain homogeneity region building the source function. Particles on their emitting paths can interact among them, which is reflected by their wave function.	21
2.12	The three-dimensional visualisation of the LCMS frame.	23
2.13	The three-dimensional visualisation of the homogeneity region (orange) and corresponding radii seen in LCMS frame.	23
2.14	Illustration of the femtoscopic radii in different directions. Colors corresponds to mass dependence of the radii: for particles with higher m_T (blue) the source volume is more confined than in case of lighter particles (red). Picture from [70].	25
2.15	Left: simulation of proton–proton correlation functions using UrQMD model for single particle source radii equal 3 fm accounting for different effects of the wave function (picture from [90]). Right: A schematic representation of correlation functions that correspond to their repulsive, attractive and bound state interpretation (picture from [91]).	26
2.16	A simplified illustration of two particles scattering in an elastic way. . .	27
2.17	A simplified illustration of a scattering problem. Left: non-interacting particles – plane waves, right: interacting particles – the wave function for interacting particles is a superposition of the plane wave and the spherical wave from the scattering.	27
2.18	The light-flavored hadron yields in central Pb–Pb collisions at $\sqrt{s_{NN}} = 5.02$ TeV measured by the ALICE experiment together with three interpretation of the statistical fit. Figure from [106].	33
2.19	Left/right: B_2 parameter measured for (anti)deuteron produced in pp collisions at $\sqrt{s} = 7$ TeV / Pb-Pb collisions at $\sqrt{s_{NN}} = 2.76$ TeV for five multiplicity/centrality ranges. Figures from [112, 105].	34
2.20	Left/right: Ratio of (anti)deuteron/(anti)3He and proton production yields as a function of the charged-particle multiplicity for different collision systems and energies. Lines corresponds to the expectations of thermal and coalescence models. Figure from [113].	35

2.21	Elliptic flow of (anti) ³ He in comparison with the predictions from the Blast-Wave model and a simple coalescence approach for the centrality intervals 0 – 20%, 20 – 40% and 40 – 60%. Figure from [116].	36
2.22	Left: a ratio of the second to first order cumulant of the \bar{d} multiplicity factor distribution, right: Pearson correlation between the measured \bar{p} and \bar{d} . Both results come from Pb-Pb collisions at $\sqrt{s_{NN}} = 5.02$ TeV and are presented as a function of collision centrality. Bands correspond to predictions coming from thermal and coalescence models. Figures from [110].	37
3.1	The CERN accelerator complex [125]. The LHC is located at the end of the complex injector chain of the CERN accelerators.	40
3.2	The ALICE detector during the <i>Run – 2</i> data taking period (2015–2018) [131].	42
3.3	The coordinate system of the ALICE detector. Left: polar space parallel to the direction of the beam, right: transversal plane perpendicular to the direction of the beam.	42
3.4	The schematic view of the Inner Tracking System at ALICE. The two outer layers are the SSD detector, the two middle layers are the SDD detector and the two inner layers are the SPD detector. Figure from [133].	45
3.5	The schematic view of the Time Projection Chamber at ALICE [134]. The inner and outer red pads indicate an active volume of the detector. .	46
3.6	The schematic view of the single sector of the Time Projection Chamber at ALICE [135]. Points indicate interactions that caused hits in the end-plates along the particle's trajectory.	47
3.7	The energy loss as a function of momentum measured by the ALICE TPC for Pb–Pb collisions at $\sqrt{s_{NN}} = 5.02$ TeV [136].	48
3.8	The particle's velocity β as a function of momentum measured by the ALICE TOF for Pb–Pb collisions at $\sqrt{s_{NN}} = 5.02$ TeV.	50
3.9	Workflow of the data reconstruction in ALICE.	53
3.10	A grid of computing nodes used to perform analysis on ALICE data. . .	54
4.1	Distribution of p_T of positive kaons vs k^* of the kaon–proton pairs calculated for kaons with p_T range 0.2–1.5 GeV/ c and protons with p_T range 0.5–3.0 GeV/ c	57

4.2	Examples of the deuteron's distributions of TOF n_σ vs p_T (upper left, bottom left and right) and p (upper right) without an additional cut on p . the deuteron's distributions of TOF n_σ vs p (bottom right) with the additional cut on p . See text for more details.	58
4.3	A DCA_{XY} distributions for protons (left) and deuterons (right) together with the template fit of underlying processes of particles production. Lines represent particles: produced in primary processes (red), coming from weak decays of other particles (green), knocked out from the material due to interaction with particles created in the collision (blue), a sum of all ingredients (magenta).	60
4.4	The TPC N_σ distributions of π^+ (top left), K^+ (top right), p (bottom left), d (bottom right) selected for purpose of this study using Pb–Pb collisions at $\sqrt{s_{NN}} = 5.02$ TeV data registered by ALICE experiment.	62
4.5	Examples of the distributions of $\Delta\phi^*$ vs $\Delta\eta$ for proton–deuteron pairs without (left) and with (right) track merging cut.	63
4.6	A TPC n_σ distributions of deuterons registered in 30 – 50% Pb–Pb collisions at $\sqrt{s_{NN}} = 5.02$ TeV for five transverse momentum ranges. Lines represent fit to data: signal (dashed magenta), background (dashed black), both (solid blue).	65
4.7	Distributions of PID purity as a function of transverse momentum for pions (top left), kaons (top right), (anti)protons (bottom left) and (anti)deuterons (bottom right).	66
4.8	Distributions of primary fraction as a function of transverse momentum for pions (top left), kaons (top right), (anti)protons (bottom left) and (anti)deuterons (bottom right).	67
4.9	A source probability distribution for pion–deuteron (left), kaon–deuteron (center) and proton–deuteron (right) in Pb–Pb collisions at $\sqrt{s_{NN}} = 5.02$ TeV simulated using hydrodynamic model LHYQUID and THERMINATOR2 generator. The colors correspond to centralities: 0 – 10% (red), 10 – 30% (blue), 40 – 50% (green). Lines are Gaussian core fits to simulation points (see text for more details).	69
4.10	Examples of the distributions of p_T vs k^* of particles from kaon–proton (first row), pion–deuteron (second row), proton–deuteron (third row), kaon–deuteron (fourth row) obtained in this thesis.	70

4.11	The correction factor as a function of k^* used in the pion–deuteron (upper left), proton–deuteron (upper right) and kaon–deuteron (bottom) studies.	71
4.12	The momentum resolution matrix for pion–deuteron (top-left), proton–deuteron (top-right), kaon–proton (bottom-left) and kaon–deuteron (bottom-right) pairs based on HIJING simulations for Pb–Pb collisions at $\sqrt{s_{NN}} = 5.02$ TeV data of the ALICE experiment.	73
4.13	Left: a Gaussian fit to $k^*_{reco} - k^*_{true}$ distribution of proton–deuteron resolution matrix for $k^* < 0.15$ GeV/ c . Right: a comparison of different smearing methods shown with colored dashed lines with the original correlation function shown as a black solid line.	75
4.14	Elliptic flow of pions and (anti)deuterons as a function of p_T for different centrality intervals measured in Pb–Pb collisions at $\sqrt{s_{NN}} = 5.02$ TeV. Left: pions, kaons, protons [156], right: (anti)deuterons [109]	77
4.15	The raw correlation functions of K^-p pairs for Pb–Pb collisions at $\sqrt{s_{NN}} = 5.02$ TeV data of the ALICE experiment for 0 – 5% (left) and 30 – 40% (right) represented by points. Lines correspond to the background predictions of polynomial fit of first and second order to experimental points in the ranges given in the legend as well as a simulation of the elliptic flow effect.	78
4.16	The raw correlation functions of π^-d pairs for Pb–Pb collisions at $\sqrt{s_{NN}} = 5.02$ TeV data of the ALICE experiment for 0 – 10% (left) and 30 – 50% (right) represented by points. Lines correspond to the background predictions of polynomial fit of first and second order to experimental points in the ranges given in the legend as well as a simulation of the elliptic flow effect.	79
4.17	The raw correlation functions of K^-d pairs for Pb–Pb collisions at $\sqrt{s_{NN}} = 5.02$ TeV data of the ALICE experiment for 0 – 10% (left) and 30 – 50% (right) represented by points. Lines correspond to the background predictions of polynomial fit of first and second order to experimental points in the ranges given in the legend as well as a simulation of the elliptic flow effect.	80

4.18	The raw correlation functions of pd pairs for Pb–Pb collisions at $\sqrt{s_{\text{NN}}} = 5.02$ TeV data of the ALICE experiment for 0 – 10% (left) and 30 – 50% (right) represented by points. Lines correspond to the background predictions of polynomial fit of first and second order to experimental points in the ranges given in the legend as well as a simulation of the elliptic flow effect.	80
4.19	Schematic representation of the fitting procedure for one-dimensional (left) and three-dimensional (right) cases. The boxes represent theoretical correlation functions generated for different values of the correlation parameters. The blue boxes represent the functions used in the numerical integration of the final solution which provides minimum χ^2 in comparison to experimental data.	83
4.20	Illustration of the shared parameters among correlation functions in the simultaneous fit to all of them.	84
5.1	Theoretical correlation functions of pion–deuteron pairs for Coulomb only (dashed lines) and Coulomb plus strong interaction (solid lines) with different input parameters of the Gaussian source size $R_{\pi d}$. Left: pairs with opposite sign of charge, right: pairs with same sign of charge.	88
5.2	The $\pi^+d \oplus \pi^-\bar{d}$ correlation functions (top row) $\pi^-d \oplus \pi^+\bar{d}$ correlation functions (bottom row) in three centrality classes (from left to right 0 – 10%, 10 – 30%, 30 – 50%) represented by points. The bands correspond to the Lednický-Lyuboshits (denoted as L-L) fit of Coulomb only (orange) and Coulomb plus strong (blue). The band widths represent the systematic uncertainties of the fits. The lower panels show the differences between the data and the fits, normalised by the statistical uncertainty σ_{stat}	90
5.3	$R_{\pi d}$ radii as a function of $\langle dN_{ch}/d\eta \rangle^{1/3}$ obtained from a common fit to all pair combinations of pion–deuteron femtoscopic functions for Pb–Pb collisions at $\sqrt{s_{\text{NN}}} = 5.02$ TeV.	91
5.4	Fits to radii obtained at collision energy $\sqrt{s_{\text{NN}}} = 2.76$ TeV performed for each m_T bin. Figure credit: Łukasz Graczykowski.	92
5.5	Femtoscopic radii of identical pions, kaons, and protons rescaled to $\sqrt{s_{\text{NN}}} = 5.02$ TeV from $\sqrt{s_{\text{NN}}} = 2.76$ TeV [77].	92
5.6	Pion’s radii as a function of m_T , together with linear and power-law fits.	93

- 5.7 Pion femtoscopic radii dependencies on m_T calculated in LHYQUID+THERMINAT2 model, 0 – 5% Pb–Pb collisions at $\sqrt{s_{NN}} = 5.02$ TeV. Different markers and colors correspond to the radii obtained in the 3D study (R_{out} — squares, R_{side} — crosses, R_{long} — tilted crosses) and for R_{inv} from the 1D study (cicles). Lines correspond to power-law fits am_T^{-b} to radii dependencies in the range above 0.25 GeV/ c and linear fits to radii dependencies in the range below 0.25 GeV/ c . The illustration derived from [157] study. 94
- 5.8 R_d radii as a function of $\langle dN_{ch}/d\eta \rangle^{1/3}$ obtained from a common fit to all pair combinations of pion–deuteron femtoscopic functions for Pb–Pb collisions at $\sqrt{s_{NN}} = 5.02$ TeV. 95
- 5.9 R_{inv} parameters versus m_T at $\sqrt{s_{NN}} = 5.02$ TeV for the three centralities for d and \bar{d} , together with other mesons and baryons (π^+ , K^+ , K_S^0 , p , \bar{p}) taken from [77] and rescaled from the energy $\sqrt{s_{NN}} = 2.76$ TeV. The bands in the plot correspond to a power-law fit to all previously measured particles with the width of the pion uncertainty. Statistical (lines) and systematic (boxes) uncertainties are shown. 96
- 5.10 Theoretical correlation functions calculated with Lednický-Lyuboshits approach using [171] scattering parameters for proton–deuteron pairs separately for $C^2S_{1/2}$ (left) and $C^4S_{3/2}$ (right) spin channels drawn for different input parameters of the Gaussian source size R_{pd} 101
- 5.11 Theoretical correlation functions calculated with Lednický-Lyuboshits approach using [171] scattering parameters for proton–deuteron pairs drawn with different input parameters of the Gaussian source size $R_{\pi d}$. 101
- 5.12 The schematic representation of the n - n partial wave in the absence of a potential $\sin(kr)$ (green), with potential $\sin(kr + \delta)$ and solving the Schrödinger equation (red) or using asymptotic form (blue). Figure credit: Scott Pratt. 102
- 5.13 The phase shifts (upper panel) and their derivatives (lower panels) as a function of k^* for different spin states and partial waves; points correspond to the phase shift measurements [171, 172], lines are the fits to the experimental points. Figure credit: Scott Pratt. 103

5.14	Theoretical correlation of proton–deuteron functions calculated with the CorAL package using for different interaction contributions to the correlation function (left) and different input parameters of the Gaussian source size R_{pd} (right). The gray region corresponds to extrapolated solutions.	104
5.15	Theoretical correlation of proton–deuteron functions describing coulomb and strong interaction calculated with CorAL framework (solid line for strong with SPD-waves, short dashed line strong with S-wave only) and Lednický-Lyuboshits model (long dashed line, strong with S-wave only).	105
5.16	Theoretical correlation of proton–deuteron functions calculated with the PISA model of the three-body interaction, taking into account antisymmetrization, Coulomb and strong (SPD-waves) effects, shown with solid lines for different input parameters of the Gaussian source size R_{pd} . The dashed lines correspond to solutions with antisymmetrization and Coulomb interaction only.	106
5.17	$pd \oplus \bar{p}\bar{d}$ correlation functions (black points) in three centrality classes together with with Coulomb plus strong fit of the three-body PISA approach (red bands) and two-body Lednický-Lyuboshits (denoted as L-L) approach with the scattering length f_0 from Arvieux et al. [168] (blue bands). The bottom panels show the signed $n\sigma$ values evaluated at each data point for theoretical bands.	107
5.18	R_{NN} (left) and R_{pd} (right) radii as a function of $\langle dN_{ch}/d\eta \rangle^{1/3}$ obtained from the fit to proton–deuteron pairs registered in Pb–Pb collisions at $\sqrt{s_{NN}} = 5.02$ TeV.	109
5.19	R_d radii as a function of $\langle dN_{ch}/d\eta \rangle^{1/3}$ obtained from a common fit to all pair combinations for Pb–Pb collisions at $\sqrt{s_{NN}} = 5.02$ TeV.	110

- 5.20 The femtoscopic source sizes in a function of m_T measured in Pb–Pb collisions at $\sqrt{s_{NN}} = 5.02$ TeV/ c represented by red, blue, and green markers as follows in 0–10%, 10–30%, 30–50% centrality intervals. The full markers corresponds to source sizes of protons measured directly in proton-proton study. The open diamonds and squares represents femtoscopic sizes measured in proton–deuteron study for nucleons R_{NN} and deuterons R_d , respectively. The vertical bars and boxes show the statistical and systematic uncertainties, respectively. The shaded bands depict the 1σ uncertainties of the fits of the power-law function: $r_{\text{eff}} = a + b \cdot \langle m_T \rangle^c$ 111
- 5.21 $pd \oplus \bar{p}\bar{d}$ correlation functions (black points) in three centrality classes together with with Coulomb plus strong fit of the three-body PISA approach (red bands), two-body Lednický-Lyuboshits (denoted as L-L) approach with the scattering length f_0 from Arvieux [168] (blue bands) and two-body CorAL functions (green band). The bottom panels show the signed $n\sigma$ values evaluated at each data point for theoretical bands. 112
- 5.22 Left: A schematic representation of different states entangled with K^-N channel at different energy together with sensitivity ranges of different experiments (figure credit: Georgy Kornakov). Right: coupled channels that can contribute in the whole span of the K^-p correlation function. . . 116
- 5.23 Left: K^-p correlation function for $R = 1$ fm, lines denotes the results of correlation function adding different channels: only K^-p (long-dashed), K^-p plus \bar{K}^0n plus K^0n (short-dashed), K^-p plus \bar{K}^0n plus K^0n plus $\pi\Sigma$ (dotted), all channels (solid), all channels but without the Coulomb interaction (dash-dotted). Right: the same as upper but for femtoscopic source $R=3\text{fm}$. Figure from [201]. 116
- 5.24 Theoretical correlation functions with different input parameters of the source size calculated using L-L approach for K^-p pairs (left) and K^+p (right). 118
- 5.25 Theoretical correlation functions of K^-p pairs for different values of the source sizes calculated using Kyoto model [201] folded to the CATS package [173]. 118

5.26	Big upper pads: $K^-p \oplus K^+\bar{p}$ correlation functions in the six centrality classes. On top of data in light cyan band the corresponding Lednický-Lyuboshits fits (denoted as L-L), orange band Kyoto model calculations. Small inserts pads of upper plots: the $K^+p \oplus K^-\bar{p}$ correlation functions in the six centrality classes. On top of data in light cyan band the corresponding Lednický-Lyuboshits fits. Bottom pads: sigma difference expressed as data minus model normalised by the statistical uncertainty of the data.	119
5.27	Theoretical correlation functions of K^-p for different source radii and scattering parameters calculated using L-L approach.	120
5.28	Kaon-proton radii as a function of $\langle dN_{\text{ch}}/d\eta \rangle^{1/3}$ obtained from a common fit to all pair combinations for Pb-Pb collisions at $\sqrt{s_{\text{NN}}} = 5.02$ TeV.	122
5.29	Comparison of kaon-proton femtosopic radii from this analysis (red) with those obtained from single-particle expectation based on kaon and proton femtoscopy (black).	123
5.30	$K^-p \oplus K^+\bar{p}$ experimental correlation function for 30–40% centrality interval together with Lednický-Lyuboshits calculations using f_0 from literature [190, 195, 196, 198, 199, 200].	124
5.31	Scattering lengths of K^-p : Lednický-Lyuboshits fit obtained in this study (red), available world data and theoretical calculations (blue) [190, 195, 196, 198, 199, 200]. Statistical uncertainties are represented as bars and systematic uncertainties, if provided, as boxes.	125
5.32	Theoretical correlation functions with different input parameters calculated using Lednický-Lyuboshits (L-L) approach for K^-d (left) and K^+d (right) figure shows the effect of changing the femtosopic source radii from 2.0 to 10.0 fm and its effect on the correlation function.	129
5.33	$K^+d \oplus K^-\bar{d}$ (top pads) and $K^-d \oplus K^+\bar{d}$ correlation functions in the three centrality classes 0–10%, 10–30%, 30–50% represented with points. The light cyan band corresponds to Lednický-Lyuboshits fits (denoted as L-L).	130
5.34	Kaon-deuteron radii as a function of $\langle dN_{\text{ch}}/d\eta \rangle^{1/3}$ obtained from a common fit to all pair combinations for Pb-Pb collisions at $\sqrt{s_{\text{NN}}} = 5.02$ TeV for kaon-deuteron pairs.	132

5.35	Scattering lengths of K^+d : Lednický-Lyuboshits fit obtained in this study (red), available world theoretical calculations (blue) provided by profs. Hyodo and Heidenbauer.	132
5.36	Scattering lengths of K^-d : Lednický-Lyuboshits fit obtained in this study (red), available world theoretical calculations (blue) [200, 196, 207, 208, 209, 210].	133
5.37	The two-particle femtoscopic source sizes of pions and protons measured in identical studies compared to measurements of non-identical pairs under the mass assumption $m_{av} = \frac{m_1+m_2}{2}$ are the subject of this work.	135
5.38	The two-particle femtoscopic source sizes of pions and protons measured in identical studies compared to measurements of non-identical pairs under the mass assumption $\mu = \frac{m_1 m_2}{m_1+m_2}$ are the subject of this work.	136
5.39	The two-particle femtoscopic source sizes of pions and protons measured in identical studies compared to measurements of non-identical pairs under the mass assumption $2\mu = 2\frac{m_1 m_2}{m_1+m_2}$ are the subject of this work.	137
6.1	Barlow check for K^-p pairs. From top to bottom centralities from 0 – 5% to 40 – 50%. From left to right variations described in Tab. 6.1: 1st column – number of events used to mix in the uncorrelated distribution, 2nd column: reconstruction based on information from TPC only and TPC+ITS, 3rd column: DCA cut, 4th column: PID N_σ selection, 5th column: z-vertex position, 6th column: minimal number of clusters used in the reconstruction.	141
6.2	Distribution of relative error as a function of k^* together with $[0]+\exp([1]*k^*)$ fit obtained in pion–deuteron study. Top: pairs of the same charge sign, bottom: pairs of opposite charge signs. From left to right: 0-10%, 10-30%, 30-50%.	142
6.3	Distribution of relative error as a function of k^* together with $[0]+\exp([1]*k^*)$ fit obtained in proton–deuteron study. From left to right: 0-10%, 10-30%, 30-50%.	143

-
- 6.4 Distribution of relative error as a function of k^* together with $[0]+\exp([1]*k^*)$ fit obtained in kaon–deuteron study. Top: pairs of the same charge sign, bottom: pairs of opposite charge signs. From left to right: 0-10%, 10-30%, 30-50%. 143
- 6.5 Distribution of fit results of the K^-d scattering length obtained for variations listed in Tab. 6.2 as described in the text. 145
- 6.6 Distribution of fit results for 1500 bootstrapped pion–deuteron correlation function sets for the pion–deuteron radii obtained from fits as a function of event centrality and separately each centrality. . . . 146

List of Tables

2.1	The Bohr radius, a_c , for particle pairs considered in this thesis. The values were calculated based on $a_c = 1/(\mu e^2)$, where μ is reduced mass of the pair. The value is positive for repulsive and negative for attractive interaction.	30
4.1	Single particle criteria for pions, kaons, (anti)protons and (anti)deuterons.	61
4.2	The track merging cut settings of $ \Delta\eta $ (s), distance (d) and fraction (f) used in the four studies considered in this thesis.	63
4.3	Number of particle pairs contributing to low k^* range.	64
4.4	Background of non-femtoscopic effects used for kaon–proton and pion–/kaon–/proton–deuteron studies.	81
5.1	Two-particle pion–deuteron source sizes, $R_{\pi d}$, together with uncertainties for 3 centrality from the fit to all pair combinations for Pb–Pb collisions at $\sqrt{s_{NN}} = 5.02$ TeV.	90
5.2	A single-particle pion radii and their uncertainty for three centrality intervals predicted for m_T of pions contributing to low k^* in the pion–deuteron sample that is considered in this thesis.	94
5.3	R_d radii for 3 centrality intervals, based on pion–deuteron functions and prediction of the pions source based on R vs. $\langle m_T \rangle$ of single pion radii measurements [77] rescaled to energy of this study.	95
5.4	The values of the scattering parameters for proton–deuteron pairs at low relative momentum, for two spin channels $^2S_{1/2}$ and $^4S_{3/2}$ [167, 168, 169, 170, 171].	100
5.5	Proton–deuteron, R_{pd} and R_{NN} source size measured in Pb–Pb collisions at nucleon energy $\sqrt{s_{NN}} = 5.02$ TeV using Lednický-Lyuboshits (denoted as L-L) parametrization with scattering parameters from [167, 168, 169, 170, 171] and PISA model, respectively.	108

5.6	A single-particle proton radii and their uncertainty for three centrality intervals predicted for m_T of protons contributing to low k^* in the proton–deuteron sample that is considered in this thesis.	109
5.7	(Anti)deuteron, R_d , source size measured in Pb–Pb collisions at $\sqrt{s_{NN}} = 5.02$ TeV using Lednický-Lyuboshits parametrization and scattering parameters from [167, 168, 171, 169, 170] and (anti)protons source measurements 5.6.	110
5.8	Values of the real and imaginary parts of the scattering length for K^-p and K^+p pairs at low relative momentum.	117
5.9	A two-particle kaon-proton source sizes, R_{Kp} , together with uncertainties for 6 centrality from the fit to all pair combinations for Pb–Pb collisions at $\sqrt{s_{NN}} = 5.02$ TeV.	121
5.10	Values of the χ^2/ndf for the deviation between the ALICE data and available model calculations and previous measurements for K^-p pairs at low relative momentum.	123
5.11	Values of the scattering parameters for K^-d and K^+d pairs at low relative momentum.	129
5.12	Two-particle kaon–deuteron source sizes, R_{Kd} , together with uncertainties for 3 centrality from the fit to all pair combinations for Pb–Pb collisions at $\sqrt{s_{NN}} = 5.02$ TeV.	131
5.13	The $\langle k_T \rangle$ values of pion–deuteron, proton–deuteron, kaon–proton, kaon–deuteron pairs of particles that contribute to the low k^* range. . . .	134
6.1	The systematic variations of the analysis settings considered in kaon–proton, pion–deuteron, proton–deuteron and kaon–deuteron studies.	140
6.2	The systematic variations of the analysis corrections, background estimation and fit settings used in kaon–proton, pion–deuteron, proton–deuteron and kaon–deuteron studies.	144
6.3	Radii (fm), real and imaginary part of the scattering parameter for kaon–proton analysis obtained for different variations of the fit. The colours indicate the lowest blue and the highest red values.	145

Dedicated to science,
which has always been the light
of my life.

Chapter 1

Preface

One of the most important roles of physics is to understand and describe the world we live in. So it should come as no surprise that many scientists are engaged in a concerted effort to build a universal picture that would explain everything we observe with a single model. Unfortunately, the current state of these efforts can be compared to children in kindergarten trying to solve a 1000-piece jigsaw puzzle. Puzzles where some pieces are missing, have no visible colours, or do not seem to follow the general framework that these children have in mind. Therefore, this thesis focuses on small gaps in knowledge by restoring some colours to mysterious puzzles concerning particles and their interactions.

A great scientific challenge is to study the strong interaction in the strangeness sector. Thanks to quantum chromodynamics (QCD), the fundamental theory of the strong interaction, we are able to describe it well over a wide range of energies. However, things get complicated at low energies, where QCD becomes unreliable due to its non-perturbative nature. Alternatively, at low energies, phenomenological models and effective theories can be used, but these require experimental input in the form of parameters describing the observed interactions. However, in the case of particles composed of strange quarks, this range is very difficult to cover even with such experimental input, which is typically derived from exotic atoms and scattering experiments. Therefore, the parameters of the strong interaction remain unknown or poorly known even for the simplest pairs of strange particles and nucleons. This thesis attempts to shed more light on the strong interaction parameters of the strange sector through kaon–proton and kaon–deuteron studies. These two pairs of particles are specific because their experimental study can also provide an indirect access to the description of the kaon–neutron interaction, since the deuteron consists of both nucleons. Their study thus responds to the request made by theorists more than 40 years ago to determine the isospin-dependent parameters of the strong interaction in

the strangeness sector.

The second motivation for this work relates to interactions with deuterons in general. Deuterons, as mentioned above, consist of both nucleons, which can make them a many body problem. Therefore, studies with deuterons are ideal for testing our models on relatively large particles. This is mainly done through pion–deuteron, kaon–deuteron and proton–deuteron studies. Moreover, such interaction studies can also be used to test a many-body dynamics, which should be particularly evident in the proton–deuteron system. This is because we can easily verify whether the proton sees the deuteron as the two nucleons allowing the application of Pauli blocking.

Finally, since the study of this work is largely based on deuterons, another motivation is to better understand the nature of deuterons in collisions where quark-gluon plasma is present. The production of composite particles such as light ions remains an open question. We still do not know whether deuterons, like other simple particles, are created in the thermal processes of hadronisation, or whether they are created later as a result of off-shell interactions between previously formed protons and neutrons. The first of these mechanisms is surprising for deuterons, since their presence in a very hot fireball with a temperature of the order of 156 MeV would be like the presence of snowflakes in hell with their limiting energy of 2.2 MeV. At the same time, both models are able to describe qualitatively well different experimental observables. In this thesis it is investigated through the source studies especially of pion–deuteron and proton–deuteron pairs.

Chapter 2

Introduction

To, co wiem, nie jest równoznaczne z tym, co istnieje.

Co może istnieć.

Stanisław Lem, *Niezwyciężony*¹

2.1 Standard Model

The Standard Model of Particle Physics (SM) is a state-of-the-art model that explains the fundamental structure of matter and particle interactions [1]. The SM groups all particles into four different classes: quarks, leptons, gauge bosons and the higgs scalar boson, see the Fig. 2.1.

The basic building blocks of matter are quarks and leptons, which are half spin fermions belonging to three mass generations. There are six quarks: *up*(*u*), *charm*(*c*), *top*(*t*) with $+2/3$ electric charge and *down*(*d*), *strange*(*s*), *bottom*(*b*) with $-1/3$ electric charge. The lepton group consists of three particles with -1 electric charge known as *electron*(*e*), *muon*(μ), *taon*(τ) and correspondingly three very light and uncharged *neutrinos*. The higgs scalar boson is responsible for the mass generation of particles at rest. Gauge bosons mediate the interactions between particles. The strong force, whose principles are governed by quantum chromodynamics (QCD), uses gluons to mediate the interaction. The W and Z bosons appear in the weak interaction described by electroweak theory (EWT). Photons mediate charged particles in the electromagnetic interaction governed by quantum electrodynamics (QED). In the fermion family, quarks can interact via all three forces, and leptons can interact electromagnetically (if they are charged) and weakly. Gravity, has not yet been unified with the other three

¹"What I know is not equivalent to what exists. What can exist." – Stanisław Lem, *The Invincible*

Standard Model of Elementary Particles

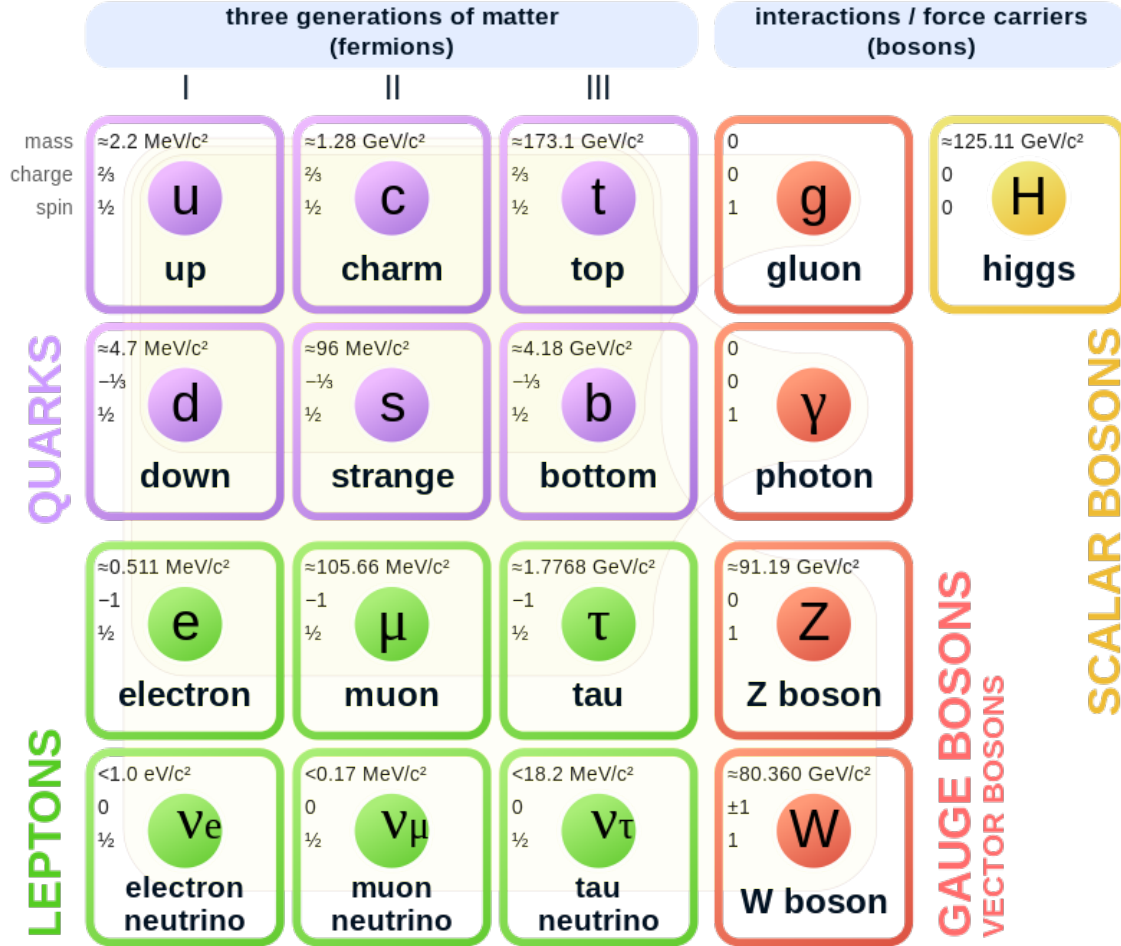


FIGURE 2.1: The Standard Model of Particle Physics. Picture from [2].

forces. SM also does not explain phenomena such as dark matter or dark energy, but it is the best tool we currently have for particle physics.

Quarks and leptons are grouped into three generations, with each higher generation having components of greater mass. Those of the first generation are the most abundant in the observed universe because the heavier ones are unstable and decay quickly into the lighter ones. Quarks also have a *colour* charge which determine possible forms of colourless bound states of multiple quarks, called hadrons. Colour should be understood as a quantum number rather than a colour itself, but for ease of visualisation the colour charge can be expressed in terms of *green*, *blue*, *red* and their

anti-colour conjugations. Hadrons are usually represented by defining their character as two or three valence quarks exchanging gluons. The colour requirement is usually satisfied by combining colours with their anticolours ($q\bar{q}$), three colours or anticolours at once ($qqq, \bar{q}\bar{q}\bar{q}$) or by their combinations (e.g. $qq\bar{q}\bar{q}, qq\bar{q}q\bar{q}$). Hadrons made up of two or three quarks are called mesons and baryons, respectively. All particles in the SM have corresponding antiparticles with the same mass, spin and lifetime as their particle counterparts with a few properties changed to the opposite value such as their colours, electric charges, magnetic moments, baryon and lepton numbers.

In this thesis, baryon–baryon and meson–baryon pairs are considered, which include protons, neutrons, pions, and kaons. Protons, neutrons, and pions are composed of first-generation u and d quarks, while kaons represent the so-called strangeness sector as they contain the s quark.

2.2 Quantum Chromodynamics

This thesis explores high-energy particle collision physics, where particles interact on femtometer scales through the strong and Coulomb electromagnetic interactions. Therefore, such collisions provide an ideal environment to investigate the hadron–hadron strong interaction, which is the subject of a large fraction of this work. The theory describing the strong interaction is QCD, which describes particle interactions via exchange of colour carried by both quarks and gluons. The colour of a quark is not persistent and can change whenever strong interaction occurs, e.g. green quark can become blue if the gluon carries away the colour difference. However, all interactions must comply with the rule of colour neutrality, as net colour does not appear alone under normal conditions. Therefore, requirement of colourless doubled or triplet is a feature of strong interaction called *confinement* [3]. Additionally, gluons always carry one of eight allowed permutations of colour–anticolour that make the QCD a gauge theory based on the SU(3) colour symmetry group. As a consequence, gluons emitted by one quark and absorbed by another can be a subject to the colour-dependent interactions due to their own colour charges. It is a distinctive feature of the strong interaction that the boson mediating the interaction can be an active participant and source of the interaction. Basic examples of quark–quark and gluons interactions are presented in Fig. 2.2.

A characteristic feature of QCD is the *coupling constant* denoted as α_s , which is the fundamental coupling constant that describes the strength of the interaction between

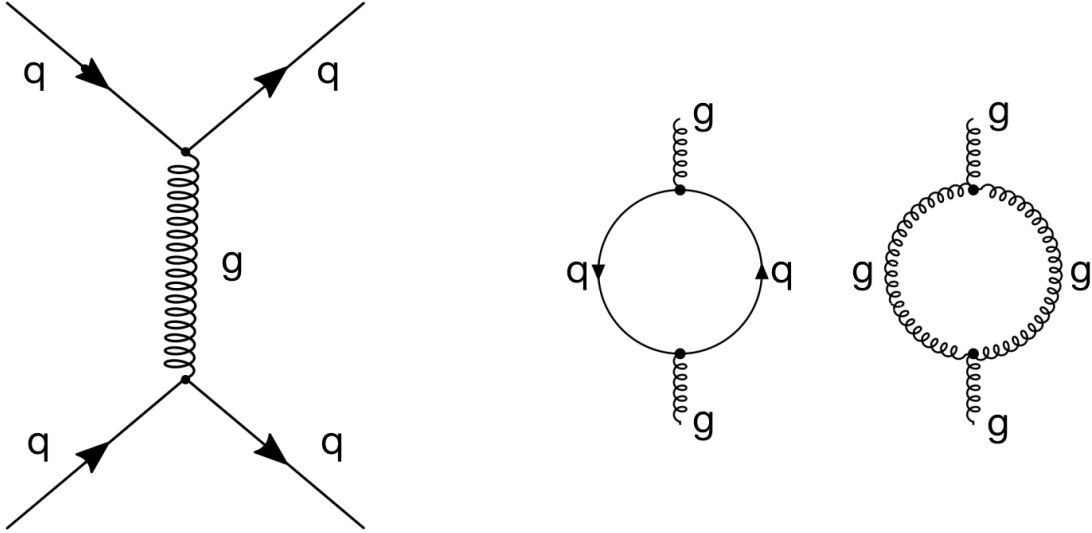


FIGURE 2.2: Right: the first order diagram of a gluon exchange between two quarks. Left: diagrams of leading order quark–gluon and gluon–gluon loop.

quarks and gluons. This constant is introduced in calculations for each of interaction points (vertexes of the diagrams like in Fig. 2.2). Because QCD is a non-Abelian gauge theory which requires renormalization, this is not a constant but rather a function of the energy scale, as expressed by the following equation:

$$\alpha_s(Q^2) = \frac{\alpha_s(\Lambda_{\text{QCD}}^2)}{1 + \frac{11N_c - 2n_f}{12\pi} \alpha_{\text{QCD}}^2 \ln(Q^2 / \Lambda_{\text{sQCD}}^2)}, \quad (2.1)$$

where N_c and n_f are the number of flavours, Q is the momentum transfer, Λ_{QCD} is the QCD scale.

In the case of strong interaction, α_s increases with the decrease of momentum exchange (increase of distance) between the colour charges. Therefore, the separation of two quarks by pulling them apart will cause a drastic increase of the α_s and thus the strong interaction force. If one would like to stretch more this system the cumulative energy would be so large that energetically the creation of a new quark-antiquark pair would be more favourable. Such a pair would be latter coupled to the original quarks preserving the colour confinement.

Another feature of the strong interaction is its *asymptotic freedom* [4, 5] that appears when one looks at the running strong interaction constant from an opposite side, thus when the momentum exchange is big (the distances are small). If the system is hot or dense enough the quarks and gluons can be asymptotically free, they almost do not interact and form the Quark–Gluon Plasma (QGP) that existed at the beginning of the universe and can be present still in the cold form inside neutron stars. The QCD coupling constant, α_s , change with the momentum exchange is presented in Fig. 2.3.

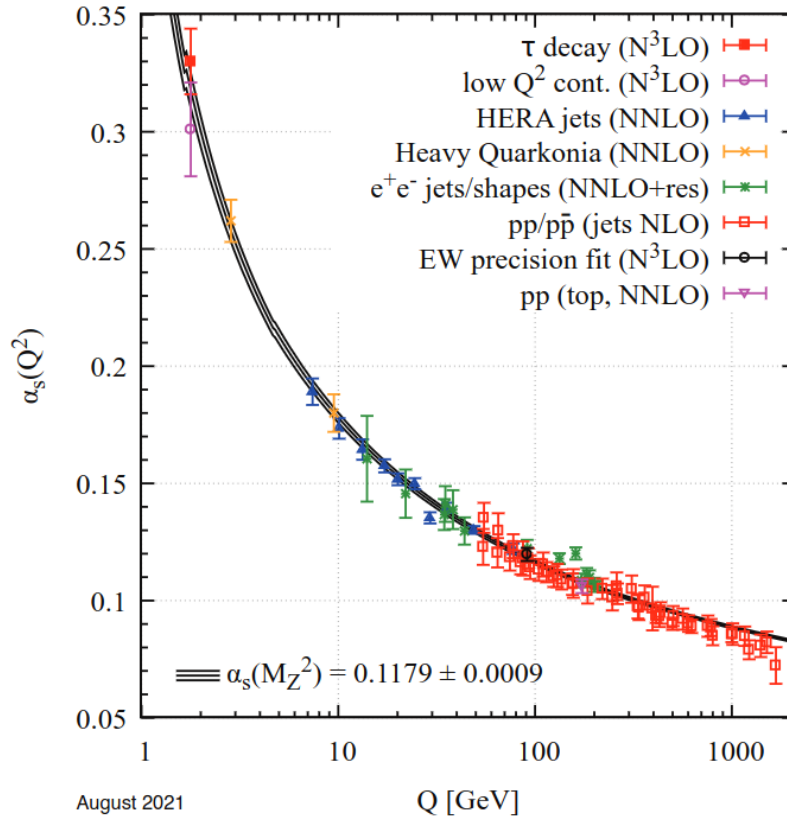


FIGURE 2.3: Summary of measurements of α_s as a function of the energy scale Q . Figure from [6].

2.3 Mass of particles

To begin, consider a fundamental nucleon, specifically a proton. The rest mass of the proton is known to be $938.272 \text{ MeV}/c^2$. However, referring to Fig. 2.1, the construction of a proton from uud quarks results in a mass of only $9.1 \text{ MeV}/c^2$. To explain this discrepancy, it is necessary to look more closely at the structure of the nucleon and

the internal processes. Deep inelastic scattering experiments on protons have revealed that the valence quarks of the nucleon contribute only a small fraction of its spin [7]. This observation is due to the presence of additional components within the particle, often described as a sea of quark–antiquark pairs. The sea of quarks arises from the fact that the gluon can interact with itself. As a result, particles made up of only a few valence quarks also contain gluons and quark–antiquark pairs that are rapidly created and destroyed during interactions. However, the presence of both sea and valence quarks cannot explain the entire mass of the proton.

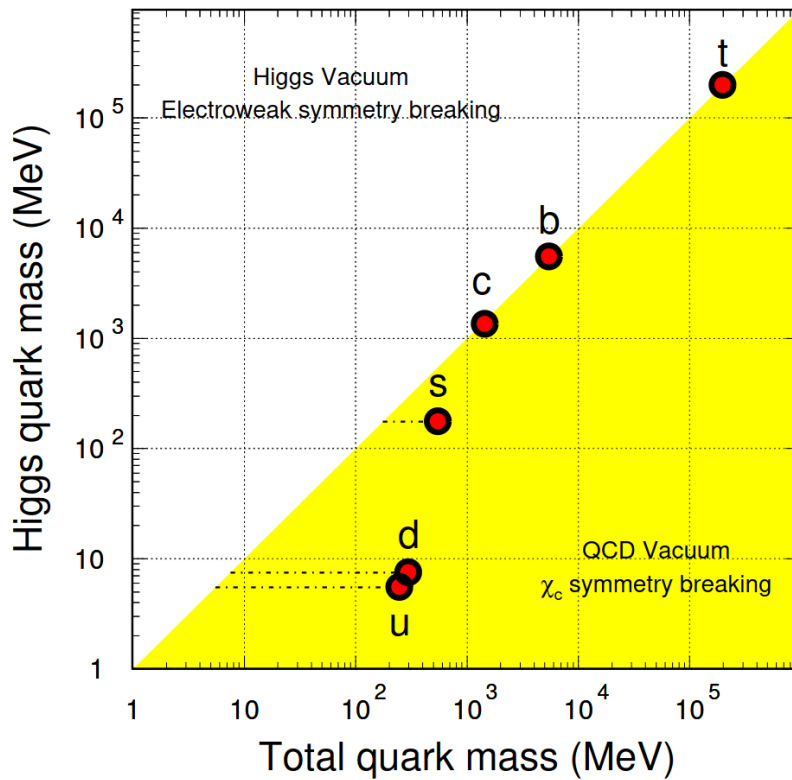


FIGURE 2.4: The masses of the six quark flavors (red circles) gained through the interaction with the Higgs field alone and with additional spontaneous chiral symmetry breaking in QCD shown in y-axis and x-axis, respectively. Picture from [8].

For a complete understanding, it is also necessary to consider the governing physical principles under extreme conditions. According to the strong interaction theory of the SM, quarks and leptons are initially massless. The mass of the particles acquired through interactions with the Higgs field [9] is shown in Fig. 2.1. Prior to this process, particles in the SM must obey to chiral symmetry. Massless particles are characterised by helicity eigenstates and have a defined chirality. This symmetry is disrupted when

the Brout-Higgs-Englert mechanism [10, 9, 11] for mass generation is introduced. The explicit chiral symmetry breaking comes from non-zero mass of u and d quarks that in consequence leads to a spontaneous symmetry breaking of the QCD vacuum dressing quarks in the additional effective mass from the QCD interaction including those arising between sea quarks. The generation of mass by chiral symmetry breaking is most significant for the lightest quarks, the u , d and s . Thus, the nuclei gain an additional 95% of mass through the process of symmetry breaking. Fig. 2.4 shows the scale of the breaking. The strange quark is known to play a special role because of its intermediate mass. It is light enough to permit a chiral expansion, yet sufficiently close to the perturbative QCD scale, Λ_{QCD} that the sea of $s\bar{s}$ quark pairs in the QCD vacuum cannot be neglected. This makes all studies of the strange sector particularly important, e.g., to explain phenomena such as the mass of neutron stars.

2.4 Hadron–hadron interactions

The study of hadron–hadron interactions is a crucial area of research in particle physics, directly linked to understanding of QCD. At high energies, where the strong coupling constant α_s becomes weak, QCD can be studied using perturbative methods. These techniques break down complex problems into simpler ones, incorporating various effects as small disturbances. The high-energy regime of QCD, thereby, has been tested with astonishing precision both in theory and experiment. Conversely, at low energies (below $\sim 200 \text{ MeV}/c$) α_s increases significantly, rendering perturbative theory inapplicable. In this regime, the strong interaction between quarks and gluons dominates, leading to their coupling into bound states, such as hadrons, which serve as the effective degrees of freedom. Corrections in this regime become large and unpredictable, and perturbative theory provides infinite values of α_s at finite, non-zero scales. To study the low-energy QCD regime non-perturbative methods, phenomenological approaches and effective theories are utilized, all of which rely on experimental inputs.

There can be distinguished three main groups of experimental techniques that serve the purpose of strong interaction studies at low-energy regime: scattering experiments, exotic atom experiments, and femtoscopy technique. These experimental methods are presented schematically in Fig. 2.5.

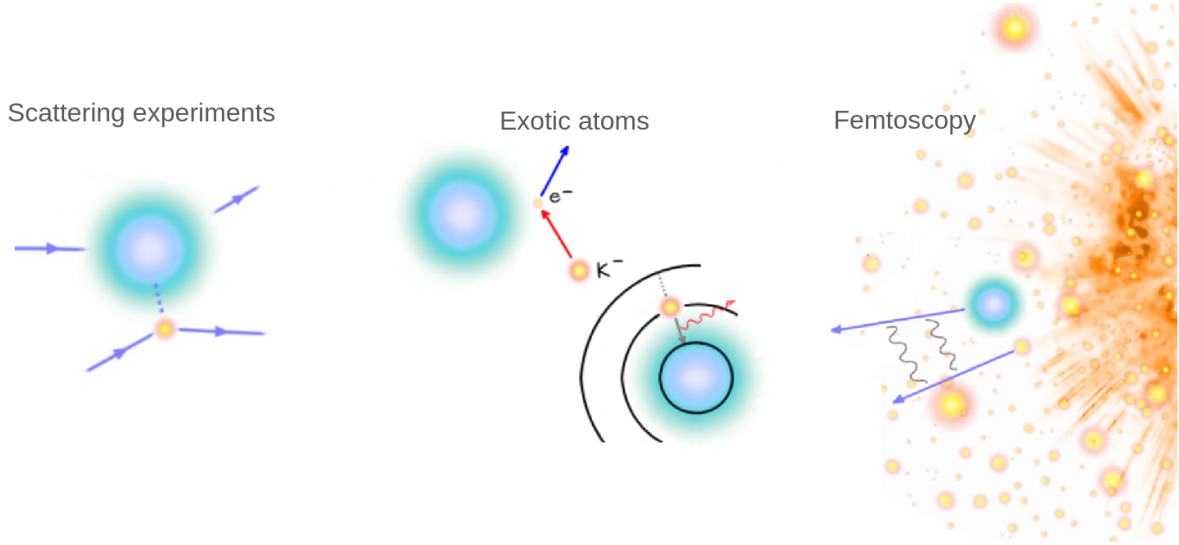


FIGURE 2.5: Schematic representation of experimental techniques used for interaction measurements among pairs of hadrons. From left to right: scattering experiments, exotic atom experiments, femtoscopy.

Scattering experiments study the scattering of a particles' beam on a target. The pattern of scattering provides insights into the underlying interactions. In this type of experiment, the initial and final states of the particles are precisely controlled. However, there are several limitations; first, the projectiles have to be long-lived to create the beam, a challenging condition for studying strange hadrons or antimatter [12]. Second, scattering experiments can face difficulties in achieving zero or very low relative momentum due to the difficulties of precisely controlling experimental conditions, including beam accuracy, measurement sensitivity, and managing background noise, which becomes more pronounced for low-momentum particles. Therefore, for some particle pairs such as those in strangeness sector, the current accuracy of measurements of cross sections and branching ratios at the threshold is not sufficient to measure the scattering amplitudes precisely.

Another important group of experiments is the study of exotic atoms. In particular, experiments in which one electron of the atom is replaced by a negatively charged particle, such as a pion, a kaon or even an antiproton. Because these are hadrons, the presence of the strong force modifies the electromagnetic interaction. As a result, the energy levels are shifted compared to the case of only electromagnetic interaction. Such exotic states exist for a short time before the de-excitation process takes place, from which X-rays can be measured. These X-rays can be used to access information

about the shifts and widths of the energy levels in exotic atoms [13, 14]. The exotic atom experiments allow for interaction measurements at the kinematic threshold. Nevertheless, this method faces some limitations, e.g. the electron can be replaced only with a negatively charged particle. Also, the performance of exotic atoms experiment for several particle species, i.e. kaon–deuteron is very challenging due to, among others, its very wide state and low X-ray yield.

The last significant group of the strong interaction studies are high-energy collision studies. The hadrons produced after particles collisions, are typically related to the low energies of the QCD scales, and therefore, they are a perfect probes for the challenging low-energy QCD. Such experiments provide an abundant source of various particle species (including strange hadrons). For instance, the number of charged particles created in a central Pb–Pb collision at the top energy available in the world is on the order of thousands [15]. The tool used to access the strong interaction is the femtoscopy technique. In femtoscopy, we measure the correlation between two or more particles as a function of their relative momentum. Correlation functions can be described with different models expressing the interaction nature. Therefore, the main limitation of this technique is the production of rare particles and the model dependencies in measurements of the interaction parameters. The femtoscopy itself is the main tool used in this thesis and it will be described in more detail in Sect. 2.6.

From the theoretical point of view, the problem of low-energy QCD is usually approached by approximate effective perturbative theories or by numerical solutions to the non-perturbative problem. The first nuclear force theory was proposed by Yukawa [16]. In his theory, the strong interaction between nucleons (pp, pn, nn) is mediated by charged mesons. The meson-exchange principle is used until now as it provides qualitatively good predictions. The typical nucleon–nucleon potential is presented in Fig. 2.6. Such nuclear interactions are divided into three regions: long-range, intermediate/medium-range and short range. The first one, long-range, covers typically the range of relative distances above ~ 2 fm and is characterised by single pion exchange (at such small energy scales pions are the relevant degrees of freedom to describe the strong interaction between nucleons). The second, the intermediate range, covers the relative distance span between ~ 1 – 2 fm where two-meson (not only pions) exchange can happen. The last one, the short-range, corresponds to distances below ~ 1 fm. In this range, quarks and gluons became active degrees of freedom.

The idea of a range-dependent nucleon–nucleon interaction including descriptions based on meson exchange has been applied in various models, e.g. [17, 18, 19]. To account for different effects of the interaction, such estimations use mainly *phenomenological models*, *effective QCD* theories, and *Lattice QCD* calculations. Symmetries such as rotation, translation, and isospin play an important role in phenomenological models [19]. Most of them include a set of free parameters that

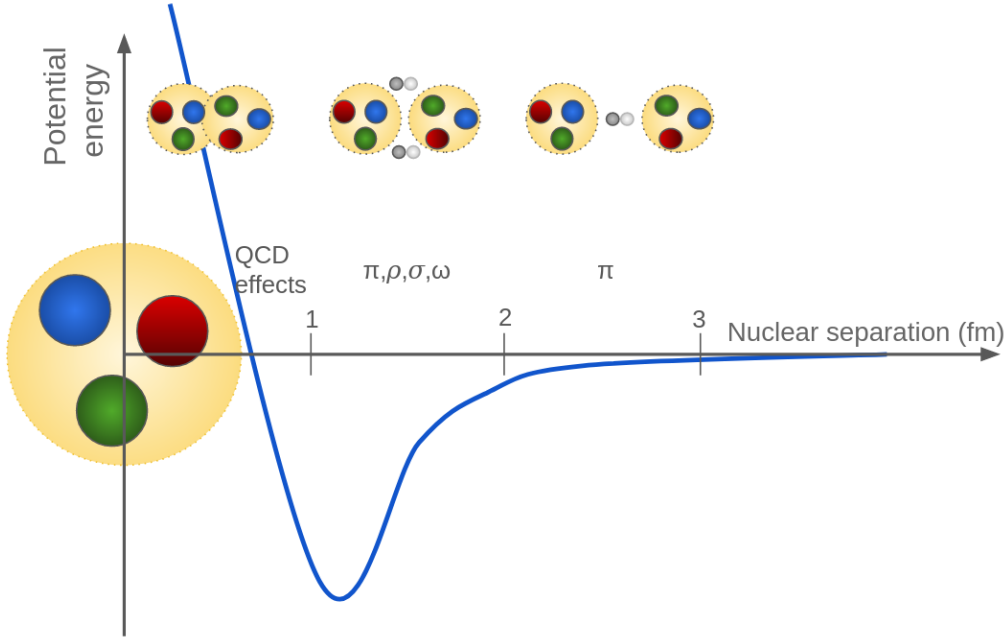


FIGURE 2.6: Schematic illustration of typical nucleon–nucleon potential together with characteristic interaction regions of short-, medium- and long-range effects.

are constrained by fits to scattering data. The hadron–hadron interaction can also be studied through effective QCD theories [20, 21], such as the chiral effective field theory (χEFT). χEFT at the low-energy scale uses pions (not quarks and gluons) as force mediators, which highly reduces the available degrees of freedom, and in the short-range distances, it uses a contact term (interaction localized at single point in space) that parametrizes QCD effects. The interaction potentials are constrained in order to reproduce the available scattering data. Similarly to phenomenological models, χEFT includes combinations of central terms that are components that do not depend on the direction of the relative positions or momenta of the nucleons. Usually, they are spin-spin, spin-orbit, and tensor terms responsible for the strong nuclear interaction. However, an important difference is that χEFT is based on an effective

Lagrangian, including terms and symmetries (also their breaking) of the underlying theory. An interesting feature of χEFT is the ordering of terms according to their relevance. This feature arises naturally as χEFT is perturbative, and therefore the order of the inclusion of effects matters. For example, the strangeness of $S = -1$ is included in the leading and the next-to-leading order processes (LO and NLO), the 3-body effects, in turn, become relevant starting from the next-to-next-to-leading order (NNLO) accuracy. However, if one would like to stress more the 3-body interaction it is still possible, i.e. by including a heavy excited baryonic state, as an effective mediator of the strong force. Another feature of χEFT is the accurate treatment of channels connected to symmetry breaking. Coupled channels appear at the hadron level when two systems have identical quark content. Therefore, it refers to a situation where different quantum states or channels interact with each other due to their underlying dynamics. This leads to mixing of the states and influences the physical properties of the system. The difference between the two systems can originate from other numbers (i.e. isospin) so, the wave function of the system is then symmetrized in different way for each of the coupled channels, which is later reflected in their masses and decay modes. However, the interaction of all channels is entangled and the total wave function comprises all channels. The coupling effects are especially manifested in small systems (i.e. pp collisions) where the combination of high sensitivity to the different channels and accurate experimental data make it possible to resolve their individual structures.

The above described potential approach works well, however, it is not based on first principles: quarks and gluons as degrees of freedom (see more potentials in [22]). One of the non-perturbative methods for calculations of the interaction between hadrons is lattice QCD (LQCD) [23]. LQCD is a numerical approach that includes quarks and gluons as degrees of freedom to describe a quantum chromodynamical system. Space and time are described as a four-dimensional lattice. Calculations of the QCD are gauge invariant and non-perturbative. The finite and discrete volume of the lattice is extrapolated towards the limit of zero lattice spacing and infinite volume approaching a continuum. The initial conditions allow for a finite number of degrees of freedom and the possibility to perform numerical computations for all variables. Lattice calculations do not require many input parameters, only the couplings and the masses of the quarks. However, this method is not suitable for all the cases and is demanding from computational point of view. It is because, as the particles involved become lighter, the computational cost increases significantly. That is why it is a

common practice to artificially increase the masses of the particles and extrapolate the results from these modified values. Systems which contain heavy quarks as those with one or more strange, top, or bottom quarks, are relatively accurate in the calculations in comparison to light flavoured hadrons. Other descriptions of non-perturbative methods for the determination of the strong interaction between hadrons [24] are the Dyson-Schwinger Equations [25, 26], the Operator Product Expansion [27] and the Gribov-Zwanziger approaches method [28, 29].

2.5 Relativistic heavy-ion collisions

Collisions of ultra-relativistic nuclei can be used to achieve high energy densities in a volume characteristic for the nuclear scale. The bigger the initial velocity and the more participants in the collision, the larger the energy exchange at the point of collision. The first instant of the collision when partons (quark and gluons) transfer large momenta and hard processes occur is called the pre-equilibrium stage. The energy released in the first stage leads to a drastic growth of the energy density and the energy density which permits the deconfinement of partons from individual nucleons. When the new state of free partons is thermally equilibrated it forms QGP. The QGP state does not last long as the system expands and, therefore, cools down. Then, the system reaches the critical energy density and the deconfined quarks and gluons undergo a phase transition known as hadronization, during which they combine to form color-neutral hadrons. This process ends with the chemical freeze-out. At this stage, all particles stop interacting in an inelastic way. Furthermore, because of system expansion and cooling, particles stop interacting, and their kinetic energy does not change any longer. The stage is known as the kinetic freeze-out. An illustration of the evolution a heavy-ion collision with and without QGP state is shown in Fig. 2.7.

2.5.1 The quark-gluon plasma

The QGP is a state of matter that appears under extreme conditions of temperature and pressure. Its nature can be visualized on the phase diagram of nuclear matter as a function of temperature and the baryon chemical potential μ_B , as illustrated in Fig. 2.8. In particular, this diagram indicates the phase boundaries between hadron matter, QGP and the colour superconductor phase. However, most of the phase transitions are not well constrained experimentally. Recent efforts have focused on mapping the

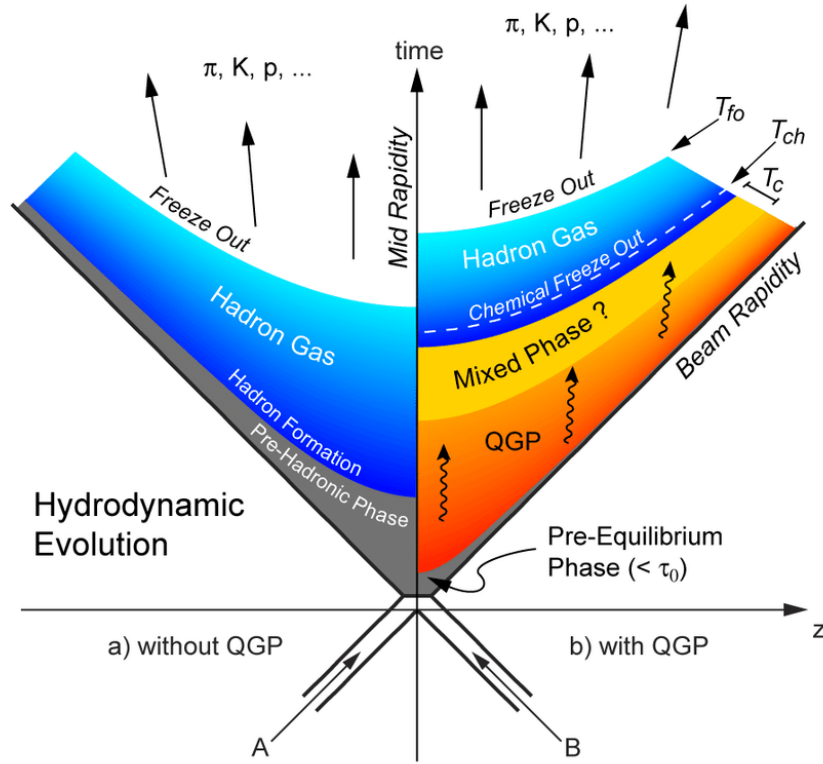


FIGURE 2.7: Schematic views of heavy-ion collision evolution (from bottom to top). The left and right sides represent the evolution without and with the QGP state. Picture from [30].

QCD phase diagram both theoretically, through lattice QCD, various effective theories, and phenomenological models and experimentally, through facilities like BNL [31], CERN [32], FAIR [33], NICA [34]. The LHC energies, being the subject of this thesis, provide conditions with vanishing μ_B . According to lattice QCD calculations, the crossover between two states at a very small μ_B should occur at a temperature around 150 MeV [35]. Experimentally, the crossover temperature has been constrained to ~ 155 MeV [36, 37].

The QGP created under laboratory conditions exists for an extremely short time $\sim 10^{-23}$ s [39, 40]. The temperature of the phase transition is equivalent to $\sim 1.8 \cdot 10^{12}$ K and is 10^5 orders of magnitude higher than the temperature of the center of the Sun. Therefore, it is impossible to directly measure the QGP state. What we measure in the detectors are particles in their final state, which are the product of the hadronization process or further unstable particles' decays. Because of that, the information about the early stages of the collision can be difficult to access experimentally. The presence

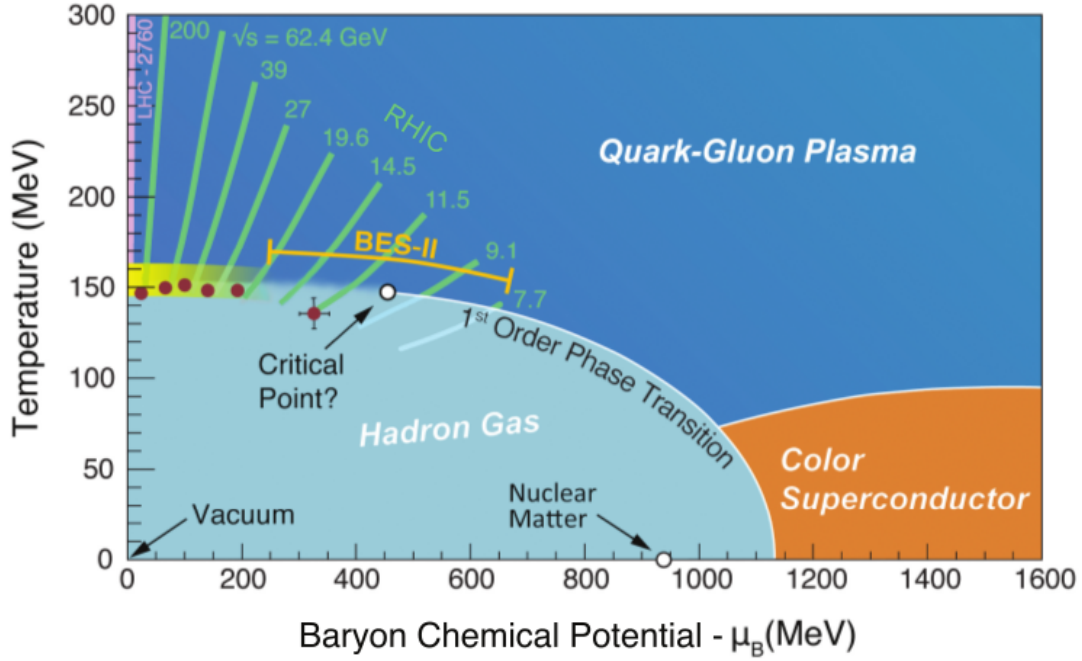


FIGURE 2.8: A phase diagram of nuclear matter as a function of temperature and baryon chemical potential μ_B . Figure from [38].

of this state of matter is proven by several signatures [41] and the discovery of QGP cannot be identified with a single observable. A detailed history of QGP discovery can be found in [42]. Below selected signatures of the QGP state are shortly described:

- strangeness enhancement: the net strangeness before the collisions is close to zero, therefore every strange particle registered after the collisions is produced in it. To produce the lightest meson containing a strange quark, a kaon, the system has to have energy sufficient for its production. The weight of kaon with single s/\bar{s} quark in hadron gas is ~ 500 MeV. However, in presence of QGP, the gluon fusion is allowed, and $s\bar{s}$ pairs can be created at a significantly lower energy threshold of ~ 300 MeV, which should increase the production of strange particles. The strangeness enhancement has been observed, demonstrating a stronger enhancement as a function of the number of constituent strange quarks. Some examples of measurements can be found in [43, 44].
- enhanced production of photons from the QGP (direct photons): photons have a small interaction cross sections, and therefore they can be used as a penetrating probes of the space-time evolution of the system. These photons are produced throughout all stages of the collision, and if the QGP is present,

a fraction of them should originate from this stage. Therefore, by analyzing the transverse momentum distributions of photons, one can show production excesses of thermal photons originating in QGP and subsequent stages of the system evolution over prompt photons that are emitted before QGP equilibrium. The momentum distributions of photons from the QGP reflect the momentum distribution of quarks and gluons within the plasma state. These measurements provide an access to the temperature of the QGP phase before the freeze-out. However, conducting this study is challenging because only a small fraction of photons can be classified as direct, and their identification and determination of the three-momentum are further complicated by their infrequent interactions compared to hadrons. Some examples of experimental studies of direct photons confirming the QGP state can be found in [45, 46].

- suppression of hadrons containing charm and beauty quarks: it is a consequence of a screening effect, analogous to Debye screening observed in electrodynamics but applied to the strong force, on $c\bar{c}$ and $b\bar{b}$ pairs. Such a screening effect reduces the binding strength of the quark-antiquark pairs due to the high density of quarks and gluons. Therefore, in case of QGP, these heavy quark pairs "dissociate". In consequence, in the QGP, the suppression of J/ψ meson that is a bound state of a $c\bar{c}$ is expected due to its dissociation into D mesons that contain one c/\bar{c} quark. This expectation is supported by observed significant reductions in the production rates of charmonium and bottomonium states in heavy-ion collisions compared to proton-proton collisions [47, 48].
- jet quenching: particles produced in the initial parton-parton scattering escape the source with very high momentum, and since they cannot exist independently, they undergo fragmentation into a shower of hadrons. Such hadron ensembles are produced in a narrow cone known as a jet. Jets have been studied extensively, particularly in pp collisions. In heavy-ion collisions, the jet can be diluted by energy loss because it must pass through the dense QGP medium. As the primary parton traverses the medium, it undergoes elastic (collisional) energy loss which is expected to scale linearly with the path length of the traversing parton and radiative energy loss which exhibit an approximately quadratic dependence on path length. The energy reduction of jets in heavy-ion collisions is called "jet quenching". See some examples of the jet quenching observations in experimental studies in [49, 50].

2.5.2 Collectivity

The sign of a formation of almost ideal liquid in heavy-ion collisions is the collectivity of the created system. This behaviour is observed through momentum-space correlation patterns, also called flow. Collective behaviour of hadrons introduces non-trivial event-wise particle correlations and therefore this phenomena is described below in more detail.

The collision of two ions can be spatially oriented in the laboratory frame using the beam direction (z -axis) and the vector representing the distance between the centers of the colliding nuclei, known as the impact parameter (the relative distance between the centers of colliding nuclei at their closest approach). The plane defined by the beam direction and the impact parameter is known as the reaction plane. In that frame the y -axis refers to the direction perpendicular to the beam line reaction plane, x is the third cartesian axis. The geometry of the collision defines the angular distribution of particles, which can be Fourier-decomposed:

$$E \frac{d^3N}{dp^3} = \frac{1}{2\pi} \frac{d^N}{p_T dp_T dy} \left(1 + \sum_{n=1}^{+\infty} 2v_n(p_T, y) \cos[n(\phi - \Psi_n)] \right), \quad (2.2)$$

where Ψ_n is the azimuths of the estimated participant reaction planes, ϕ is the azimuthal angle of outgoing particles, v_n are Fourier coefficients defined as:

$$v_n = \left\langle \cos[n(\phi - \Psi_n)] \right\rangle \quad (2.3)$$

The harmonics of the Fourier decomposition with the most prominent magnitudes are called as *directed*, *radial* and *elliptic* flows. They are schematically shown in Fig. 2.9.

The directed flow is created in the pre-equilibrated phase of the collisions and therefore is sensitive to the early pressure gradients in the evolving nuclear matter. This flow should be understood as a collective deflection of particles in the reaction plane. Directed flow can be calculated as a first-order (v_1) harmonic of the Fourier expansion of a particle distribution [51]. The larger is the energy of the collision per nucleon $\sqrt{s_{NN}}$ the smaller directed flow.

Shortly after collision the system does not have a high transverse velocity. This velocity arises due to hydrodynamic expansion originating from the non-zero pressure gradient of the fireball. We can distinguish flow in the longitudinal direction (along

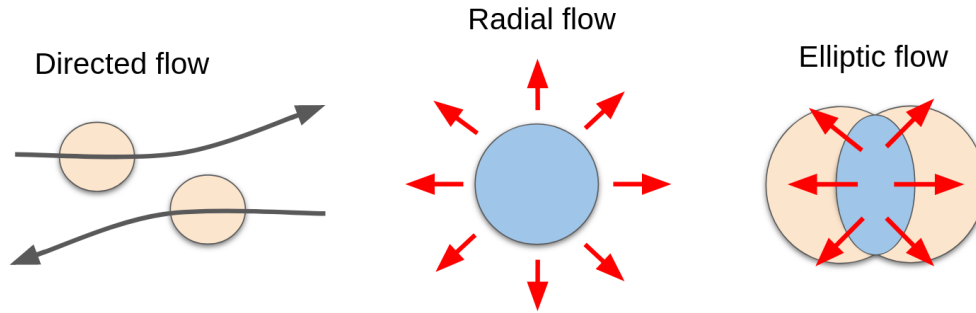


FIGURE 2.9: Geometrical illustration of first order Fourier decomposition of flow patterns. From left to right: directed, radial and elliptic flow.

the beam axis) and this in transverse directions (perpendicular to the beam axis). An average in the transverse direction is called radial flow [52, 53, 54]. For a collision with perfect overlap of ions it is isotropic. It corresponds to inside-out movement due to which particles are pushed away from the center of the collision reaching higher momenta. It is the main and by far the largest fraction of the Fourier expansion (identified as v_0). Radial flow is analysed using transverse momentum spectra distributions.

The colliding ions do not have to perfectly overlap and therefore formed structures are more almond than spherically shaped. Therefore, the flow in the transverse direction becomes anisotropic which is reflected in the moment distributions of particles. Non-central collisions characterize different density gradients and pressure distribution along the in-plane direction of the formed system which is characterised by more intensive radiation of particles along the direction of the reaction plane. This contribution is known as the elliptic flow [52, 53, 55] and is a second Fourier component (v_2).

The observed physics of flow depends on common relations of three velocities: thermal velocity (depends on the temperature and the mass of the particle), average radial expansion velocity and anisotropic velocity. In non-central collisions with presence of elliptic flow the anisotropy velocity will contribute negatively/positively in the out-plane/in-plane direction, which is schematically shown in fig. 2.10. This means that the part of the system that initially had smaller radii will expand faster. Moreover, models describing the evolution of the system using relativistic hydrodynamic equations predict a clear mass ordering of elliptic flow [56]. As the collective radial motion boosts particles to higher average velocities, heavier particles gain more momentum than lighter ones.

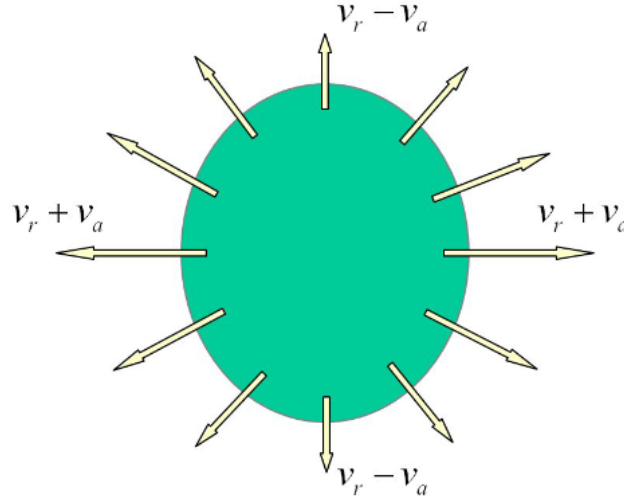


FIGURE 2.10: Schematic representation of the interplay between the radial and elliptic flows. Picture from [53].

2.6 Femtoscopy

The femtoscopy technique originates in particle interferometry that has been initially motivated mainly by two-photon correlation studies in astronomy (known as Hanbury-Brown–Twiss (HBT) [57, 58]). Later, it was found that this method provides similar results to those coming from two identical-bosons quantum effects of momentum correlations for close particle sources (first experimental [59] and theoretical [60, 61] works). The main difference between the two, is that in astronomy it is measured the light intensities, whereas in particle physics, this approach is employed to measure the yield of particle pairs as a function of their relative momentum. Therefore, the original correlation studies served the purpose of finding the angular size of the particle-emitter, such as the size of stars, through measurement of the momentum spread of registered particles. In the case of application of this method to small-radiating sources the measured size does not reflect the overall size because the study concern the space-time spread of particles from the emitter identified as its homogeneity region [62, 63]. Such homogeneity region should be understood as an area of the source from which particles are emitted with similar velocities and directions. Later, the technique has been further developed into the direction of small radiating sources [64, 65, 66, 67, 68, 69], allowing for studies of the space-time structure of the expanding sources such as those that are created, i.e.

in particle and heavy-ion collisions. This particular application of the technique to the study of the correlation of particles originating from small sources is known as femtoscopy, and its detailed overview can be found in [70].

The particle correlation encodes interaction between the particles and the source. The femtoscopic correlation function can be illustrated as in Fig. 2.11 and expressed by the Koonin-Pratt formula [64, 71]:

$$C(\vec{k}^*) = \int S(\vec{r}^*) \left| \Psi(\vec{k}^*, \vec{r}^*) \right|^2 d^3r^*, \quad (2.4)$$

where $\vec{k}^* = (\vec{p}_1 - \vec{p}_2)/2$ is half of relative momentum of two particles in the pair rest frame (PRF, the pairing centre of mass is at rest, $\vec{p}_1 = -\vec{p}_2$), \vec{r}^* is the relative separation vector, $S(\vec{r}^*)$ is two-particle emitting source function and $\Psi(\vec{k}^*, \vec{r}^*)$ is the pair wave function.

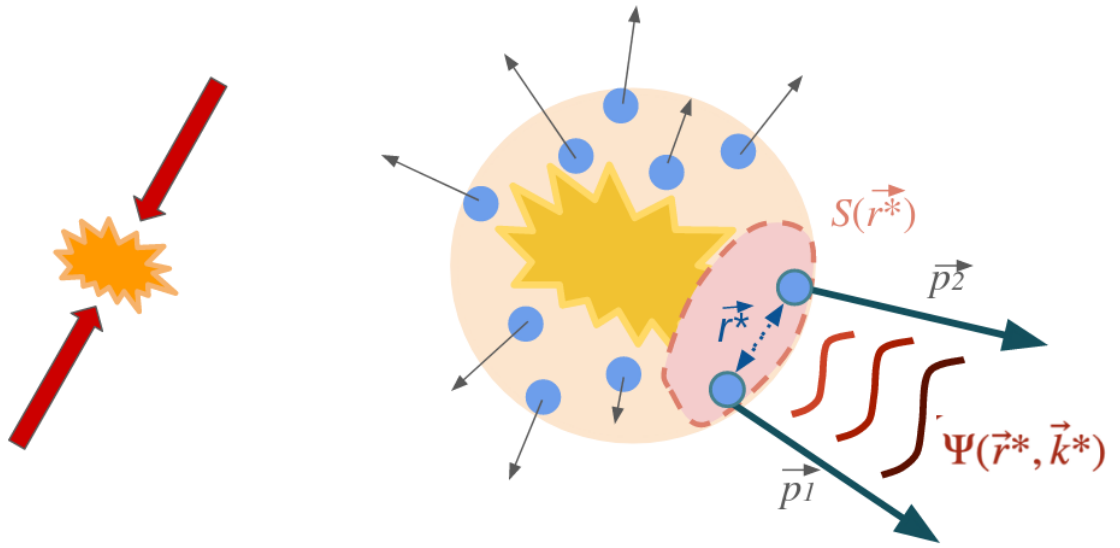


FIGURE 2.11: Illustration of the femtoscopy technique. Two particles/ions collide creating a particle-emitting source. The drawing shows a schematic measurements of the emitted correlated pair that contribute to certain homogeneity region building the source function. Particles on their emitting paths can interact among them, which is reflected by their wave function.

2.6.1 Source function

The source part in the correlation function definition corresponds to the description of the homogeneity region and therefore, all femtosopic sizes/radii/widths mentioned in this thesis do not refer to the overall size of the source created after collisions. The definition expressed in Eq. 2.4 is a three-dimensional integral over the source distribution that is usually defined using the Gaussian parametrization. Such parametrization is a standard description which applied to different experimental studies enables basic comparisons of sources parameters. The definition of the source using the Longitudinal Co-Moving System (LCMS) frame, which is schematically shown in the Fig. 2.12 can be defined as:

$$S(\vec{r}) \sim \exp \left(-\frac{r_{out}^2}{2R_{12out}^2} - \frac{r_{side}^2}{2R_{12side}^2} - \frac{r_{long}^2}{2R_{12long}^2} \right), \quad (2.5)$$

where $r_{out/side/long}$ expresses the relative distance of particle 1 and 2 in a pair ($r = r_1 - r_2$) in *out*, *side* and *long* directions along each axis of LCMS frame; $R_{12out/side/long}$ describe the two-particle source radii at certain direction (see Fig. 2.13).

The R_{12} is the two-particle source radii coming from pair of particles 1 and 2. The two particle source is an effect of convolution of two Gaussian distributions [72] and therefore the R_{12} is:

$$R_{12} = \sqrt{R_1^2 + R_2^2}, \quad (2.6)$$

where R_i is the homogeneity lengths of a certain particle. In identical particle studies R_1 and R_2 are equal and the radii can be simplified to $R_{12} = \sqrt{2}R_1$. In non-identical studies, the R_i of each particle can be different as the correlation refers to different particles that meet having similar velocities, not other characteristics.

The three-dimensional analysis is a precise description of the source as it can reflect the sources that is characterised by an anisotropy and time-dependence [73]. Such disturbances lead latter to differences in the width of the Gaussian distribution in spatial directions [70], that is schematically shown in Fig. 2.13. Three-dimensional analyses allow study of the source geometry in detail and are usually applied to particles such as pions [70, 74] or kaons [75]. However, the studies of low-abundant particles species are reduced to the analysis of one-dimensional source where particles, described at their center of mass frame, are moving slowly to each others minimizing the effect of non-equal emission time for $k^* \rightarrow 0$. Such downgrade to

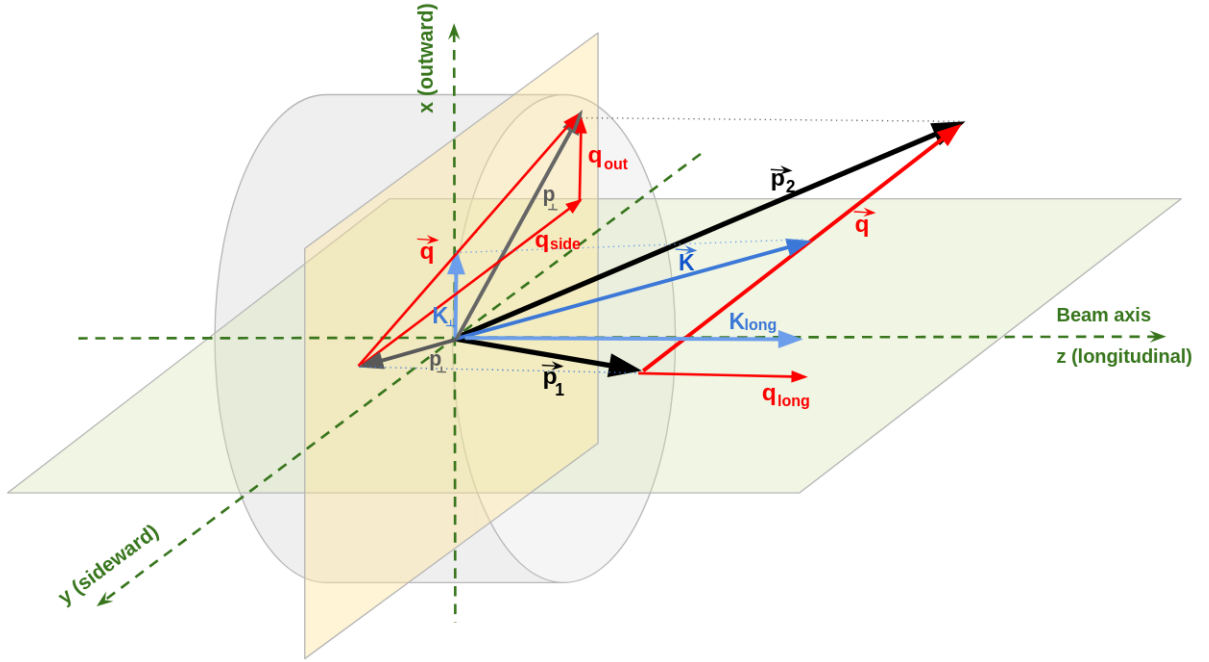


FIGURE 2.12: The three-dimensional visualisation of the LCMS frame.

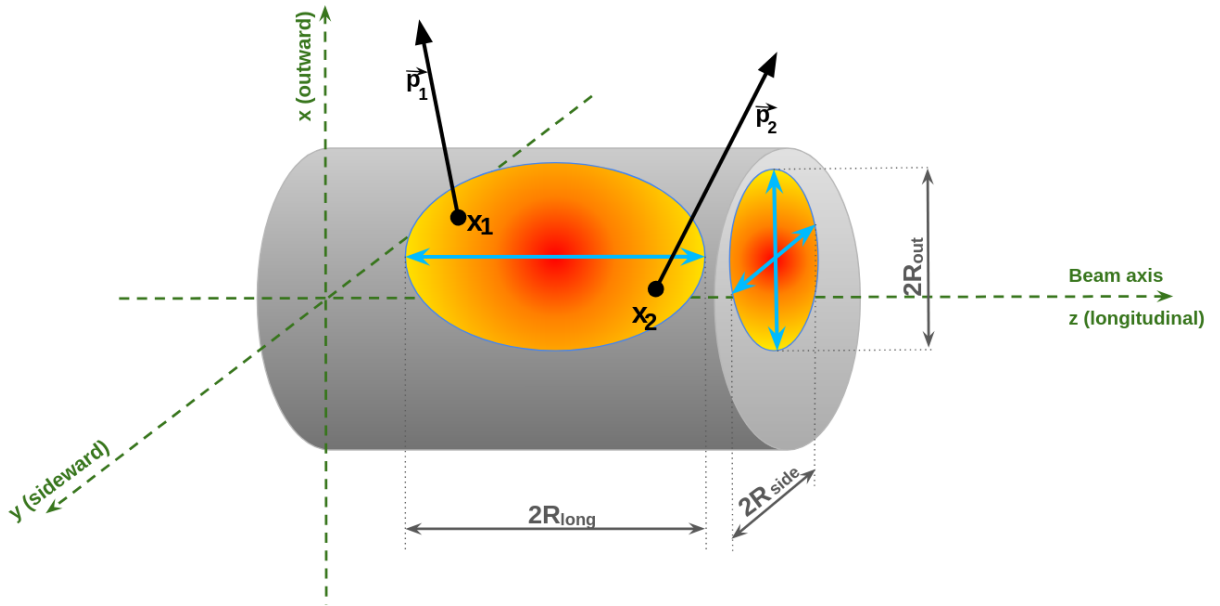


FIGURE 2.13: The three-dimensional visualisation of the homogeneity region (orange) and corresponding radii seen in LCMS frame.

one dimension does not provide direct observables of the source but a non-trivial average information over three directions. It is therefore a less-trivial solution of the

source than the three-dimensional case. Because this work concerns relatively rare particle species the source measurement is performed through such one-dimensional description, which is defined by the following formula:

$$S(\vec{r}^*) = \left(\frac{1}{2\pi R_{12}^2} \right)^{\frac{3}{2}} e^{-\frac{r^{*2}}{2R_{12}^2}}, \quad (2.7)$$

where r^* denotes the particles separation in the PRF ($\vec{p}_1^* = -\vec{p}_2^*$).

It is important to underline that the source radii depend on the particle species, collision type and energy. So far, we observed experimentally several universal scaling dependencies of femtoscopic sizes. Firstly, for a given colliding system and collision energy a linear scaling of the femtoscopic radii is observed versus cube root of the final state particle multiplicity $\langle dN_{ch}/d\eta \rangle^{1/3}$ [76, 77, 78, 74, 79, 77, 80, 81]. A similar scaling across collision energies and colliding systems is only approximate. Secondly, the radii versus the pair transverse momentum (m_T) exhibit a power-law-like scaling [82, 83, 84, 85, 76, 77, 86]. The m_T can be defined as:

$$m_T = \sqrt{\langle k_T \rangle^2 + m^2}, \quad (2.8)$$

where $\langle k_T \rangle$ is an average pair transverse momentum $k_T = |\vec{p}_{T1} + \vec{p}_{T2}|/2$, and m is the rest mass of particle. The higher m_T the larger is the confinement of the source as illustrated with red and blue regions in 2.14. In heavy-ion collisions, both of the scalings are predicted by hydrodynamic models [87, 88, 89]. Specifically, the m_T scaling is explained as a direct consequence of the collective radial flow of the system [72].

The source size have a direct impact on the shape of the correlation function because the smaller the size the more pronounced the interaction effects. Originally, the source characteristics were one of the main outcome of the femtoscopic studies as for many particles species, e.g. pion-pion the interaction parameters are well known. Therefore, the correlation functions can focus on the source parameters based on particular shape of experimental correlation function. However, the role of femtoscopy can be extended for interaction studies. For this purpose, scattering experiments or exotic atoms experiments were used. Nevertheless, in particles of the strangeness sector or those that are rare, these experiments are very challenging, and femtoscopy is unique to provides access to the interaction at very low relative momentum. However, the interaction is only part of Eq. 2.4 and to precisely control the measured output a description of the source part should be determined before.

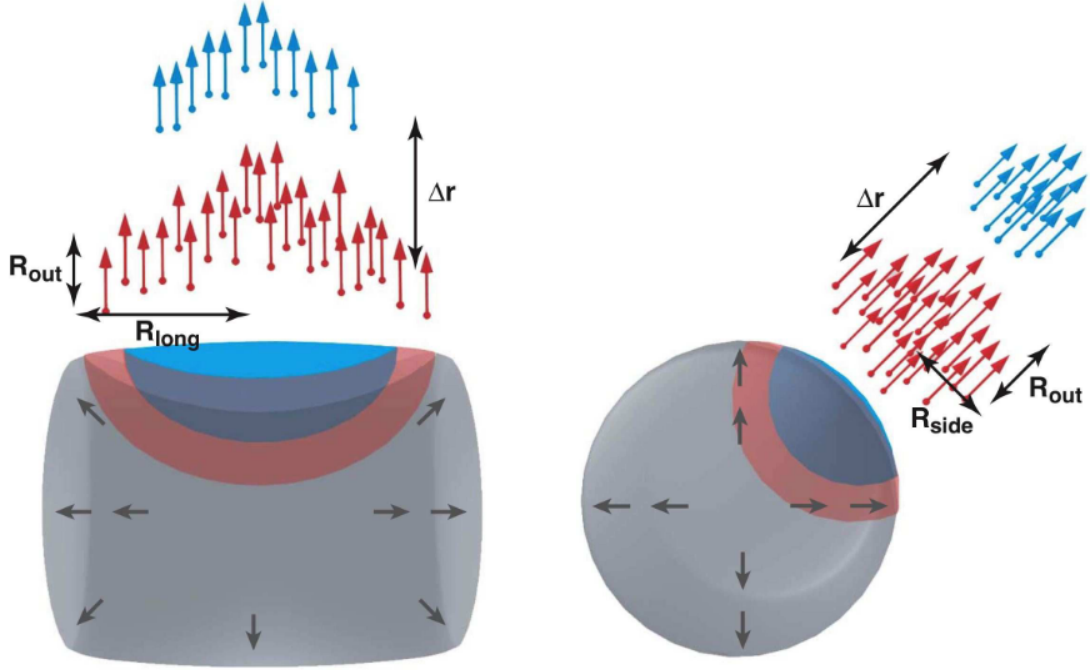


FIGURE 2.14: Illustration of the femtoscopic radii in different directions. Colors corresponds to mass dependence of the radii: for particles with higher m_T (blue) the source volume is more confined than in case of lighter particles (red). Picture from [70].

The source size can be determined using observed phenomena such as, i.e. m_T scaling which is well established experimentally for many particle species. The description of such prediction method and application of the femtoscopy technique to interaction studies are a part of this thesis.

2.6.2 Two-particle wave function

The pair wave function refers to the quantum statistics effects (for identical particles – bosons or fermions) and/or to Final State Interactions (FSI), such as Coulomb interactions (if particles are charged) and strong force interactions (if they are hadrons). In the case of non-identical pairs, the effects of symmetrization/antisymmetrization arising from quantum statistics are naturally not considered. For non-identical pairs, the wave function is constructed from FSIs that will vary for different particle species analyzed in the pair, and this variation should be reflected in the overall shape of the correlation function, as presented in the Fig. 2.15 (left). The nature of the interaction

is derived through an analysis of the final shape of the correlation function. Thus, if the correlation function is below/above unity, it means that the interaction is repulsive/attractive. Shapes that cross unity with a bump/dip structure correspond to the formation of bound states of the analyzed pair. The correlation function equal unity in the absence of any correlations. The function is also expected to reach the unity at very high relative momenta where the particles separate fast enough to avoid the FSI which should also leads to lack of correlation. A schematic representation of the shape interpretation is shown in Fig. 2.15 (right). The particle pairs considered in this thesis primarily involve Coulomb and strong interactions. Therefore, the necessary explanations behind these types of interactions are provided below:

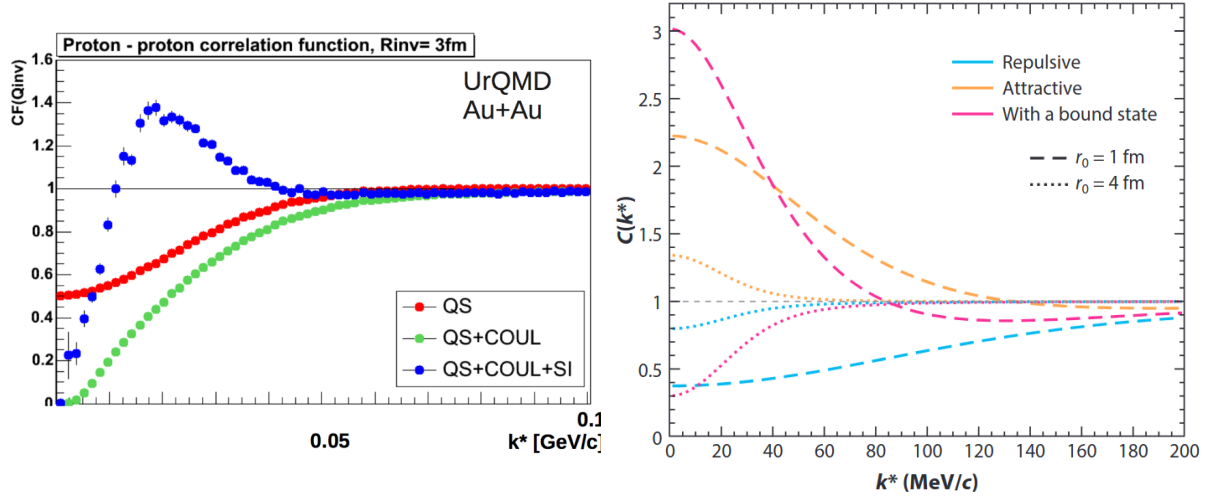


FIGURE 2.15: Left: simulation of proton–proton correlation functions using UrQMD model for single particle source radii equal 3 fm accounting for different effects of the wave function (picture from [90]). Right: A schematic representation of correlation functions that correspond to their repulsive, attractive and bound state interpretation (picture from [91]).

■ Strong interaction only

The interaction between two particles, from a classical point of view, can be imagined in form of elastic scattering of one particles on another (as presented in the Fig. 2.16), which provides us such parameters like the cross-section and the scattering angle [92]. However, if we look on the problem from quantum point of view the description of interaction became more complicated. Particles can be described as plane waves traveling in a certain direction. In the case of lack of external potential, two particles do not interact and can propagate freely. However, upon introducing a strong interaction

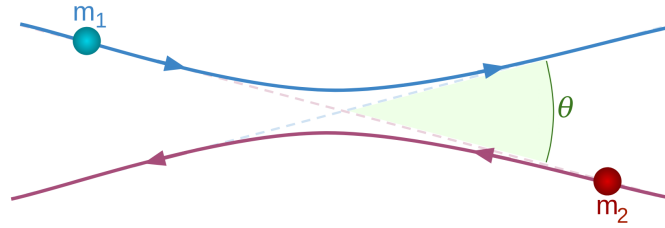


FIGURE 2.16: A simplified illustration of two particles scattering in an elastic way.

between the two particles, they become sources of an external scattering potential for each other. A solution of elastic scattering of one particle on another is a spherical wave. Therefore, an incident wave “collides” with spherical waves emitted from scattering region. This problem can be considered as the scattering of a quasi-particle (represented by μ , the reduced mass) on the potential V . The problem can be solved with the Schrödinger equation and is a superposition of an incident plane wave (ψ_{in}) and the scattered spherical waves (ψ_{scat}), as schematically shown in Fig. 2.17 and through the following formula:

$$\psi_{\text{final}} = \psi_{\text{in}} + \psi_{\text{scat}}, \quad (2.9)$$

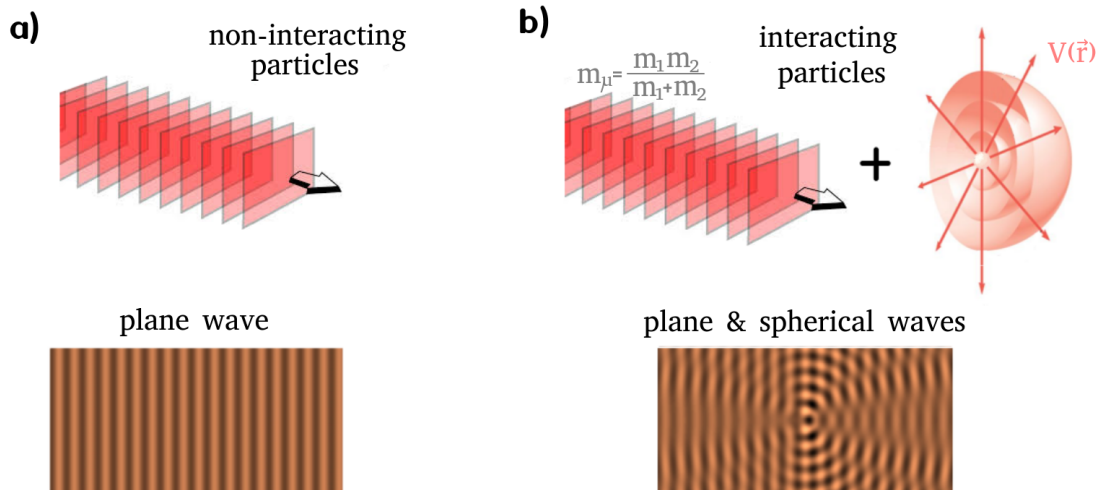


FIGURE 2.17: A simplified illustration of a scattering problem. Left: non-interacting particles – plane waves, right: interacting particles – the wave function for interacting particles is a superposition of the plane wave and the spherical wave from the scattering.

The plane wave can be decomposed as a sum of all partial wave components corresponding to different angular momenta l taking a following form:

$$e^{i\vec{k}^* \cdot \vec{r}^*} = e^{ik^* r^* \cos\theta} = \sum_l i^l (2l+1) \frac{i}{2k^*} \left(\frac{e^{-i(k^* r^* - l\pi/2)}}{r^*} + \frac{e^{i(k^* r^* - l\pi/2)}}{r^*} \right) P_l(\cos\theta), \quad (2.10)$$

where θ is a scattering angle of the particle and P_l are Legendre polynomials.

The Eq. 2.10 shows that such a wave is composed of incoming and outgoing waves of equal amplitude. If we switch on the potential that causes outgoing waves, we affect the pre-existing outgoing waves coming from the plane wave. The outgoing term will take the following form:

$$\frac{e^{i(k^* r^* - l\pi/2)}}{r^*} \longrightarrow \frac{e^{2i\delta_l} e^{i(k^* r^* - l\pi/2)}}{r^*}, \quad (2.11)$$

where δ is a phase shift. A phase shift measures the range of displacement of the scattering solution. For free particles the $\delta = 0$.

The wave function can be further expressed as:

$$\Psi_{\text{final}} = e^{i\vec{k}^* \cdot \vec{r}^*} + \sum_l \left((2l+1) P_l(\cos\theta) \frac{e^{2i\delta_l} - e^0}{2ik^*} \right) \frac{e^{ik^* r^*}}{r^*} = e^{i\vec{k}^* \cdot \vec{r}^*} + f(\theta) \frac{e^{ik^* r^*}}{r^*}, \quad (2.12)$$

where $f(\theta)$ is so-called the scattering amplitude.

The phase shift is l -dependent, which means that each partial wave has its own individual phase shift. Each partial wave corresponds to a certain angular momentum quantum number, which later defines the influence of the potential. However, the scattering amplitude in long wavelength limit, does not see a structure of the outgoing spherical waves depending on l as the wave become too large to see disturbances (the scattering became isotropic). In such a case we lose a sensitivity on direction. The expression of $l = 0$ is referred to the s-wave scattering amplitude. In this thesis the discussion concerns mostly to this s-wave limit (f^s) as scattering amplitude of higher partial waves (e.g. p-waves and d-waves of angular momentum $l=1$ and $l=2$, respectively) are usually negligible in comparison to the contribution of s-waves at low relative momenta.

The scattering amplitude can also be expressed in terms of scattering parameters, which take specific values for different particle pairs:

$$f^s(\vec{k}^*) = \left(\frac{1}{f_0} + \frac{d_0 k^{*2}}{2} - i k^* \right)^{-1}, \quad (2.13)$$

where f_0 is the scattering length and d_0 is an effective range of interaction. The two scattering parameters are usually determined from scattering cross-section measurements. The scattering length is directly linked to the total cross-section of the process [93, 94]. These parameters can also be determined through a modification of the energy transition width and position with respect to the pure electromagnetic interaction measured in exotic atoms experiments [95, 96]. In general, there is a direct relation between δ_0 and f_0, d_0 . The effective range expansion provides a prescription to expand:

$$k^* \cot(\delta(k^*)) \stackrel{k^* \rightarrow 0}{\approx} \frac{1}{f_0} + \frac{1}{2} d_0 k^{*2} + \mathcal{O}(k^{*4}). \quad (2.14)$$

The correlation function expressing the pure strong interaction and the one-dimensional Gaussian emission function can take an analytical formula known as the Lednický-Lyuboshits formula [97] which is expressed as:

$$C(k^*) = 1 + \sum_s \rho_s \left[\frac{1}{2} \left| \frac{f^s(k^*)}{R} \right|^2 \left(1 - \frac{d_0^s}{2\sqrt{\pi}R} \right) + \frac{\Re f^s(k^*)}{\sqrt{\pi}R} F_1(2k^*R) - \frac{\Im f^s(k^*)}{R} F_1(2k^*R) \right], \quad (2.15)$$

where ρ_s are the pair spin fractions, R is the Gaussian source width, $F_1(z) = \int_0^z dx e^{x^2 - z^2} / z$ and $F_2(z) = (1 - e^{-z^2}) / z$.

This method is based on the asymptotic solution of the interaction [97], which scattering theory approximates using the effective range expansion. The typical range of the strong interaction is short-ranged, about 2–3 fm. A typical source size in heavy-ion collisions starts from around ~ 3 fm. Therefore, describing the asymptotic solution of the correlation over the asymptotic region is not a problem in heavy-ion collisions. In small sources, this definition has to be corrected.

The Lednický-Lyuboshits approach is based on s-wave. It is not trivial to add higher-order partial waves to the formalism, as the modification would need to be done at the level of the wave function. Nevertheless, such parametrisation allows for relatively easy decomposition of the correlation function into the weighted sum of contributions associated with each spin or isospin channel (if there is more than one).

■ Coulomb interaction only

The Coulomb force, which can be another source of final state interactions, is long-range. The potential falls to zero at large distances ($V(r) \rightarrow 0$ as $r \rightarrow \infty$), however, it drops very slowly compared to the strong interaction. Therefore, the Coulomb interaction problem is described differently from the strong interaction. The wave function for non-identical particle studies accounts for relative distance and can be expressed as [98]:

$$\psi_{\vec{k}^*}(\vec{r}^*) = e^{i\delta_0^c} \sqrt{A_c(\eta)} e^{-i\vec{k}^* \cdot \vec{r}^*} F(-i\eta, 1, i\zeta), \quad (2.16)$$

$\zeta = k^* r^* (1 \pm \cos\theta^*)$ (θ^* is an angle between k^* and r^*), δ_0^c is the Coulomb s-wave phase shift that can be expressed as $\arg\Gamma(1 + i\eta)$, $\eta = 1/(k^* a_c)$, a_c is the Bohr radius of the system (+/- repulsion/attraction depending if we consider same/opposite charge pairs) which values of used for presented in this thesis pairs can be found in Tab. 2.1, A_c is the Gamow factor that provides the threshold of the Coulomb barrier and can be defined by Eq. 2.17, F is a confluent hypergeometric function.

$$A_c(k^*) = \frac{2\pi}{k^* a_c} \left[\exp\left(\pm \frac{2\pi}{k^* a_c}\right) - 1 \right]^{-1}. \quad (2.17)$$

The above definitions determine that the impact of the Coulomb interaction increases with the mass of the system.

TABLE 2.1: The Bohr radius, a_c , for particle pairs considered in this thesis. The values were calculated based on $a_c = 1/(\mu e^2)$, where μ is reduced mass of the pair. The value is positive for repulsive and negative for attractive interaction.

Pair	$a_c(fm)$
Kp	± 83.59
πd	± 208.16
Kd	± 69.19
pd	± 43.23

■ Coulomb and strong interaction

The studies in this thesis consider charged hadrons; therefore, the strong interaction has to be considered in addition to the presence of Coulomb interaction. These two

interactions are not simply additive; the modification occurs at the level of the plane and scattered length. The final formula for both Coulomb and strong forces can be expressed using the Lednický-Lyuboshits formalism:

$$\psi_{-\vec{k}^*}(\vec{r}^*) = \sqrt{A_C(\eta)} \frac{1}{\sqrt{2}} [e^{-i\vec{k}^* \cdot \vec{r}^*} F(-i\eta, 1, i\xi) + f_c(\vec{k}^*) \frac{G}{r^*}], \quad (2.18)$$

where G is a combination of regular and singular s-wave Coulomb functions described in more detail in [99], f_c can be expressed by Eq. 2.19

$$f_c(k^*) = \left(\frac{1}{f_0} + \frac{d_0 k^{*2}}{2} - \frac{-2h(k^* a_c)}{a_c} - ik^* A_C(k^*) \right)^{-1}, \quad (2.19)$$

where $h(x) = \frac{1}{x^2} \sum_{n=1}^{\infty} \frac{1}{n(n^2+x^2)} - C + \ln|x|$.

2.7 Particle production and formation of light-ions

The production mechanism of simple nuclei in heavy-ion collisions is directly associated with the hadronization processes. Particles produced before the chemical freeze-out in a final composition correspond to the so-called thermal model of particle formation. This approach assumes that all particle species are created at the same temperature in chemical equilibrium and can be later reproduced by statistical models. The particle production rate can be predicted using just few parameters such as temperature, volume and chemical potentials. This model provides good predictions of particles' ratios even for those of bound nature like deuteron, helium-3 etc. This observation can be interpreted as all particles can be created with the same temperature. Light ions, in turn, are bound states where ingredients are kept together thanks to the attractive strong interaction which results in binding energies of the order of ~ 1 MeV/nucleon [100]. Such energy is several orders of magnitude smaller than the chemical freeze-out temperature of a Pb–Pb collision (~ 155 MeV). Therefore, it is very likely that such ions would not survive the energetic medium leading to the breakup process. This paradox from the energetic point of view challenges the thermal formation mechanism of light ions at the freeze-out stage calling them *snowballs in hell* [101]. Nevertheless, we observe a significant yield of them in heavy-ion collisions and one of the arguments behind thermal snowflake is that such objects could be produced at the phase transition as compact colorless quark clusters which are expected to interact little with the surrounding matter. Another argument that try to explain

why we observe composed particles in heavy-ion collisions is that they are created in a different mechanism than simple hadrons, via the so-called coalescence process. The coalescence model is based on assumption that if two hadrons find each other in phase space with certain relative momentum (usually assumed as value of order of 100 MeV/c) there is a chance that they will form bound states. Such cluster formation from already existing protons and neutrons would happen after the chemical and before the kinetic freeze-out. In a simple coalescence scenario it is assumed that nucleons are point-like objects and phase-space considerations are ignored. The simple coalescence scenario works to some extent in pp collisions but usually does not describe well all considered observables in heavy-ion collisions data. There are also more sophisticated state-of-the-art implementations of the coalescence approach that consider particles through the quantum-mechanical properties, calculating the formation probability based on the wave function of the nucleus ingredients. Such sophisticated models use phase-space distributions of protons and neutrons generated by production models such as, e.g. AMPT [102]. The advanced coalescence model, similarly to thermal production model, provides qualitative description of composed particle production in heavy-ion data. The typical methods used for studies of the particle production are: yield studies [103, 104, 105, 106], flow observables [107, 108, 109] and event-by-event fluctuations [110].

2.7.1 Particles' yield

Ultrarelativistic heavy-ions give access to a great abundance of particles produced in their collisions. The number of charged particles registered in the detectors depends on pseudorapidity (η) defined as:

$$\eta = -\ln \left[\tan \left(\frac{\theta}{2} \right) \right] = \frac{1}{2} \ln \left(\frac{|p| + p_z}{|p| - p_z} \right), \quad (2.20)$$

where θ is the angle between the particle momentum and the beam axis, p_z is the momentum in the direction of the beam, or depends on rapidity (y):

$$y = \frac{1}{2} \ln \left(\frac{E + p_z}{E - p_z} \right) \quad (2.21)$$

where E is a total energy of the particle.

The pseudorapidity/rapidity describes a relation of longitudinal angle, with respect to the beam axis. Therefore, the value of $dN_{ch}/d\eta$ or dN_{ch}/dy can be understood as a multiplicity density. Different detectors are characterised by different coverage of pseudorapidity, however the characteristic values of particle yields are usually obtained around the center (mid-rapidity, $|y| < 0.5$). In Fig. 2.18 is shown the yield of particles for particles species from light-flavored hadrons up to hypertriton ${}^3_{\Lambda}H$ measured in central (0 – 10%) Pb–Pb collisions at $\sqrt{s_{NN}} = 5.02$ TeV [106].

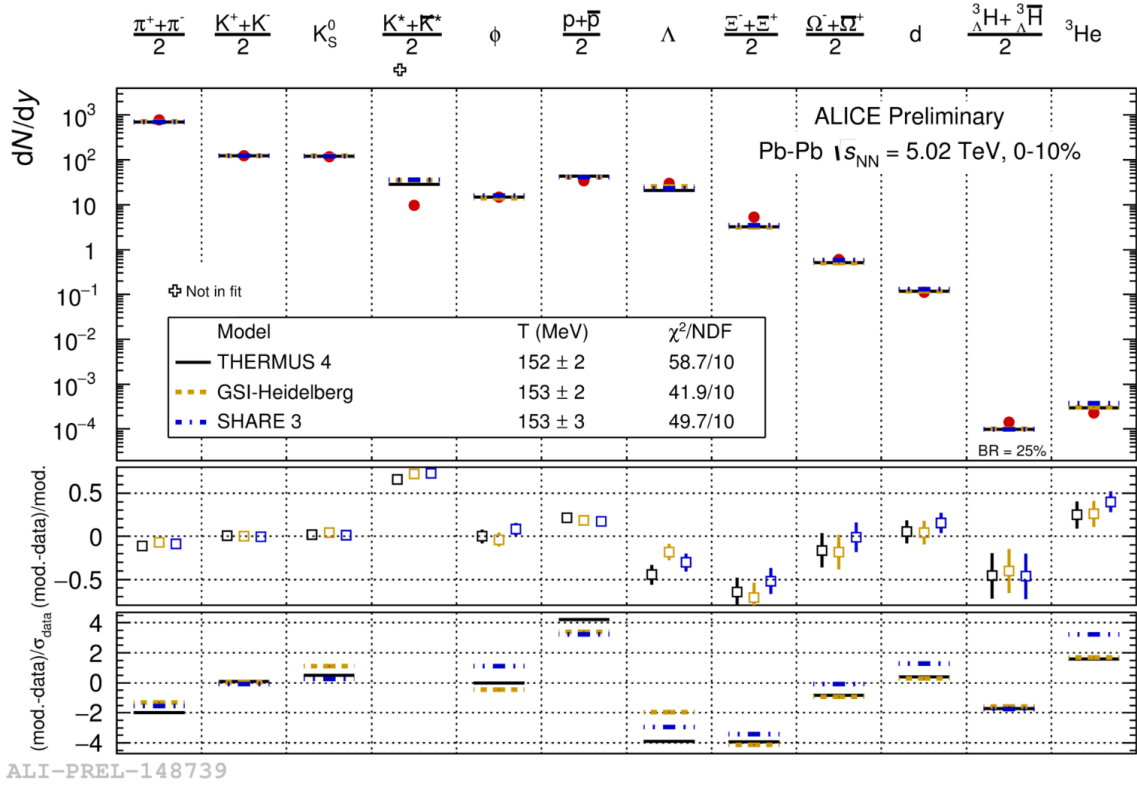


FIGURE 2.18: The light-flavored hadron yields in central Pb–Pb collisions at $\sqrt{s_{NN}} = 5.02$ TeV measured by the ALICE experiment together with three interpretation of the statistical fit. Figure from [106].

The particle yield is the one of the observables that we can use to constrain the production mechanism of particles. To do so, one has to compare the yield measured in the experiment to the one predicted using a certain model. The experimental measurement of particle yields together with predictions of statistical model are presented in Fig. 2.18. This figure shows that thermal model is able to describe the light ions yields within 1 sigma for deuterons and 2–3 sigma ${}^3_{\Lambda}H$ nuclei.

When analyzing light-ion production (deuteron) from the coalescence perspective, a typical parameter used for evaluating the accuracy is called B_A which is a ratio of the invariant yield of deuterons and that of protons squared. For simple coalescence, the cross section for the production of a cluster with mass number A is related to the probability that the A nucleons have a relative momentum less than p_0 , which is a free parameter of the model [111]. The simplified expression of B_A can be defined as Eq. 2.22.

$$B_A = \left(\frac{4\pi}{3} p_0^3 \right)^{A-1} \frac{M}{A! m^A} \quad (2.22)$$

where p_0 is so called coalescence radius, M is a mass of nuclei, m mass of nucleus and A is a number of nucleons of composed particle that we are interested in.

The coalescence parameter B_A does not depend on the momentum of the particles, and therefore, it should be constant for different p_T and centralities. Some examples of the B_2 parameter (deuteron) as a function of p_T for different centralities are presented in Fig. 2.19.

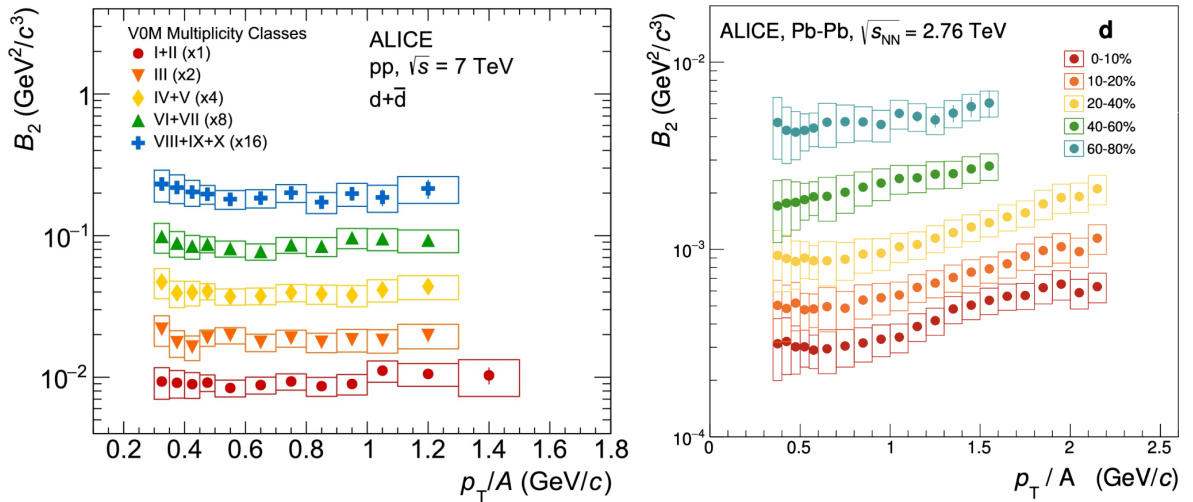


FIGURE 2.19: Left/right: B_2 parameter measured for (anti)deuteron produced in pp collisions at $\sqrt{s} = 7$ TeV / Pb-Pb collisions at $\sqrt{s_{NN}} = 2.76$ TeV for five multiplicity/centrality ranges. Figures from [112, 105].

The values from pp collisions are rather constant, whereas the Pb–Pb data shows a growing trend, which means simple coalescence is not satisfactory describing the production in heavy-ion data.

Another key observable of the coalescence model done based on particle production yield is the ratio between observed deuterons and protons. An example of such a ratio for different collision systems from pp to Pb–Pb collisions is presented in Fig. 2.20, together with the thermal and coalescence predictions. As we can see, both models describe the data well. The coalescence model seems to better represent the trend in pp/pPb collisions even if the thermal prediction stays within uncertainties. However, in Pb–Pb data it is still under debate, which is better.

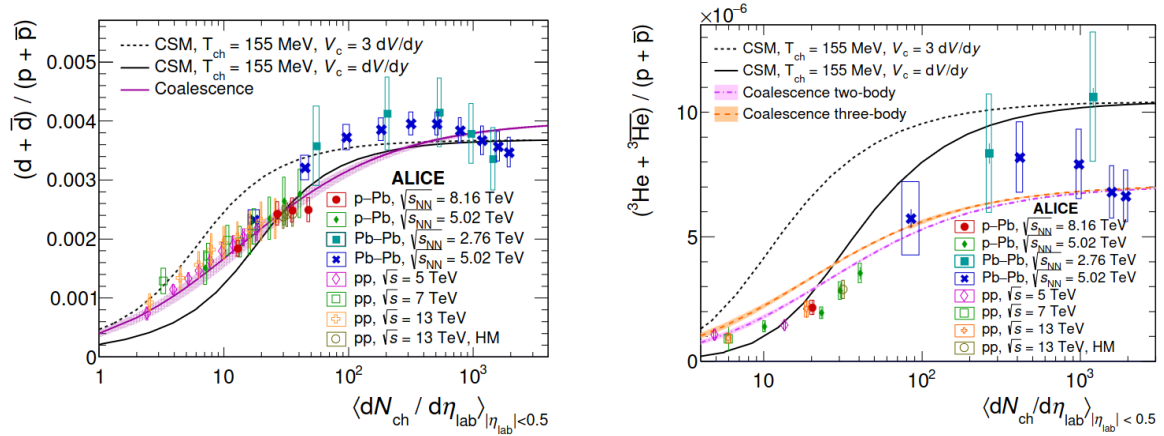


FIGURE 2.20: Left/right: Ratio of (anti)deuteron/(anti)3He and proton production yields as a function of the charged-particle multiplicity for different collision systems and energies. Lines corresponds to the expectations of thermal and coalescence models. Figure from [113].

2.7.2 Elliptic flow

The elliptic flow, known as v_2 , measured as a function of the transverse momentum is another tool to study the creation mechanism of particles' production. Elliptic flow expresses a collective effect among produced particles and is sensitive to the system conditions in the early stages of the evolution [53]. One of the most recent results that concern heavy-ion data come from the STAR Au–Au collisions at $\sqrt{s_{NN}} = 200$ GeV [107], where v_2 was compared to Blast-Wave hydrodynamic model (thermal production [114, 115]) and to sophisticated coalescence model (with the phase-space distributions of nucleons generated using string-melting AMPT [102]). Those results showed that thermal scenario cannot reproduce data and coalescence approach is the one that works for composed particles. Simultaneously, the ALICE results of Pb–Pb collision data at $\sqrt{s_{NN}} = 2.76$ TeV [108] were well reproduced by the

Blast-Wave model and sophisticated coalescence model using default AMPT settings (the predictions obtained using the AMPT version, which described RHIC data, are not consistent with the ALICE measurement). Further work on ALICE $\sqrt{s_{NN}} = 5.02$ TeV [109] showed also that none of two approaches is able to perfectly reproduce the v_2 in all centralities and p_T ranges. However, a good agreement provides predictions from mixed approaches of, e.g. hydrodynamics models coupled to hadronic afterburners. An example of the elliptic flow checks for composite particles is presented in Fig. 2.21.

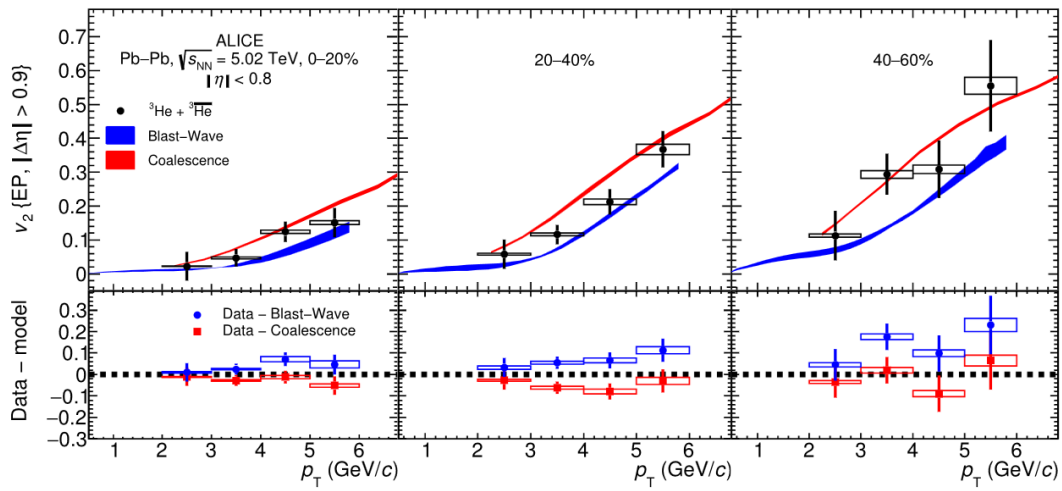


FIGURE 2.21: Elliptic flow of (anti) ^3He in comparison with the predictions from the Blast-Wave model and a simple coalescence approach for the centrality intervals 0 – 20%, 20 – 40% and 40 – 60%. Figure from [116].

2.7.3 Event-by-event fluctuations

The event-by-event studies are based on calculation of cumulants (κ) of different order (m) that is expressed as:

$$\kappa_m = \langle (n - \langle n \rangle)^m \rangle, \quad (2.23)$$

where n is a the event-by-event particle number. The higher order cumulants of particle multiplicity distributions are used to study the thermodynamics of expanding system [117, 118, 119]. In particular, it has been shown in [120] that cumulants of event-by-event deuteron number distribution will be different for thermal and coalescence approaches. Together with cumulants the linear correlation between two

variables is studied using the Pearson correlation coefficient of particles a and b , (ρ_{ab}):

$$\rho_{ab} = \langle (n_a - \langle n_a \rangle)(n_b - \langle n_b \rangle) \rangle / \sqrt{\kappa_{2a}\kappa_{2b}}, \quad (2.24)$$

In the statistical model, the ratios between different cumulants is expected to be a unity as the event-by-event nuclei distributions are expected to follow a Poisson distribution. In a simple coalescence scenario, the nuclei distribution will differ from Poisson providing a negative correlation between the measured proton and deuteron numbers because deuteron creation needs to assimilate some of the protons and neutrons produced in the collision. In the approach where particles undergo direct thermal production, protons and deuterons are uncorrelated as they are created independently. In Fig. 2.22, recent results of event-by-event study done by ALICE are shown [110]. The presented ratio between cumulants of order 1 and 2 in heavy-ion collision data is close to unity. Also, the Pearson correlation coefficient between measured antideuterons and antiprotons is presented. In both cases, thermal production is the only one describing well the experimental data. However, in this analysis one have to keep in mind that used coalescence models are the simple models, which could not be suitable for the heavy-ion collision data.

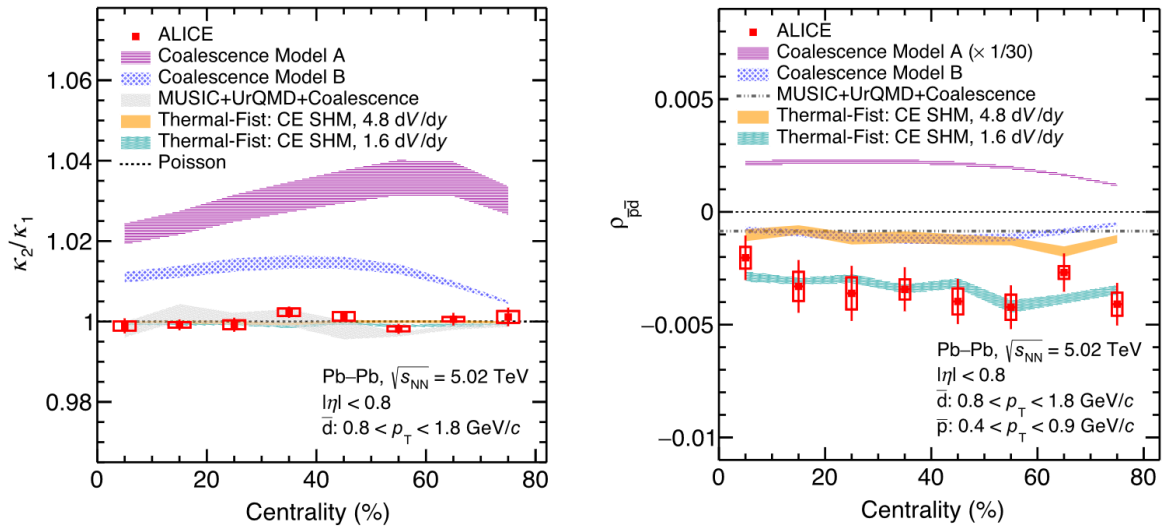


FIGURE 2.22: Left: a ratio of the second to first order cumulant of the \bar{d} multiplicity factor distribution, right: Pearson correlation between the measured \bar{p} and \bar{d} . Both results come from Pb-Pb collisions at $\sqrt{s_{NN}} = 5.02$ TeV and are presented as a function of collision centrality. Bands correspond to predictions coming from thermal and coalescence models.

Figures from [110].

2.7.4 Femtoscopy – a tool revealing the production mechanism of light ions

It has been shown in previous subsections that the coalescence and thermal scenarios of light-ion production have been extensively studied, but a clear evidence supporting one scenario over the other has not yet been established. Recently, the femtoscopy technique has also been proposed as a tool that can be used to identify the mechanism of production of light ions, such as deuterons [121, 122, 123, 124]. In these works, it was pointed out that the information about the creation mechanism of the deuteron should be reflected in the femtoscopic size of the correlation function. According to this, thermally produced deuterons behave like elementary particles and therefore their source size should be as the protons' source at the m_T of deuterons. The source size of deuterons produced in the coalescence scenario should be larger due to a process of spatial extent. The calculations presented in these study [121] were particularly devoted to the proton–deuteron case derived $\sqrt{4/3} \approx 1.15$ as a scalar factor that distinguishes the coalescence/thermal source size scenario. Such factor should be even bigger for such systems like proton–helium 3 [122] (factor $\sqrt{3/2} \approx 1.22$) or deuteron–deuteron [123] (factor $\sqrt{2} \approx 1.41$), however, so far the collected statistics by ALICE at the LHC necessary to performed studies in such rare systems is not sufficient. Therefore, this thesis is partially an answer to the theoretical study [121] and one of the motivation of this thesis is the measurement of deuterons source sizes and their comparisons with other thermally produced particles. If deuterons are created thermally, their source size should behave as other not composed particles and when they are produced via coalescence the radii should be bigger. Also, another motivation is the measurement of the proton–deuteron source sizes in order to compare them to expectations from both scenarios of particles production. Nevertheless, a femtoscopic examination of the creation mechanism is only feasible if the theoretical correlation functions do not assume any specific creation mechanisms and the interactions are well-controlled, which are very non-trivial challenges in proton-deuteron system.

Chapter 3

Experimental data

'Oh, you can't help that,' said the Cat : 'We're all mad here. I'm mad. You're mad.

'How do you know I'm mad?' said Alice.

'You must be,' said the Cat, 'or you wouldn't have come here.'

Lewis Carroll, Alice's Adventures in Wonderland

Myśl o tym, że zwariowałem, uspokoiła mnie.

Stanisław Lem, Solaris ²

3.1 CERN accelerator complex

CERN, the European Organisation for Nuclear Research, was founded in 1954 with a facility at the French-Swiss border near Geneva International Airport. The main mission of the organization is to uncover what the universe is made of and how the physics at the elementary particle level works. This mission is currently carried out by 23 main member states (~7 000 researches) as well as associated members, observers and other states (~5 000 researches). The facility of CERN is composed of different linear and circular accelerators that successively boost a beam of particles into higher and higher energies. This boosting, many-steps system allows various experiments to use particles at different levels of acceleration. A schematic representation of the CERN complex is shown in Fig. 3.1.

The best-known accelerator of CERN is the Large Hadron Collider (LHC) [126], being the biggest and the most powerful particle accelerator ever built. LHC is a two-ring-superconducting-hadron accelerator working in collider mode, which means that the two particle beams are collided after acceleration in opposite directions. Their

²"The thought that I was going crazy calmed me down." – Stanisław Lem, Solaris

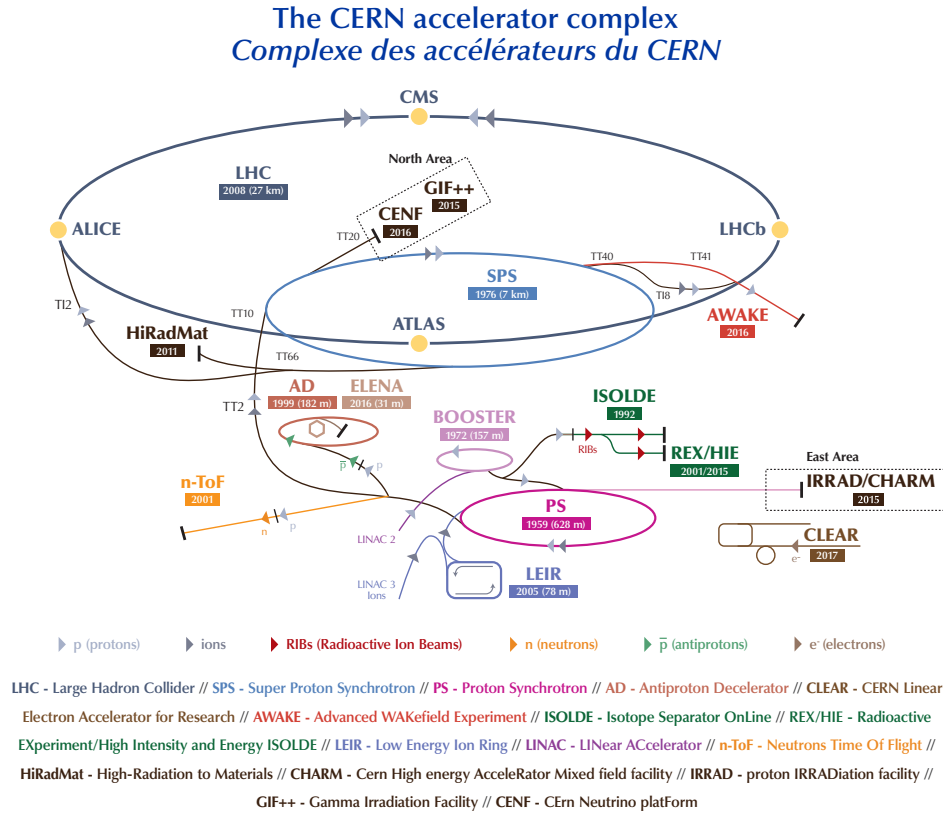


FIGURE 3.1: The CERN accelerator complex [125]. The LHC is located at the end of the complex injector chain of the CERN accelerators.

acceleration ring is 26.7 km long and is placed in the tunnel which was used before by the Large Electron-Positron (LEP) machine. The LHC consists of eight straight sectors (each 528 m long) and eight arcs. The straight sectors are used as places for experiments and for acceleration, whereas arcs form the ring shape. In order to bend the beam, the LHC uses superconducting dipole magnets. Another set of quadrupoles, sextupoles, octupoles and decapoles magnets are used to focus the beam in the ring. The beam of particles is split into bunches of particles moving at speeds close to the speed of light. Each beam can store up to 2808 bunches with a spacing of 25 ns. For most of the operating time, the LHC collides hydrogen ions – protons with a collision energy of up to 14 TeV. It is also possible to collide heavier ions. A significant part of the data therefore comes from collisions such as p–Pb or Pb–Pb. The operating time of the LHC is divided by *shutdown* periods, during which the main experiments, as well as the LHC itself, have time for maintenance, upgrades or changes of the technologies. The period during which the LHC collects data is known as the *Run* period. The following

runs have been carried out so far: *Run* – 1 (2010-2013), *Run* – 2 (2015-2018). The *Run* – 3 (2022-2025) period of data taking is currently ongoing. The four largest experiments working at the LHC ring are ALICE (A Large Ion Collider) [127], ATLAS (A Toroidal LHC Apparatus) [128], LHCb (The Large Hadron Collider beauty) [129] and CMS (Compact Muon Solenoid) [130]. This thesis concerns the analysis of data collected by the ALICE Experiment during the *Run* – 2 period. That is why the following description refers only to this particular experiment.

3.2 ALICE Experiment

ALICE Experiment is located at Point 2 of the LHC. The ALICE detector can measure different collision systems available at the LHC, but was specifically designed for ultra-relativistic heavy-ion collisions. The main motivation for this design was to study the QGP state. The existence of such a state of matter is characterised by the creation of up to thousands of particles almost simultaneously in the hadronisation process. Such particle densities can only be studied with large detectors. This is because, in order to identify the particle, the shape of the track must be well captured, and at such densities the design faces the problem of capacity and track separation, as well as the radiation hardness. Therefore, the size of the ALICE detector reaches an impressive $16 \times 16 \times 26 \text{ m}^3$ with a total weight of 10000 tonnes. Also, a characteristic feature of the ALICE Experiment is its excellent tracking and particle identification and the possibility to measure charged particles with very low momentum. Such particle identification is possible thanks to the ALICE magnet, that is the L3 solenoid, which provides a homogeneous magnetic field of 0.5 T in the direction parallel to the beam axis. These features make the experiment ideal for low relative momentum studies. The main limitation of the detector is its relatively low read-out rate of $\sim 1 \text{ kHz}$ (*Run* – 3 improved it by providing continuous read-out). The full apparatus utilised during the *Run* – 2, used in this thesis, consists of 19 sub-detectors and is shown in Fig. 3.2. The coordinate system used to describe the detectors is shown in Fig. 3.3.

The following sub-sections describe in detail the four main components of the ALICE detector, namely the trigger system and three detectors of the central barrel region, which provide the information used in the study of this thesis. Other sub-detectors that make up the ALICE experiment are also briefly described below, however, a detailed description of all components can be found in [127].

THE ALICE DETECTOR

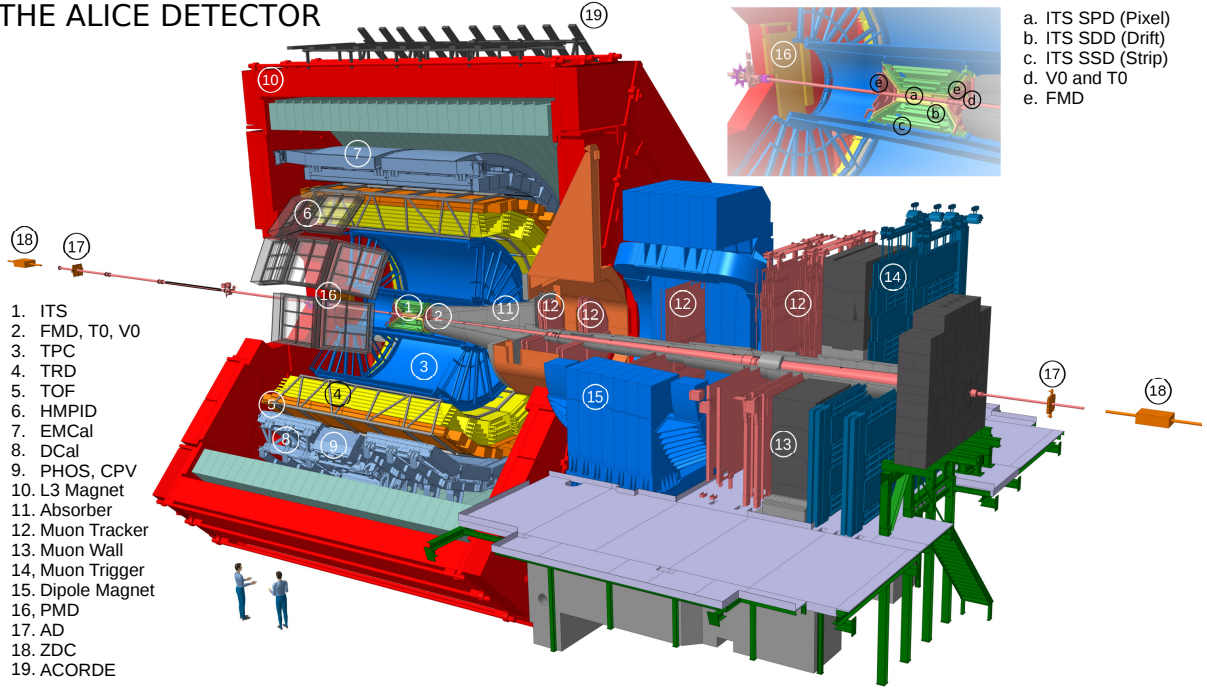


FIGURE 3.2: The ALICE detector during the *Run – 2* data taking period (2015–2018) [131].

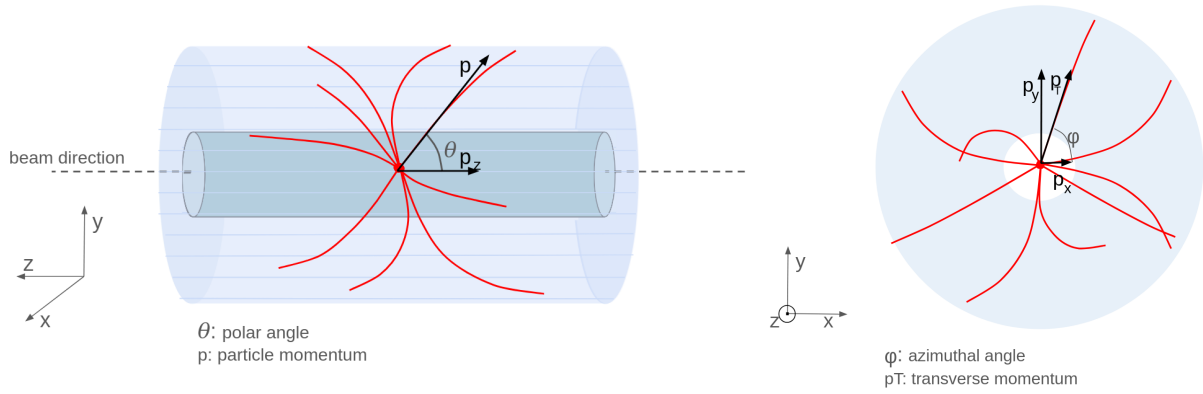


FIGURE 3.3: The coordinate system of the ALICE detector. Left: polar space parallel to the direction of the beam, right: transversal plane perpendicular to the direction of the beam.

3.2.1 Trigger system

The LHC can provide up to 1 billion particle collisions per second. However, not all events contain the searched information, and to save resources the trigger system is introduced. In principle, the trigger system activates the read-out sequence when the required conditions of the event are fulfilled. The ALICE *Run – 2* triggers belong to

two groups: a low-level hardware trigger called a Central Trigger Processor (CTP) and a purely software-based trigger called High-Level Trigger (HLT). The CTP triggers are responsible for starting the process of event data buffering in the front-end electronics and later for sending the recorded data to the HLT and the Data Acquisition (DAQ) system. The HLT is responsible for fast reconstruction and data compression. Before taking any further action, the triggers decide in real time during data taking whether the registered event should be considered in further steps or should be rejected. In this study, the trigger system is based on information from two V0s detectors (V0A, V0C) that are installed on both sides of the ALICE collision vertex point along the beam axis. V0A and V0C consist of arrays of 32 scintillator counters covering the full azimuth and more than four units of pseudorapidity, in the ranges $2.8 < \eta < 5.1$ and $-3.7 < \eta < -1.7$, respectively. In this study, a requirement to trigger the saving process, was the registration of signals in two V0s detectors in coincidence to the collision at the centre of the ALICE detector. Following the procedure described in [132], the amplitudes of signals in V0 were further used to constrain the centrality of the collision, expressed as a percentage of the total hadronic cross-section. The larger the overlap region of the two colliding ions the smaller the number in percentage of the centrality interval. In this way 0% corresponds to a perfect overlap, while 100% corresponds to zero overlap between the ions. In *Run - 2* the data can be distinguished into minimum-bias (MB) trigger and in addition the so-called 'rare' triggers. The former is fulfilled by any collision and therefore, does not introduce any physical bias into the recorded events. The latter is used to have events selected toward specific physics-driven conditions and is introduced to increase the statistics of certain types of events (the amount of recorded events is limited by the long read-out time). In this thesis data collected with 3 types of triggers have been used:

- kINT7**, a minimum bias trigger that is activated when at least one hit in each V0A and V0C scintillators is registered.

- kCentral** and **kSemiCentral**, which are 'rare' triggers that are activated when the collisions are characterised by a multiplicity above the threshold of registered signals for events corresponding to 0–10% and 30–50% collision centrality, respectively.

3.2.2 The Inner Tracking System

The Inner Tracking System (ITS) is the ALICE detector closest to the beam line. In this thesis, ITS is used for precise reconstruction of the collision's primary vertex (PV), but it

can also be used to improve the momentum and angle resolution in the reconstruction algorithm of other detectors. The *Run* – 2 ITS consists of six coaxial cylindrical layers with radii ranging from 3.9 cm to 43.0 cm (the outer radius of the beam pipe is 3 cm). The six layers are part of 3 sub-systems, called Silicon Pixel Detector (SPD), Silicon Strip Detector (SSD) and Silicon Drift Detector (SDD). All subsystems are lightweight silicon-based detectors in order to avoid stopping particles on their way to further detectors. The SPD is the two layers of the ITS that are closest to the PV and plays a crucial role in its accurate reconstruction. The design uses silicon pixel detectors with 200 μm thick diodes. It is designed to operate in high radiation environments with high energy densities up to 50 particles/ cm^2 . The SDD forms the middle two layers of the ITS and is made up of homogeneous high-resistivity silicon layers 300 μm wide. Unlike the SPD, information from the SDD can be used for particle identification as the energy loss information can be retrieved by analogue readout. The SSD forms the two outermost layers of the ITS and consists of double-sided detectors with silicon microstrips. It enables both energy loss measurement and track position determination in two dimensions. A detailed description of the *Run* – 2 ITS and its layers can be found in [133]. The entire ITS system covers the pseudorapidity range of $|\eta| < 0.9$ (SPD can cover $|\eta| < 1.95$). The detector can reconstruct the trajectory of the particles with very high resolution, and because of this the precision of the PV reconstruction is better than 100 μm . Such precision is also very useful for the detection of possible events with multiple vertexes resulting from the simultaneous registration of more than one collision. The schematic view of the ALICE ITS *Run* – 2 construction is shown in Fig. 3.4.

3.2.3 The Time Projection Chamber

The Time Projection Chamber (TPC) is one of the main ALICE detectors used for particle tracking and identification. The TPC has a cylindrical shape with a hole for the ITS detector and the beam pipe. The detector cylinder is 5 m long in the direction of the beams, with inner and outer radii equal to 85 and 247 cm from the interaction point, respectively. The total active volume is 90 m^3 . This design allows the TPC detector to cover the pseudorapidity range of $|\eta| < 0.9$. The schematic representation of the TPC is shown in Fig. 3.5.

The TPC chamber is divided into two regions by the central cathode, which provides an electric field of ~ 400 V/cm. The volume of the detector is filled

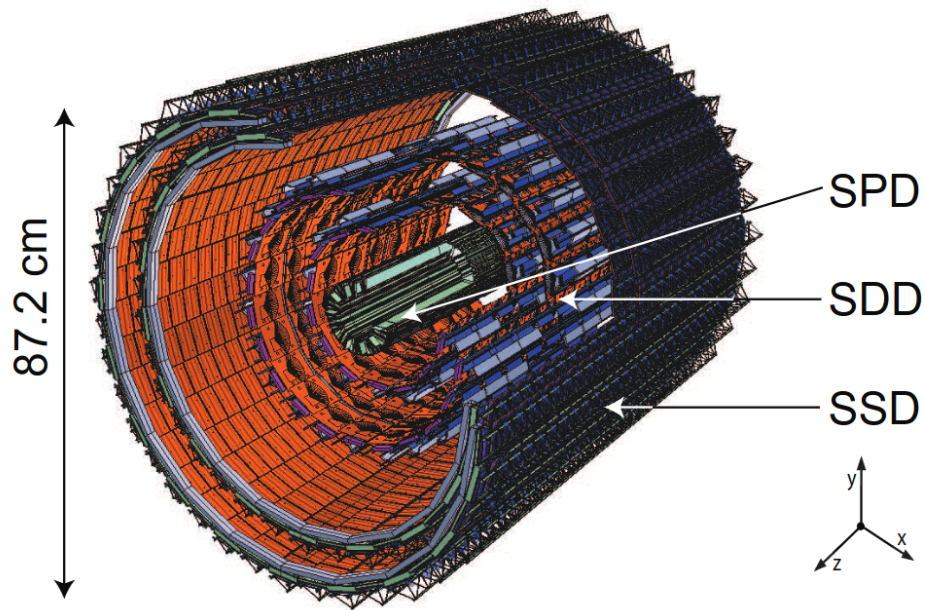


FIGURE 3.4: The schematic view of the Inner Tracking System at ALICE. The two outer layers are the SSD detector, the two middle layers are the SDD detector and the two inner layers are the SPD detector. Figure from [133].

with a gaseous medium which, depending on the period, is Ar – CO₂ (88:12) or Ne – CO₂ – N₂ (90:10:5). Such gas mixtures can be ionised relatively easily by charged particles travelling through the active volume and, thanks to the electric field, electrons drift towards two end plates of the detector. The signal is amplified before reaching the detectors. The total drift time of the electrons is about 100 μ s. A dead time of about 200 μ s is then applied to neutralise the environment of electrons that can distort the amplification region by drifting back to the barrel after reaching the end plates. This results in a total time of about 300 μ s per read operation. Such a period drastically limits the readout rates to ~ 1 kHz and makes the ALICE detector slower than other detectors at the LHC (the recent upgrade of the readout technology for Run – 3 allows to reach 50 kHz).

The TPC is characterized by an accurate tracking. As can be seen in the Fig. 3.5, the end plates are divided into smaller pads. There are 18 sectors in the azimuthal angle ϕ , each divided into 159 rows. As a particle travels through the active volume, it interacts with the gas, ionising or exciting the electrons of the atom, many times before leaving

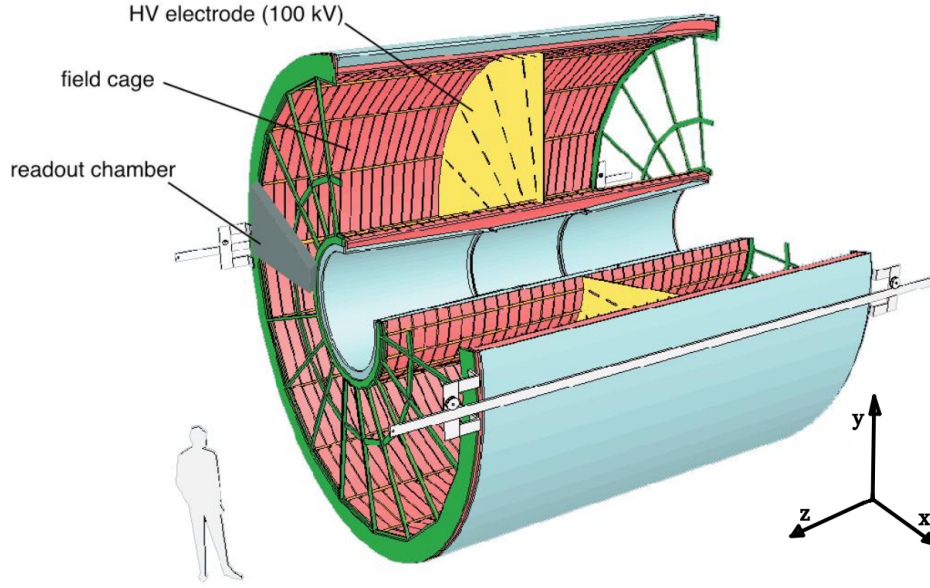


FIGURE 3.5: The schematic view of the Time Projection Chamber at ALICE [134]. The inner and outer red pads indicate an active volume of the detector.

the detector. Electrons drifting from their creation at a particular xy position will travel to the end plates, leaving the signal in the pad corresponding to their initial xy position. At the same elapsed time, the time from the collision to the moment when the electrons reach the endplates can be used to calculate the z position of each ionisation. Thus, by collecting the xyz information for each interaction, the trajectory of the particles can be reconstructed (schematic example in Fig. 3.6). During *Run – 2* it was possible to reconstruct up to 10,000 charged particles from a single collision, making the device ideal for reconstructing Pb–Pb collisions.

The trajectory of the particle is deflected proportionately to the particle's momentum and charge due to the presence of the constant magnetic field along the beam axis, according to the formula:

$$r = p/(qB), \quad (3.1)$$

where r is the radius of curvature produced by the magnetic field, q is the charge of the particle, and B is the magnetic field strength. The sign of the charge can therefore be obtained from the direction of the deflection in the magnetic field. The value of the momentum can be recovered from the measurement of r .

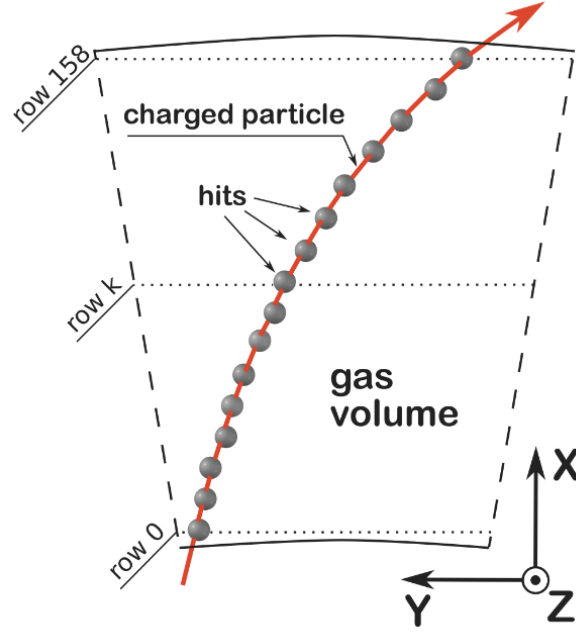


FIGURE 3.6: The schematic view of the single sector of the Time Projection Chamber at ALICE [135]. Points indicate interactions that caused hits in the end-plates along the particle's trajectory.

The amplitude of the signal left in the end-plates of the TPC can be translated into the specific energy loss of the particle $\frac{dE}{dx}$ and later used for the identification of the particle. For this purpose, the measured energy loss and momentum are compared with the Bethe-Bloch which relates the $\frac{dE}{dx}$ with the velocity of the particle expressed as: 3.2.

$$\left\langle \frac{dE}{dx} \right\rangle = A_1 \cdot \frac{z^2}{\beta^2} \left[\ln \left(A_2 \cdot \frac{\beta^2}{1 - \beta^2} \right) - \beta^2 \right], \quad (3.2)$$

where $A_{1,2}$ are coefficients that depend on the material of the active volume, z is the charge number, and β is the velocity of the particle.

The particles' momentum that reaches the end-plates is relativistic and is can be expressed as:

$$p = \frac{m \cdot \beta}{\sqrt{1 - \beta^2}}, \quad (3.3)$$

where m corresponds to the rest mass of the particle.

The final energy loss dependence on momentum and mass can be then described:

$$\left\langle \frac{dE}{dx} \right\rangle = A_1 \cdot z^2 \cdot \frac{m^2 + p^2}{p^2} \left[\ln \left(A_2 \cdot \frac{p^2}{m^2} \right) - \frac{p^2}{m^2 + p^2} \right], \quad (3.4)$$

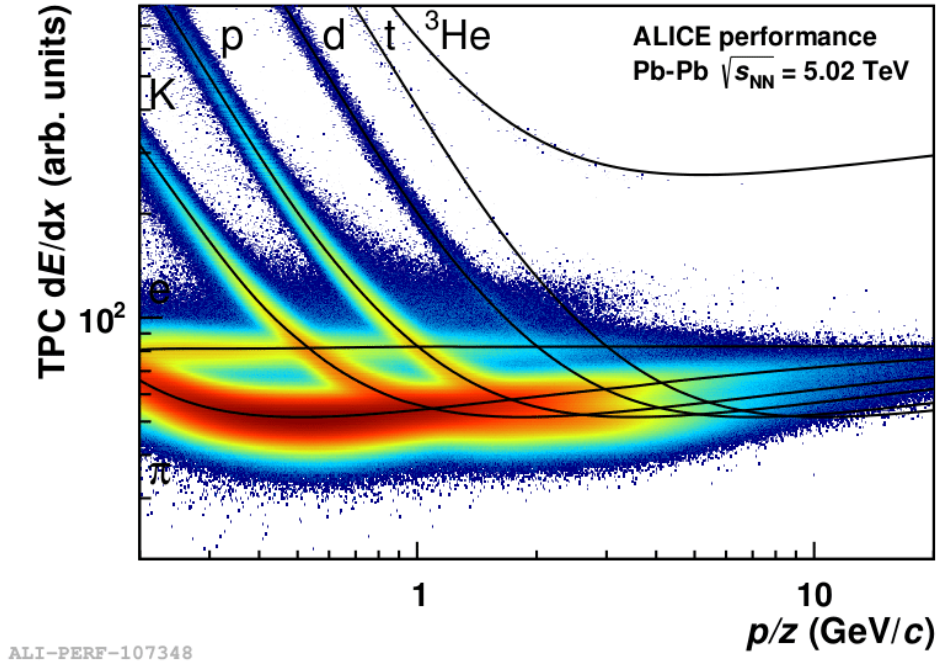


FIGURE 3.7: The energy loss as a function of momentum measured by the ALICE TPC for Pb-Pb collisions at $\sqrt{s_{NN}} = 5.02$ TeV [136].

An example of the ALICE TPC energy loss dependence for charged particles is shown in Fig. 3.7. In the figure, the black lines correspond to the theoretical prediction of the signal for different particle species using a given mass hypothesis. The entries in the 2D histogram represent recorded tracks that are characterised by a certain energy loss and momentum. The correlation between the momentum and energy loss sometimes deviates due to detector resolution effects, creating a band around the expected value. To identify the particle, each track is compared with the prediction of the mass hypothesis and can be described by the σ value, which is the difference between the measured and expected values for a given mass hypothesis normalised by the detector uncertainty. It can also be seen from Fig. 3.7 that the TPC detector of the ALICE experiment separates the particle species at low momenta (e.g. p of kaons up to 0.45 GeV/c or deuterons up to 1.3 GeV/c), whereas, in the high-momentum region, the bands of different particle species overlap. To identify particles coming

from such overlapping regions, other ALICE sub-detectors have to be used in addition to the TPC. More information about the TPC can be found in [134].

3.2.4 The Time-Of-Flight detector

The Time-Of-Flight detector (TOF) is used to complement particle identification provided by the TPC detector. The TOF system, similarly to TPC, is cylindrical-shaped hollow barrel with the inner and outer radius from the beam axis equal to 370 and 399 cm, respectively. It is placed behind the TPC and covers the pseudorapidity range of $|\eta| < 0.9$. The TOF detector consists of 1593 Multi-gap Resistive Plate Chambers (MRPC) with a size of $7.4 \times 120 \text{ cm}^2$ each. It is build by 2 cathodes separated with 5 layers of glass, an anode and 5 more layers of glass with the whole volume filled with the drift gas. Because the anode and cathodes are under the different high voltage when particles traverse the detector, an avalanche of electrons is released. The TOF detector measures the time it takes the particle to fly from the collision point to the TOF system. The resolution of this measurement is about 80 ps. The time of flight is next translated into the velocity of the particle. The particle's rest mass can be measured by combining the information about its velocity (β) and the momentum:

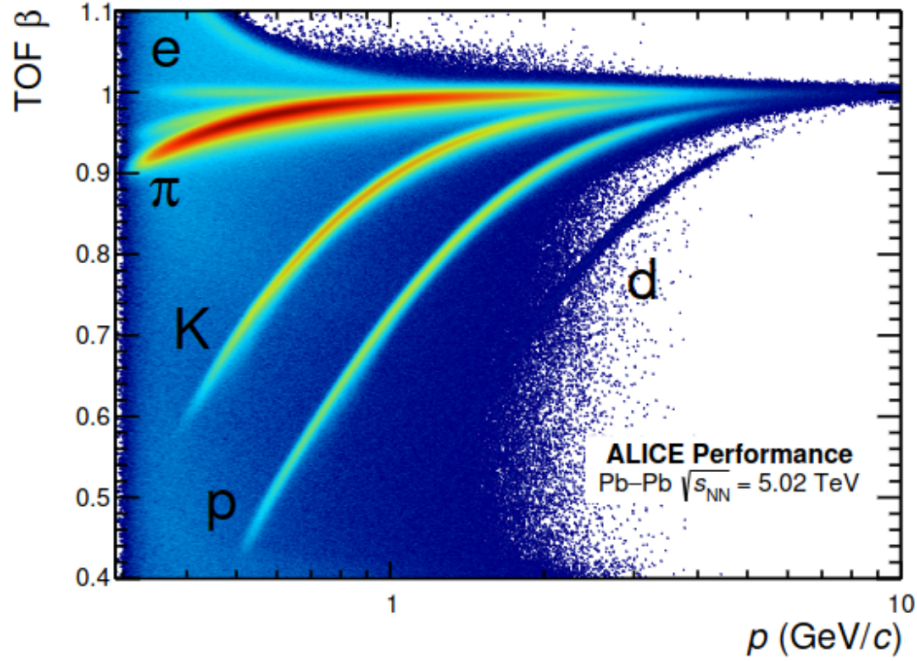
$$m = p \cdot \sqrt{\beta^2 - 1}, \quad (3.5)$$

The particle identification in the TOF detector is performed based on the distribution of β as a function of momentum. An example of such distribution is presented in Fig. 3.8. Similarly to TPC energy loss distributions, here also different bands for different particle species can be distinguished. Not all particles reach the TOF detector as it is placed relatively far away from the interaction point. Particles, especially those with low momentum, can be absorbed or bent back into the TPC. Therefore, TOF is usually included into particles identification in the higher momentum range where the TPC is no longer able to distinguish particles alone. More information about TOF can be found in [137].

3.2.5 Other sub-detectors of the ALICE experiment

Transition Radiation Detector

The Transition Radiation Detector (TRD) [138] is used for electron identification and triggering, but can also be used for particle reconstruction and calibration in the ALICE



ALI-PERF-106336

FIGURE 3.8: The particle's velocity β as a function of momentum measured by the ALICE TOF for Pb-Pb collisions at $\sqrt{s_{\text{NN}}} = 5.02$ TeV.

central barrel. The TRD detector is located at radii from 290 to 370 cm and is composed of 18 sectors, each consisting of six layers. The methodology is based on measurements of the transition radiation emitted by charged particles crossing the boundary between media with different dielectric constants.

High-Momentum Particle Identification Detector

The High-Momentum Particle Identification Detector (HMPID) [139] is used for identification of high-momentum hadrons with p_T from 1 to 5 GeV/c. It is located ~ 500 cm away from the center of the interaction point and consists of 7 identical liquid Cherenkov radiator modules. The HMPD detector uses Ring Imaging Cherenkov counters with CsI photo-catode.

Photon Spectrometer

The Photon Spectrometer (PHOS) [140] is used for the detection of photons in a broad momentum range from 0.5 to 10 GeV/c, for the measurement of hadron spectra via their radiative decays and for the triggering system. The PHOS detector consists of 12544 detection channels based on lead-tungstate crystals. It is located 460 cm from the interaction point at the bottom of the ALICE structure. The detector measures the particle signal by suppressing charged particle contamination in the proportional

chambers of the Charged Particle Veto Detector (CPV), located in front of the PHOS modules.

Electromagnetic Calorimeter detector and Di-jet Calorimeter

The Electromagnetic Calorimeter (EMCal) [141] is used to trigger and reconstruct high energy photons, electrons, neutral pions and particle jets. The EMCAL detector is located 4.5 m from the interaction point and consists of 4416 individual modules. Particle detection is performed by a lead scintillator sampling calorimeter. The Di-jet Calorimeter (DCAL) is a six-module extension of the EMCAL installed at the bottom of the magnet, 460 cm from the interaction point.

Photon Multiplicity Detector

The Photon Multiplicity Detector (PMD) [142] it is used to measure photon distribution and multiplicity. The detector is located 580 cm from the interaction point at the door of the ALICE magnet and consists of 2 plates, each containing 24 gas-tight modules with proportional chambers.

Forward Multiplicity Detector

The Forward Multiplicity Detector (FMD) [143] is used for precise charge multiplicity information at very high forward speeds. The FMD detector consists of 51200 silicon strip channels forming 5 ring counters each with 20 or 40 sectors in the azimuthal angle. The rings are located 320 cm in front and 80 cm in front and behind the nominal collision point.

Zero-Degree Calorimeter detector

The Zero-Degree Calorimeter (ZDC) [144] is used to measure the energy of the spectator nucleons in heavy-ion collisions and thus to measure the centrality. The ZDC is located 116 m from the interaction point in the direction of the beamline on both sides of the ALICE detector. It uses three types of calorimeters: neutron, proton and electromagnetic, which detect the Cherenkov light produced by the shower particles in silica optical fibres embedded in a dense absorber.

MUON Spectrometer

The MUON spectrometer [145] is used to measure particles containing heavy quarks via the muonic channel. The muon spectrometer is located after the ALICE detector. It consists of 3 absorbers to filter the background, a set of tracking chambers before, inside and after the magnet, a trigger and a tracking system.

ALICE Cosmic Ray Detector

The ALICE Cosmic Ray Detector (ACORDE) [146] is used as a cosmic ray trigger and

detector. It is located on the three upper faces of the ALICE magnet and consists of an array of plastic scintillator counters.

T0 Detector

The T0 detector (T0) [147] is used as a fast trigger, providing a wake-up call for the TRD and a collision time reference for the TOF. The detector consists of 2 arrays placed on opposite sides of the interaction point at a distance of 360 cm and 60 cm. It consists of photomultiplier tubes equipped with Cherenkov radiators.

ALICE diffractive detector The ALICE Diffractive Detector (AD) [148] is used to optimise trigger efficiencies and purities in event selection. The AD detector consists of two layers of scintillator pads placed on either side of the interaction point.

3.3 Data overview

The data used to perform the analyses presented in this thesis were collected by the ALICE experiment between 25.11-13.12 of 2015 and 2.11-2.12 of 2018. Both periods were a part of the ALICE *Run – 2*. During this time, lead ions were collided in the LHC at an energy of $\sqrt{s_{NN}} = 5.02$ TeV with an interaction rate of 300-400 Hz or 1-7.5 kHz in 2015 data and 7.5 kHz in 2018. In total, 600 and 890 million events were collected in the considered periods of 2015 and 2018 periods, respectively. The kaon–proton study presented in this thesis is performed on data from 2015. The pion–deuteron, proton–deuteron and kaon–deuteron studies are performed on data from 2018.

The process of data taking refers to many individual *runs* that can last from several minutes to hours. During one individual *run*, the configuration of detectors used to register collisions remains the same. The status of all components of the ALICE detector is monitored all the time and displayed to operators present in the ALICE control room. Signals left by particles after each triggered event are a subject to online reconstruction, which allows the initial quality of the data collected during each *run* can be already checked during the process of data taking. Based on the status of both the detector and the collected data, operators decide if the *run* should be stopped, e.g. to change the configuration of detectors or to correct a possible malfunction of the system. All the parameters influencing the data taking and the reconstruction process in each *run* are stored and used later to calibrate the data.

The raw data collected by ALICE first go initially through the process of local reconstruction where all the sub-detectors used are searched for clusters (hits in the detector caused, for example, by a crossing particle). Next, the primary vertex of

the collision is pre-found based on hits in the ITS SPD layer (at this step, possible pileup of two events is also checked). Information about the vertex is further used to help in the track reconstruction, starting from the outer TPC part inward to ITS applying a Kalman filter algorithm. Next, backpropagation is performed from the interaction vertex through the TPC to the outer detectors, associating points there with already reconstructed tracks. Then, the re-fit is performed again through the outer to the inner detectors. At each step of the reconstruction, new information is added to improve the quality of the track reconstructions, e.g. corrections for energy loss or calculation of the length of the tracks. After the track reconstruction, the vertex of the collision is recalculated using new information from the tracks. At this stage, the reconstruction of particles that decay is also added. At the same time, the data are a subject to the calibration process for detector effects. The calibration process can be improved at a later stage if any particular issues are spotted that could bias the studies. All information, starting with the initial vertex reconstruction of a given event, is stored in ESD files. The reconstruction strategy is shown in a block form in Fig. 3.9. The processes of reconstruction, calibration, simulation, visualisation and general data processing are carried out by a software framework called *AliRoot*, which is based on ROOT [149].

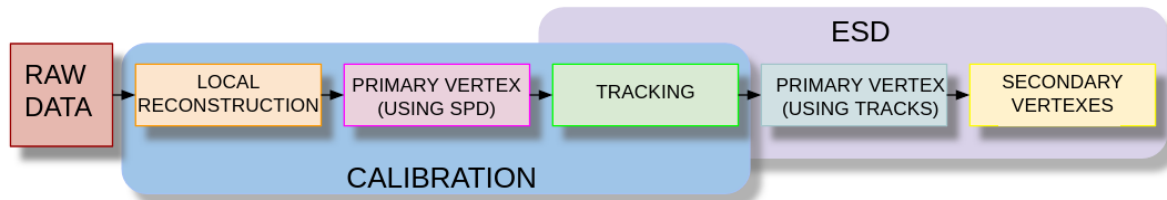


FIGURE 3.9: Workflow of the data reconstruction in ALICE.

The ESD files used to store the data contain the full reconstruction information which are not required in most of studies, and therefore reading and processing this complete data format is not justified from a resource point of view. For this reason, ESD files are filtered into reduced files called AOD files. The AOD format contains all the data required for the studies of this thesis and therefore all derived results are based on them.

The LHC *Run – 2* produced on average one petabyte of data per day. These data were initially processed by the CERN Data Center, the leading part of the CERN’s scientific, administrative, and computing infrastructure. The CERN Data Centre

performs the initial data reconstruction and stores one copy of the data. The second copy is sent to several large-scale data centres around the world. To process, analyse and store data for particular purposes the Worldwide LHC Computing Grid (WLCG) is used. The WLCG combines about 1.4 million computer cores and 1.5 exabytes of storage. These computing resources are distributed over 170 sites in 42 countries.

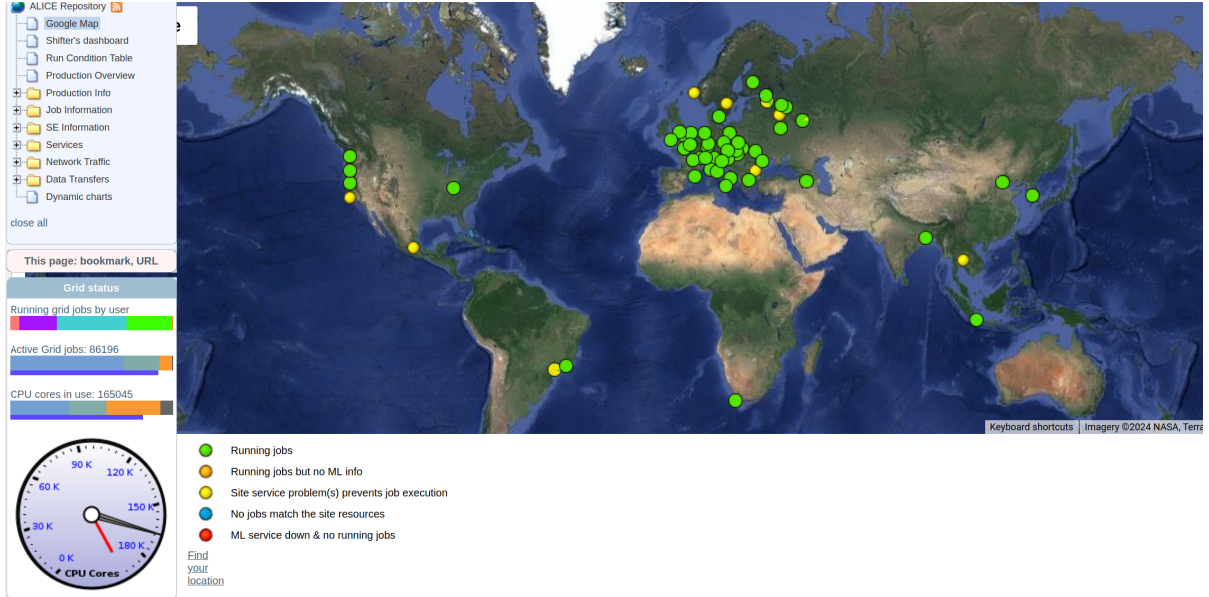


FIGURE 3.10: A grid of computing nodes used to perform analysis on ALICE data.

The ESD and AOD files of *Run – 2* are structured using the ROOT format [149]. Therefore, the C/C++ based ROOT software is used to analyse them. The ROOT framework was originally designed especially for particle physics data analysis. The data produced by the LHC experiments have to be accessible to all of members of the collaboration. This requires extremely large storage, computing power and network infrastructure to provide access to it. The grid infrastructure capable of providing all these requirements is AliEn [150], which is a software specific to the ALICE experiment used for the computations of this work. The AliEn uses grid computing technologies to allow analysers to process ALICE data. An example of the grid computing nodes available to execute jobs of analysers with file access transparent to the user, wherever in the world a file might be, is shown in Fig. 3.10.

Chapter 4

Analysis technique

*The dream – child moving through a land
Of wonders wild and new,
In friendly chat with bird or beast
And half believe in true.*

Lewis Carroll, Alice's Adventures in Wonderland

*A przecież porządnie wiedzieć, czego się nie wie,
to już dowiedzieć się niejednego o wiedzy przyszłej.*
Stanisław Lem, Wizja lokalna³

4.1 Experimental correlation function

In collision studies, the experimental correlation function is defined as a correlated distribution of particle relative momentum which is divided by an analogous uncorrelated distribution. The correlated distribution is obtained by pairing particles from the same collision. The uncorrelated distribution reflects the non-physical correlation and is obtained by pairing particles from different collisions where there is no possibility of the two particles interacting with each other:

$$C_{exp}(k^*) = N \frac{A(k^*)}{B(k^*)}, \quad (4.1)$$

where A and B are the correlated and uncorrelated distributions, respectively, and N is a normalisation factor between the two distributions. The factor N is calculated

³"But to know properly what you don't know is to learn a lot about future knowledge." – Stanisław Lem, Observation on the Spot

by dividing the integrals of the uncorrelated and correlated distributions in the range where femtoscopic and non-femtoscopic effects are not present or have a negligible magnitude. For the pion–deuteron study, this range covered k^* from 0.12 to 0.25 GeV/ c , in the proton–deuteron from 0.25 to 0.5 GeV/ c , in the kaon–proton study from 0.3 to 0.6 GeV/ c , and in the kaon–deuteron from 0.20 to 0.35 GeV/ c .

4.2 Data selection criteria

This thesis considers several analyses involving different types of particles. The combinations of kaon–proton (K^+p , K^-p , $K^+\bar{p}$, $K^-\bar{p}$), pion–deuteron (π^+d , π^-d , $\pi^+\bar{d}$, $\pi^-\bar{d}$), proton–deuteron (pd , $\bar{p}d$) and kaon–deuteron (K^+d , K^-d , $K^+\bar{d}$, $K^-\bar{d}$) pairs are examined. The study involving kaon–proton pairs is chronologically the first of the four studies and is based on ALICE Pb–Pb collisions at a centre-of-mass energy of $\sqrt{s_{NN}} = 5.02$ TeV data collected in 2015. All studies involving deuterons were performed with analogous Pb–Pb data, but registered in 2018 as these data had an improved efficiency for the deuteron reconstruction.

The kaon–proton analysis relies entirely on events selected by the minimum bias trigger, while the deuteron studies were analysed using additional central and semi-central triggers, which account for events classified as 0–10% or 30–50% (these triggers were previously described in Sec. 3.2.1). Only collisions with an event vertex within 10 cm from the center of the detector along the beam axis are accepted to the analysis. This requirement ensures a uniform detector coverage. Because of the same reason, all considered particles must have a pseudorapidity, η , between -0.8 and 0.8. The mixing buffer used for the non-correlated distribution is constructed to combine particles from events with similar parameters such as the centrality or the vertex position. In this case, the vertex and centrality spaces are divided into bins of equal size. The bin width is determined by the maximum and minimum range of the vertex position in the beam direction $(\text{vertex}_{\text{max}} - \text{vertex}_{\text{min}})/8$ and the considered centrality $(\text{centrality}_{\text{max}} - \text{centrality}_{\text{min}})/2$. For example, $\text{vertex}_{\text{max}} = 10$ cm and $\text{vertex}_{\text{min}} = -10$ cm, $\text{centrality}_{\text{max}} = 10\%$ and $\text{centrality}_{\text{min}} = 0\%$. The two particles are combined to contribute to the non-correlated distribution if the collisions from which they came were classified into the same bin of vertex and centrality.

In order to obtain an optimal quality of particle identification, the tracks of the candidate particles must satisfy several criteria. One of the most fundamental

constraints concerns the transverse momentum (p_T) of the particles, which is typically chosen based on detector acceptance, the ability to efficiently and cleanly reconstruct the tracks, and the characteristics of the overall sample. In this thesis:

■ Charge pion candidates are required to have p_T greater than 0.10 GeV/ c , which is the lowest possible acceptance of pions in ALICE *Run – 2*, and less than 1.5 GeV/ c , which is chosen to ensure high sample quality (above this range the signal of pions starts to overlap with other particle species in both TPC and TOF detectors).

■ (Anti)proton candidates are required to have p_T greater than 0.5 GeV/ c and less than 3 GeV/ c , which is chosen based on properly reconstructed and matched signals from the detectors which are characterised by high sample quality.

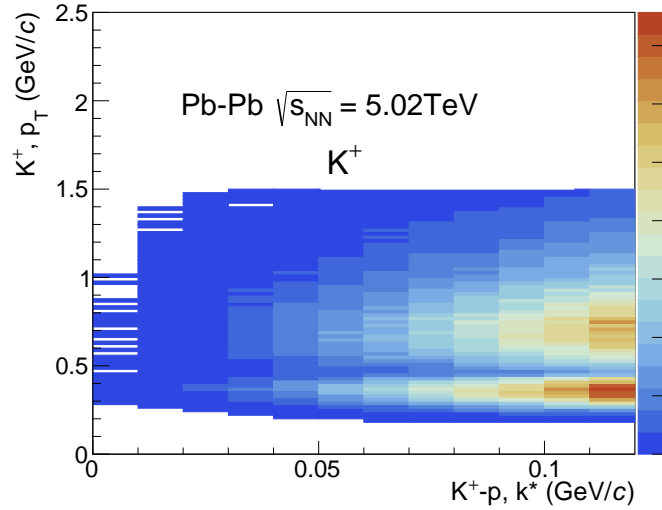


FIGURE 4.1: Distribution of p_T of positive kaons vs k^* of the kaon-proton pairs calculated for kaons with p_T range 0.2–1.5 GeV/ c and protons with p_T range 0.5–3.0 GeV/ c .

■ For kaons, p_T is required to be greater than 0.2 GeV/ c and smaller than 0.45 GeV/ c in the kaon-proton study and 1.5 GeV/ c in the kaon-deuteron study. The lower limit is determined by the acceptance of low-momentum kaons in the ALICE detector during *Run – 2*. The selection of the upper range of kaons in two studies differs between the kaon-proton and kaon-deuteron studies, because by including the TOF at certain p_T of the selection, the two well-separated maxima contributing similarly to low k^* are observed (see Figs. 4.1, 4.10). It is more pronounced in the kaon-proton study, where kaons from the whole range can match the velocity of protons and contribute to low k^* . Such double maxima can further leads to source measurements

reflecting a non-trivial average of two sources. Therefore, in the kaon–proton study the sample has been limited to the lower range (the higher range has been considered in the evaluation of the systematic uncertainties). Similarly, the issue of the two mean values is observed in other pairs, e.g. kaon–deuteron. However, the low k^* region is dominated by only one (lower) range. Also in case of deuteron, the statistics after exclusion of one of the regions would not reach the required statistical significance of the signal.

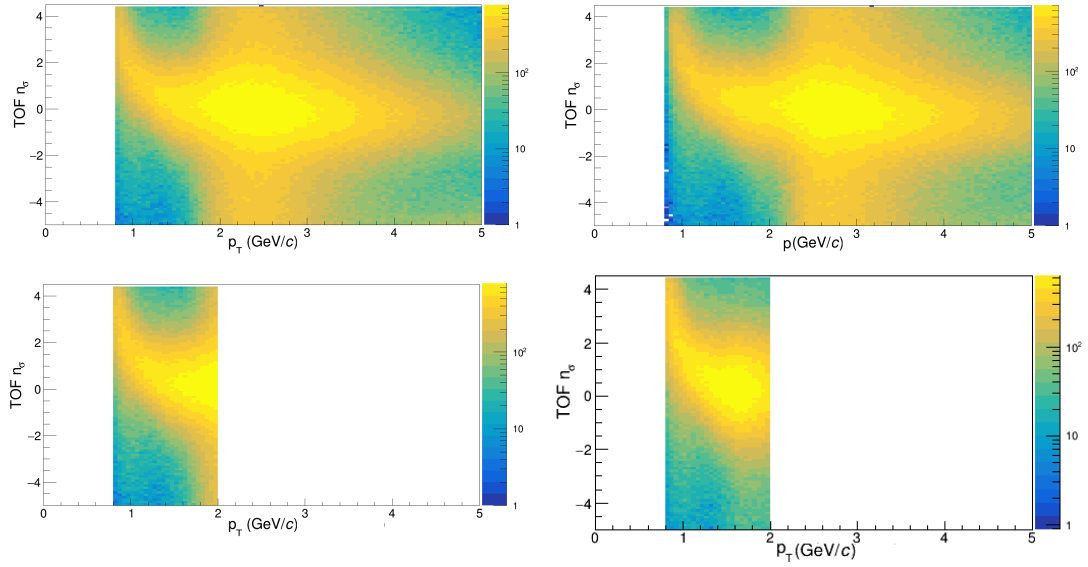


FIGURE 4.2: Examples of the deuteron's distributions of TOF n_σ vs p_T (upper left, bottom left and right) and p (upper right) without an additional cut on p . the deuteron's distributions of TOF n_σ vs p (bottom right) with the additional cut on p . See text for more details.

■ (Anti)deuterons are required to have p_T greater than 0.8 GeV/c and less than 2.0 GeV/c. Deuterons, are detectable even earlier outside of that selected range, however, deuterons below 0.8 GeV/c have a significant fraction of spallation deuterons from the material budget of the detector and thus are not considered in the study. An additional cut on the momentum (p) is also applied, which is required to be less than 2.2 GeV/c. This additional requirement has been added to remove the contamination from other particles in the p_T range 1.6–2.0 GeV/c (Fig. 4.2 (left)) and thus increase the statistics of deuterons by accessing higher p_T . The cut has been chosen based on the momentum distribution, because there the mentioned contamination starts at (~ 2.2 GeV/c) (Fig. 4.2 (right)). This means that both deuterons with p range 1.6–2.2 GeV/c and contaminating particles above $p = 2.2$ GeV/c can

contribute to p_T range 1.6-2.2 GeV/ c . However, by applying this constraint at p , the contribution of contamination to the p_T region is removed (Fig. 4.2 (bottom right)).

Another important constraint of this study is the check on a distance to the collision vertex (DCA). The particles has to have DCA below a given limit chosen based on the impact of the primary and secondary contributors on different regions of the DCA distribution. The secondary particles are the particles that are produced at a macroscopic distance from the initial collision but they are not a direct product of the hadronization processes. The most important secondary contributors are particles from weak decay processes and spallation of particles within the detector material. In this study, pions, kaons and antideuterons are required to pass the DCA cut within 2.4 cm in the transverse direction (XY) and within 3.2 cm in the beam direction (Z). This is a wide range, because for pions and kaons the DCA distribution of secondary particles is similar to those of the primary nature. Therefore, the two are not well separable in the DCA spectra. Antideuterons, on the other hand, are expected to have no contributions from the material of the detectors (which are not made of antimatter), and negligible contributions from weak decays. (Anti)protons and deuterons have to fulfil a stricter selection, since protons are expected to contain a non-negligible fraction of weak decay contributions, and protons and deuterons are contaminated by particles knocked out of the detector material. In the (anti)proton and deuteron DCA distributions, the primary particles are most concentrated around the event vertex, while weak decay particles and those from the detector material also contribute to the tail structure of the DCA distributions (see examples in Fig 4.3 which will be described in more details in the following subsection). Therefore, by applying stricter criteria to the DCA, we can limit the contribution of secondary particles to the analysed sample. The DCA_{XY} for the three particle species is described by the p_T dependent cut $DCA_{XY} < 0.0105 + 0.0350/(p_T/(\text{GeV}/c)^{-1.1})$ cm with a simultaneous 1 cm limit of the DCA_Z .

A charged particle traversing the TPC release electrons from the gas which further induce a signal on a given pad-row, called as a cluster. All tracks considered in this study must contain at least 70 clusters recorded in TPC pad-rows. The maximum number of pad-rows in the TPC is 159 however, some of the TPC clusters along the track trajectory can be missing, because e.g they go though some dead zones of the detector or the charge is below threshold. Therefore, this selection is provided to

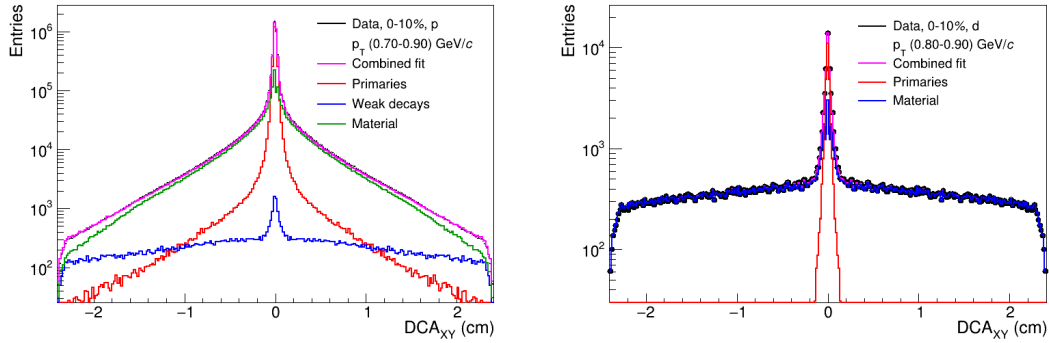


FIGURE 4.3: A DCA_{XY} distributions for protons (left) and deuterons (right) together with the template fit of underlying processes of particles production. Lines represent particles: produced in primary processes (red), coming from weak decays of other particles (green), knocked out from the material due to interaction with particles created in the collision (blue), a sum of all ingredients (magenta).

assure that tracks with sparse space points, large continuous missing areas along their trajectory or fake tracks that are short are excluded from the analysis.

The last crucial set of single particle requirements is connected to the so-called N_σ -requirements that refers to difference between the measured and expected signals of energy loss in the TPC and velocity measured with TOF expressed in units of detector resolution, N_σ . Particles are accepted if the N_σ is smaller than a given value that is determined based on the ability to recognise clearly particles in ALICE detector. The N_σ requirements are summarized in Tab. 4.1. An example of TPC N_σ distributions of pions, kaons, protons and deuterons is presented in Fig. 4.4.

Next, the tracks that pass the above requirements are combined into pairs. However, such pairs before including them into the correlation function have to also pass by additional pair selection. Such filtering serves the purpose of reducing detector effects such as track merging and/or splitting, and conversion that are described below.

In general, for high-multiplicity collisions, the products can be very close to each other and therefore, two tracks can be recognised as one by the reconstruction algorithm. To reduce such situations the merge fraction (MF) selections have been applied. The selection method is described below:

- First TPC radius range, R : (0.8, 2.5) m has been selected,

TABLE 4.1: Single particle criteria for pions, kaons, (anti)protons and (anti)deuterons.

Track selection	
$\pi^\pm p_T$	$0.1 < p_T < 1.5 \text{ GeV}/c$
$K^\pm p_T$ (kaon–proton analysis)	$0.2 < p_T < 0.45 \text{ GeV}/c$
$K^\pm p_T$ (kaon–deuteron analysis)	$0.2 < p_T < 1.5 \text{ GeV}/c$
$p/\bar{p} p_T$	$0.5 < p_T < 3.0 \text{ GeV}/c$
$d/\bar{d} p_T$	$0.8 < p_T < 2.0 \text{ GeV}/c$
$all \eta $	< 0.8
$\pi^\pm, K^\pm, \bar{d} \text{ DCA}_z$	3.2 cm
$d, p, \bar{p} \text{ DCA}_z$	1.0 cm
$\pi^\pm, K^\pm, \bar{d} \text{ DCA}_{xy}$	2.4 cm
$d, p, \bar{p} \text{ DCA}_{xy}$	$< 0.0105 + 0.0350/(p_T/(\text{GeV}/c))^{-1.1} \text{ cm}$
Pion selection	
$N_{\sigma, \text{TPC}} (0.1 < p < 0.5 \text{ GeV}/c)$	< 3
$\sqrt{N_{\sigma, \text{TOF}}^2 + N_{\sigma, \text{TPC}}^2} (0.5 < p < 1.5 \text{ GeV}/c)$	< 3
Kaon selection	
$N_{\sigma, \text{TPC}} (0.2 < p < 0.4 \text{ GeV}/c)$	< 2
$N_{\sigma, \text{TPC}} (0.4 < p < 0.45 \text{ GeV}/c)$	< 1
$N_{\sigma, \text{TPC}}; N_{\sigma, \text{TOF}} (0.45 < p < 0.8 \text{ GeV}/c)$	$< 3; 2$
$N_{\sigma, \text{TPC}}; N_{\sigma, \text{TOF}} (0.8 < p < 1.0 \text{ GeV}/c)$	$< 3; 1.5$
$N_{\sigma, \text{TPC}}; N_{\sigma, \text{TOF}} (1.0 < p < 1.5 \text{ GeV}/c)$	$< 3; 1$
(Anti)proton selection	
$\sqrt{N_{\sigma, \text{TOF}}^2 + N_{\sigma, \text{TPC}}^2} (0.5 < p < 3.0 \text{ GeV}/c)$	< 3
$\sqrt{N_{\sigma, \text{TOF}}^2 + N_{\sigma, \text{TPC}}^2}$ of signal interpretation as e, π or K ($0.5 < p < 3.0 \text{ GeV}/c$)	> 2
(Anti)deuteron selection	
$N_{\sigma, \text{TPC}} (0.8 < p < 1.3 \text{ GeV}/c)$	< 2
$\sqrt{N_{\sigma, \text{TOF}}^2 + N_{\sigma, \text{TPC}}^2} (1.3 < p < 2.2 \text{ GeV}/c)$	< 2

— $|\Delta\eta| < s$, e.g. $s = 0.01$ where merging may occur,

— Maximum allowed distance between two tracks d , e.g. $d = 0.05 \text{ m}$

After applying the above three selections, the merged fraction (MF) is calculated as:

$$MF = \frac{N_{pass}}{N_{total}} \quad (4.2)$$

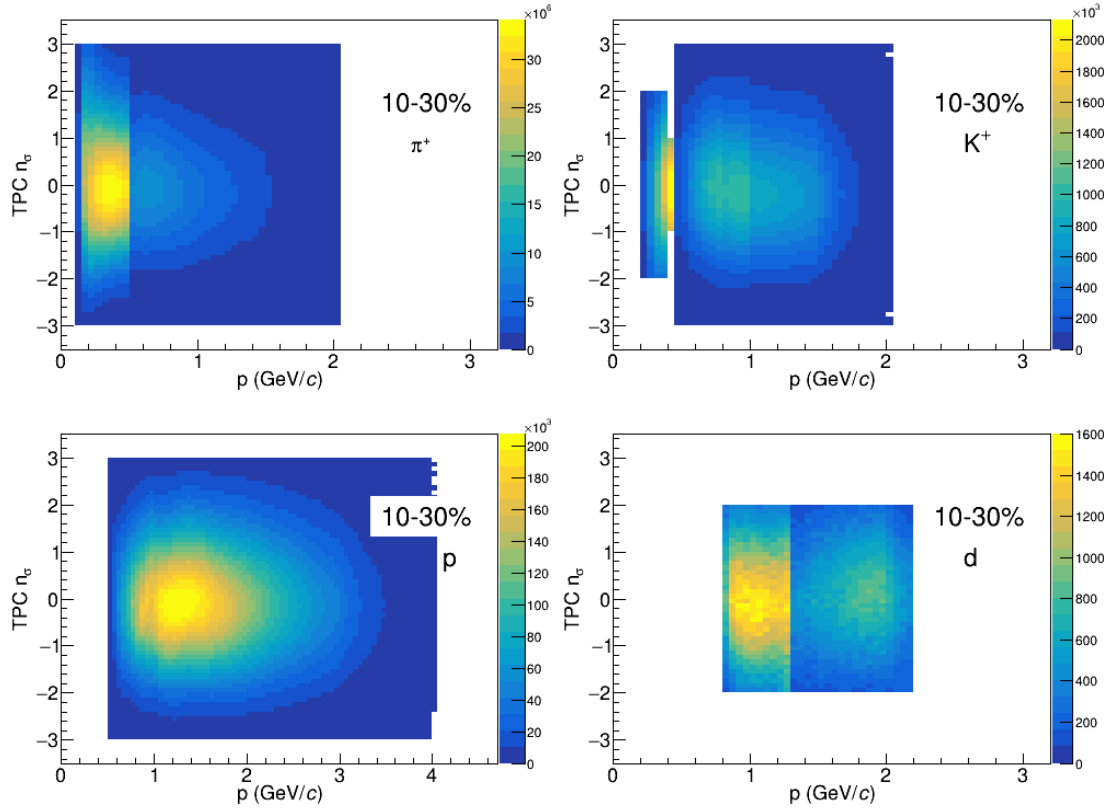


FIGURE 4.4: The TPC N_σ distributions of π^+ (top left), K^+ (top right), p (bottom left), d (bottom right) selected for purpose of this study using Pb–Pb collisions at $\sqrt{s_{NN}} = 5.02$ TeV data registered by ALICE experiment.

where N_{pass} is the number of points for a distance between tracks $< d$ that have been calculated in the R range in steps of 1.0 cm and divided by N_{total} which is the total number of points. The pairs are removed if their MF is more than the selected fraction, f e.g. $f = 0.03$. The values of s , d and f used for these studies are summarised in the Tab. 4.2 and were chosen based on the distribution of $\Delta\phi^*$ vs $\Delta\eta$ without any cut to cover the merged region. In this distribution $\Delta\phi^*$ is a difference of the two particles in azimuthal angle (see Fig. 3.3) calculated in the PRF, and $\Delta\eta$ is the two-particle difference in the pseudorapidity space. An example of such a distribution with and without the cut is presented in Fig. 4.5.

A second requirement applied for the pairs called pair quality removes split tracks in two segments in the TPC, e.g. by the TPC central membrane or a TPC sector boundary. Such segments should be correctly connected in the tracking procedure to form a single track if the detector calibration is perfect. However, in a few rare cases this does not happen and a split track can appear. Such pairs would consist

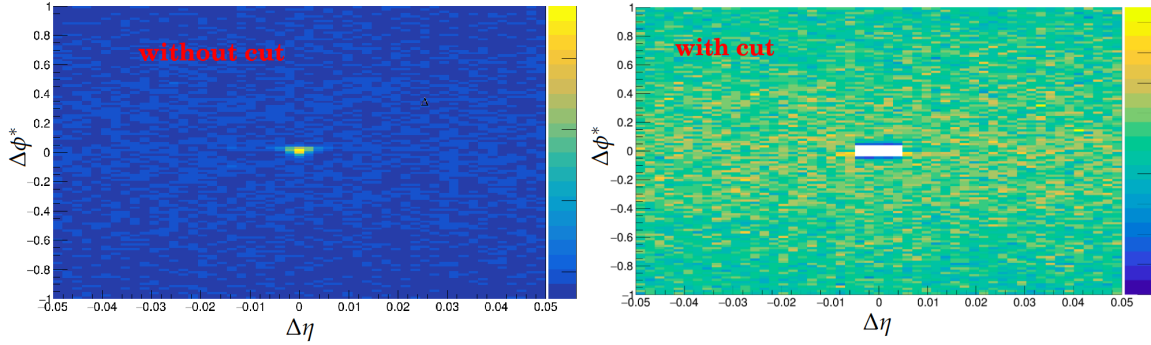


FIGURE 4.5: Examples of the distributions of $\Delta\phi^*$ vs $\Delta\eta$ for proton–deuteron pairs without (left) and with (right) track merging cut.

TABLE 4.2: The track merging cut settings of $|\Delta\eta|$ (s), distance (d) and fraction (f) used in the four studies considered in this thesis.

	s	d (m)	f
kaon–proton	0.010	0.03	0.02
pion–deuteron	0.005	0.03	0.03
proton–deuteron	0.005	0.03	0.02
kaon–deuteron	0.005	0.03	0.02

of two tracks that have a relatively small number of TPC clusters and they would rarely both have a cluster in the same TPC pad-row. Therefore, we count, for each pair, the number of times that both tracks have a separate (non-shared) cluster in a TPC pad-row. Pairs for which this number is less than the half of the total number of clusters (if both have clusters in the same row) are removed. In this thesis the fraction of shared clusters was required to be $< 5\%$. The summary of number pairs contributing to low k^* range is presented in Tab. 4.3.

4.3 Corrections

The ideal experimental correlation function of this work should be constructed using only particles that are primarily produced in the hadronization processes following particle or ion collisions, and that are not misidentified for other particle species in the identification procedure. However, the experimental sample of particles and the information about the recorded signals themselves are never perfect. Several effects can be distinguished that have a direct impact on the observed correlation functions as presented in the following subsections.

TABLE 4.3: Number of particle pairs contributing to low k^* range.

Particle pair	0 – 5%	5 – 10%	10 – 20%	20 – 30%	30 – 40%	40 – 50%
$\pi^+ d$	2.4×10^7		2.5×10^6		1.7×10^6	
$\pi^- \bar{d}$	1.3×10^7		1.4×10^6		1.2×10^6	
$\pi^+ \bar{d}$	1.3×10^7		1.4×10^6		1.2×10^6	
$\pi^- d$	2.3×10^7		2.3×10^6		1.7×10^6	
pd	6.0×10^4		7.0×10^3		5.6×10^3	
$\bar{p}\bar{d}$	2.8×10^4		3.5×10^3		3.0×10^3	
$K^+ p$	2.5×10^6	1.8×10^6	2.2×10^6	1.1×10^6	5.5×10^5	2.5×10^5
$K^- \bar{p}$	1.8×10^6	1.3×10^6	1.6×10^6	8.1×10^5	4.0×10^5	1.8×10^5
$K^+ \bar{p}$	1.8×10^6	1.3×10^6	1.6×10^6	8.3×10^5	4.2×10^5	1.9×10^5
$K^- p$	2.4×10^6	1.7×10^6	2.1×10^6	1.1×10^6	5.5×10^5	2.5×10^5
$K^+ d$	2.5×10^5		2.5×10^4		1.9×10^4	
$K^- \bar{d}$	1.2×10^5		1.4×10^4		1.2×10^4	
$K^+ \bar{d}$	1.3×10^5		1.5×10^4		1.1×10^4	
$K^- d$	2.4×10^5		2.3×10^4		1.5×10^4	

4.3.1 PID purity

Firstly, particles can be incorrectly identified. Typically, selection criteria aim to maximize identification quality by restricting momentum and n_σ ranges to only cover detector signals where different particle species are distinguishable. To assess particle identification quality (*PID purity*) a dedicated Monte Carlo (MC) simulations of events containing comprehensive particle information are utilized. By applying the same selections as those used on experimental data, one can assess the effectiveness of the selection requirements by direct verification of the nature of particles passing them. In this thesis, such calculations rely on GEANT3 and HIJING [151] simulations of Pb–Pb $\sqrt{s_{\text{NN}}} = 5.02$ TeV collisions, aligned with corresponding experimental data, incorporating all technical aspects encountered during data acquisition. The PID purity of kaons and protons is constrained by dividing the distribution of e.g. p_T of particles that passed the cuts and are checked if they are truly kaons or protons, by the distribution where the check is based only on the selection requirements. For pions and (anti)deuterons, the PID purity is calculated using a data-driven approach where the particle signal in a TPC and TOF detectors is examined without any n_σ cuts, and the signal-to-background fraction in the cut range is determined as a final PID purity value. An example of the data-driven method is presented in Fig. 4.6. This method is applied for pions because the ultra-soft region affected by electrons is not

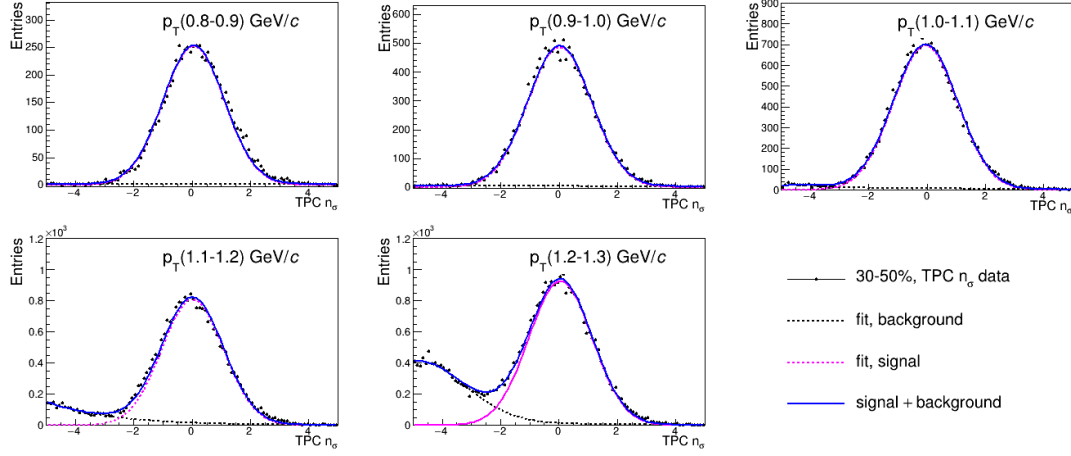


FIGURE 4.6: A TPC n_σ distributions of deuterons registered in 30 – 50% Pb–Pb collisions at $\sqrt{s_{NN}} = 5.02$ TeV for five transverse momentum ranges. Lines represent fit to data: signal (dashed magenta), background (dashed black), both (solid blue).

fully represented in available MC. Also, the production of primary (anti)deuterons in processes following ion collisions is not originally included in the HIJING simulations. Composite particles are typically injected and entangled with the main simulations using GEANT3 [152]. Therefore, a direct calculation of PID purity from such MC is unfeasible and the data-driven approach is crucial for its proper calculations. The PID purity for each particle species considered in this thesis is presented in Fig. 4.7.

4.3.2 Primary fraction

Secondly, as it was already mentioned particles registered in the detectors can originate from various processes occurring after the hadronization stage such as weak decays and the spallation of particles within the detector material. The fraction of particles created in primary processes (*primary fraction*) within the entire accepted sample can be calculated using MC data, where the origin of all particles can be directly verified. This method has been applied to study pions and kaons. (Anti)protons and deuterons are analyzed using a data-driven approach based on a template fit of expected DCA distributions of primaries, secondaries, and particles from the detector material budget to the distribution obtained from experimental data. For protons, the template of the distributions of weak decays and material particles is obtained from MC simulations. Primary deuterons are not directly included in the simulations, thus cannot be considered in the same manner. However, for (anti)deuterons the

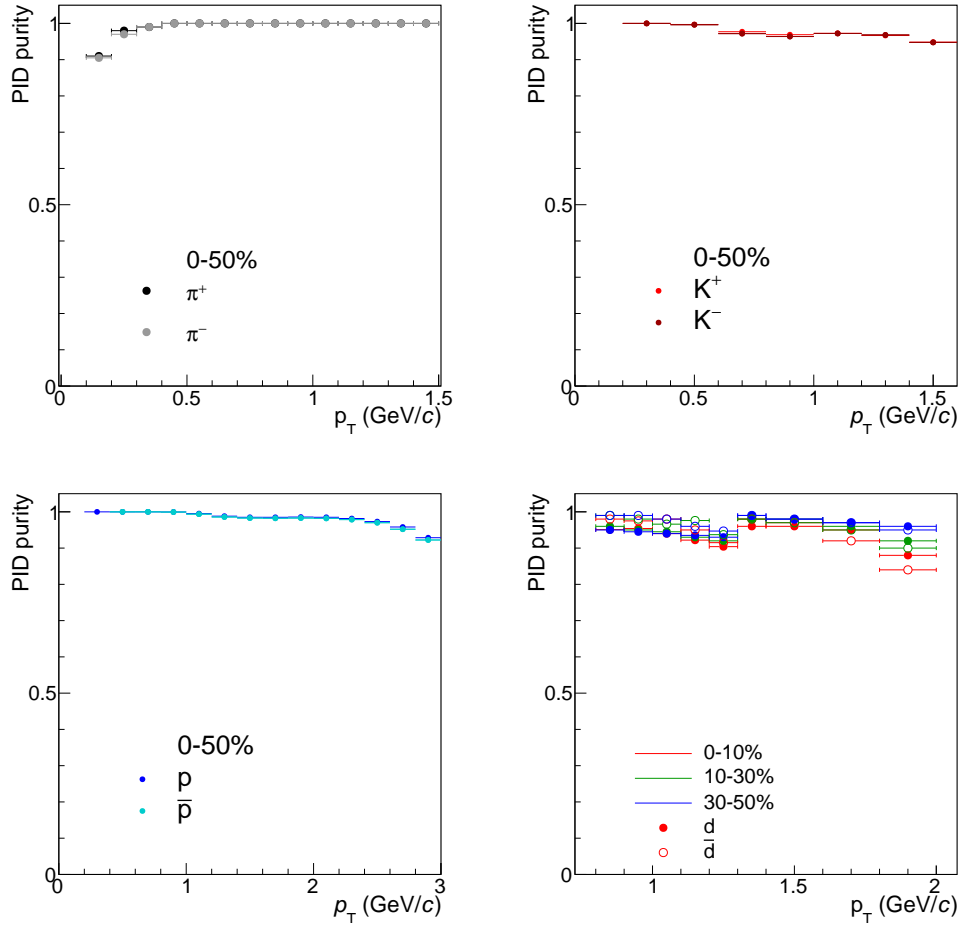


FIGURE 4.7: Distributions of PID purity as a function of transverse momentum for pions (top left), kaons (top right), (anti)protons (bottom left) and (anti)deuterons (bottom right).

impact of weak decays is expected to be negligible and also antideuterons cannot be produced via material knock-out as a consequence of baryon number conservation. Therefore, the DCA distribution of antideuterons is assumed to reflect the behavior of primary particles that is one hundred percent pure and is used as a template of primary deuterons. Deuterons originating from the detector material are derived from the MC. Such contamination from particles knocked out from the detector material is particularly pertinent for samples of low momentum deuterons and protons, as such dislodged particles typically possess very low momentum. Because the influence of secondary contamination varies with the momentum of particles, template fits are also conducted across different momentum intervals to better characterize the sample quality. An example of such fits for protons and deuterons is presented in Fig. 4.3. The

final distributions of primaries to all particles of a certain type within appropriate DCA cuts are depicted in Fig. 4.8.

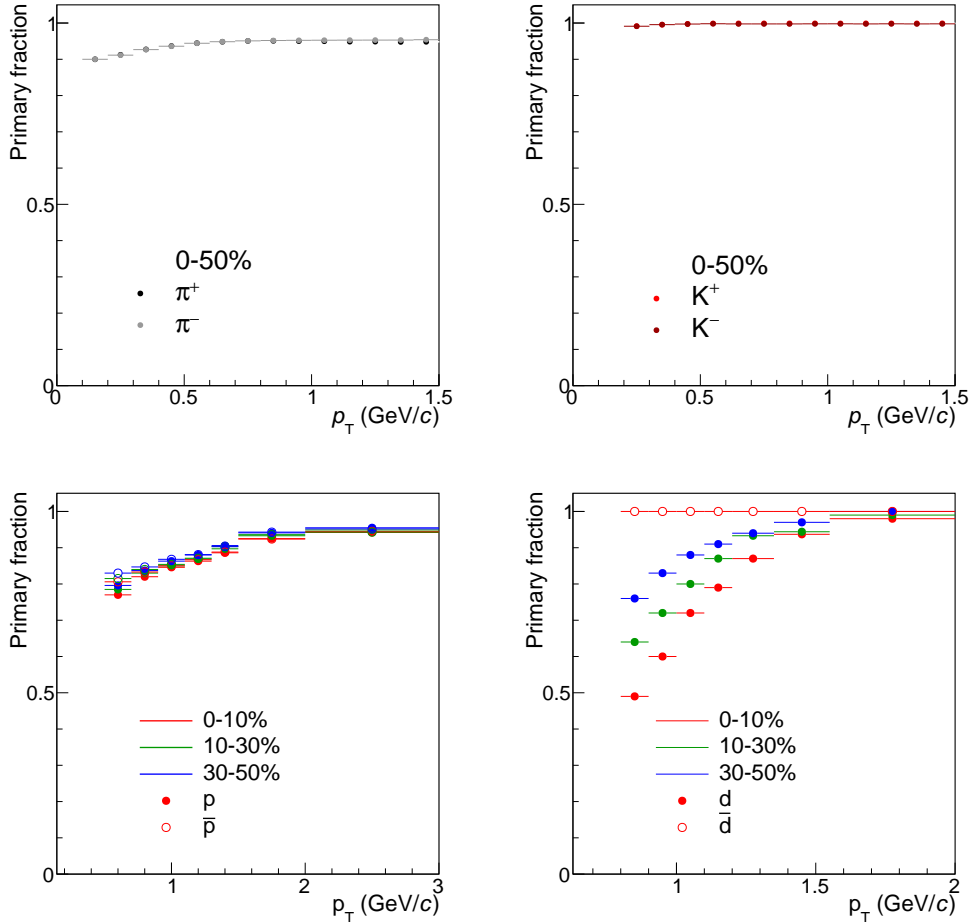


FIGURE 4.8: Distributions of primary fraction as a function of transverse momentum for pions (top left), kaons (top right), (anti)protons (bottom left) and (anti)deuterons (bottom right).

4.3.3 Gaussianity fraction

The source function of the theoretical correlation functions considered in this thesis is based on the Gaussian source assumption. However, the true source can have an additional tail caused mostly by presence of long-lived resonances and the conversion of three-dimensional source into one-dimensional description [153]. This effect has a different nature than defects of particle's sample such as missidentification or their non-primary nature, because it is related to the definition of the particle-emitter

itself. However, the Gaussianity of the source gives an analogous correction as the PID purity and primary fraction and that is why it is presented as a third effect that imperfection can cause the inconsistency between theoretical and experimental correlation functions. The effect of the non-Gaussian tail of the source is considered as an additional correction factor (*Gaussianity*) as suggested in [72]. The Gaussianity correction is the fraction of particles belonging to the main Gaussian core divided by all particles that build the source. For the kaon–proton study, the Gaussianity factor is taken directly from [72], where this value was found to be 0.95 on average. However, such a non-Gaussianity effect has never been checked for pairs containing deuterons, and in order to find an appropriate correction, a special study has been carried out in this thesis. For this purpose, the Pb–Pb collisions at $\sqrt{s_{NN}} = 5.02$ TeV were simulated using the hydrodynamic model LHYQUID [154] coupled to the statistical generator THERMINATOR2 [155]. The LHYQUID+THERMINATOR2 have already been successfully used to describe the relativistic heavy-ion collisions [154, 87, 88] and in the aforementioned non-Gaussianity study of kaon–proton pairs [72]. The hydrodynamic part of the simulation with initial conditions given by the optical Glauber is performed by the hypersurface provided by prof. Piotr Bożek from AGH (Kraków, Poland) as described in [154]. The THERMINATOR-2 is used to generate particles at the freeze-out temperature and hypersurface according to statistical rules, including unstable states, e.g. resonances, which propagate and decay according to their known properties listed in the PDG [6]. The collisions of each of the centralities considered in this thesis were generated on the WUT computing resources. Then, following the procedure described in [72], the distributions of k^* vs R_{inv} for pion–deuteron, kaon–deuteron and proton–deuteron pairs were calculated and restricted to low k^* contributing to the femtoscopic effect. Such ranges were further projected to obtain the R_{inv} fitted by the Eq. 2.7.

The final calculations derived in these simulation studies are shown in Fig. 4.9 together with the Gaussianity fractions. It was found that the values of the Gaussianity fraction depend on the centrality and the type of pair. The highest Gaussianity fraction of the three analysed pairs is present in the proton–deuteron case, which shows almost no additional tail, as we do not expect any significant effect of long-lived resonances in this case. The long-lived resonances are expected to contribute more to samples with kaons and pions, where we expect such states as e.g. ω , K^{0*} and K^{0*} , respectively. Therefore, the studies with pions and kaons contain visible tails in the source. However, the values of the Gaussianity fraction are still rather high for

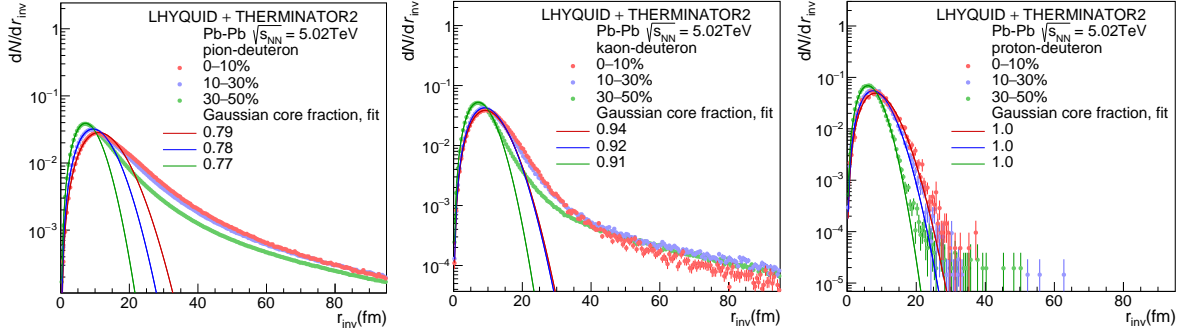


FIGURE 4.9: A source probability distribution for pion-deuteron (left), kaon-deuteron (center) and proton-deuteron (right) in Pb-Pb collisions at $\sqrt{s_{NN}} = 5.02$ TeV simulated using hydrodynamic model LHYQUID and THERMINATOR2 generator. The colors correspond to centralities: 0 – 10% (red), 10 – 30% (blue), 40 – 50% (green). Lines are Gaussian core fits to simulation points (see text for more details).

kaon-deuteron pairs, averaging 0.92. The largest tail is observed for pion-deuteron pairs, where the highest contribution of long-lived strongly decaying resonances is expected, giving the Gaussianity fraction of about 0.78.

Correction factor

The three effects mentioned above that are PID purity, primary fraction and Gaussianity fraction are composed in this thesis into one pair correction value ($corr$) in the following way:

$$corr = PID\ purity_a \cdot PID\ purity_b \cdot primary\ fraction_a \cdot primary\ fraction_b \cdot gaussianity_{ab}, \quad (4.3)$$

where a and b correspond to first and second particle of the pairs. The correction is further applied to a direct modification of the experimental correlation function as expressed in the formula 4.4.

$$C_{exp}^{corrected}(k^*) = \frac{C_{exp}^{not\ corrected}(k^*) - 1}{corr(k^*)} + 1, \quad (4.4)$$

In the kaon-proton study the kaon and proton purity were momentum-independent and therefore the same correction factor has been estimated for all k^* values, that in average equal 0.87 for all centrality intervals and charge combinations of the pair. However, such a simplification for pairs containing deuterons is not properly capturing their reconstruction as their PID purity and primary fraction are very

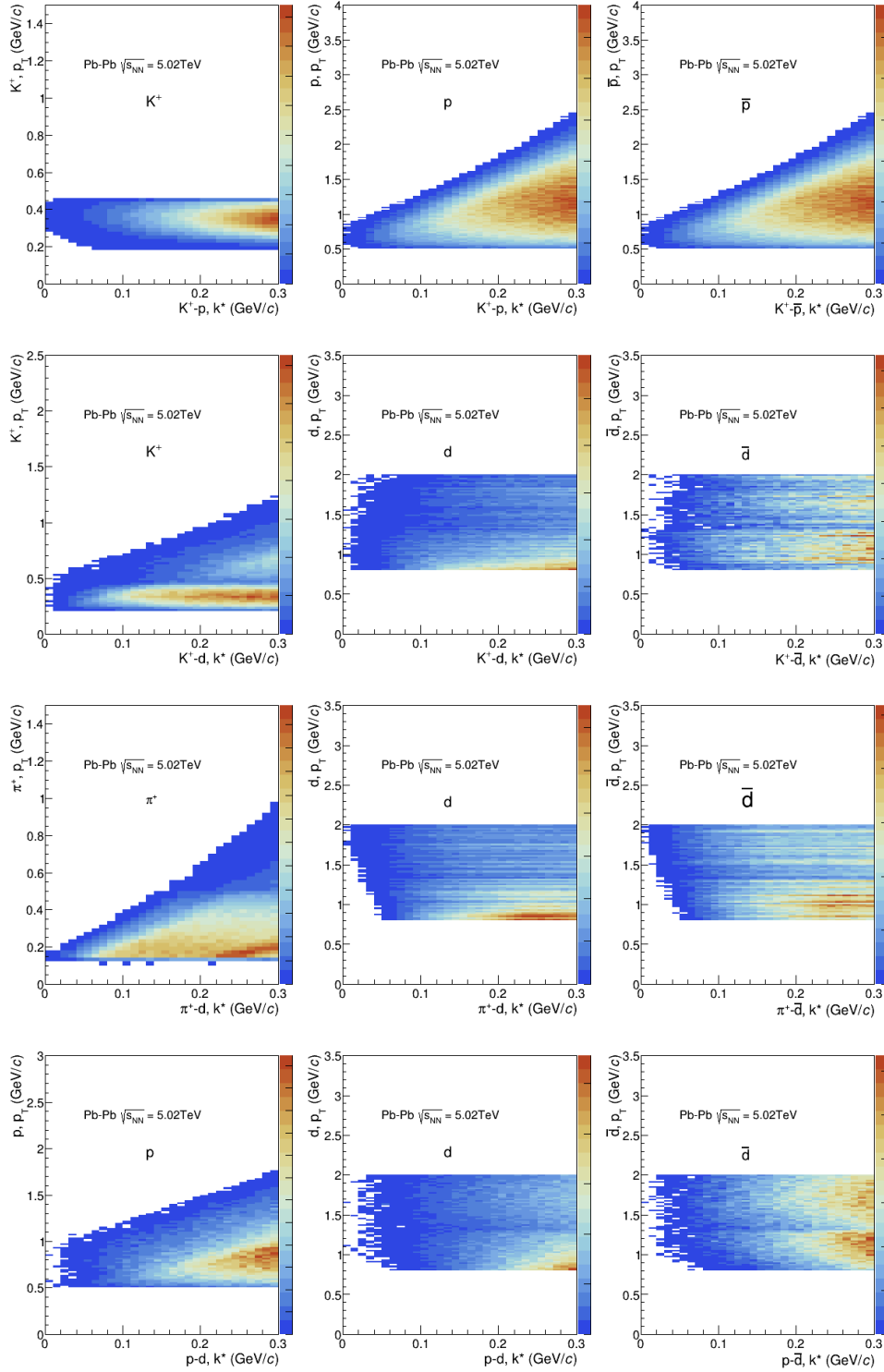


FIGURE 4.10: Examples of the distributions of p_T vs k^* of particles from kaon-proton (first row), pion-deuteron (second row), proton-deuteron (third row), kaon-deuteron (fourth row) obtained in this thesis.

momentum-dependent. It is presented in the Fig. 4.10 that particles of different momentum can contribute differently to different k^* regions. Therefore, a weighted average over all particles that contribute to the correlation function would be biasing the results for such pairs. In order to better reflect the nature of particles that contribute to certain k^* the correction factor 4.3 is calculated separately for each k^* .

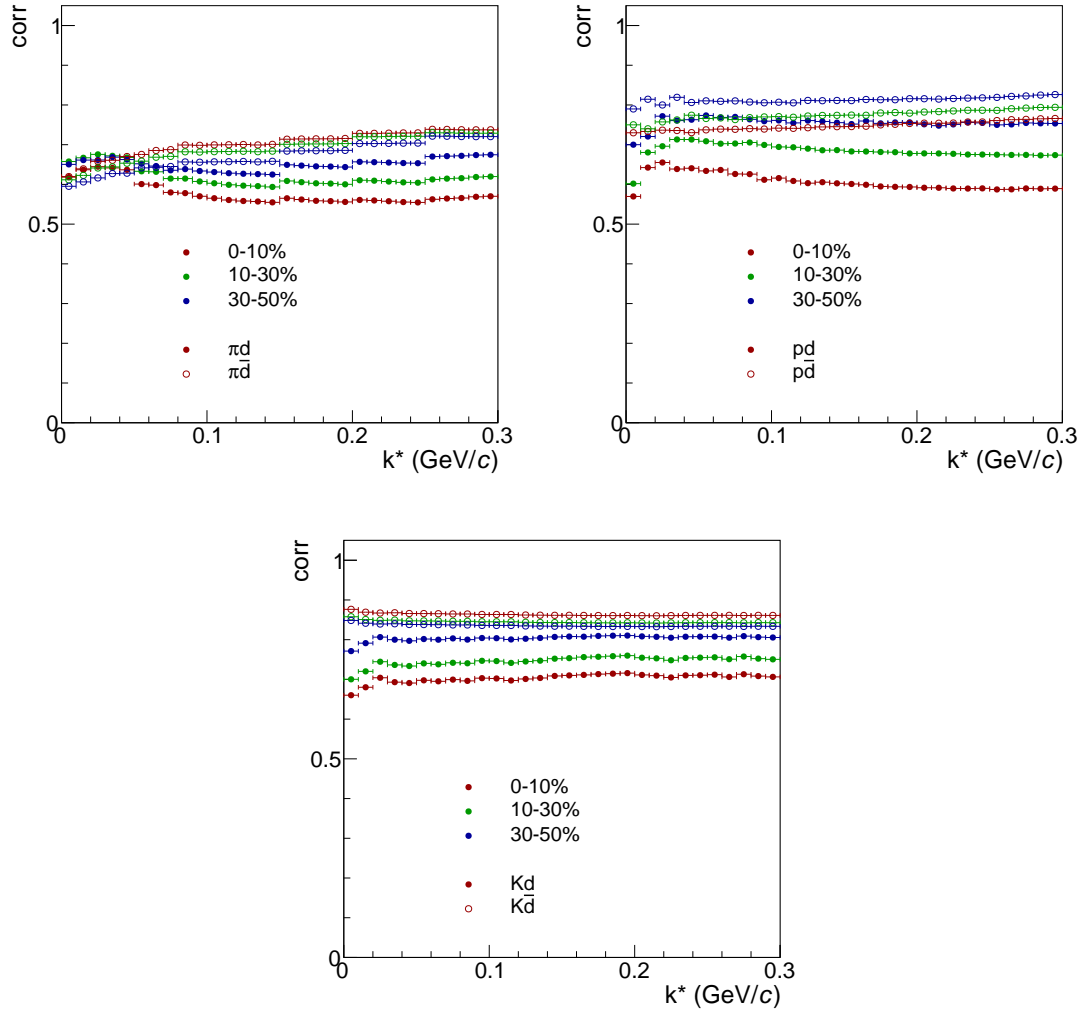


FIGURE 4.11: The correction factor as a function of k^* used in the pion–deuteron (upper left), proton–deuteron (upper right) and kaon–deuteron (bottom) studies.

Because the distributions of PID purities and primary fractions are originally calculated as a function of p_T they are transformed into k^* space. To do so, for each bin of k^* , the weighted average of these distributions is calculated with weights being the

yield of particles at a given p_T of that k^* bin. The final correction factor are summarised in Fig. 4.11.

4.3.4 Momentum resolution

Fourthly, the correlation function depends on momentum of particles that in experiment is measured with limited resolution. In other words, the measured momentum can differ from this real one. Therefore, the experimental or theoretical functions have to be corrected for this effect by the so-called smearing procedure. In this thesis the theoretical functions are smeared to account for the resolution effects. For this purpose, the resolution matrix of reconstructed (experimental) k^* vs true (theoretical) k^* is calculated for all considered particle pairs as shown in Fig. 4.12.

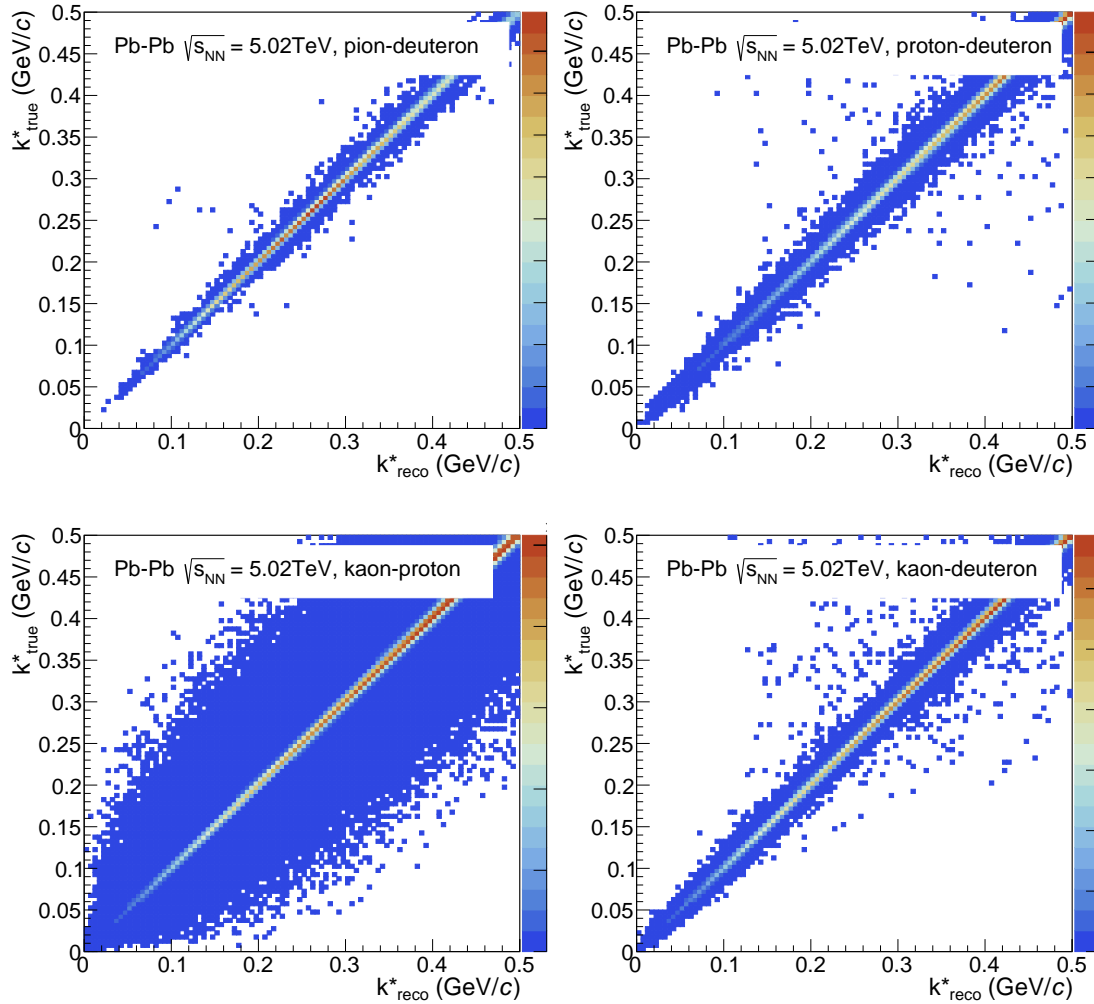


FIGURE 4.12: The momentum resolution matrix for pion–deuteron (top-left), proton–deuteron (top-right), kaon–proton (bottom-left) and kaon–deuteron (bottom-right) pairs based on HIJING simulations for Pb–Pb collisions at $\sqrt{s_{NN}} = 5.02$ TeV data of the ALICE experiment.

In principle, such a matrix can be used directly for smearing by applying the following procedure:

$$C_{th}(k_{reco}^*) = \frac{\sum_{k_{true}^*} \mathbf{M}_{k_{reco}^*, k_{true}^*} C_{th}(k_{true}^*)}{\sum_{k_{true}^*} \mathbf{M}_{k_{reco}^*, k_{true}^*}}, \quad (4.5)$$

where $\mathbf{M}_{k_{reco}^*, k_{true}^*}$ corresponds to matrix value at given reconstructed and true k^* , C_{th} is the theoretical function.

The smearing directly on resolution matrix is one of the method that can be used for accounting the resolution effects. As a variation method a description of this matrix with functional form is used, which is especially useful for particles that are not very statistically abundant. The function is the multiplication of Gaussian and weight functions as it is expressed in formula 4.6. The procedure of smearing is analogous as direct matrix smearing however here the $\mathbf{M}_{k_{reco}^*, k_{true}^*}$ component of formula 4.5 is replaced with eq. 4.6

$$F_{k_{true}^*, k_{reco}^*} = W(k_{reco}^*) \cdot \exp\left(-\frac{k_{true}^* - k_{reco}^*}{2\sigma^2}\right), \quad (4.6)$$

where, W function corresponds to the denominator distribution of correlation function obtained from data, σ is a constant value obtained from Gaussian fit to the $k_{reco}^* - k_{true}^*$ distribution for $k^* < 0.15$ GeV/ c . An example of such a fit is presented in the Fig. 4.13.

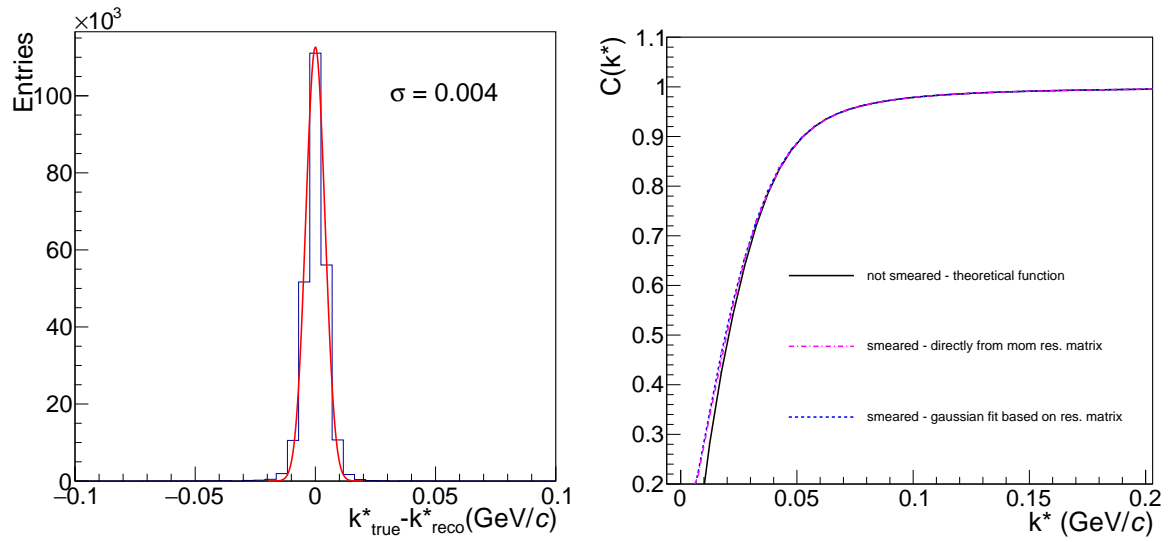


FIGURE 4.13: Left: a Gaussian fit to $k^*_{reco} - k^*_{true}$ distribution of proton-deuteron resolution matrix for $k^* < 0.15$ GeV/c. Right: a comparison of different smearing methods shown with colored dashed lines with the original correlation function shown as a black solid line.

4.3.5 Non-femtoscopic effects

The correlation function, defined as the ratio of pairs from the same and different events, contains all possible correlation effects and not only those which occur due to FSI, or quantum statistics. These include information about the source and mutual interactions, but also the effects of collective motion of particles, total momentum conservation, resonances and jets. However, theoretical predictions usually do not include these additional non-femtoscopic effects, so the experimental or theoretical correlation function should be corrected for them.

The first method of the background modeling is based on hydrodynamical model simulations and for this purpose, a dedicated multi-phase transport model AMPT [102] and LHYQUID+THERMINATRO2 data were considered. Both models describe the hydrodynamic expansion of relativistic heavy-ion collisions and, by default, do not include any femtoscopic effects. Therefore, the correlation function derived from data of such models should reflect the non-femtoscopic background distribution. The AMPT simulations are taken from ALICE resources and are derived particularly for Pb–Pb collisions at $\sqrt{s_{NN}} = 5.02$ TeV anchored to data used for this study. The LHYQUID+THERMINATRO2 events were calculated locally. The non-femtoscopic effects have been obtained in the kaon–proton study providing reasonable output for both AMPT and LHYQUID+THERMINATRO2 models (see example in Fig. 4.15). However, due to limited available statistics of the AMPT data were insufficient for obtaining the non femtoscopic effects in peripheral Pb–Pb collisions. LHYQUID+THERMINATRO2 in turn does not perfectly reflect the elliptic flow effect in the first centrality intervals due to centrality selection bias based on a fixed impact parameter. Therefore, in the kaon–proton study the default selection of the background is AMPT for central collisions up to 10% and LHYQUID+THERMINATRO2 above that centrality. Deuterons' studies do not apply this technique of elliptic flow background determination because deuterons are usually not included in the generated simulations, or if they do appear, the statistics is insufficient to provide statistically significant correlation functions.

The second method used in this thesis is the data-driven approach where the background in the femtoscopic region is obtained based on the extrapolation of the polynomial fit to the non-femtoscopic region where the correlation functions show a functional dependence which cannot be described with FSI in a wide k^* range. As it can be seen in Figs. 4.15–4.18 the method provides solutions comparable to other

methods. However, the background prediction depends on the fit range and the order of the polynomial. To obtain a stable fit that reflects the similar behaviour in all centralities require high statistical significance with small bin-to-bin fluctuations of the correlation function. The reason for this, is that different non-femtoscopic effects can modify the correlation functions in specific k^* regions, i.e. momentum conservation can be very visible in the high k^* region and elliptic flow will be more prominent in the low k^* range and therefore, extrapolation based only on the high k^* would not be justified. Such a data-driven method is used for systematic variations in kaon–proton study and as a default and systematic solutions in deuteron studies.

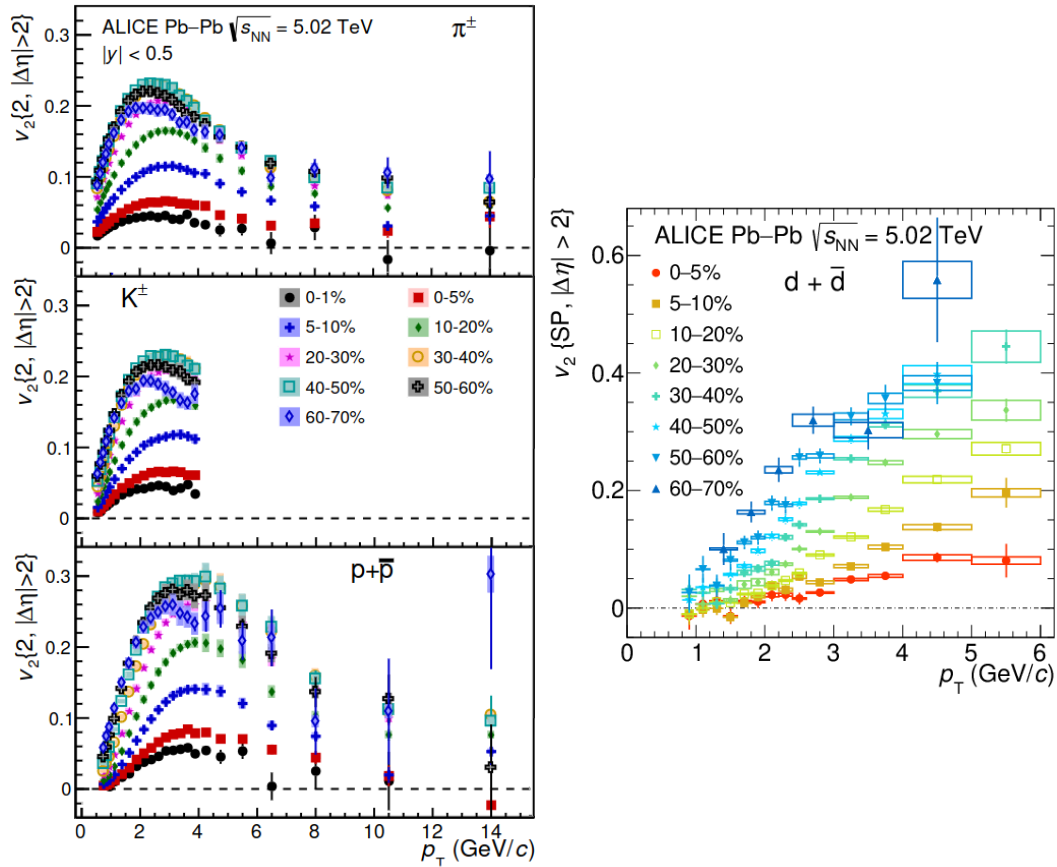


FIGURE 4.14: Elliptic flow of pions and (anti)deuterons as a function of p_T for different centrality intervals measured in Pb–Pb collisions at $\sqrt{s_{NN}} = 5.02$ TeV. Left: pions, kaons, protons [156], right: (anti)deuterons [109]

The third background method has been applied in all deuteron studies and is based on numerical sampling of single particles of their measured momentum-dependent

azimuthal distributions before combining them into pairs. The generation works as follows: the p_T distribution of particles measured in the study is randomly sampled and for the selected p_T , a new ϕ distribution that describes the generation angle of the particle is created. The ϕ distribution can be described by the formula 4.7. The same procedure is used for the two particles of the pair. For pairs of particles combined in this way, four-momentum vectors are created, and these pairs are used for filling the numerator histogram. The denominator distribution is created by sampling an angle of generation from a uniform distribution (the effect of the flow is not included in the denominator). The calculations have been performed using computers at WUT using resources developed by Jakub Zieliński and Georgy Kornakov. An example of the simulated effect of the elliptic flow is presented in Figs. 4.15–4.18.

$$N(\phi) = 1 + 2 \sum_{n=2} v_n(p_T) \cos(n\phi), \quad (4.7)$$

where, v is the flow coefficient (v_2) distribution for considered particle [156, 109]. The v_2 distribution for pions, (anti)deuterons are presented in Fig. 4.14.

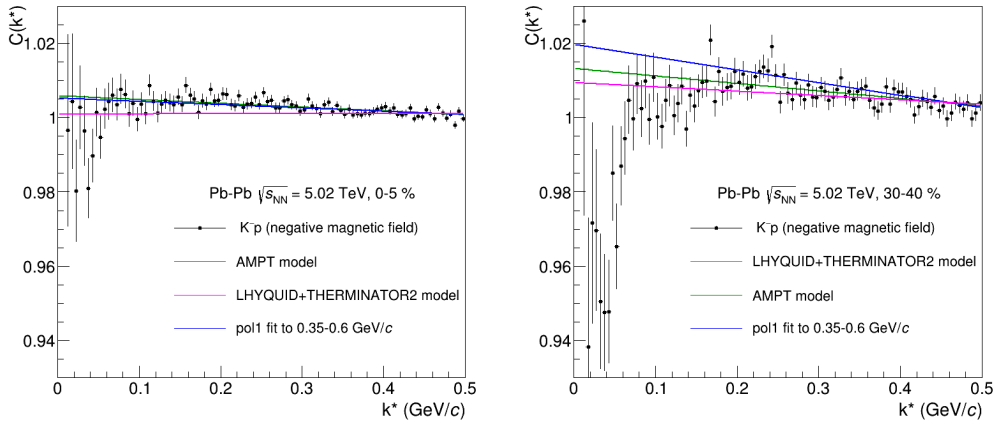


FIGURE 4.15: The raw correlation functions of K^-p pairs for Pb–Pb collisions at $\sqrt{s_{NN}} = 5.02$ TeV data of the ALICE experiment for 0 – 5% (left) and 30 – 40% (right) represented by points. Lines correspond to the background predictions of polynomial fit of first and second order to experimental points in the ranges given in the legend as well as a simulation of the elliptic flow effect.

As can be seen in Figs. 4.15–4.18, all the methods give similar solutions, which demonstrate the consistency of the different approaches. The experimental correlation functions are divided by the corresponding background before comparison with

the theoretical functions. The summary of the background functions used for these studies can be found in Tab. 4.4. Nevertheless, the background contribution to the correlation function is a small effect, especially in such pairs as kaon–deuteron and proton–deuteron.

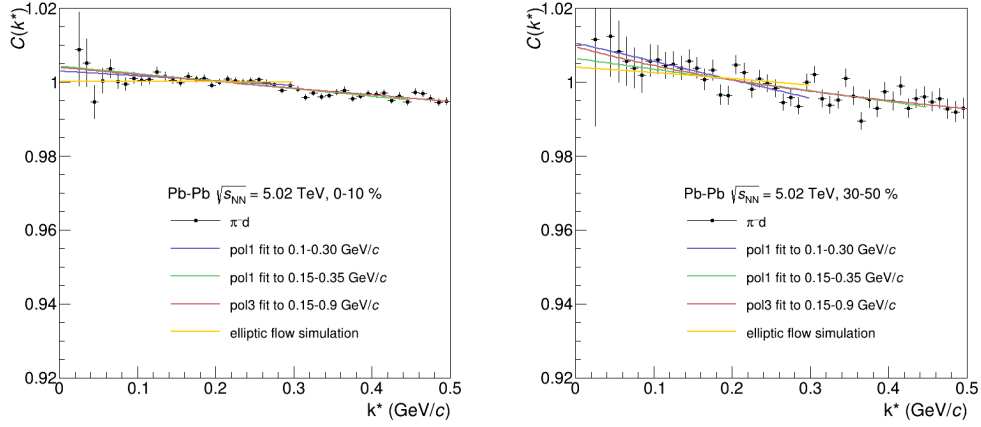


FIGURE 4.16: The raw correlation functions of $\pi^- d$ pairs for Pb–Pb collisions at $\sqrt{s_{NN}} = 5.02$ TeV data of the ALICE experiment for 0 – 10% (left) and 30 – 50% (right) represented by points. Lines correspond to the background predictions of polynomial fit of first and second order to experimental points in the ranges given in the legend as well as a simulation of the elliptic flow effect.

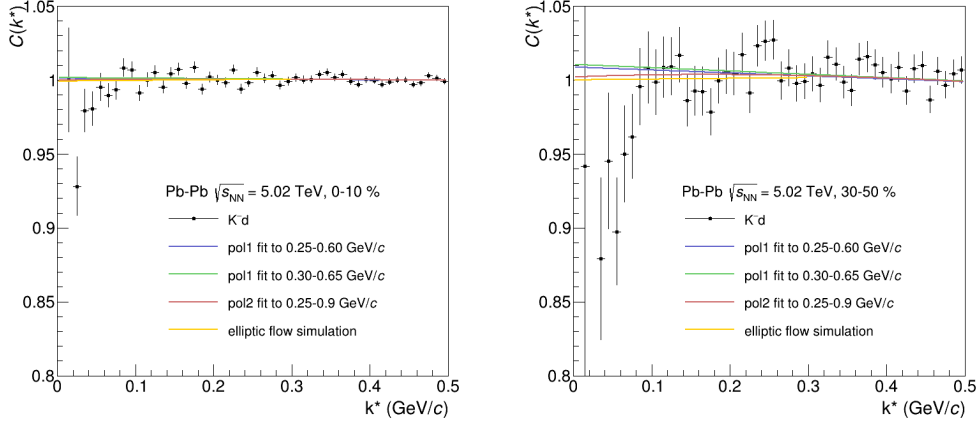


FIGURE 4.17: The raw correlation functions of K^-d pairs for Pb-Pb collisions at $\sqrt{s_{NN}} = 5.02$ TeV data of the ALICE experiment for 0 – 10% (left) and 30 – 50% (right) represented by points. Lines correspond to the background predictions of polynomial fit of first and second order to experimental points in the ranges given in the legend as well as a simulation of the elliptic flow effect.

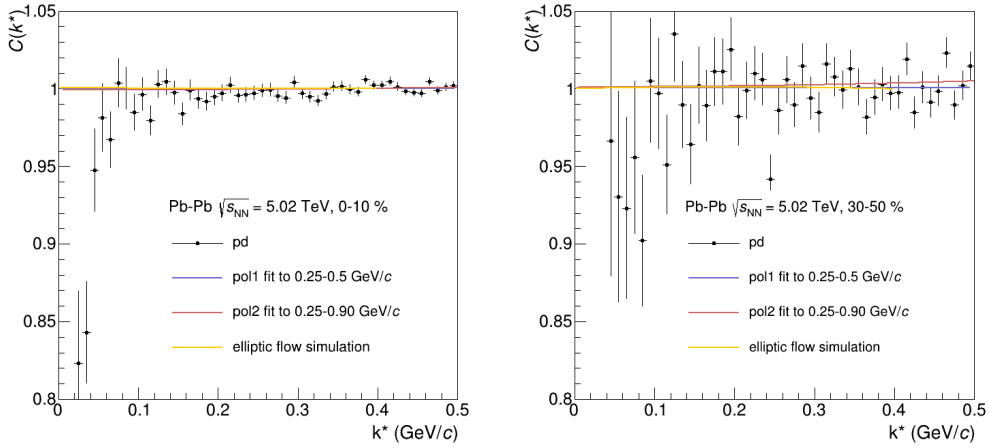


FIGURE 4.18: The raw correlation functions of $p-d$ pairs for Pb-Pb collisions at $\sqrt{s_{NN}} = 5.02$ TeV data of the ALICE experiment for 0 – 10% (left) and 30 – 50% (right) represented by points. Lines correspond to the background predictions of polynomial fit of first and second order to experimental points in the ranges given in the legend as well as a simulation of the elliptic flow effect.

TABLE 4.4: Background of non-femtoscopic effects used for kaon–proton and pion–/kaon–/proton–deuteron studies.

kaon–proton	
AMPT	default (centralities < 10%)
LHYQUID+THERMINATOR2	default (centralities > 10%)
1 st order polynomial fit to 0.35-0.6 GeV/ <i>c</i>	systematic variation
Average of polynomial fit with AMPT/LHYQUID+THERMINATOR2	systematic variation
pion–deuteron	
1 st order polynomial fit to 0.15-0.35 GeV/ <i>c</i>	default
1 st order polynomial fit to 0.1-0.3 GeV/ <i>c</i>	systematic variation
3 rd order polynomial fit to 0.15-0.9 GeV/ <i>c</i>	systematic variation
elliptic flow simulations	systematic variation
kaon–deuteron	
1 st order polynomial fit to 0.25-0.6 GeV/ <i>c</i>	default
1 st order polynomial fit to 0.3-0.65 GeV/ <i>c</i>	systematic variation
2 nd order polynomial fit to 0.25-0.9 GeV/ <i>c</i>	systematic variation
elliptic flow simulations	systematic variation
proton–deuteron	
1 st order polynomial fit to 0.25-0.5 GeV/ <i>c</i>	systematic variation
2 nd order polynomial fit to 0.25-0.90 GeV/ <i>c</i>	systematic variation
elliptic flow simulations	default

4.4 Numerical fitting

The experimental functions considered in this thesis pertain to charged hadrons, and thus, their theoretical description is primarily based on Coulomb plus strong interactions. However, the analytical description using the Lednický-Lyuboshits formalism can only be applied to cases with a Gaussian source and strong interaction. To obtain the desired description of the correlation function, a numerical fitting procedure is used.

The numerical procedure provides an additional degree of flexibility as it allows to modify the source function or the interaction between the two particles whereas the analytical solution is restricted to the Gaussian source function with specific FSI cases. In the numerical approach, the wave function integration procedure is repeated numerous times for different parameters of the interaction and source. Consequently, obtaining a continuous description for all possible values of certain parameters, such as source size, is impossible. Therefore, the numerical solution relies on pre-calculated correlation functions, which form a grid of solutions with different parameter values at specific intervals (steps).

Experimental measurements are then compared with this matrix of solutions, which can be one-, two-, or even three-dimensional, depending on number of unknown parameters. Since there are no continuous spectra of such solutions, the step size is crucial in determining exact solutions as each of them is then a numerical interpolation between two pre-calculated functions. In the simplest case, one can consider the one-dimensional scenario where the interaction part is well-known, but the source size is unknown. Here, the function will be pre-computed for different size parameters which will further help in the scan of the solutions among the parameter values' constrained by given limits. Such solutions are compared to the experimental functions. Finally, we obtain a function that represent the minimum χ^2 being the interpolation between the two closest solutions, effectively underestimating and overestimating the data. In higher-dimensional cases, such as when one or two scattering parameters are unknown, we search for the best solutions analogously, but the interpolation is done based on four sub-functions for the case with 2 unknown parameters or eight sub-functions for the case with 3 unknown parameters. The schematic representation of the procedure is presented in Fig. 4.19.

Furthermore, to constrain the parameters, the algorithm that searches for the minimum solution checks multiple functions simultaneously. For example, particle

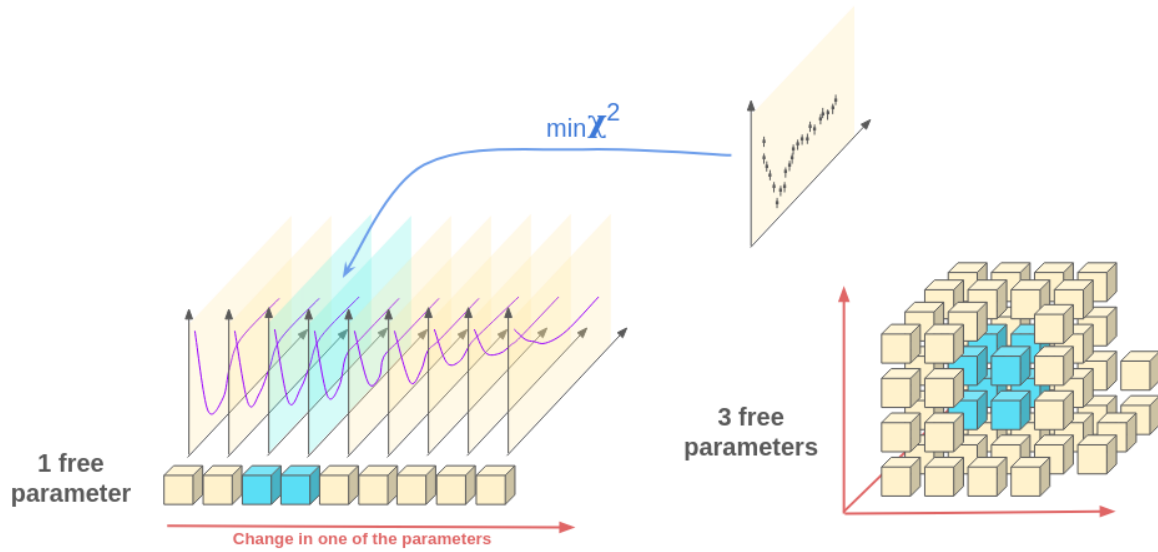


FIGURE 4.19: Schematic representation of the fitting procedure for one-dimensional (left) and three-dimensional (right) cases. The boxes represent theoretical correlation functions generated for different values of the correlation parameters. The blue boxes represent the functions used in the numerical integration of the final solution which provides minimum χ^2 in comparison to experimental data.

pairs with the same and opposite charges have different interactions and theoretical prescriptions of the function, but they can share the same source size. Similarly, the interaction between certain particle-pairs does not change during relativistic heavy-ion collisions across different centrality intervals. Therefore, for them, while the sources will differ, the interaction parameters can be shared. Ultimately, the fit must provide the best parameters from the perspective of the source size checked among functions within the same centrality interval, and the scattering parameters (if are unknown) checked among both a given charge combination of the pair simultaneously. The schematic representation of the simultaneous fit is presented in Fig. 4.20. The form of the numerical fitting for particle pairs considered in this thesis has been developed specifically for the purposes of this research.

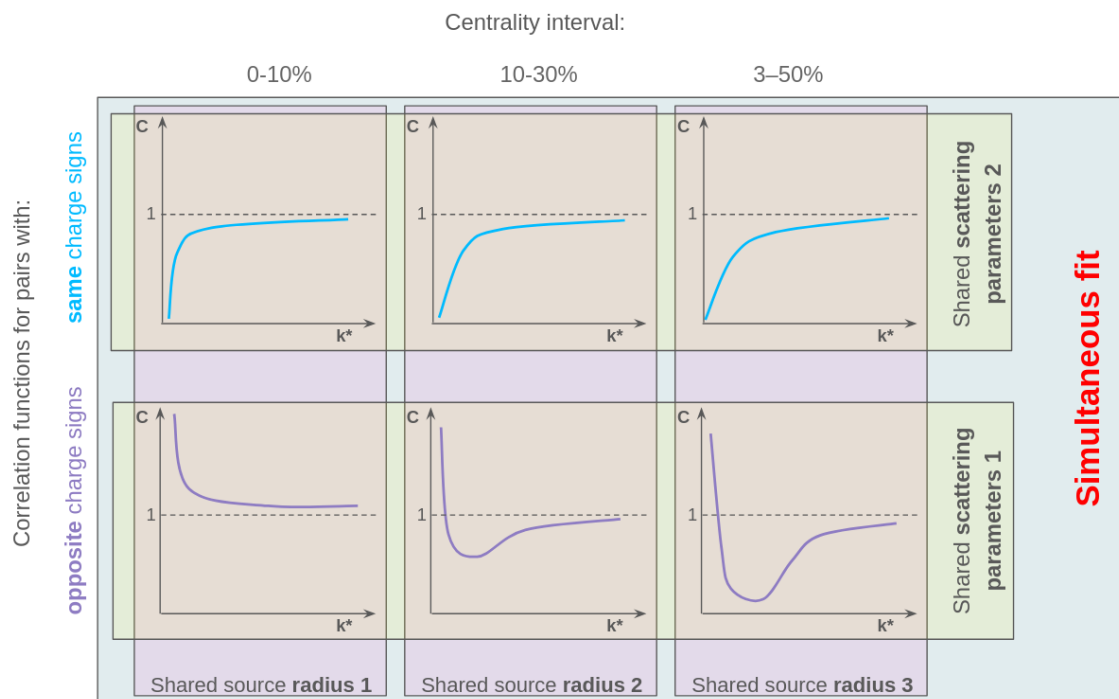


FIGURE 4.20: Illustration of the shared parameters among correlation functions in the simultaneous fit to all of them.

Chapter 5

Results

*Tylko odbijając się w oczach, które na nie patrzą,
kształty materii nabierają piękna i znaczenia.*⁴

Stanisław Lem, Astronauci

Ale CO zobaczę?

*Nie wiem. W pewnym sensie to zależy od ciebie.*⁵

Stanisław Lem, Solaris

⁴"Only by being reflected in the eyes that look at them, the shapes of matter gain beauty and meaning." – Stanisław Lem, The Astronauts

⁵"But what am I going to see? I don't know. In a certain sense, it depends on you." – Stanisław Lem, Solaris

5.1 Pion–deuteron

Disclaimer

I hereby declare that the pion–deuteron study presented below is the work that I performed within the ALICE collaboration. In this study I did the following:

- ☐ *quality assurance of the selection of charged pions and (anti)deuterons,*
- ☐ *selection of the final analysis settings,*
- ☐ *calculation of the correlation functions,*
- ☐ *calculation and application of all the corrections on particle identification, primary fraction, non-Gaussianity of the source, momentum resolution and non-femtoscopic effects,*
- ☐ *calculation of set of the theoretical functions describing the pion–deuteron interaction using Lednický-Lyuboshits model (based on the code originally developed by Adam Kisiel) which were later applied for fitting,*
- ☐ *preparation of the code for fitting the pion–deuteron system,*
- ☐ *performance of the fitting,*
- ☐ *performance of the femtoscopic simulation study of pion-pion pairs used later as an assumption of the pion’s source size and being the chair in the published article on the method [157],*
- ☐ *calculation of the statistical and systematic uncertainties for data points, fit and measured parameters,*
- ☐ *preparation of all the check and final figures,*
- ☐ *presentation of the analysis at different stages of advancement within the collaboration,*
- ☐ *presentation and defence of the results for acceptance during preliminary approvals and for the paper proposal approvals within collaboration,*
- ☐ *writing the analysis note of the study for the collaboration,*
- ☐ *being the chair of the paper committee of the upcoming paper.*

Nevertheless, despite the fact that the analysis part of work has been performed by me, this work has been advised and checked by my supervisors and collaboration members in many internal meetings as well as by selected and experienced collaboration members that went through the details of the performed steps and results. Also, the study is based on data collected and prepared by other members of the collaboration and therefore the analysis would not be possible without other people responsible for technical aspects of the experiment, e.g. those responsible for detector construction, maintenance, operation and calibration as well as those managing the computing resources and the cloud infrastructure.

5.1.1 Introduction and model description

The pion–deuteron study is mainly motivated by the fact that this system concerns the basic interactions with both nucleons at once which together with pion–nucleon studies can be used further as a baseline for other systems and their general dynamic. However, this particle combination has never been studied using the femtoscopic technique. It is therefore an opportunity to reveal our understanding of the pion–deuteron interaction. The pion–deuteron study is also a feasibility analysis to access the femtoscopic source and interaction of rare particles, which are difficult to study due to their low statistical production. Most measurements of the source properties of particles are based on the measurement of identical particle pairs, where there is a direct access to the single particle source. However, the statistics collected so far for many particle species is not sufficient to build a solid correlation function, e.g. to perform a reliable deuteron–deuteron femtoscopy in Pb–Pb collisions. Fortunately, access to the single-particle femtoscopic source may also be possible through non-identical studies. Because most of the particles produced in heavy-ion collisions are pions, they seem to be a high-statistics probe to construct non-identical correlation functions. Therefore, by accessing especially low-momentum pions, one can form low k^* pairs with high-momentum particles like deuterons. This is important because, as mentioned before, femtoscopic access to deuterons can shed more light on their behaviour compared to other particles that share some common patterns, e.g. m_T scaling. It is worth mentioning that so far we know almost nothing about the source characteristics of composite particles in heavy-ion collisions.

To determine the pion–deuteron correlation function, the description of their interaction is needed. The first measurements of the interaction came from experiments with pionic deuteron atoms in 1974 [158] 1983 [159] 1985 [160]. In this case, an electron from a hydrogen atom is replaced by a negatively charged pion. The scattering length is obtained by applying the Trueman–Deser formula [95, 96] to measured shift and width of the energy levels with respect to a pure QED calculation. Later, in 1997 [161] (updated in 1998 [162]), another study of pionic deuterium was carried out using more precise X-ray spectroscopy, improving the precision of the energy level shift by more than an order of magnitude compared to the two previous experiments. The new experiment also provided the first measurement of the width of the energy levels. The latest study establishes the $\pi^- d$ scattering length at $f_0 = -0.037 + i0.008$ fm. The value of the scattering length itself for the $\pi^- d$ system has

been described theoretically with good agreement in recent papers [163] [164]. This agreement between theoretical and experimental values leads to conclusion that the value of the scattering length is well known and the influence of the strong interaction on the correlation function is rather marginal. The π^+d is already repulsive due to the charge combination and therefore the effect of the strong force is expected to be even smaller than in the π^-d pairs. Furthermore, there are no known experimental or theoretical studies that would investigate the scattering length of the strong interaction of π^+d pairs. Therefore, in this work the assumption of Coulomb only interaction is made for pairs of the same charge. The theoretical correlation function is calculated using the Lednický-Lyuboshits formalism. The calculations have been performed with the assumption that the effective range parameter (d_0) of the strong interaction is fixed to 0. Such approximation is called the zero effective range approximation and is a common practice in heavy-ion collision as the sources are large and the functions are not sensitive to d_0 . The source contribution to the correlation function is determined using a Gaussian source with radius $R_{\pi d}$. An example of such theoretical

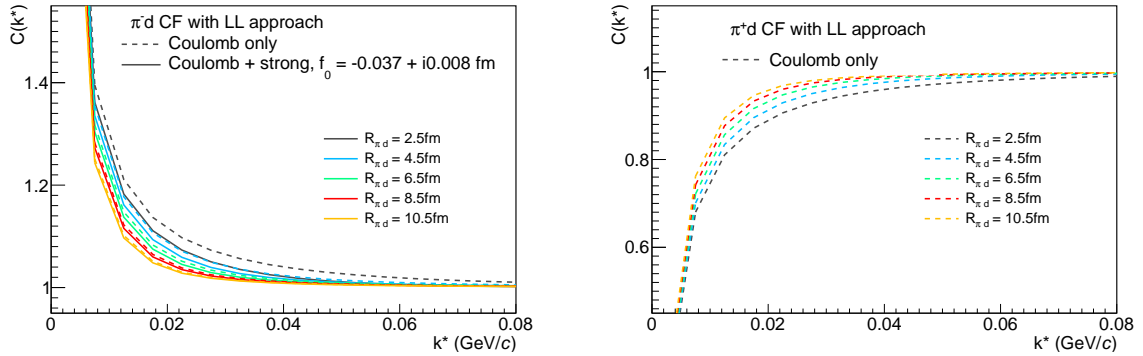


FIGURE 5.1: Theoretical correlation functions of pion–deuteron pairs for Coulomb only (dashed lines) and Coulomb plus strong interaction (solid lines) with different input parameters of the Gaussian source size $R_{\pi d}$. Left: pairs with opposite sign of charge, right: pairs with same sign of charge.

correlation functions is shown in Fig. 5.1. The pion–deuteron correlation functions tend quickly to unity (deviations are visible mostly below 0.08 GeV/c). There is also no large difference between the two radii, which differ by 2.0 fm (low sensitivity to source dependence). In Fig. 5.1 the difference between the Coulomb and Coulomb plus strong approaches for pairs of unlike charge signs is presented, showing that in large sources the sensitivity to strong interaction effect is limited.

5.1.2 Results

The correlation function of $\pi^-d \oplus \pi^+\bar{d}$ and $\pi^+d \oplus \pi^-\bar{d}$ pairs for three centrality intervals 0 – 10%, 10 – 30%, 30 – 50% obtained from Pb–Pb collisions $\sqrt{s_{\text{NN}}} = 5.02$ TeV data collected by ALICE in 2018 are shown in Fig. 5.2. The statistical uncertainties are represented by vertical lines, while the systematic uncertainties are represented by grey squared boxes. The evaluation of all the uncertainties is described in Sec. 6.

The $\pi^+d \oplus \pi^-\bar{d}$ correlation functions show a clear repulsive interaction (points below unity). The $\pi^-d \oplus \pi^+\bar{d}$ correlation functions, on the other hand, are fully attractive (functions above unity), with no sign of a possible bound state between the interacting particles. The deviation from unity becomes larger with more peripheral collisions due to the decrease in femtoscopic source sizes connected with the decrease of the overall fireball created after the collision.

In order to extract the value of $R_{\pi d}$ femtoscopic source sizes, two sets of calculated functions have been prepared for Coulomb only ($\pi^+d \oplus \pi^-\bar{d}$) and Coulomb plus strong ($\pi^-d \oplus \pi^+\bar{d}$) that consists of functions generated for $R_{\pi d}$ [0.5,12.5] fm with a step of 0.5 fm. Following the procedure described in Sec. 4.4 the fit is performed simultaneously on the six correlation functions (three centralities, same and opposite sign pairs) and assumed that the source has the same size for same- and opposite-charge pairs at a given centrality. The best solutions are selected from the set of pre-calculated functions based on the χ^2 minimisation in k^* up to 0.12 GeV/ c that is calculated between theoretical functions and derived data points. The final fit function is an effect of interpolation between two solutions the closest to data. The fit to the data using the Lednický-Lyuboshits formalism is shown in Fig. 5.2. The model provides a qualitative description of the experimental correlation functions in all three centrality intervals for particle pairs of the same and opposite charge sign. The only parameter derived directly from the fit is the femtoscopic source size of the pion–deuteron pairs, $R_{\pi d}$, one per centrality. The values of $R_{\pi d}$ are summarised in the Tab. 5.1 together with statistical and systematic uncertainties. The schematic representation of these values as a function of $\langle dN_{ch}/d\eta \rangle^{1/3}$ is presented in Fig. 5.3 showing a linear dependence.

To measure the deuteron source from the two-particle $R_{\pi d}$, the formula 2.6 has been inverted into:

$$R_d = \sqrt{R_{\pi d}^2 - R_{\pi}^2}, \quad (5.1)$$

where $R_{\pi d}$ is the measured two-particle pion–deuteron femtoscopic source size and

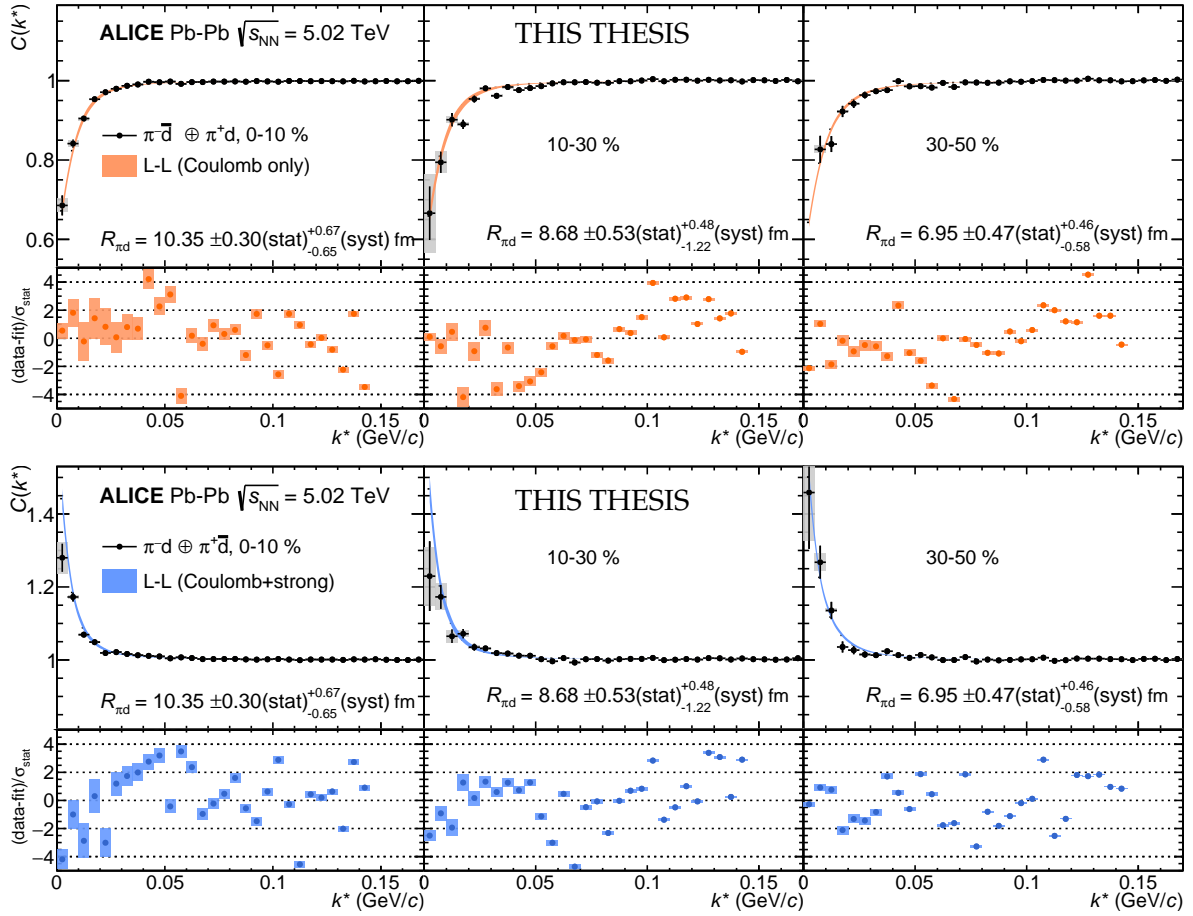


FIGURE 5.2: The $\pi^+ d \oplus \pi^- \bar{d}$ correlation functions (top row) $\pi^- d \oplus \pi^+ \bar{d}$ correlation functions (bottom row) in three centrality classes (from left to right 0 – 10%, 10 – 30%, 30 – 50%) represented by points. The bands correspond to the Lednický-Lyuboshits (denoted as L-L) fit of Coulomb only (orange) and Coulomb plus strong (blue). The band widths represent the systematic uncertainties of the fits. The lower panels show the differences between the data and the fits, normalised by the statistical uncertainty σ_{stat} .

TABLE 5.1: Two-particle pion–deuteron source sizes, $R_{\pi d}$, together with uncertainties for 3 centrality from the fit to all pair combinations for Pb–Pb collisions at $\sqrt{s_{\text{NN}}} = 5.02$ TeV.

Centrality	$R_{\pi d}$ (fm)	stat. unc. \pm (fm)	syst. unc. + (fm)	syst. unc. – (fm)
0-10%	10.35	0.30	0.67	0.65
10-30%	8.68	0.53	0.48	1.22
30-50%	6.95	0.47	0.46	0.58

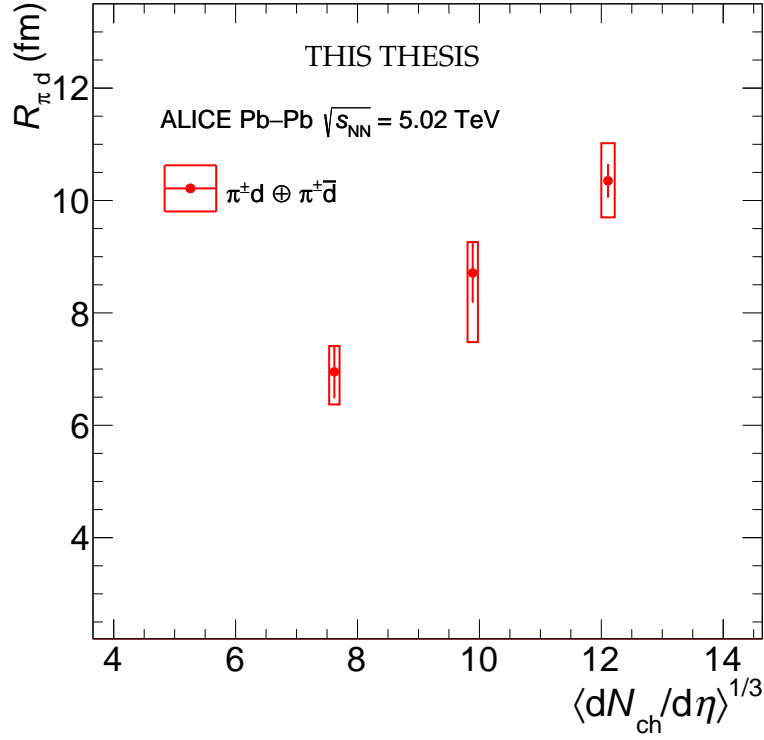


FIGURE 5.3: $R_{\pi d}$ radii as a function of $\langle dN_{ch}/d\eta \rangle^{1/3}$ obtained from a common fit to all pair combinations of pion–deuteron femtoscopic functions for Pb–Pb collisions at $\sqrt{s_{NN}} = 5.02$ TeV.

R_{π} is the single-particle pion femtoscopic source size that has to be provided to the calculations.

The R_{π} can be obtained from the known m_T scaling of mesons and baryons [77] measured in Pb–Pb collisions. This study provided the femtoscopic pion source sizes in the corresponding centrality intervals of this work for seven m_T bins. However, these measurements were made at an energy of $\sqrt{s_{NN}} = 2.76$ TeV, whereas in this work a collision energy of $\sqrt{s_{NN}} = 5.02$ TeV is considered. In order to use the dependencies shown in [77], the femtoscopic source sizes have to be scaled to the energy $\sqrt{s_{NN}} = 5.02$ TeV. The scaling can be done by using information on $\langle dN_{ch}/d\eta \rangle^{1/3}$ for both energies [165, 15], since it is known experimentally that the cube root dependence of the charge particle multiplicity density is linear. The scaling is based on the following formula:

$$R_{inv} = a \cdot \langle dN_{ch}/d\eta \rangle^{1/3} + b, \quad (5.2)$$

where a and b values are free parameters of the fit to experimental radii.

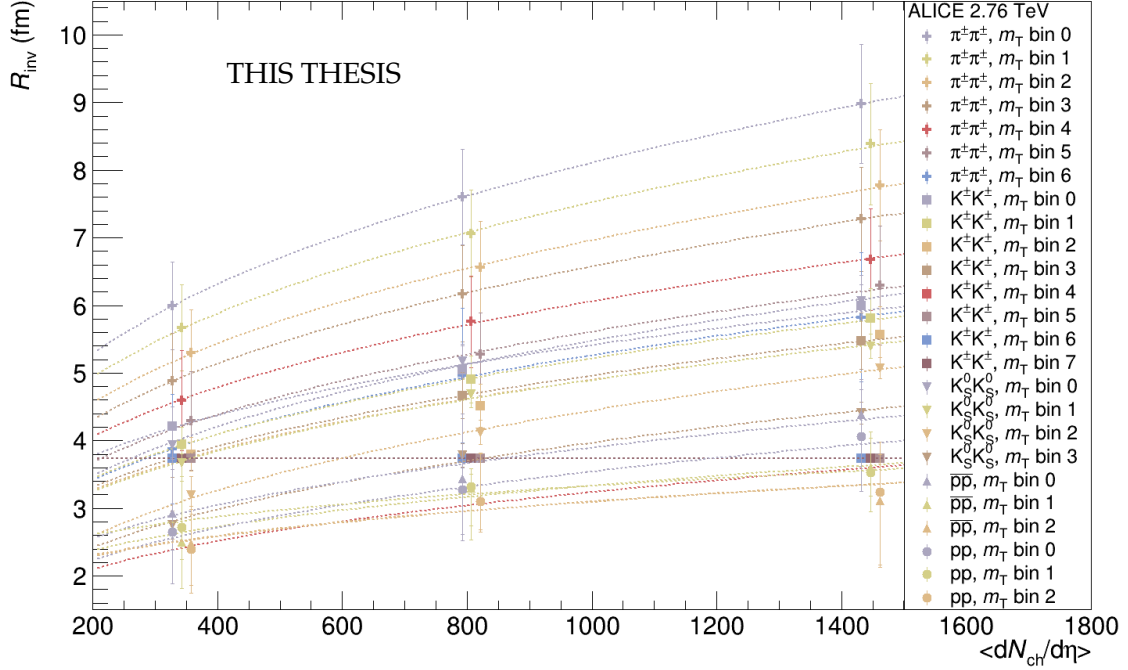


FIGURE 5.4: Fits to radii obtained at collision energy $\sqrt{s_{NN}} = 2.76$ TeV performed for each m_T bin. Figure credit: Łukasz Graczykowski.

The rescaled radii of identical pions, kaons, and protons to energy $\sqrt{s_{NN}} = 5.02$ TeV are shown in Fig. 5.5.

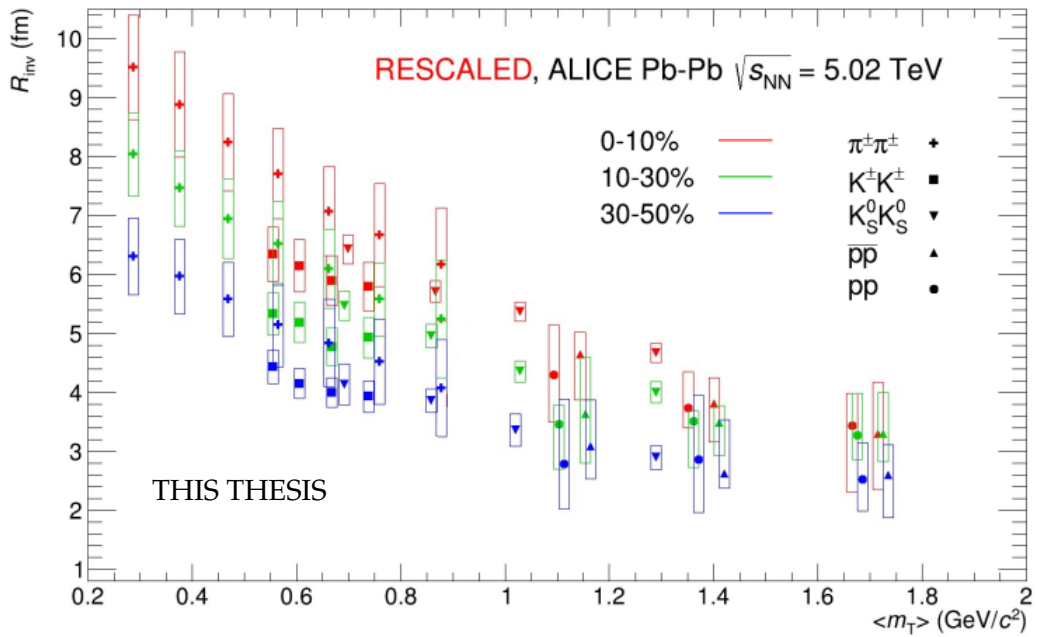


FIGURE 5.5: Femtoscopic radii of identical pions, kaons, and protons rescaled to $\sqrt{s_{NN}} = 5.02$ TeV from $\sqrt{s_{NN}} = 2.76$ TeV [77].

Given the m_T scaling of pions, the source size of pions that contribute to the low k^* of pion–deuteron pairs can be predicted. The m_T has been calculated using the formula:

$$m_T = \sqrt{\langle p_T \rangle^2 + m_0^2}, \quad (5.3)$$

where m_0 is a pion rest mass, $\langle p_T \rangle$ is derived from the p_T vs k^* distribution in the range $k^* < 0.08 \text{ GeV}/c$. The m_T value for pions of this study is $0.24 \text{ GeV}/c$. However, in the Fig. 5.6 it can be seen that this m_T lies below the first measured m_T bin and an extrapolation of the points to reach this region is necessary. Usually, the power law fit is used to fit the m_T scaling of the experimental data. Unfortunately, low m_T particles have not been well studied in the past, both experimentally and theoretically, and the low m_T of such points seems to be better described by the linear rather than the exponential trend. The two types of fits are shown in Fig. 5.6.

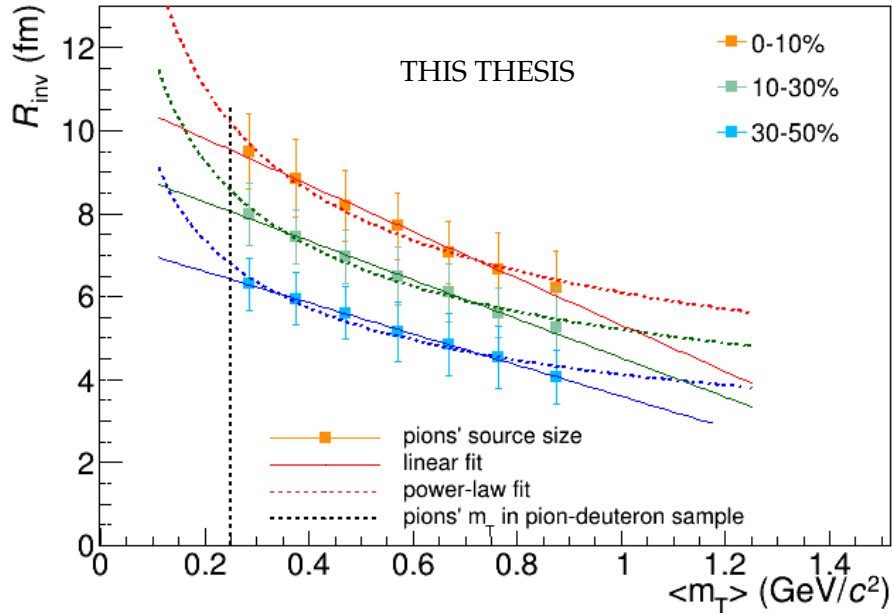


FIGURE 5.6: Pion’s radii as a function of m_T , together with linear and power-law fits.

In order to determine the correct fit for a realistic extrapolation, an extensive 1D and 3D femtoscopic study was carried out in six centrality intervals and ten m_T bins of pion–pion femtoscopy. The simulations were carried out separately with two hydrodynamical models, iHKM [166, 89] and LHYQUID [154]+THERMINATOR2 [155], which describe Pb–Pb $\sqrt{s_{NN}} = 5.02 \text{ TeV}$ collisions. It is shown there that at low m_T (ultra-soft pions) the behaviour of the radii m_T scaling is not fully power-law and

linear description reproduces better the trends. The proposed explanation for this is a trap of low momentum pions resulting from the expansion mechanism of the system. Slow particles from the centre, due to pressure resulting from small density gradient, are trapped in the centre of the system and escape later from the collision area. An example of results for one of the centralities derived in that study is shown in Fig. 5.7. The study details can be found in [157]. Because of the above, in this thesis the pion source sizes have been predicted using a linear fit to the data. These values are summarised in the table 5.2 (the uncertainty corresponds to the experimental uncertainty of femtoscopic source sizes of pions).

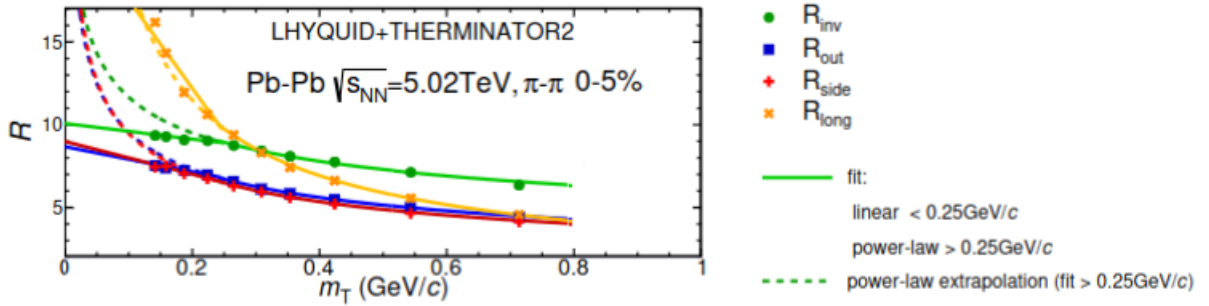


FIGURE 5.7: Pion femtoscopic radii dependencies on m_T calculated in LHYQUID+ THERMINATOR2 model, 0 – 5% Pb–Pb collisions at $\sqrt{s_{NN}} = 5.02$ TeV. Different markers and colors correspond to the radii obtained in the 3D study (R_{out} — squares, R_{side} — crosses, R_{long} — tilted crosses) and for R_{inv} from the 1D study (cicles). Lines correspond to power-law fits am_T^{-b} to radii dependencies in the range above 0.25 GeV/c and linear fits to radii dependencies in the range below 0.25 GeV/c. The illustration derived from [157] study.

TABLE 5.2: A single-particle pion radii and their uncertainty for three centrality intervals predicted for m_T of pions contributing to low k^* in the pion–deuteron sample that is considered in this thesis.

Centrality	Expected R_π (fm)	Stat. unc. \pm (fm)	Syst. unc. \pm (fm)
0-10%	9.60	0.06	0.88
10-30%	8.09	0.05	0.70
30-50%	6.45	0.04	0.65

In this analysis, the source sizes of the (anti)deuterons are estimated in a separate fitting. The fitting procedure of this part is analogous to that described for the $R_{\pi d}$ radii, but with the assumption that the source size 2.6 already contains the component

of the single pion source size (Tab. 5.2). The output value of this fitting is only the femtoscopic source size of the (anti)deuteron. The radii values from this method are presented in a table 5.3. The pictorial representation of these radii is shown in Fig. 5.8 showing a liner dependence of radii with cube root of charged multiplicity density.

TABLE 5.3: R_d radii for 3 centrality intervals, based on pion–deuteron functions and prediction of the pions source based on R vs. $\langle m_T \rangle$ of single pion radii measurements [77] rescaled to energy of this study.

Centrality	R_d (fm)	stat. unc. \pm (fm)	syst. unc. + (fm)	syst. unc. – (fm)	unc. pions (fm)
0-10%	3.88	0.48	1.10	0.64	0.75
10-30%	3.29	1.21	0.97	1.51	1.06
30-50%	2.72	0.99	1.15	1.05	0.82

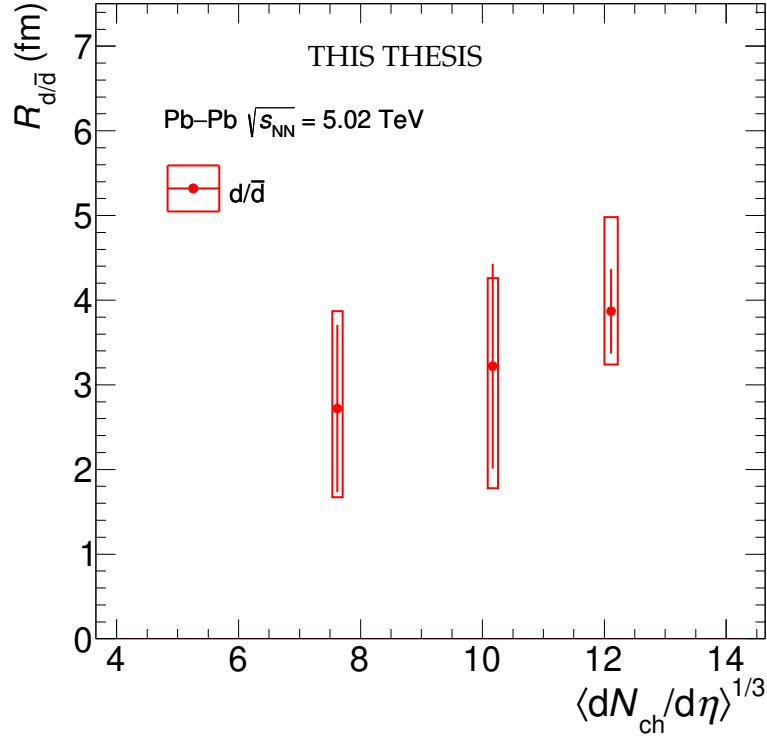


FIGURE 5.8: R_d radii as a function of $\langle dN_{ch}/d\eta \rangle^{1/3}$ obtained from a common fit to all pair combinations of pion–deuteron femtoscopic functions for Pb–Pb collisions at $\sqrt{s_{NN}} = 5.02$ TeV.

Finally, in Fig. 5.9 the points rescaled to energy $\sqrt{s_{NN}} = 5.02$ TeV from $\sqrt{s_{NN}} = 2.76$ TeV for pions, kaons and protons are shown together with the power-law fit to all points along with the deuteron source extracted in this thesis. The width of the band corresponds to the uncertainty of the pions. The Fig. 5.9 clearly shows that

the (anti)deuteron source sizes follow the m_T scaling as they are within the power-law trend of other barions. This may be a sign of a common expansion of deuterons with other particles. Also it shows that for high m_T and for composite objects like deuterons, the m_T scaling seems to remain valid. This is the first measurement of the deuteron source properties in relativistic heavy-ion data where the QGP state is present showing that we are able to obtain features of the source of rare particles by non-identical analysis. It is important to emphasize that such analysis would not be possible with deuteron–deuteron pairs due to insufficient statistics and that the performed analysis does not introduce any bias in the model description of deuteron production.

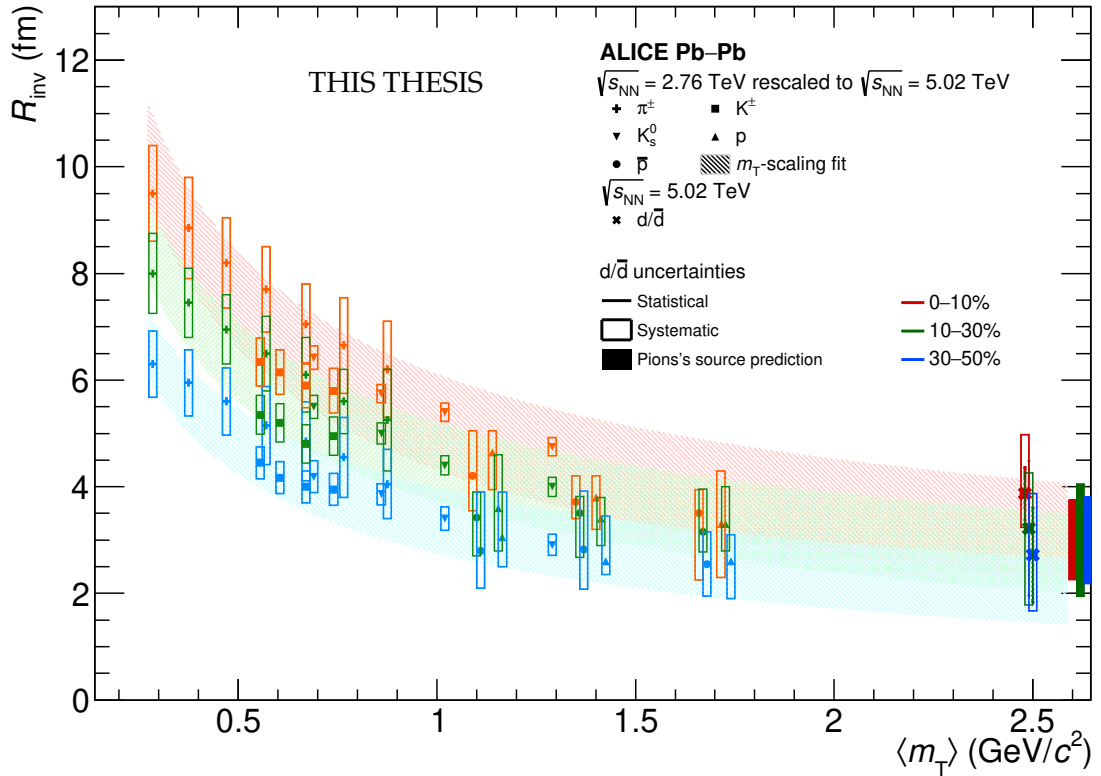


FIGURE 5.9: R_{inv} parameters versus m_T at $\sqrt{s_{\text{NN}}} = 5.02$ TeV for the three centralities for d and \bar{d} , together with other mesons and baryons (π^+ , K^+ , K_S^0 , p , \bar{p}) taken from [77] and rescaled from the energy $\sqrt{s_{\text{NN}}} = 2.76$ TeV. The bands in the plot correspond to a power-law fit to all previously measured particles with the width of the pion uncertainty. Statistical (lines) and systematic (boxes) uncertainties are shown.

In *Run – 2* data the pion–deuteron correlation function already represents statistically stable shapes, however, predictions of pions' sources have relatively large uncertainties. Therefore, it would be highly beneficial to repeat this study in *Run – 3*

with bigger statistics together with the pion–pion source size study in order to obtain more precise measurements of deuteron source sizes. The statistics would increase the quality of the fit to the pion–deuteron theoretical functions that are not highly sensitive on the source size. Similarly, the uncertainty of pion sizes in *Run* – 3 should be smaller and reach smaller m_T , which should would improve the calculations of pion’s source part.

5.2 Proton–deuteron

Disclaimer

I hereby declare that the proton–deuteron study presented below is the work that I performed within the ALICE collaboration. In this study I did the following:

- ☐ *quality assurance of the selection of charged (anti)protons and (anti)deuterons,*
- ☐ *selection of the final analysis settings,*
- ☐ *calculation of the correlation functions,*
- ☐ *calculation and application of all the corrections on particle identification, primary fraction, non-Gaussianity of the source, momentum resolution and non-femtoscopic effects,*
- ☐ *running the calculation of the theoretical functions describing the proton–deuteron interaction using the Lednický-Lyuboshits formalism (based on code originally developed by Adam Kisiel),*
- ☐ *preparation of the code for fitting the proton–deuteron system using Lednický-Lyuboshits model and performance of the fitting,*
- ☒ *running the calculation of the theoretical functions and fitting with three-body PISA model has been done by Dongfang Wang,*
- ☒ *development of the code for proton–deuteron correlations in CorAL framework has been done by Scott Pratt,*
- ☐ *running calculations of proton–deuteron with CorAL framework and performance preliminary comparisons to experimental data,*
- ☐ *calculation of the statistical and systematic uncertainties for data points, fit and measured parameters using Lednický-Lyuboshits model,*
- ☒ *calculation of the statistical and systematic uncertainties of the fit and measured parameters using PISA model has been done by Dongfang Wang,*
- ☐ *preparation of all the check and final figures (together with Dongfang Wang),*
- ☒ *performance of the proton–proton study used as a baseline has been fully done by Dongfang Wang,*
- ☐ *presentation of the analysis at different stages of advancement within the collaboration,*
- ☐ *presentation and defence of the results for acceptance during paper proposal approvals within collaboration (together with Dongfang Wang),*
- ☐ *writing the analysis note of the study for the collaboration (together with Dongfang Wang),*
- ☐ *being the chair of the paper committee in the upcoming paper.*

Nevertheless, despite the fact that the analysis part of work has been performed in big part by me, this work is as shared study especially with Dongfang Wang who was present in many of aforementioned steps. The study has been advised and checked by my supervisors and collaboration members in many internal meetings as well as by selected and experienced collaboration members that went through the details of the performed steps and results. Also, the study is based on data collected and prepared by other members of the collaboration and therefore the analysis would be not possible without other people responsible for technical aspects of the experiment, e.g. those responsible for detector construction, maintenance, operation and calibration as well as those managing the computing resources and the cloud infrastructure.

5.2.1 Introduction and model description

One of the most compelling topics in recent years is the understanding of the behaviour of the proton–deuteron system. This is because the proton–deuteron pair refers to the interaction between basic nucleons, which can also reveal the role of two- and three-body interactions. Moreover, the proton–deuteron system as described in Sect. 2.7.4 has been pointed as useful for discrimination of the creation mechanism of (anti)deuterons in heavy-ion collisions.

The proton–deuteron interaction is characterised by its description in two spin channels: the doublet with spin state $S = 1/2$ and the quartet with $S = 3/2$. This thesis reviews several measurements and calculations that have provided scattering parameters of the proton–deuteron pair for the two spin channels. It covers predictions that are a result of the scattering experiments and the inclusion of various effects in their theoretical description, namely Oers et al. [167], Arvieux [168], Huttel et al. [169], Kievsky et al. [170] and Black et al. [171]. The corresponding scattering parameters of these works are listed in Tab. 5.4. The values show a consistency in the predictions of the proton–deuteron scattering lengths that is characterised by rather small values of the doublet, $^2S_{1/2}$, and large values of the quartet, $^4S_{3/2}$. Also the thesis refers to improved precise phase shifts measurements of the proton–deuteron system [172].

□ Two-body approach

The concept of two-particle femtoscopy always refers to the relationship between two particles. Therefore, in terms of composite particles, the deuteron can be considered as a single object. It is a so-called point-like particle or a two-body approach (N-NN). Then, even though deuterons are made up of two nucleons in terms of interaction,

TABLE 5.4: The values of the scattering parameters for proton–deuteron pairs at low relative momentum, for two spin channels $^2S_{1/2}$ and $^4S_{3/2}$ [167, 168, 169, 170, 171].

Scattering parameters	f_0 (fm)	d_0 (fm)	f_0 (fm)	d_0 (fm)
pd	$^2S_{1/2}$		$^4S_{3/2}$	
Van Oers et al. [167]	$-1.30^{+0.20}_{-0.20}$	-	$-11.40^{+1.80}_{-1.20}$	$2.05^{+0.25}_{-0.25}$
Arvieux [168]	$-2.73^{+0.10}_{-0.10}$	$2.27^{+0.12}_{-0.12}$	$-11.88^{+0.40}_{-0.10}$	$2.63^{+0.01}_{-0.02}$
Huttel et al. [169]	-4.0	-	-11.1	-
Kievsku et al. [170]	-0.024	-	-13.7	-
Black et al. [171]	$0.13^{+0.04}_{-0.04}$	-	$-14.70^{+2.30}_{-2.30}$	-

they are considered as a single object, not as a construct of independent proton and neutron. The implications of this understanding are huge, because if we consider external proton in the vicinity of the deuteron, that proton will not see the nucleons individually. Therefore, in the two-body approach, quantum effects of Pauli blocking are not present.

The correlation function of multi-spin channels can be calculated using the Lednický-Lyuboshits formalism of the Coulomb plus strong interactions, but the calculations are performed separately for the two channels. The calculations of the two different spin states using the Lednický-Lyuboshits method are shown in Fig. 5.10. The doublet mainly shows the repulsive nature of the interaction. The quartet in turn represents a large peak at low k^* , which may indicate an attractive part of the interaction that is not expected from the phase shift measurements (e.g. [171]). The two spin states can be accounted for by adding the Clebsch-Gordon coefficients [173], leading to the sum expressed as:

$$C_{pd}^{total} = \frac{1}{3}C_{pd}^{^2S_{1/2}} + \frac{2}{3}C_{pd}^{^4S_{3/2}}, \quad (5.4)$$

where $C^{^2S_{1/2}}$ and $C^{^4S_{3/2}}$ account for correlation function of the two proton–deuteron spin channels.

The effect of coupling the two spin states is shown in Fig. 5.11. One can easily see a significant difference between the prediction of Coulomb only and Coulomb plus strong interaction. The functions for smaller sizes tend to reach unity for $k^* < 0.25$ GeV/c. However, the total interaction is also characterized by a peak at low $k^* \sim 0.02$ GeV/c, especially visible in small femtoscopic sources. Such a peak has not been observed in any experimental study so far, and therefore, the point-like solutions

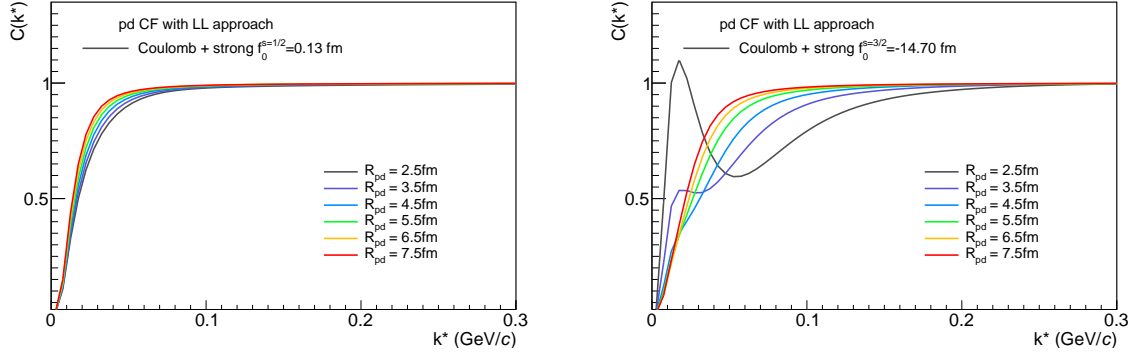


FIGURE 5.10: Theoretical correlation functions calculated with Lednický-Lyuboshits approach using [171] scattering parameters for proton–deuteron pairs separately for $C^2S_{1/2}$ (left) and $C^4S_{3/2}$ (right) spin channels drawn for different input parameters of the Gaussian source size R_{pd} .

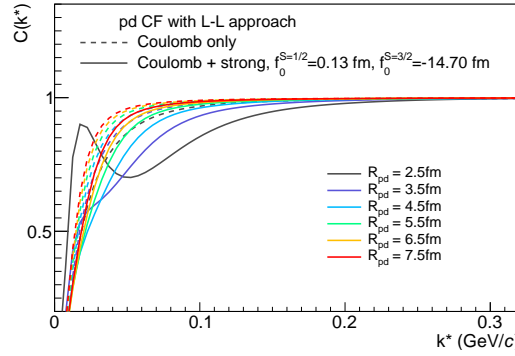


FIGURE 5.11: Theoretical correlation functions calculated with Lednický-Lyuboshits approach using [171] scattering parameters for proton–deuteron pairs drawn with different input parameters of the Gaussian source size R_{pd} .

for the proton–deuteron system became questionable. In [174, 175], it was suggested that the problem lies in the lack of three-body interactions, since the biggest problem is in the quartet state, where all particles are in the same spin state and Pauli blocking would strongly prevent strong interaction. However, the applied Lednický-Lyuboshits point-like approach does not take such effects into account.

It is clear from the very detailed work of [175] that the three-body effects and higher order partial waves play a not negligible role, especially in pp collisions where the sources are small and the interaction occurs at very short distances (even smaller than the radii of the deuteron itself). Also from this study, there is no question that the

two-body Lednický-Lyuboshits failed to reproduce the experimental proton–deuteron data in small collision systems. However, this work adds another argument to the discussion about two- or three-body interaction, which is related to the way of modeling the proton–deuteron correlation function.

It should be emphasized that the Lednický-Lyuboshits parameterization was originally intended to describe interactions of small and simple hadrons. The deuteron, however, is a relatively large composite object. The situation can become even more complicated if the second particle cannot be considered very small either, and if the strong interaction is relatively significant. For small sources, the particles must be very close to each other. In particular, if we consider a source size of the order of 1.5 fm, the particles in the proton–deuteron system are essentially stuck together. Therefore, the Lednický-Lyuboshits method, which asymptotically extrapolates its solutions to zero relative distance in cases where the interaction is pronounced, can lead to very suspect solutions. This may be because such a solution does not give zero potential values at zero relative distance, and the true wave function differs from extrapolations as shown by the illustration in Fig. 5.12.

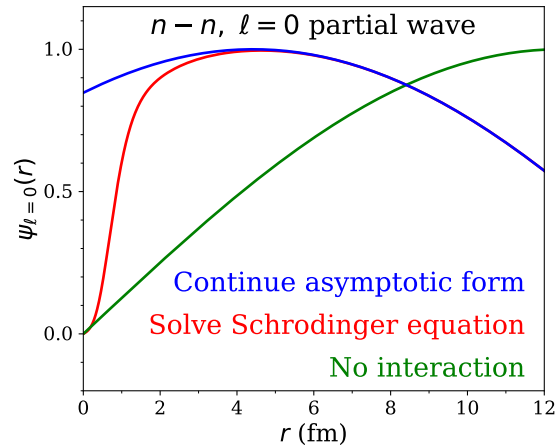


FIGURE 5.12: The schematic representation of the n - n partial wave in the absence of a potential $\sin(kr)$ (green), with potential $\sin(kr + \delta)$ and solving the Schrödinger equation (red) or using asymptotic form (blue).

Figure credit: Scott Pratt.

In other words, the asymptotic solution is exact only when relative distance, r is greater than some r_0 . When the relative distances became smaller than r_0 the potential should vanish and decrease to 0 at $r = 0$. In the case of the asymptotic solution the potential is extrapolated. Then the boundary conditions $\Psi_{\vec{k}}(\vec{r}) \rightarrow 0$ as $r \rightarrow 0$,

where the true wave function simply disappears, are not satisfied. Such asymptotic solutions are accurate, especially for correlations of relatively small particles, and/or large sources, and/or not very prominent interaction.

In this thesis, the exact calculations based on the solution of the Schrödinger equation are computed. The theoretical calculations were performed in collaboration with Prof. Scott Pratt from MSU (Michigan, USA) and Maria Stefaniak from OSU (Ohio, USA). The calculation of the proton–deuteron correlation functions was performed using the CorAL (Correlation Algorithm Library) package [176]. In this case, the wave functions were found by solving the Schrödinger equation for the two particles under the influence of their Coulomb repulsion plus the strong interaction. The calculations were performed on the basis of the total potential built up for two spin channels and for orbital angular momenta $l = 0, 1, 2$ (s-, p- and d-waves) parameterized using fits to phase shift measurements [171, 172] (shown in Fig. 5.13).

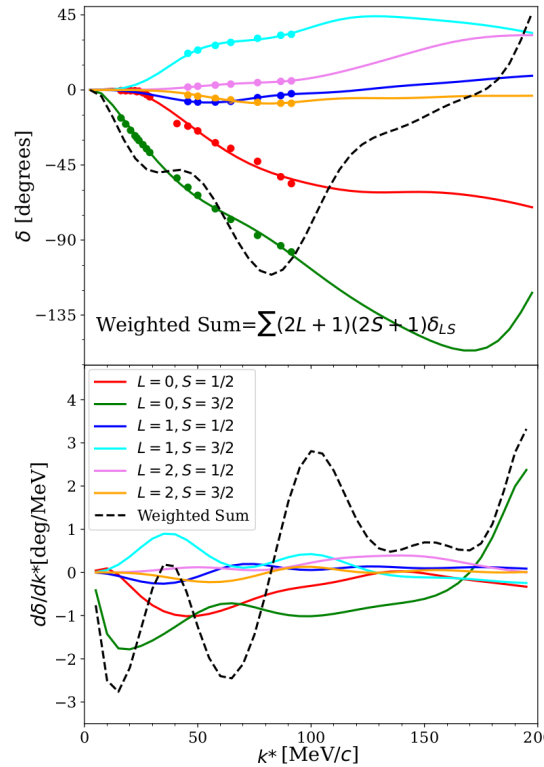


FIGURE 5.13: The phase shifts (upper panel) and their derivatives (lower panels) as a function of k^* for different spin states and partial waves; points correspond to the phase shift measurements [171, 172], lines are the fits to the experimental points. Figure credit: Scott Pratt.

In Fig. 5.14(left) proton–deuteron correlation functions calculated in the CorAL

package are presented. The two-body solution with exact calculations of the wave function do not show any unexpected peak structure as in the Lednický-Lyuboshits approach in the corresponding solutions of interaction with the Coulomb plus strong with s-wave only. However, the difference between Coulomb and Coulomb plus strong solutions is also evident. Moreover, in Fig. 5.14 it is also shown that the higher partial waves has significant impact on the correlation function. Especially the p-waves provide a visible attractive contribution to the correlation function which as pointed in [177] is caused by the possible formation of the ^3He bound state in the $S = 1/2$ spin channel.

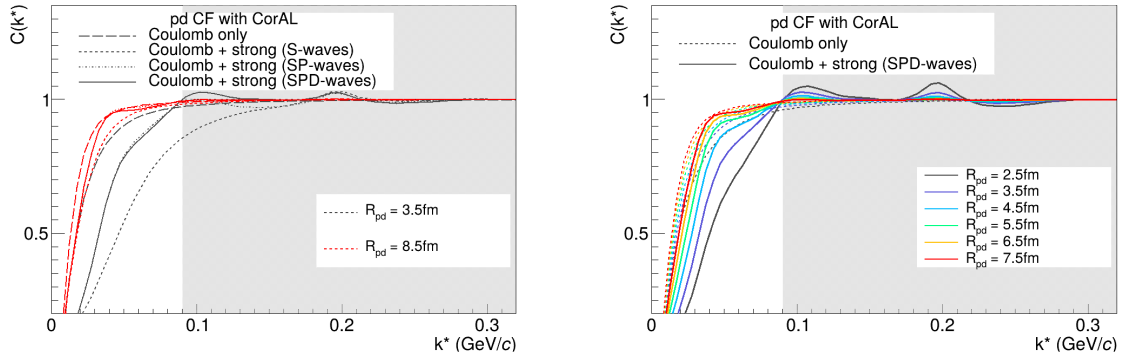


FIGURE 5.14: Theoretical correlation of proton–deuteron functions calculated with the CorAL package using for different interaction contributions to the correlation function (left) and different input parameters of the Gaussian source size R_{pd} (right). The gray region corresponds to extrapolated solutions.

However, the functions calculated with CorAL package are realistic for the range up to ~ 0.09 GeV/ c because up to this range there are exact experimental data of the phase shifts. Everything above that range is an extrapolation and therefore any further peaks and structures are questionable. The proton–deuteron correlation functions calculated with CorAL package for different source sizes are shown in Fig. 5.14.

Furthermore, the two-body Lednický-Lyuboshits and CorAL calculations have been compared in Fig. 5.15. It is clearly seen that at small sources the s-wave provided for the two approaches are very different which is a confirmation that Lednický-Lyuboshits should not be used to describe proton–deuteron interaction at small relative distances. At the same time for bigger sources the s-wave solutions become very similar and also the impact of higher order partial waves become less prominent. Despite the fact that the solutions of the proton–deuteron correlation

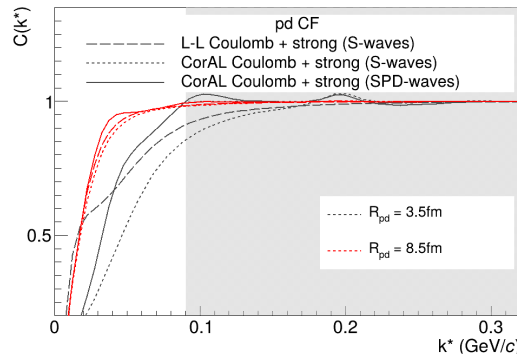


FIGURE 5.15: Theoretical correlation of proton–deuteron functions describing coulomb and strong interaction calculated with CorAL framework (solid line for strong with SPD-waves, short dashed line strong with S-wave only) and Lednický-Lyuboshits model (long dashed line, strong with S-wave only).

function provided by CorAL framework are already very reasonable they are not included in the main scope of this thesis as they are still under checks and development. Nevertheless, in heavy-ion collisions the correlation functions are not expected to be sensitive to the differences between the two two-body approaches especially with statistics of *Run* – 2. However, it would be highly beneficial to reconsider them in the future studies of proton–deuteron system in pp and Pb–Pb collisions of *Run* – 3.

□ Three-body approach

Alternatively, instead of considering the proton–deuteron interaction in an N-(NN) system, we can treat it as a three-body interaction of the N-N-N type. The model presented in this work has been derived specifically for the purpose of proton–deuteron study in pp collisions [175] by Michele Viviani, Alejandro Kievsky and Laura Marcucci from INFN (Pisa, Italy), Sebastian König from NCSU (North Carolina, USA), Oton Vazquez Doce from INFN (Frascati, Italy) and Bhawani Singh from TUM (Munich, Germany). The same three-body interaction model was extended to Pb–Pb collisions in collaboration with DongfangWang from FU (Fudan, China) and the TUM group (Munich, Germany).

A detailed definition of the three-body correlation function is given in [178, 179] and it's application to proton–deuteron interaction [174]. It is necessary to stress that this three-body model assumes coalescence production of the deuteron, following the approach proposed by Mrówczyński [124]. Therefore, this method employs a complete

three-body treatment of the proton–deuteron system within the Hyperspherical Harmonics (HH) approach [177], taking into account the strong interactions in the proton–deuteron by using the Argonne v_{18} two-nucleon (NN) [19] and the Urbana IX (UIX) for three-nucleon (NNN) [180], as well as the Coulomb potentials for the short and the asymptotic range. The full calculations include s-, p- and d- partial waves, providing an excellent description of the proton–deuteron correlation function in pp collisions [175]. In the following, the full three-body calculations will be referred to as PISA calculations. Note that the PISA calculations use nucleons as degrees of freedom. Therefore the source radii refer to nucleon–nucleon radii and not to p-d femtoscopic radii. In this paper, the radii of the three-body study are denoted as R_M or R_{NN} , both in the single-particle expression of the radii. However, please note that this source describes nucleons itself and it cannot be directly compared to two-particle proton–deuteron radii just by its multiplication by factor $\sqrt{2}$ (in this case $\sqrt{2}R_M \neq R_{pd}$!).

Fig. 5.16 shows the full three-body calculations of the proton–deuteron system for Coulomb plus strong interaction and including antisymmetrization effects. It is also expected that the three-body effect should become small for sources with femtoscopic radii above ~ 4 fm. Therefore, for femtoscopic sources of Pb–Pb collisions the two-body and three-body solutions should become very similar.

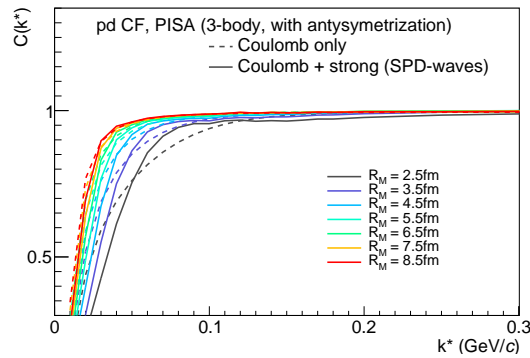


FIGURE 5.16: Theoretical correlation of proton–deuteron functions calculated with the PISA model of the three-body interaction, taking into account antisymmetrization, Coulomb and strong (SPD-waves) effects, shown with solid lines for different input parameters of the Gaussian source size R_{pd} . The dashed lines correspond to solutions with antisymmetrization and Coulomb interaction only.

5.2.2 Results

The correlation function of $pd \oplus \bar{p}\bar{d}$ pairs for three centrality intervals 0–10%, 10–30%, 30–50% obtained from Pb–Pb collisions $\sqrt{s_{NN}} = 5.02$ TeV data collected by ALICE in 2018 are shown in Fig. 5.17. The statistical uncertainties are represented by vertical lines, while the systematic uncertainties are represented by gray squared boxes. The evaluation of all the uncertainties is described in Sec. 6. The $pd \oplus \bar{p}\bar{d}$ correlation functions show a clear repulsive interaction (functions below unity).

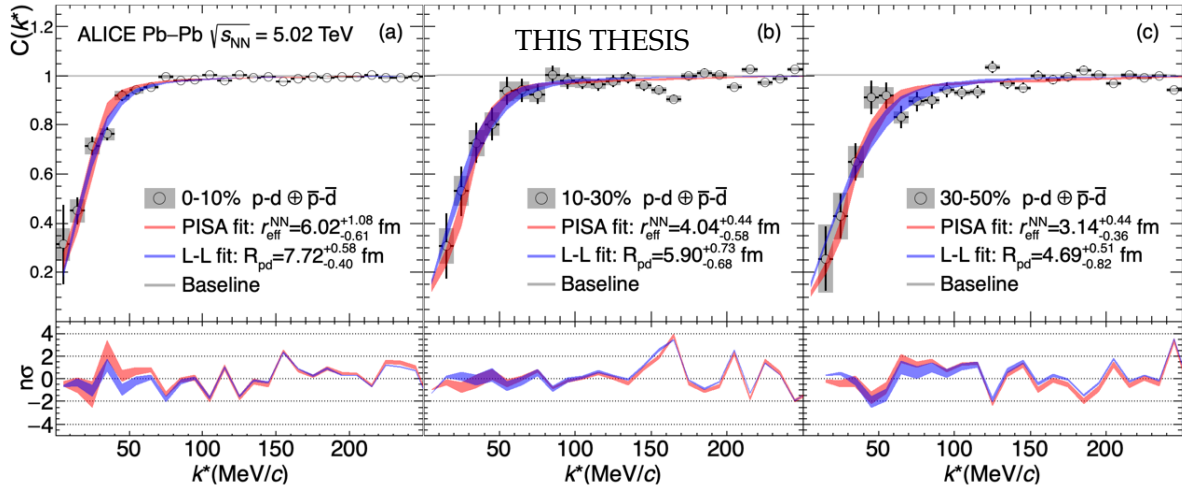


FIGURE 5.17: $pd \oplus \bar{p}\bar{d}$ correlation functions (black points) in three centrality classes together with with Coulomb plus strong fit of the three-body PISA approach (red bands) and two-body Lednický-Lyuboshits (denoted as L-L) approach with the scattering length f_0 from Arvieux et al. [168] (blue bands). The bottom panels show the signed $n\sigma$ values evaluated at each data point for theoretical bands.

The experimental correlation functions are further fitted according to the procedure described in Sec. 4.4 using the χ^2 minimization technique in k^* up to 0.25 GeV/c. For this purpose, two sets of precalculated theoretical correlation functions have been prepared, one for the three-body PISA model R_{NN} in the range [1.5, 9.5] fm with a step of 0.01 fm, and the other for the two-body Lednický-Lyuboshits model in R_{pd} in the range [1.5, 9.5] fm with a step of 0.5 fm. The Lednický-Lyuboshits calculations require scattering parameters which in this study are taken from five different analyses of proton–deuteron scattering data [167, 168, 171, 169, 170] for which calculations were performed separately. The theoretical correlation function obtained from the fit is represented by bands in Fig. 5.17. Both two- and three-body calculations provide an excellent description of the experimental data, unlike the

proton–deuteron measurement in pp collisions [175], where the large peak at low k^* in the Lednický-Lyuboshits model completely discriminates the two-body solutions. The corresponding values of the measured sources R_{NN} and R_{pd} are summarized in Tab. 5.5. The agreement between the two approaches in describing the heavy-ion data supports the expectation that the three-body effects diminish in large femtoscopic sources.

TABLE 5.5: Proton–deuteron, R_{pd} and R_{NN} source size measured in Pb–Pb collisions at nucleon energy $\sqrt{s_{\text{NN}}} = 5.02$ TeV using Lednický-Lyuboshits (denoted as L-L) parametrization with scattering parameters from [167, 168, 169, 170, 171] and PISA model, respectively.

	0 – 10%			10 – 30%			30 – 50%		
2-body L-L	$R_{\text{pd}}(fm)$	<i>stat.</i>	<i>syst.</i>	$R_{\text{pd}}(fm)$	<i>stat.</i>	<i>syst.</i>	$R_{\text{pd}}(fm)$	<i>stat.</i>	<i>syst.</i>
Van Oers et al. [167]	7.44	+0.36 –0.31	+0.50 –0.23	5.76	+0.59 –0.47	+0.26 –0.51	4.26	+0.64 –0.41	+0.55 –0.20
Arvieux [168]	7.72	+0.34 –0.32	+0.47 –0.24	5.90	+0.66 –0.45	+0.32 –0.51	4.69	+0.40 –0.70	+0.32 –0.42
Huttel et al. [169]	7.79	+0.36 –0.32	+0.44 –0.21	6.15	+0.63 –0.49	+0.26 –0.46	5.20	+0.42 –0.47	+0.22 –0.28
Kievsku et al. [170]	7.15	+0.37 –0.30	+0.50 –0.22	5.62	+0.54 –0.49	+0.25 –0.53	4.24	+0.52 –0.42	+0.42 –0.15
Black et al. [171]	7.10	+0.38 –0.30	+0.51 –0.22	5.58	+0.55 –0.49	+0.26 –0.54	4.23	+0.50 –0.40	+0.37 –0.16
3-body PISA	$R_{\text{NN}}(fm)$	<i>stat.</i>	<i>syst.</i>	$R_{\text{NN}}(fm)$	<i>stat.</i>	<i>syst.</i>	$R_{\text{NN}}(fm)$	<i>stat.</i>	<i>syst.</i>
	6.02	+0.98 –0.57	+0.46 –0.23	4.04	+0.55 –0.41	+0.19 –0.15	3.14	+0.38 –0.32	+0.23 –0.17

In Fig. 5.18 the measured radii as a function of $\langle dN_{\text{ch}}/d\eta \rangle^{1/3}$ are presented. The femtoscopic source sizes shows the growing values with increasing system size.

In addition, following the same methodology as in the pion–deuteron study, the deuteron source size is extracted using the expression $R_{\text{d}} = \sqrt{R_{\text{pd}}^2 - R_{\text{p}}^2}$, where R_{p} is the single particle source size for protons, constrained by the m_{T} scaling of proton–proton pairs shown in Fig. 5.20 calculated for the same dataset as the proton–deuteron analysis within the ALICE collaboration by Dongfang Wang from FU (Shanghai, China). The R_{p} values for $m_{\text{T}} = 1.20$ GeV/ c of protons in proton–deuteron pairs contributing to the low k^* region are summarized in the Tab. 5.6. The R_{d} values are evaluated by taking the average of the results obtained by fitting the Lednický-Lyuboshits model with the five different scattering parameters [167, 168, 171, 169, 170] for the strong interaction. The values of R_{d} are summarized in Tab. 5.7 and plotted in Fig. 5.19 as a function of $\langle dN_{\text{ch}}/d\eta \rangle^{1/3}$.

Furthermore, the R_{d} and R_{NN} values are plotted together with the m_{T} scaling of nucleons, represented by the squares and diamonds in Fig. 5.20. Both values are in agreement with the m_{T} -scaling of single nucleons, suggesting that deuterons, as composite light nuclei, share a common flow velocity with nucleons in Pb–Pb

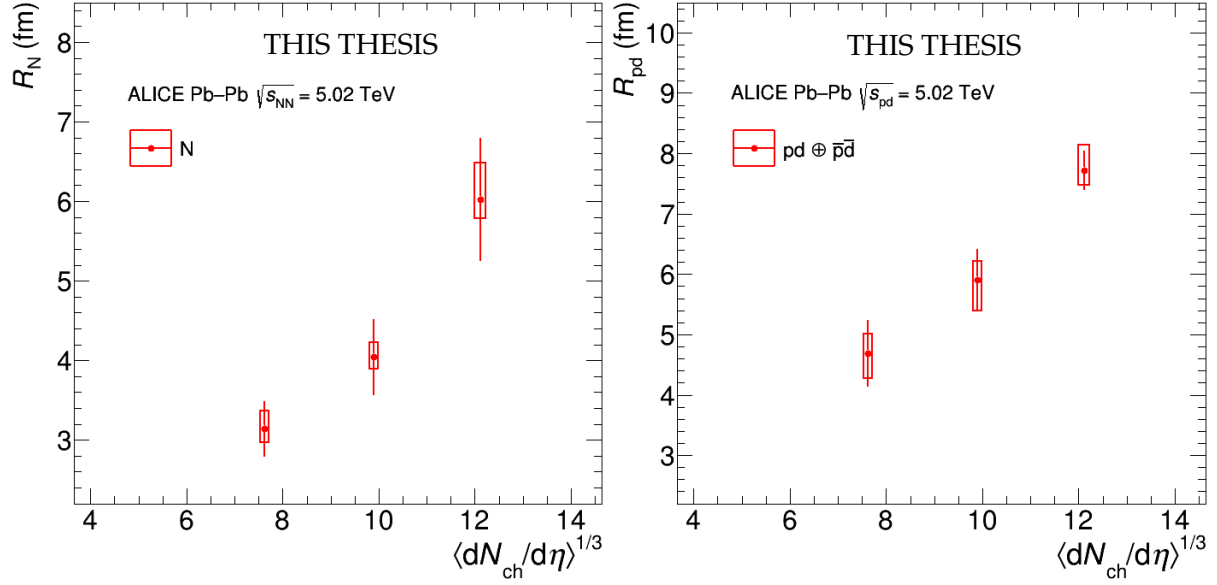


FIGURE 5.18: R_{NN} (left) and R_{pd} (right) radii as a function of $\langle dN_{ch}/d\eta \rangle^{1/3}$ obtained from the fit to proton–deuteron pairs registered in Pb–Pb collisions at $\sqrt{s_{NN}} = 5.02$ TeV.

TABLE 5.6: A single-particle proton radii and their uncertainty for three centrality intervals predicted for m_T of protons contributing to low k^* in the proton–deuteron sample that is considered in this thesis.

Centrality	Expected R_p (fm)	Stat. unc. \pm (fm)	Syst. unc. \pm (fm)
0-10%	5.60	0.12	0.10
10-30%	4.53	0.10	0.08
30-50%	3.32	0.05	0.04

collisions. The radii extracted for different m_T values within the same centrality classes for the proton–deuteron system are currently compatible within the uncertainties of the two methods. However, more precise measurements could allow us to test the m_T scaling for proton–deuteron pairs with a precision comparable to that already achieved for proton–proton pairs.

As mentioned above, the correlation functions provided by the CorAL framework are not included in the calculations of this work, as they are still under development. However, a very preliminary check is presented in Fig. 5.21, where the CorAl band has been added for exemplary radii measured with the Lednický-Lyuboshits two-body approach using scattering parameters from [168]. All three approaches are in very good agreement within the uncertainties supporting the statement of vanishing

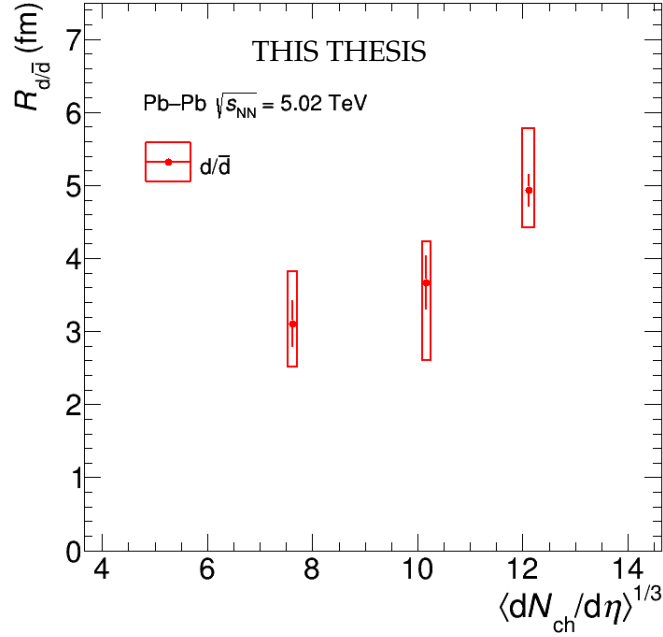


FIGURE 5.19: R_d radii as a function of $\langle dN_{ch}/d\eta \rangle^{1/3}$ obtained from a common fit to all pair combinations for Pb–Pb collisions at $\sqrt{s_{NN}} = 5.02$ TeV.

TABLE 5.7: (Anti)deuteron, R_d , source size measured in Pb–Pb collisions at $\sqrt{s_{NN}} = 5.02$ TeV using Lednický-Lyuboshits parametrization and scattering parameters from [167, 168, 171, 169, 170] and (anti)protons source measurements 5.6.

	0 – 10%			10 – 30%			30 – 50%		
L-L	$R_d(fm)$	stat.	syst.	$R_d(fm)$	stat.	syst.	$R_d(fm)$	stat.	syst.
Van Oers et al. [167]	4.90	+0.55 –0.44	+0.74 –0.37	3.56	+0.82 –0.79	+0.47 –1.00	2.65	+0.99 –0.72	+0.81 –0.36
Arvieux [168]	5.31	+0.50 –0.44	+0.68 –0.36	3.78	+0.91 –0.74	+0.53 –0.92	3.32	+0.69 –0.96	+0.45 –0.67
Huttel et al. [169]	5.42	+0.51 –0.42	+0.62 –0.32	4.16	+0.81 –0.71	+0.40 –0.78	4.01	+0.57 –0.53	+0.29 –0.39
Kievsku et al. [170]	4.45	+0.58 –0.45	+0.77 –0.39	3.33	+0.78 –0.89	+0.47 –1.06	2.65	+0.82 –0.61	+0.62 –0.28
Black et al. [171]	4.36	+0.62 –0.45	+0.80 –0.39	3.26	+0.82 –0.91	+0.49 –1.08	2.63	+0.82 –0.56	+0.56 –0.29
Combined fit	4.92	+0.53 –0.51	+0.87 –0.47	3.76	+0.84 –0.82	+0.55 –1.07	3.14	+0.83 –0.55	+0.63 –0.65

three-body effects and significance of higher partial waves in heavy-ion femtosopic sources. It also shows that the Lednický-Lyuboshits formalism and the exact solution of the Schrödinger equation are consistent in heavy-ion data.

As already mentioned in section. 2.7.4, the production mechanism of deuterons can be distinguished by the femtosopic measurement of the deuteron source sizes. However, to do so, the model description cannot make any assumption about the creation mechanism of the particles. Therefore, the PISA model cannot be used

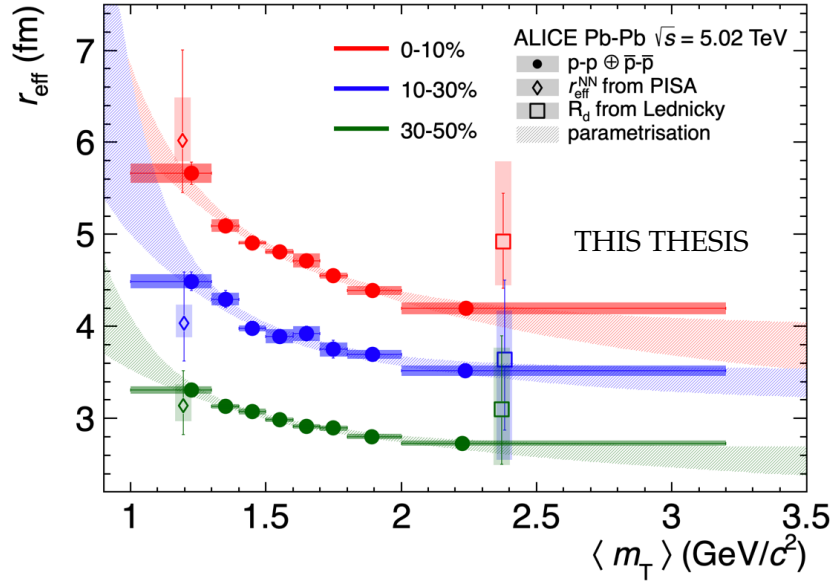


FIGURE 5.20: The femtoscopic source sizes in a function of m_T measured in Pb–Pb collisions at $\sqrt{s_{NN}} = 5.02$ TeV/ c represented by red, blue, and green markers as follows in 0–10%, 10–30%, 30–50% centrality intervals. The full markers corresponds to source sizes of protons measured directly in proton–proton study. The open diamonds and squares represents femtoscopic sizes measured in proton–deuteron study for nucleons R_{NN} and deuterons R_d , respectively. The vertical bars and boxes show the statistical and systematic uncertainties, respectively. The shaded bands depict the 1σ uncertainties of the fits of the power-law function: $r_{\text{eff}} = a + b \cdot \langle m_T \rangle^c$.

for this purpose because it is based on the assumption of coalescence and also its source does not refer to the deuterons but to separate nucleons. Furthermore, the Lednický-Lyuboshits two-body approach cannot be used for this purpose either, because even though it provides a nice description of the data, it does not contain higher partial waves, which in the proton–deuteron system may change the conclusion about the creation mechanism (expected factor of coalescence / thermal radii in the proton–deuteron system is only ~ 1.15). A potential for this purpose may have functions provided by the CorAL framework that account for higher order partial waves and does not have any assumption on production mechanism of deuterons. However, the measured sources should be characterized by smaller statistical uncertainties than the one derived in *Run – 2* data to allow for conclusions at least at the level of 3σ , which might be possible in *Run – 3* data.

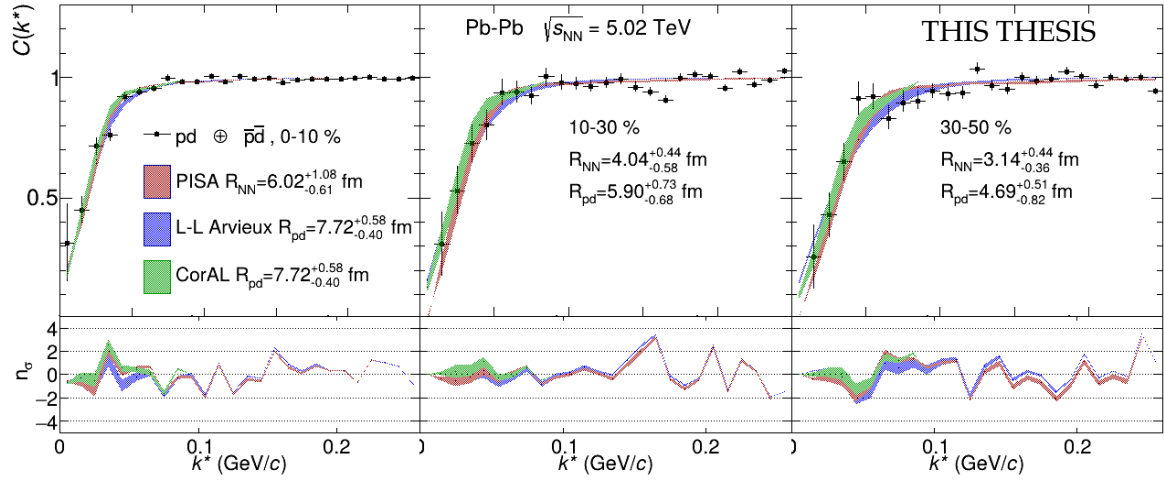


FIGURE 5.21: $pd \oplus \bar{p}\bar{d}$ correlation functions (black points) in three centrality classes together with with Coulomb plus strong fit of the three-body PISA approach (red bands), two-body Lednický-Lyuboshits (denoted as L-L) approach with the scattering length f_0 from Arvieux [168] (blue bands) and two-body CorAL functions (green band). The bottom panels show the signed $n\sigma$ values evaluated at each data point for theoretical bands.

5.3 Kaon–proton

Disclaimer

I hereby declare that the kaon–proton study presented below is the work that I performed within the ALICE collaboration. In this study, I did the following:

- ☐ *quality assurance of the selection of charged kaons and (anti)protons,*
- ☐ *selection of the final analysis settings which has been done together with Georgy Kornakov, Łukasz Graczykowski, Małgorzata Janik and Adam Kisiel,*
- ☐ *calculation of the correlation functions,*
- ☐ *calculation and application corrections on particle identification, primary fraction,*
- ☐ *helping in calculation and application corrections on momentum resolution and non-femtoscopic effects which has been done together with Georgy Kornakov,*
- ☒ *running the calculation of the theoretical functions with Lednický-Lyuboshits approach has been fully done by Georgy Kornakov (based on code originally developed by Adam Kisiel),*
- ☒ *running the calculation of the theoretical functions with Kyoto model has been fully done by Dimitar Michailov,*
- ☐ *helping in the preparation of the code for fitting the kaon–proton system. The code has been initially developed by Adam Kisiel,*
- ☐ *performance of the fitting,*
- ☐ *helping in the calculation of the uncertainty for data points, fit and measured parameters which has been done together with Georgy Kornakov, Łukasz Graczykowski and Małgorzata Janik,*
- ☐ *preparation of all the check and final figures,*
- ☐ *presentation of the analysis at different stages of advancement within the collaboration,*
- ☐ *presentation and defence of the results for acceptance during preliminary approvals within collaboration,*
- ☐ *helping in the defence of the results for acceptance during paper proposal approvals within collaboration which has been defended by Georgy Kornakov,*
- ☐ *helping in writing the analysis note of the study for the collaboration. This work has been done together with Georgy Kornakov, Małgorzata Janik and Łukasz Graczykowski,*
- ☐ *being a member of the paper committee in the published paper.*

Nevertheless, despite the fact that the significant part of this analysis has been performed by me, this work has been advised, checked and contributed by my supervisors (especially, the direct contribution belong to Georgy Kornakov, Adam Kisiel, Małgorzata Janik and Łukasz

Graczykowski) and collaboration members in many internal meetings as well as by selected and experienced collaboration members that went through the details of the performed steps and results. It was my first femtoscopic study and many of the steps would be not possible without transfer of experience and knowledge especially from the WUT ALICE team. Also, the study is based on data collected and prepared by other members of the collaboration and therefore the analysis would be not possible without other people responsible for technical aspects of the experiment, e.g. those responsible for detector construction, maintenance, operation and calibration as well as those managing the computing resources and the cloud infrastructure. The kaon–proton study described in this section was started during my Master’s degree and finished at the beginning of my Ph.D. It was published by the ALICE collaboration in 2021 [181].

5.3.1 Introduction and model description

The kaon–proton study deals with the problem of the kaon–nucleon (KN) and antikaon–nucleon ($\bar{\text{K}}\text{N}$) interactions in the strangeness sector of the low-energy QCD. The main aim is to determine the scattering parameters, the real and imaginary parts of the scattering length together with the femtoscopic radii, which describe the observed correlations at low relative momentum of both particle pairs in Pb–Pb collisions. These correlations help to constrain the interactions in the strange sector and shed more light on the nuclear equation of state in order to better understand the properties of matter under extreme conditions, such as those found in the core of neutron stars. Moreover, it has been already shown in small sources of pp collisions [182] that this pair combination is highly influenced by coupled-channels effects. Therefore, this study also reveals the behaviour of the kaon–proton correlation functions in large femtoscopic sources present in heavy-ion collisions.

There have been several attempts to access the $\text{K}^- \text{p}$ system. Firstly, by scattering experiments using a K^- beam and a hydrogen target. So far, the scattering experiments were able to reach a relative momentum above $\sim 100 \text{ MeV}/c$ of kaons and protons [183, 184, 185, 186, 187, 188, 189] and therefore, the scattering amplitude was difficult to constrain. In this thesis, the scattering length derived by only one scattering experiment is considered [190]. The $\text{K}^- \text{p}$ interaction has also been studied by exotic atom experiments. In this case, an electron from a hydrogen atom is replaced by a negatively charged kaon, forming so-called kaonic hydrogen. Thanks to the measurement of the width and shift of the energy levels in comparison to QED

expectations the scattering length is obtained using the Trueman-Deser formula and corrected for isospin-breaking coupling and the Coulomb interaction. There have been several experiments on kaonic hydrogen and kaonic deuteron, such as DEAR [191], KpX experiment at KEK [192], or SIDDHARTA experiment [193] at the DΦNE electron-positron collider [194], which provides the scattering length (f_0) used in this work [195, 196]. Refined calculations of f_0 use the SIDDHARTA measurements together with chiral effective SU(3) calculations anchored to kaonic atoms measurements [197, 198]. Other calculations which are based on the chiral effective SU(3) theories are [199, 200].

There are several measurements and calculations that constrain the scattering length of the $\bar{K}N$ system. The values are rather consistent in both, real and imaginary parts of the scattering length but most of them have large uncertainties. The interaction can be also studied by the femtoscopy technique and this is one of the purposes of this work. However, the modeling of the K^-p interaction in the femtoscopy studies should also include coupled channels. Coupled channels do not play a crucial role in scattering experiments because there the initial and final states are experimentally fixed and one can only focus on one channel. Exotic atoms are dominated by the threshold channel because they measure the function at almost zero relative momentum. On the other hand, in ultrarelativistic collision studies the final function is a composition of different initial states such as K^0n or Λ -s. Possible states contributing to the $\bar{K}N$ system are shown in Fig. 5.22.

The work presented in this thesis is directly related to the kaon–proton study performed in pp collisions [182], where the measured correlation functions are compared with several models and interaction hypotheses to demonstrate the sensitivity of the femtoscopy method. In particular, this pp collision study showed clear evidence for the presence of coupled channels in the measured correlation function, e.g. through evidence for an opening of the K^0n isospin-breaking channel with a cusp structure at its threshold of ~ 60 MeV/ c . However, it is also theoretically predicted that the coupled channel effects are strongly reduced for source sizes larger than 3 fm. The difference between theoretical prediction of 1 fm source (typical source size in pp collisions) and a 3 fm source (typical in very peripheral heavy-ion collisions) is shown in Fig. 5.23. Therefore, the analysis of K^-p pairs in Pb–Pb collisions can be limited to the study of the single channel $K^-p \rightarrow K^-p$, since the contribution of other channels is expected to be marginal.

The kaon–proton study presented in this thesis considers also K^+p pairs. Their

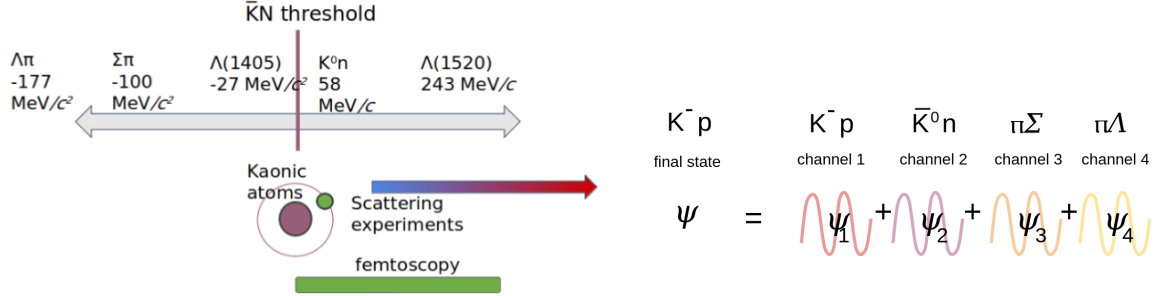


FIGURE 5.22: Left: A schematic representation of different states entangled with K^-N channel at different energy together with sensitivity ranges of different experiments (figure credit: Georgy Kornakov). Right: coupled channels that can contribute in the whole span of the K^-p correlation function.

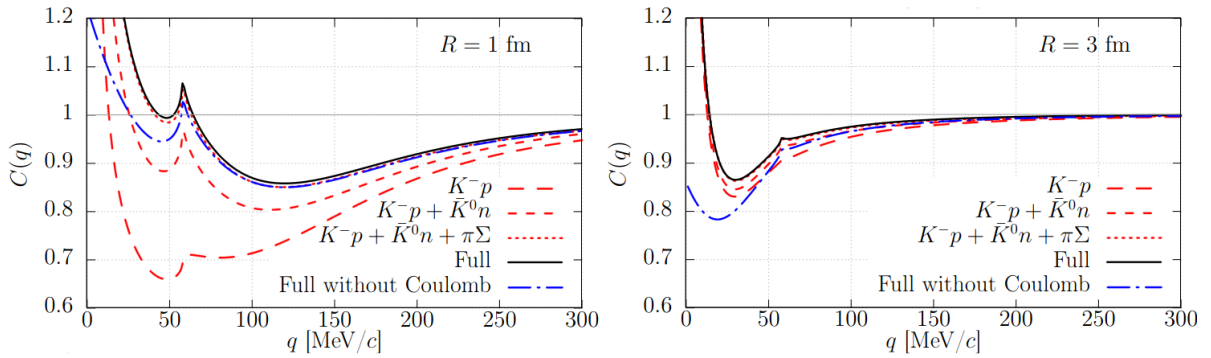


FIGURE 5.23: Left: K^-p correlation function for $R = 1$ fm, lines denotes the results of correlation function adding different channels: only K^-p (long-dashed), K^-p plus \bar{K}^0n plus K^0n (short-dashed), K^-p plus \bar{K}^0n plus K^0n plus $\pi\Sigma$ (dotted), all channels (solid), all channels but without the Coulomb interaction (dash-dotted). Right: the same as upper but for femtoscopic source $R=3$ fm. Figure from [201].

description is simpler than the case of K^-p as in K^+p the coupling to other channels close or below threshold is not expected. Moreover, the scattering parameters of the strong interaction are precisely constrained from partial waves studies and scattering experiments [202].

All the values of the scattering length considered in the kaon-proton study are summarised in the Tab. 5.8.

TABLE 5.8: Values of the real and imaginary parts of the scattering length for K^-p and K^+p pairs at low relative momentum.

Scattering parameters	$\Re f_0$ (fm)	$\Im f_0$ (fm)
K^-p		
Hoshino et al. [196]	-0.66	0.89
Martin [190]	-0.67 ± 0.1	0.64 ± 0.1
Ikeda et al. [197, 198]	-0.7	0.89
SIDDHARTA [197, 198]	-0.65 ± 0.1	0.81 ± 0.15
Liu et al. [200]	-0.75	0.80
Ito et al. [195]	-0.78 ± 0.15	0.49 ± 0.25
Borasoy et al. [199]	-1.05 ± 0.5	0.75 ± 0.4
K^+p		
Dalitz et al. [202]	-0.308 ± 0.003	-

The first method used in this thesis for the calculations of the $K^-p \oplus K^+\bar{p}$ correlation functions is based on the Lednický-Lyuboshits model. The s-wave scattering lengths, f_0 of $K^-p \oplus K^+\bar{p}$ pairs is expected to have a large imaginary part due to coupling to resonances. Such expectations are confirmed by already measured values [190, 196, 195, 198, 199, 200]. These values can be further used as an fixed input to Lednický-Lyuboshits model, however, this work focuses on their measurements by fitting experimental correlation functions. The $K^+p \oplus K^-\bar{p}$ pairs are also modeled using the Lednický-Lyuboshits model and set value of f_0 as in [202]. All calculations are performed with zero effective range approximation ($d_0=0$) and with the Gaussian source assumption of the same size shared between same- and opposite-charge sign particle pairs. The examples of Lednický-Lyuboshits kaon-proton functions are presented in Fig. 5.24. In both, same- and opposite-charge pairs the strong interaction contribution is significant. In the K^-p case the strong interaction contribution form a characteristic dip structure below unity which increase with decreasing femtoscopic source size.

The second method used in this study is known as the Kyoto model [201]. The model takes into account the Coulomb and strong interactions as well as coupled channels together with their threshold energy difference between isospin multiplets. This is implemented by a realistic coupled channel potential based on chiral SU(3) [201]. The model provides the K^-p wave function, which is then folded with a Gaussian source using the CATS package [173]. The only input parameter

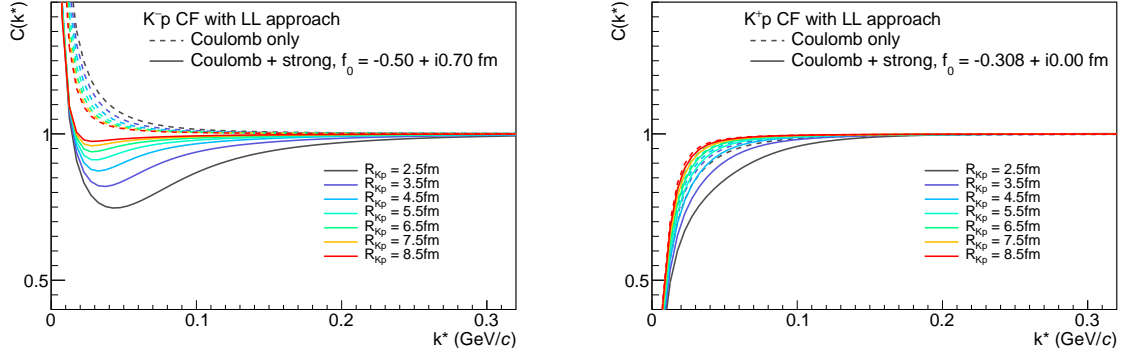


FIGURE 5.24: Theoretical correlation functions with different input parameters of the source size calculated using L-L approach for K^-p pairs (left) and K^+p (right).

is the source size. The calculations for the Kyoto model derived for the purpose of this study were provided by Dimitar Michailov from TUM (Munich, Germany). In Fig. 5.25 examples of the K^-p correlation functions for different femtoscopic source sizes are shown. For smaller sources we can observe a characteristic cusp structure expected for a K^0n coupled channel.

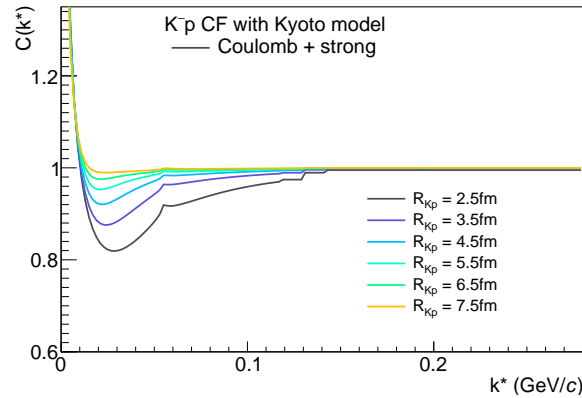


FIGURE 5.25: Theoretical correlation functions of K^-p pairs for different values of the source sizes calculated using Kyoto model [201] folded to the CATS package [173].

5.3.2 Results

The correlation functions of $K^-p \oplus K^+\bar{p}$ and $K^+p \oplus K^-\bar{p}$ pairs for six centrality intervals 0 – 5%, 5 – 10%, 10 – 20%, 20 – 30%, 30 – 40%, 40 – 50% obtained from

Pb–Pb collisions at $\sqrt{s_{NN}} = 5.02$ TeV data collected by ALICE in 2015 are shown in Fig. 5.26. The statistical and systematic uncertainties of the measured data points are added in quadrature and shown as vertical bars. The evaluation of all the uncertainties is described in Sec. 6.

The $K^+p \oplus K^-\bar{p}$ correlation function shows a clear repulsive nature (the functions

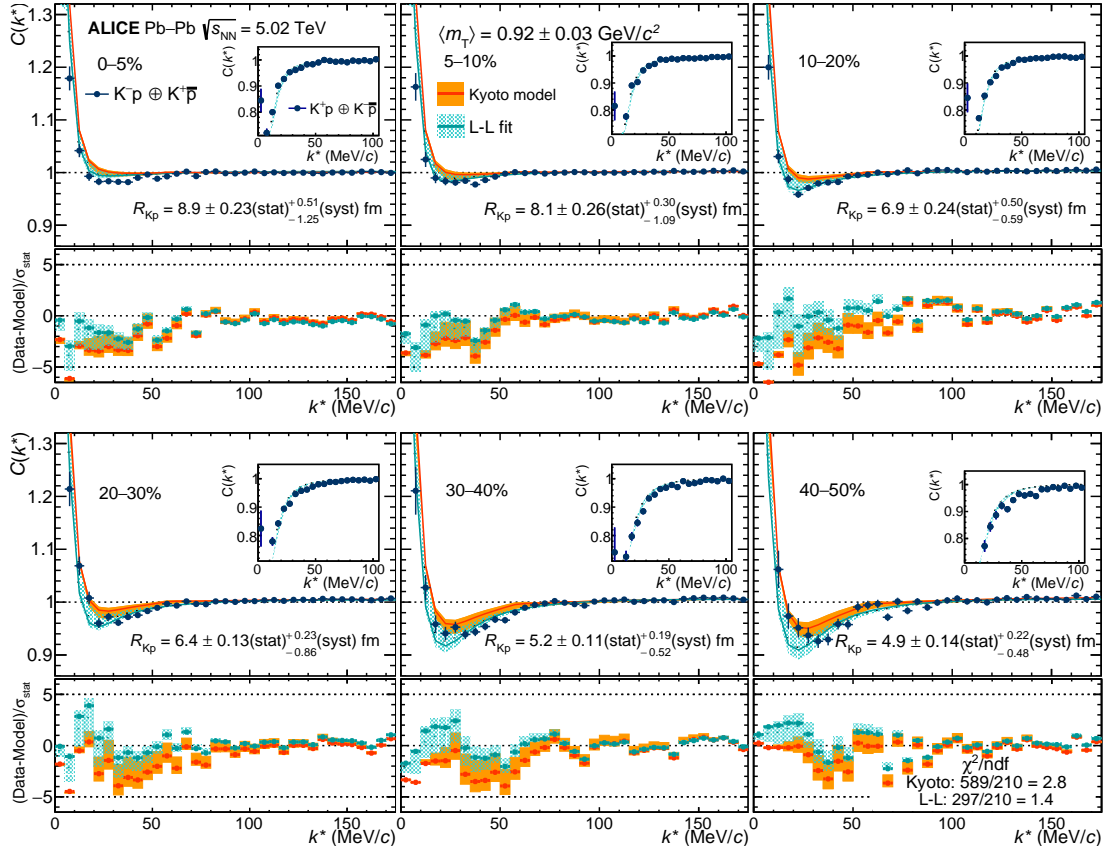


FIGURE 5.26: Big upper pads: $K^-p \oplus K^+\bar{p}$ correlation functions in the six centrality classes. On top of data in light cyan band the corresponding Lednický-Lyuboshits fits (denoted as L-L), orange band Kyoto model calculations. Small inserts pads of upper plots: the $K^+p \oplus K^-\bar{p}$ correlation functions in the six centrality classes. On top of data in light cyan band the corresponding Lednický-Lyuboshits fits. Bottom pads: sigma difference expressed as data minus model normalised by the statistical uncertainty of the data.

are below unity). The $K^-p \oplus K^+\bar{p}$ correlation functions show an attractive interaction with a repulsive part, seen as a dip below unity at $k^* \sim 20\text{--}50$ MeV/c. The dip is caused by the repulsive strong force, whose effects are well pronounced in this system. The deviation from unity of the correlation functions becomes larger for peripheral

collisions and hence smaller femtoscopic source sizes in which interaction effects are more pronounced due to shorter distances. Importantly, these correlation functions do not show any cusp structure at ~ 60 MeV/ c , which would indicate the opening of an isospin-breaking channel as in [182]. It is therefore the first experimental confirmation of the theoretical prediction that the effects of coupled channels diminish in heavy-ion collisions, where the source sizes are relatively large. Therefore, it has been followed up by further kaon–proton femtoscopic analyses but in peripheral Pb–Pb and p–Pb collisions which investigates precisely the intermediate femtoscopic sources and vanishing coupled channels effects [203].

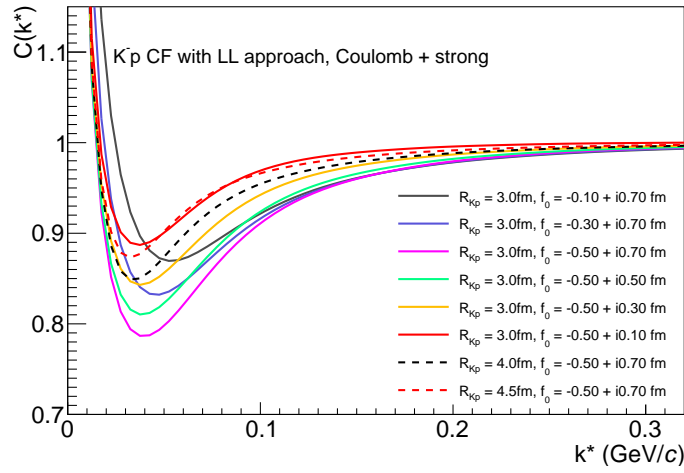


FIGURE 5.27: Theoretical correlation functions of $K^- p$ for different source radii and scattering parameters calculated using L-L approach.

Following the procedure described in Sec. 4.4, the fit is performed simultaneously on the twelve correlation functions (six centralities, same and opposite sign pairs) and assumed that the source has the same size for same- and opposite-charge pairs at a given centrality. The fitting in the kaon–proton study is performed with the Lednický-Lyuboshits approach only (the Kyoto model is used only for comparison with the measured radii). For its purpose, a set of calculated functions is prepared using the Lednický-Lyuboshits formalism for opposite- and same-charge pairs with radii [1.5, 9.0] fm with a step of 0.5 fm, the real part of $K^- p$ f_0 [-1.1, 0.0] fm with a step of 0.1 fm, imaginary part $K^- p$ f_0 [0.0, 1.2] fm with a step of 0.1 fm, and the real part of $K^+ p$ $f_0 = -0.308 \pm 0.003$ fm. The ranges of scattering parameters are chosen with a large margin around theoretically predicted interaction parameters to provide

the fitting procedure a wide space of functions and prevent obtaining solutions at the border of ranges of parameter.

The fitting of the three parameters for the K^-p can lead to a potential risk of leaving too big freedom for the fit. As shown in Fig. 5.27, e.g. changes of three parameters at once may lead to similar solutions. Therefore, one of the parameters must be limited to keep control over the fit. In this case, Gaussian source radii are initially constrained from $K^+p \oplus K^-\bar{p}$ measurement where the scattering length is known. There are six different radii measured among functions representing certain centrality interval. Later, with initially limited femtoscopic source sizes all functions are simultaneously fitted this time looking mostly for two parameters for the scattering length (real and imaginary part of f_0) shared between $K^-p \oplus K^+\bar{p}$ correlation function. The theoretical functions are then interpolated between the closest solutions to the data selected based on the minimum χ^2 . The simultaneous fit to experimental correlation functions is presented in Fig. 5.26.

The fit determines six femtoscopic source sizes, R_{Kp} that vary from around 4.5 fm for the most peripheral collisions to around 9 fm for the most central (summarised in Tab. 5.9). The source sizes determined in the Lednický-Lyuboshits fit were further used as an input to the theoretical predictions of the correlation functions using Kyoto model wave function in the CATS package shown also in Fig. 5.26. Both models describe the data qualitatively and quantitatively well.

TABLE 5.9: A two-particle kaon-proton source sizes, R_{Kp} , together with uncertainties for 6 centrality from the fit to all pair combinations for Pb–Pb collisions at $\sqrt{s_{NN}} = 5.02$ TeV.

Centrality	R_{Kp} (fm)	stat. unc. (fm) \pm	syst. unc. + (fm)	syst. unc. – (fm)
0-5%	8.9	0.23	0.51	1.25
5-10%	8.1	0.26	0.30	1.09
10-20%	6.9	0.24	0.50	0.59
20-30%	6.4	0.13	0.23	0.86
30-40%	5.2	0.11	0.19	0.52
40-50%	4.9	0.14	0.22	0.48

The kaon–proton source size dependence as the function of cube root of multiplicity density is presented in Fig. 5.28. The trend, as expected, is linear. In order to qualitatively check if the values derived in this fitting are similar to the expected ones for kaon–proton system, the femtoscopic source sizes can be predicted using Eq. 2.6. The source sizes of kaons for the corresponding average

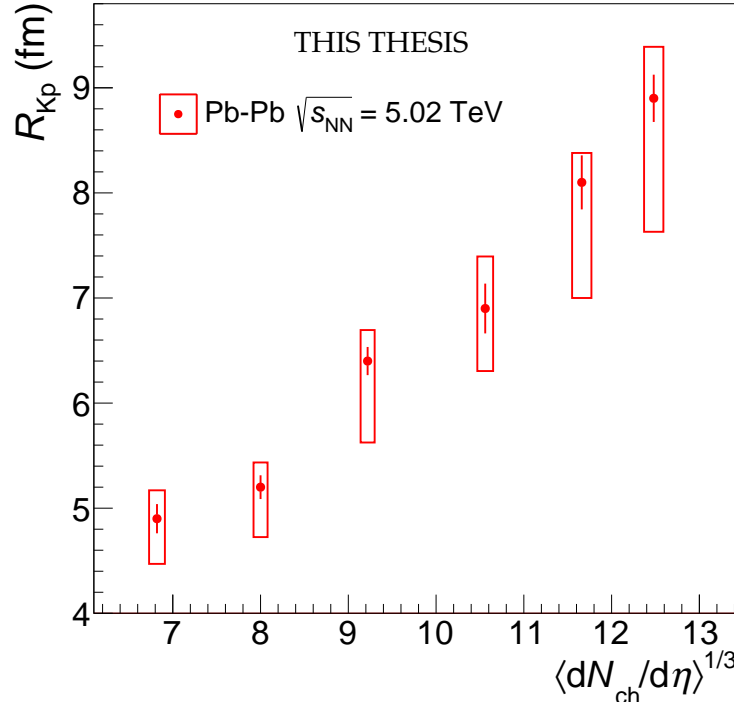


FIGURE 5.28: Kaon-proton radii as a function of $\langle dN_{ch}/d\eta \rangle^{1/3}$ obtained from a common fit to all pair combinations for Pb–Pb collisions at $\sqrt{s_{NN}} = 5.02$ TeV.

m_T of $0.61 \text{ GeV}/c$ are obtained from the rescaled m_T scaling plot to energy 5.02 TeV obtained based on measurements of Pb–Pb [77] (as described in Sec. 5.1.2). The proton’s femtoscopic source sizes, in turn, can be taken from the proton’s m_T -scaling presented in the previous section for $m_T = 1.18 \text{ GeV}/c$. The procedure is analogic to the one calculated in pion–deuteron and proton–deuterons studies. The expected and measured values are presented in form of Fig. 5.29 as kaon’s and proton’s studies were performed in different centrality intervals. The figure shows that the measurements of this works follow the expectations.

The values of f_0 reported in the literature [190, 195, 196, 198, 199, 200] were further used with source sizes measured in this study to calculate correlation functions using the Lednický-Lyuboshits and compared with measured correlation functions. The χ^2 of the theoretical functions for each of parametrization compared to experimental data for of all considered centralities is summarised in Tab. 5.10. All literature values can describe the data qualitatively well, but the experimental correlation functions favour those with the smallest imaginary part of the scattering length. An example of the comparison of the theoretical functions to experimental data in one of centrality is presented in Fig. 5.30.

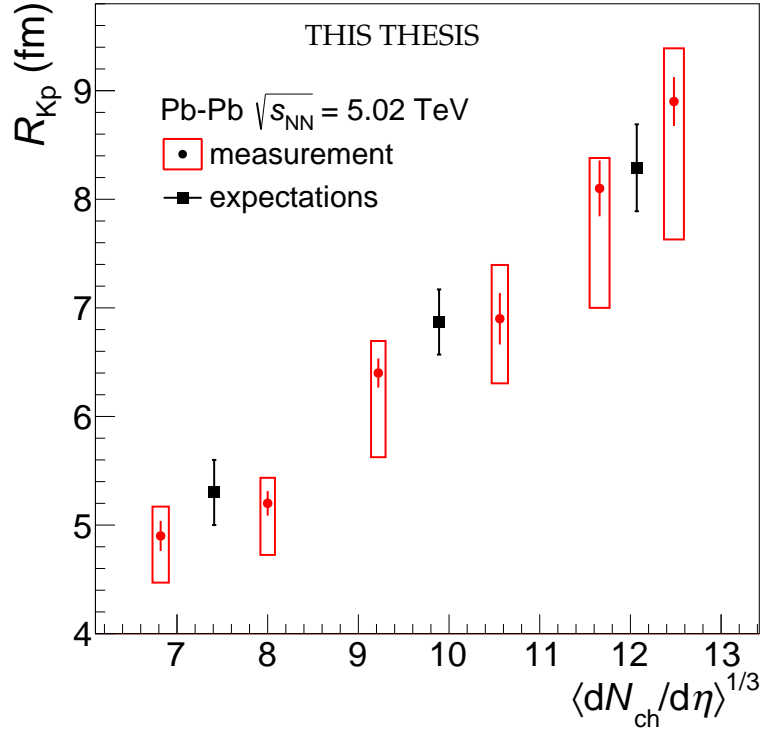


FIGURE 5.29: Comparison of kaon-proton femtosocpic radii from this analysis (red) with those obtained from single-particle expectation based on kaon and proton femtoscopy (black).

TABLE 5.10: Values of the χ^2/ndf for the deviation between the ALICE data and available model calculations and previous measurements for K^-p pairs at low relative momentum.

Model calculation:		χ^2/ndf
Lednický-Lyuboshits fit to data		1.4
Kyoto [201, 173]		2.8
Lednický-Lyuboshits with fixed parameters from:		
Hoshino et al. [196]		2.0
Martin [190]		3.3
Ikeda et al. [197, 198]		1.9
SIDDHARTA [197, 198]		2.3
Liu et al. [200]		1.9
Ito et al. [195]		4.2
Borasoy et al. [199]		1.6

The $K^-p \oplus K^+\bar{p}$ scattering length obtained from the fit are:

■ $\Re f_0 = -0.91 \pm 0.03(\text{stat})_{-0.03}^{+0.17}(\text{syst}) \text{ fm}$

■ $\Im f_0 = 0.92 \pm 0.05(\text{stat})_{-0.33}^{+0.12}(\text{syst}) \text{ fm}.$

These values are compared directly to literature's scattering length parameters in

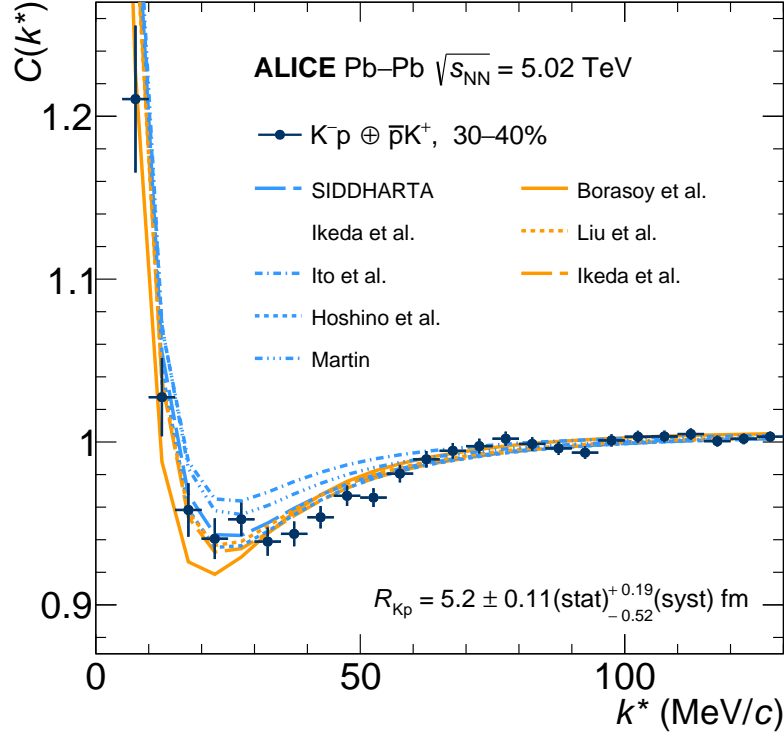


FIGURE 5.30: $K^- p \oplus K^+ \bar{p}$ experimental correlation function for 30–40% centrality interval together with Lednický-Lyuboshits calculations using f_0 from literature [190, 195, 196, 198, 199, 200].

Fig. 5.31. The result obtained in this analysis is larger in absolute value of both the imaginary and the real parts of the scattering length in comparison to literature's values. At the same time, the errors reported previously are in general $1\text{--}2\sigma$ off the current value. This study could be also repeated in higher statistics sample, e.g. in *Run – 3* in order to decrease the uncertainty of measured scattering parameters.

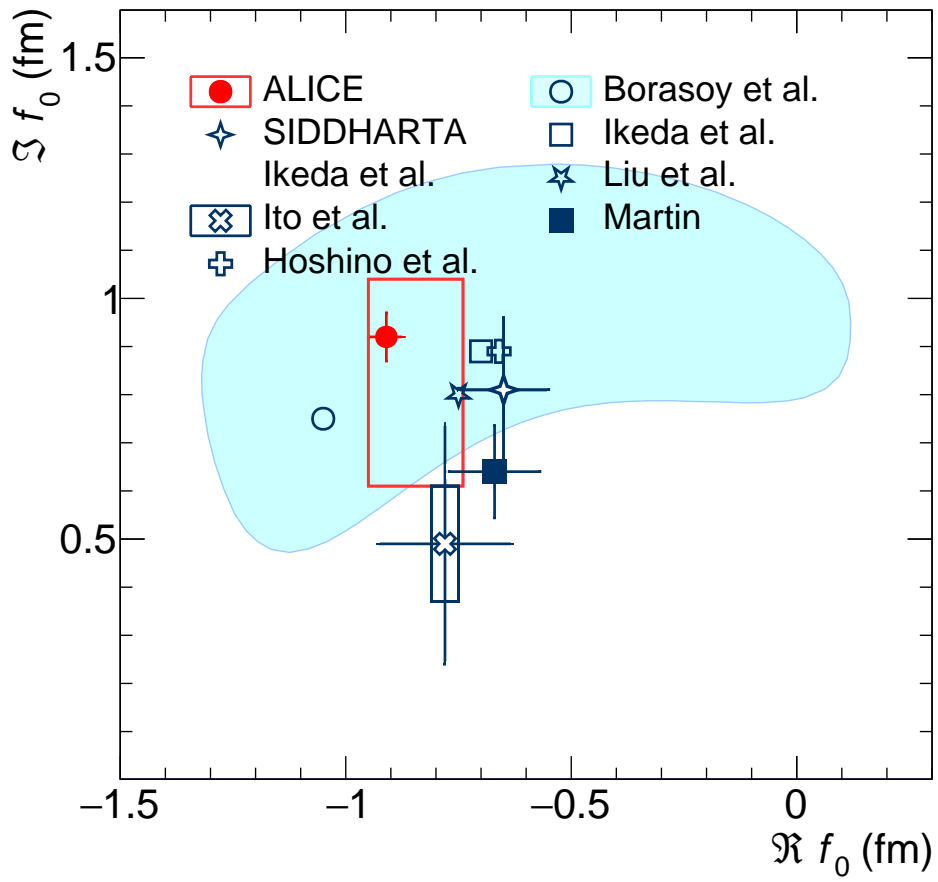


FIGURE 5.31: Scattering lengths of K^-p : Lednický-Lyuboshits fit obtained in this study (red), available world data and theoretical calculations (blue) [190, 195, 196, 198, 199, 200]. Statistical uncertainties are represented as bars and systematic uncertainties, if provided, as boxes.

5.4 Kaon–deuteron

Disclaimer

I hereby declare that the kaon–deuteron study presented below is the work that I performed within the ALICE collaboration. In this study I did the following:

- ☐ *quality assurance of the selection of charged kaons and (anti)deuterons,*
- ☐ *selection of the final analysis settings,*
- ☐ *calculation of the correlation functions,*
- ☐ *calculation and application of all the corrections on particle identification, primary fraction, non-Gaussianity of the source, momentum resolution and non-femtoscopic effects,*
- ☐ *calculation of set of the theoretical functions describing the kaon–deuteron interaction using Lednický-Lyuboshits model (based on code originally developed by Adam Kisiel),*
- ☐ *preparation of the code for fitting the kaon–deuteron system,*
- ☐ *performance of the fitting,*
- ☐ *calculation of the statistical and systematic uncertainties for data points, fit and measured parameters,*
- ☐ *preparation of all the check and final figures,*
- ☐ *presentation of the analysis at different stages of advancement within the collaboration including preliminary and paper proposal,*
- ☐ *writing the analysis note of the study for the collaboration,*
- ☐ *being the chair of the paper committee of the upcoming paper.*

Nevertheless, despite the fact that the analysis part of work has been performed by me, this work has been advised and checked by my supervisors and collaboration members in many internal meetings as well as by selected and experienced collaboration members that went through the details of the performed steps and results. Also, the study is based on data collected and prepared by other members of the collaboration and therefore the analysis would be not possible without other people responsible for technical aspects of the experiment e.g. those responsible for detector construction, maintenance, operation and calibration as well as those managing the computing resources and the cloud infrastructure. This study got already status preliminary in the ALICE collaboration and is currently under preparation for paper proposal.

5.4.1 Introduction and model description

The study of the K^-p interaction presented in the Sect. 5.3.1 is an important step towards a better understanding of the nature of the strangeness sector. However, while the K^-p interaction is significant on its own, its broader applications become evident when considering K^-d pairs. The interactions between kaons and both protons and deuterons provide valuable insights because the deuteron consists of a proton and a neutron. It is important to emphasize that experimental measurements of neutral particles are highly challenging due to their lack of charge. However, by examining these two systems, we can indirectly access properties of neutrons and in the same time derive a description of fundamental interactions in the strangeness sector. It is because the parametrization of the strong interaction between kaons and nucleons allows us to derive isospin-dependent scattering parameters ($I=0,1$) for K^-N . This is particularly important because the kaon is a boson associated with the spontaneous breaking of chiral $SU(3)$ symmetry in QCD and their relevance for the EOS in neutron star studies. The relationships between the kaon–proton, kaon–neutron, and kaon–deuteron scattering lengths, as well as the isospin scattering lengths (a_0, a_1) are determined by following formulas:

$$f_{0(K^-p)} = \frac{1}{2}[a_0 + a_1] \quad (5.5)$$

$$f_{0(K^-d)} = \frac{[m_N + m_K]}{[2m_N + m_K]}[a_0 + 3a_1] + C \quad (5.6)$$

$$f_{0(K^-n)} = a_1 \quad (5.7)$$

where m denotes the mass of the kaon or nucleon, C is a correction term of nuclear effects, $f_{0(K^-p/d/n)}$ denotes the scattering lengths of the K^-p , K^-d and K^-n pairs.

The scattering parameters of the kaon–proton and kaon–deuteron strong interactions were first identified by Dalitz et al. [204] as crucial in understanding the strangeness sector over 40 years ago. However, while we already have some experimental input for the kaon–proton using a variety of techniques, the situation is much worse for the kaon–deuteron, where no experimental measurements are available. Consequently, measuring the kaon–deuteron scattering parameters remains the most significant missing piece of experimental information in the study of low-energy antikaon-nucleon interactions. So far, scattering experiments have only provided data on kaon–deuteron scattering cross sections [205]. Kaonic atoms, on

the other hand, have very low X-ray yield of kaonic deuterium that is one order of magnitude less than in kaonic hydrogen which makes the measurement process very inefficient. Nevertheless, SIDDHARTA-2 has recently improved its technology considerably [206] and is currently collecting data specifically for the kaon–deuteron case. So far, we have several theoretical calculations with assumptions based on kaonic hydrogen measurements and effective field theories with different corrections. The most recent K^-d theoretical predictions of the scattering lengths that were used in this work are [200, 196, 207, 208, 209, 210]. These works mostly differ in input parameters, e.g. KEK or SIDDHARTA measurements of kaonic hydrogen, in treatment of the Λ state at threshold that is under debate (one-pole/two-pole), application of different corrections, e.g. recoil corrections.

The K^+d interaction is also highly non-trivial to study, as there are no published theoretical predictions available. Recently, the K^+d system was examined using the femtoscopy technique in pp collisions [175]. Although that study focused on revealing the three-body dynamics, it demonstrated that the system can be effectively described using a two-body dynamics and the Lednický-Lyuboshits approach, even for small sources. While no scattering length values were measured in that study, the experimental data showed very good agreement with values provided through private communication with Prof. Tetsuo Hyodo from TMU (Tokyo, Japan) and Prof. Johann Haidenbauer from IAS (Jülich, Germany). The calculation of K^+d provided by Prof. Hyodo used so-called fixed-center approximation approach [211], the one provided by Prof. Haidenbauer used the effective range formula fitted to the available elastic scattering cross-section data [212].

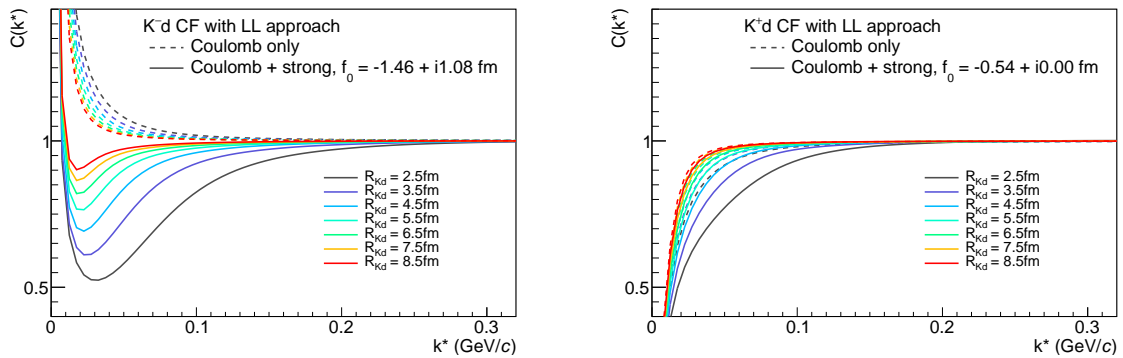
All the scattering parameter values used in this work are listed in Tab. 5.11. Since experimental values for these parameters are not yet available and theoretical knowledge about kaon–deuteron strong interactions is still limited, all scattering parameters presented here are theoretical. Notably, most theoretical predictions for the kaon–deuteron interaction focus on a significantly negative real part and a similarly significant positive imaginary part for the K^-d scattering length. For the K^+d interaction, the values are smaller and pertain only to the real part of the scattering length, as it is elastic only interaction. Therefore, the primary objective of the kaon–deuteron study in this thesis is to determine the scattering parameter values for K^+d and K^-d pairs using the femtoscopy technique.

The kaon–deuteron correlation functions can be modeled using the Lednický-Lyuboshits parametrization, which accounts for both Coulomb and strong interactions,

TABLE 5.11: Values of the scattering parameters for K^-d and K^+d pairs at low relative momentum.

Scattering parameters	$\Re f_0$ (fm)	$\Im f_0$ (fm)
K^-d		
Liu et al. [200]	−0.59	2.70
Hoshino et al. [196]	−1.42	1.62
Mizutini et al. [207]	−1.58	1.37
Revai (one-pole) [208]	−1.52	0.98
Revai (two-pole) [208]	−1.60	1.12
Shevehenko (one-pole) [209]	−1.51	1.23
Shevehenko (two-pole) [209]	−1.48	1.22
Doring et al. [210]	$-1.46 \pm 25\%$	$1.08 \pm 25\%$
K^+d		
Haidenbauer (priv. com.)	−0.54	−
Hyodo (priv. com.)	−0.47	−

assuming a Gaussian source and a zero effective range approximation ($d_0 = 0$). Example correlation functions for kaon–deuteron pairs with different femtoscopic source sizes and fixed scattering parameters are shown in Fig. 5.32. The presented correlation functions tend to reach unity before $k^* = 0.20$ GeV/ c . The functions are sensitive to changes in the source size. Additionally, the comparison between the Coulomb only and Coulomb plus strong interaction models highlights the significant impact of the strong interaction on the final correlation function. Moreover, these functions are similar in behaviour to those observed in the kaon–proton study.

FIGURE 5.32: Theoretical correlation functions with different input parameters calculated using Lednický-Lyuboshits (L-L) approach for K^-d (left) and K^+d (right) figure shows the effect of changing the femtoscopic source radii from 2.0 to 10.0 fm and its effect on the correlation function.

5.4.2 Results

The correlation functions of $K^+d \oplus K^- \bar{d}$ and $K^-d \oplus K^+ \bar{d}$ pairs for three centrality intervals 0–10%, 10–30%, 30–50% obtained from Pb–Pb collisions $\sqrt{s_{NN}} = 5.02$ TeV data collected by ALICE in 2018 are shown in Fig. 5.33. The statistical uncertainties are represented by vertical lines, while the systematic uncertainties are represented by gray squared boxes. The evaluation of all the uncertainties is described in Sec. 6.

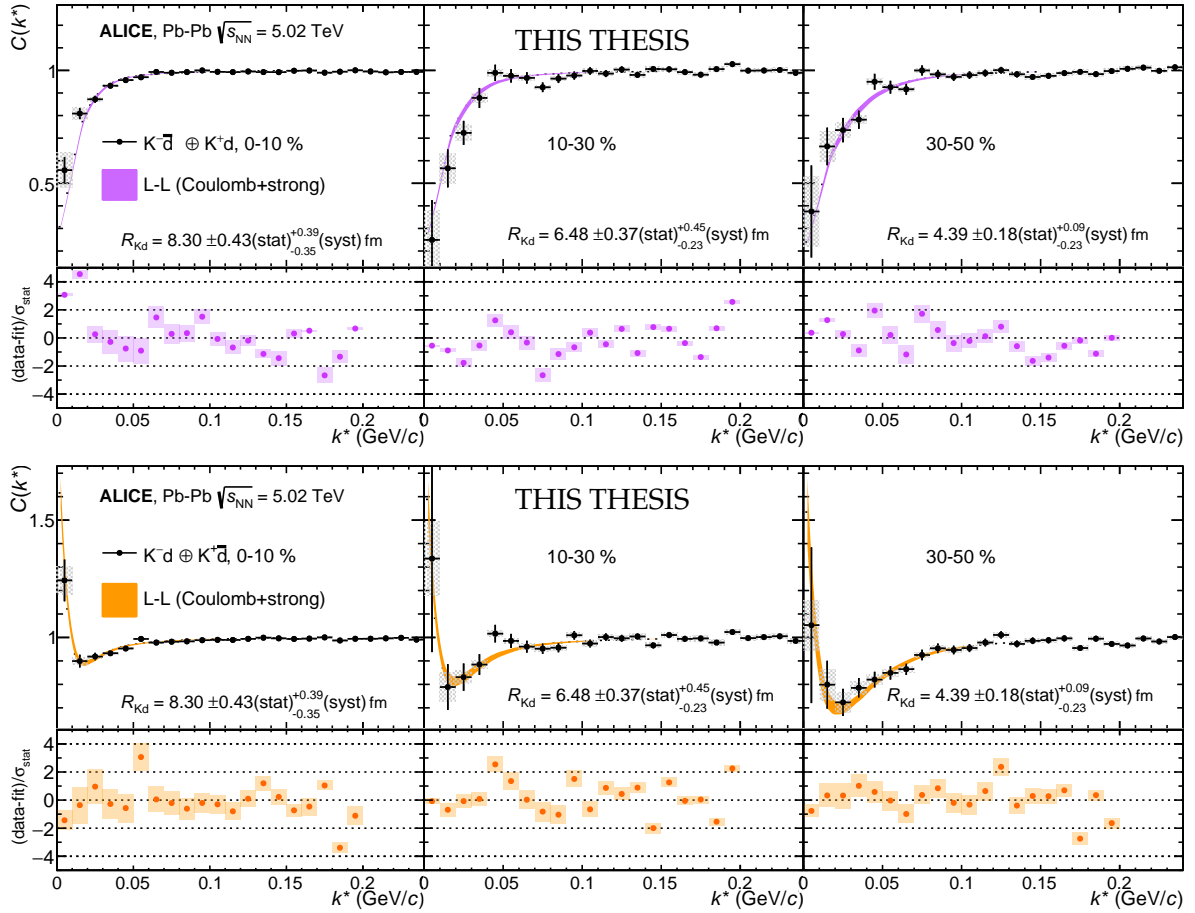


FIGURE 5.33: $K^+d \oplus K^- \bar{d}$ (top pads) and $K^-d \oplus K^+ \bar{d}$ correlation functions in the three centrality classes 0–10%, 10–30%, 30–50% represented with points. The light cyan band corresponds to Lednický-Lyuboshits fits (denoted as L-L).

The $K^+d \oplus K^- \bar{d}$ correlation function shows a clear repulsive nature (the functions are below unity). The $K^-d \oplus K^+ \bar{d}$ correlation functions show an attractive interaction with a repulsive part, seen as a dip below unity at $k^* \sim 20\text{--}50$ MeV/c. The behaviour is similar to measured before in kaon–proton study but here the effect is visibly stronger.

Also as in other function, the deviation from unity is larger for peripheral collisions hence smaller femtoscopic source sizes.

The fitting in the kaon–deuteron study is performed following the fitting procedure described in Sec. 4.4. A set of precalculated functions for particles with opposite charges for radii [3.0, 9.5] fm with a step of 0.5 fm, real part of K^-d f_0 [-2.5, 0.0] fm with a step of 0.1 fm, imaginary part K^-d f_0 [0.8, 2.0] fm with a step of 0.1 fm and real part of K^+d f_0 [-1.0, 0.0] fm with a step of 0.1 fm. The ranges of scattering parameters are chosen with a large margin around theoretically predicted interaction parameters and to provide the fitting procedure a wide space of functions and prevent getting solutions at the border of ranges of parameter. The final function is an interpolation between the closest solutions to the data selected based on minimum χ^2 . The fit is done for k^* up to 0.2 GeV/ c where the most of femtoscopic effects are expected. It is a simultaneous fit to 6 functions where same and opposite-sign particles share the same source size within centrality and one scattering parameter values for three centralities of same- or opposite-sign pairs.

The measured kaon–deuteron, R_{Kd} source size are summarised in the Tab. 5.12 and their dependence as a function of multiplicity density is presented in Fig. 5.34. The sources shows growing trend with growing number of particles created after the collision.

TABLE 5.12: Two-particle kaon–deuteron source sizes, R_{Kd} , together with uncertainties for 3 centrality from the fit to all pair combinations for Pb–Pb collisions at $\sqrt{s_{NN}} = 5.02$ TeV.

Centrality	R_{Kd} (fm)	stat. unc. \pm (fm)	syst. unc. + (fm)	syst. unc. – (fm)
0-10%	8.30	0.43	0.39	0.35
10-30%	6.48	0.37	0.45	0.23
30-50%	4.39	0.18	0.05	0.19

The scattering length for $K^-d \oplus K^+\bar{d}$ system obtained from the fit are:

■ $\Re f_0 = -1.44 \pm 0.15(\text{stat})_{-0.10}^{+0.10}(\text{syst})$ fm,

■ $\Im f_0 = 1.34 \pm 0.33(\text{stat})_{-0.15}^{+0.21}(\text{syst})$ fm,

and for $K^+d \oplus K^-\bar{d}$ system :

□ $\Re f_0 = -0.68 \pm 0.16(\text{stat})_{-0.09}^{+0.09}(\text{syst})$ fm.

The scattering parameters obtained in the fitting are compared to literature's values in Figs. 5.36, 5.35. The obtained result are in agreement in both the imaginary and the real parts of the scattering length with theoretical values. These measurements are the first experimental values of kaon–deuteron system obtained so far.

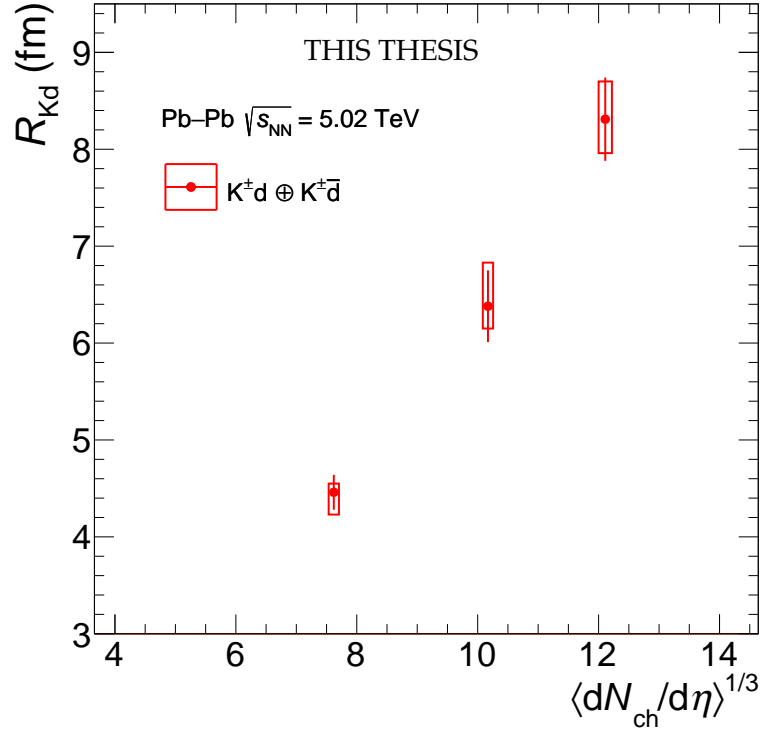


FIGURE 5.34: Kaon-deuteron radii as a function of $\langle dN_{ch}/d\eta \rangle^{1/3}$ obtained from a common fit to all pair combinations for Pb–Pb collisions at $\sqrt{s_{NN}} = 5.02$ TeV for kaon–deuteron pairs.

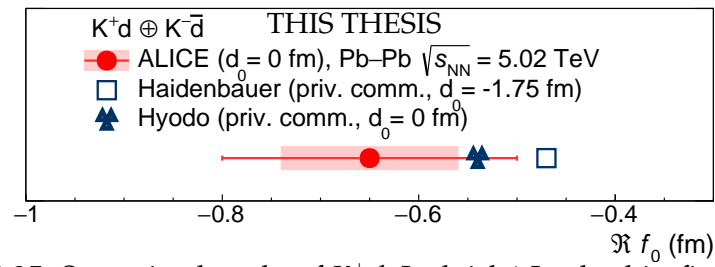


FIGURE 5.35: Scattering lengths of K^+d : Lednický-Lyuboshits fit obtained in this study (red), available world theoretical calculations (blue) provided by profs. Hyodo and Heidenbauer.

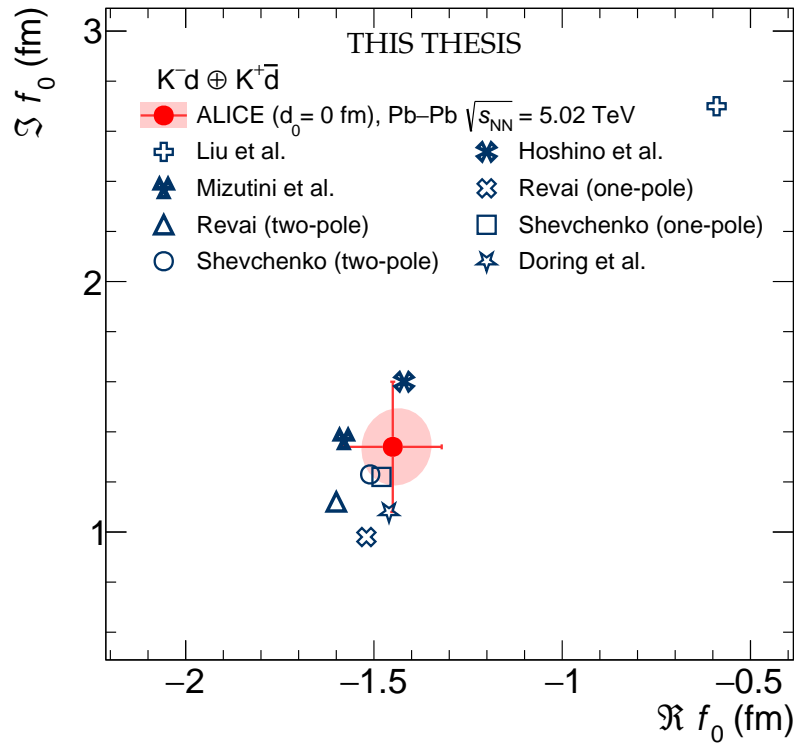


FIGURE 5.36: Scattering lengths of K^-d : Lednický-Lyuboshits fit obtained in this study (red), available world theoretical calculations (blue) [200, 196, 207, 208, 209, 210].

5.5 Non-identical sources and m_T scaling

The definition of m_T for the case of identical particles is well defined for single particle distributions as $m_T = \sqrt{\langle p_T \rangle^2 + m_0^2}$ or for identical pairs as $m_T = \sqrt{\langle k_T \rangle^2 + m_0^2}$, where m_0 is the rest mass, p_T and k_T are the transverse momentum of the single particle spectra and the average of the transverse momenta of the particles in the pair, respectively. In the case of non-identical particles, the pair m_T value in order to be comparable to single-particle analysis is not fully defined because there is no one and certain way to constrain the mass component of the m_T . For this purpose mainly two options are in use: reduced mass or averages.

Below three comparisons are presented that test different approaches of mass definition in non-identical systems for pairs studied in this thesis. The resulting $\langle k_T \rangle$ values contributing to $k^* < 0.15 \text{ GeV}/c$ values are summarized in Tab. 5.13. The measured non-identical sources are referred to R_{12} which corresponds to two-particles sources. Therefore, in the following plots the single particles sources of identical pairs were first rescaled by a factor $\sqrt{2}$ to two-particle size form of non-identical sources.

TABLE 5.13: The $\langle k_T \rangle$ values of pion–deuteron, proton–deuteron, kaon–proton, kaon–deuteron pairs of particles that contribute to the low k^* range.

Pair	$\langle k_T \rangle$ (GeV/c)
pion–deuteron	0.73
proton–deuteron	1.09
kaon–proton	0.60
kaon–deuteron	0.77

□ **Mass as a an average of the two masses.** $m_{av} = \frac{m_1 + m_2}{2}$

The non-identical sources measured in this thesis for m_T calculated as $m_T = \sqrt{\langle k_T \rangle^2 + (m_{av})^2}$ are presented in Fig. 5.37. This approximation work rather well for particles with small mass difference. In drastic case of pions and deuterons this approach completely fails. The advantage of this method is the fact that the average of identical particles is the same as in the original definition ($\frac{m_0 + m_0}{2} = m_0$).

□ **Mass as a reduced mass.** $\mu = \frac{m_1 m_2}{m_1 + m_2}$

The non-identical sources measured in this thesis for m_T calculated as $m_T = \sqrt{\langle k_T \rangle^2 + \mu^2}$ are presented in Fig. 5.38. The non-identical radii follow the scaling. However, this approach is inaccurate for identical pairs as their mass component would be 2 times smaller ($\frac{m_0 m_0}{m_0 + m_0} = \frac{1}{2} m_0$).

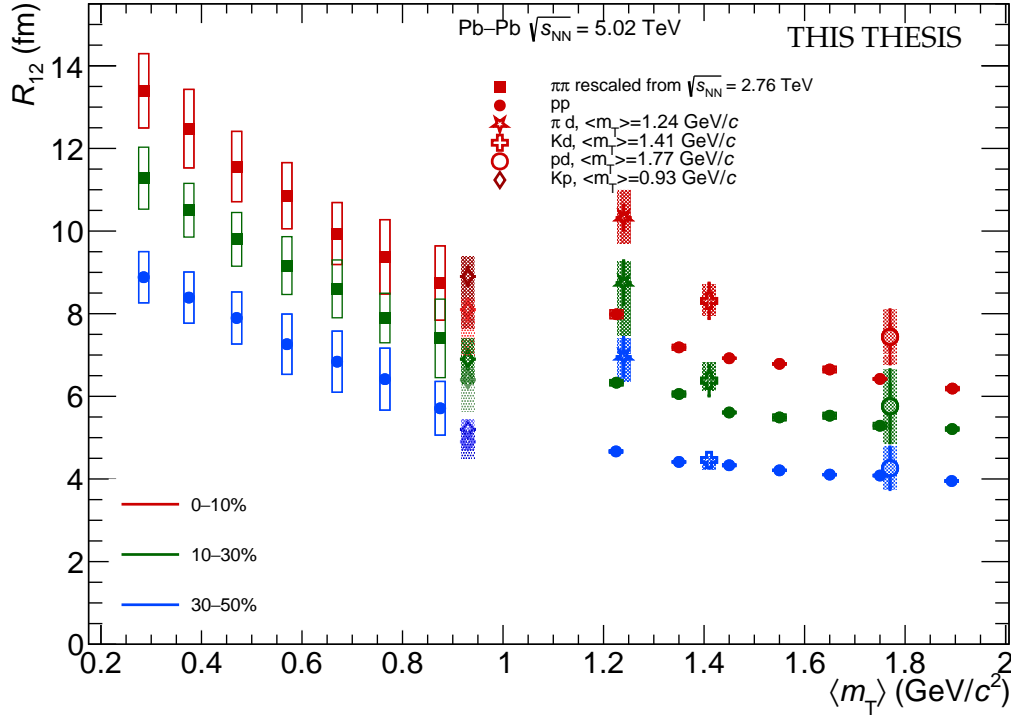


FIGURE 5.37: The two-particle femtoscopic source sizes of pions and protons measured in identical studies compared to measurements of non-identical pairs under the mass assumption $m_{av} = \frac{m_1 + m_2}{2}$ are the subject of this work.

□ **Mass as a two times reduced mass.** $2\mu = 2\frac{m_1 m_2}{m_1 + m_2}$

The non-identical sources measured in this thesis for m_T calculated as $m_T = \sqrt{\langle k_T \rangle^2 + (2\mu)^2}$ are presented in Fig. 5.39. The sources follow the scaling quite well even for pairs of large mass difference like pion-deuteron. Also the advantage of this definition is the fact that the mass of the identical particle pairs is the same as in the original definition ($2\frac{m_0 m_0}{m_0 + m_0} = m_0$).

The purpose of this section is to show that it is very non-trivial to place non-identical femtoscopic source sizes on identical particle pictures of the m_T scaling. Within one system, there is no problem of defining m_T , the issue comes when one needs to compare it to other particles/pairs. The simple average scaling is only approximately good for particles with similar masses. The reduced mass is not accurate for identical particles. The reduced mass multiplied by a factor of 2 seems to describe all cases the best, even if the mass difference is significant. Nevertheless, the two identical and non-identical sources should not be drawn together, since the effect of the mass definition is biasing the results.

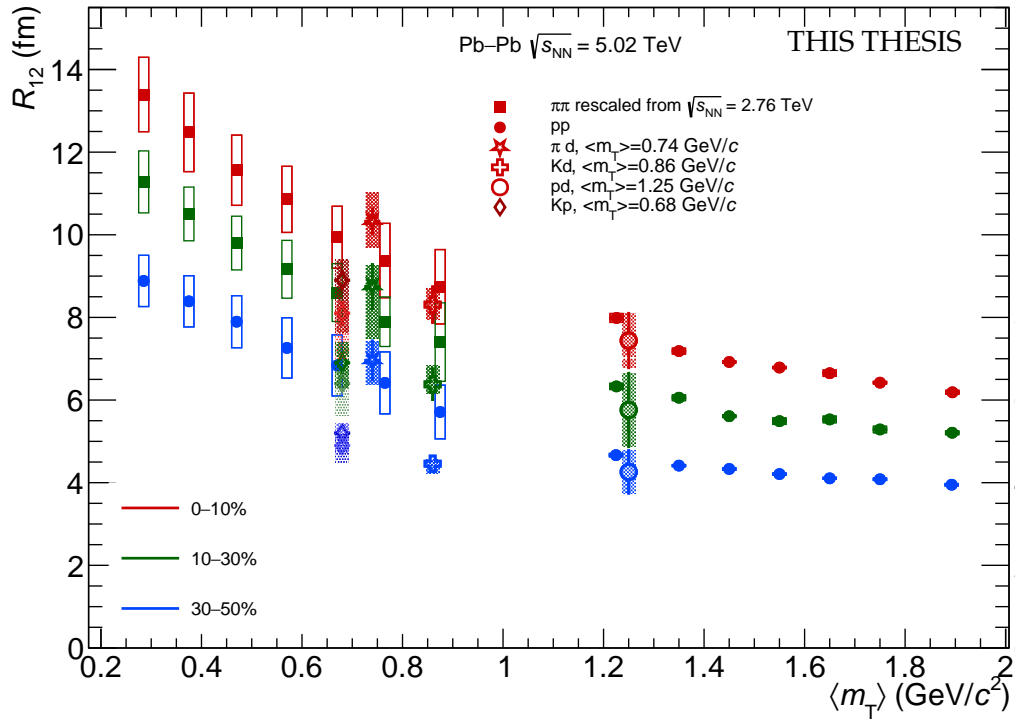


FIGURE 5.38: The two-particle femtoscopic source sizes of pions and protons measured in identical studies compared to measurements of non-identical pairs under the mass assumption $\mu = \frac{m_1 m_2}{m_1 + m_2}$ are the subject of this work.

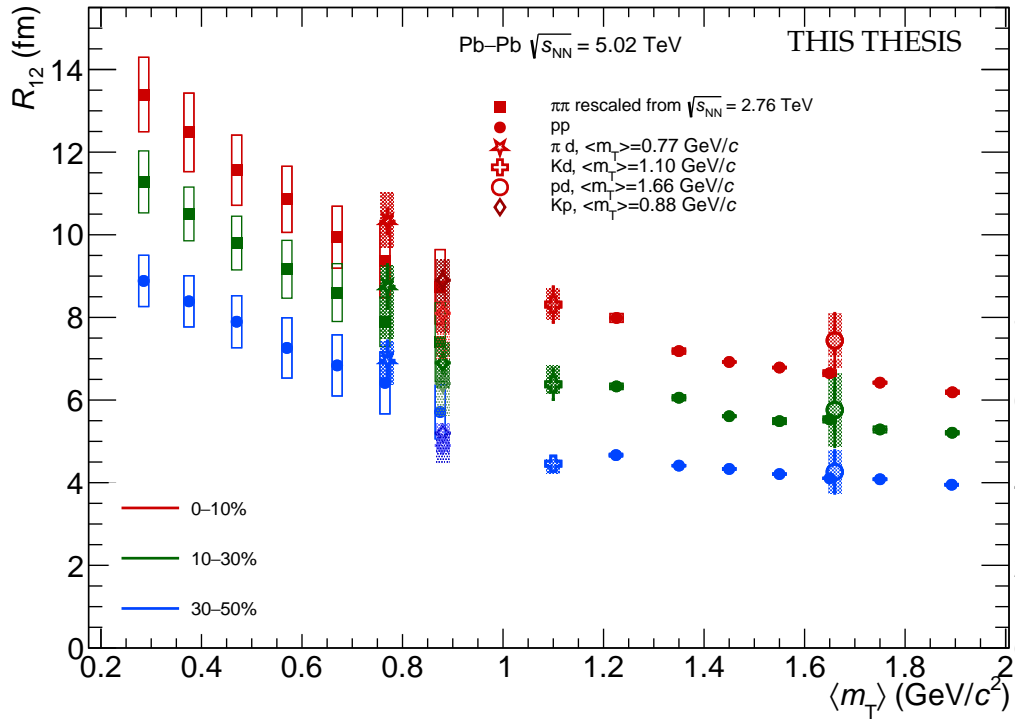


FIGURE 5.39: The two-particle femtoscopic source sizes of pions and protons measured in identical studies compared to measurements of non-identical pairs under the mass assumption $2\mu = 2\frac{m_1 m_2}{m_1 + m_2}$ are the subject of this work.

Chapter 6

Uncertainties

W obliczeniach był błąd.

Stanisław Lem, Eden ¹

Tylko przez morze głupstw dochodzi się do prawdy.

Stanisław Lem, Katar ²

This section describes the uncertainty calculations for all experimental results obtained in this thesis. The uncertainty estimation is based on advanced techniques and attempts to include any possible systematic bias that could influence the measurements. It is therefore important to emphasize that the studies, in particular the kaon–proton and the three deuteron studies, differ in the applied methodology as they were carried out in different time periods. However, despite the differences in the final approach, all these studies examine a very wide range of possible sources of uncertainty, such as those arising from the selection criteria of particles and events, the estimation of corrections, the statistical uncertainty, and the performance of the fit. These are described in the following subsections.

6.1 Particle and event selection uncertainties

The raw form of the experimental correlation functions is obtained using several default settings, which have already been described in Sec. 4. These settings have been chosen to balance efficient selection and sample purity. Nevertheless, many of them

¹"There was an error in the calculation." – Stanisław Lem, Eden

²"You can't reach the truth without crossing a sea of mistakes." – Stanisław Lem, Katar

are constrained by strict values. To assess the impact of changing these constraints on the final results, one default setting at a time is varied and the correlation function calculations are repeated. The new raw correlation functions are then used for comparison with the default one. Variations include: the depth of the mixing buffer; the minimum number of clusters in the TPC used in the track reconstruction; the maximum position of the primary vertex from the centre of the detector; the maximum η range; the maximum N_σ acceptance range; the maximum DCA in transverse (XY) and beam (Z) directions; the reconstruction algorithm based on information from selected detector(s); the settings of the maximum allowed distance between two tracks where the minimum fraction of the merging track is checked; the application of the pair quality cut. The summary of all variations considered in the four studies of this thesis is presented in Tab. 6.1.

TABLE 6.1: The systematic variations of the analysis settings considered in kaon–proton, pion–deuteron, proton–deuteron and kaon–deuteron studies.

	kaon–proton	pion–deuteron	proton–deuteron	kaon–deuteron
Setting name	Variation value			
Number of events to mix	5	5;15	5;15	5;15
Number of clusters	50	60;80	60;80	60;80
Primary vertex	7cm	8cm	8cm	8cm
η range	-	0.77;0.83	0.77;0.83	0.77;0.83
PID N_σ range	$2\sigma (K^+ / K^-)$ $3\sqrt{2}\sigma (p / \bar{p})$	$+0.5\sigma (\pi^+ / \pi^-)$ $+0.5\sigma (d / \bar{d})$	$+0.5\sigma (p / \bar{p})$ $+0.5\sigma (d / \bar{d})$	$+0.5\sigma (K^+ / K^-)$ $+0.5\sigma (d / \bar{d})$
DCA_{XY}	2.4cm	0.1cm	0.1cm	0.1cm
DCA_Z	$0.42+0.37\left(\frac{p_T}{\text{GeV}/c}\right)^{-0.066}$ cm	1cm	1cm	1cm
Track reconstruction using	ITS and TPC	ITS and TPC	ITS and TPC	ITS and TPC
Track merging cut (distance, fraction)	disabled	5cm, 2%	3cm, 1%	3cm, 1%
Pair quality cut	disabled	disabled	disabled	disabled

In the kaon–proton study, the particle and event selection criteria are used to perform a so-called Barlow check of the two correlation functions following the dependence (variation-default)/($\sigma_{\text{variation}} \pm \sigma_{\text{default}}$), where sign + or – corresponds to uncorrelated or correlated variations, respectively. An example of the Barlow check for K^+p pairs and some of variations of the settings are shown in Fig. 6.1. The distributions shows that all the variations considered give a deviation below 2σ and no systematic effects are observed. Therefore, they pass the Barlow criteria for a systematic contribution and none of them were included in the systematic of experimental points. However, the DCA and track reconstruction variations are

included in the systematic of the fit as described in the next subsection. The systematic uncertainty of the data-points in kaon–proton study has been estimated based only on variations of the predictions of non-femtoscopic effects defined as the maximum and minimum deviation of the correlation function.

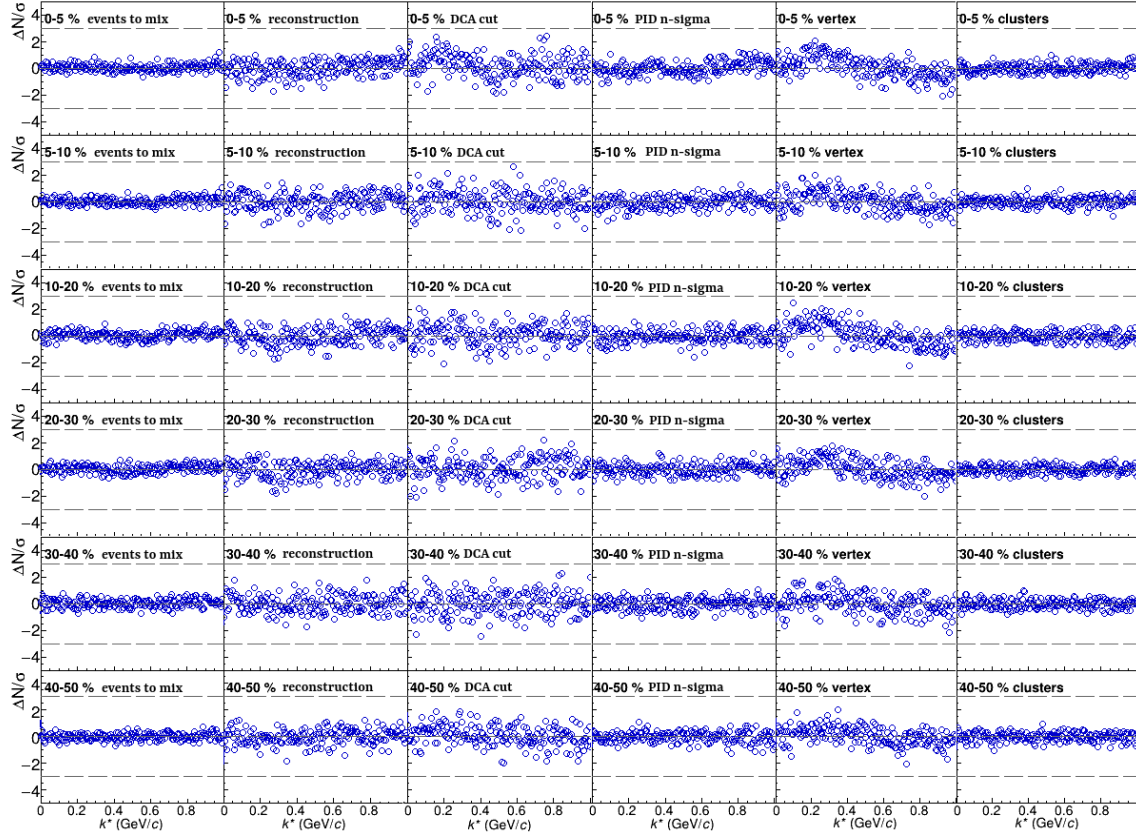


FIGURE 6.1: Barlow check for K^-p pairs. From top to bottom centralities from 0 – 5% to 40 – 50%. From left to right variations described in Tab. 6.1: 1st column – number of events used to mix in the uncorrelated distribution, 2nd column: reconstruction based on information from TPC only and TPC+ITS, 3rd column: DCA cut, 4th column: PID N_σ selection, 5th column: z-vertex position, 6th column: minimal number of clusters used in the reconstruction.

In the pion–deuteron, proton–deuteron and kaon–deuteron studies, the Barlow check has been also performed and, similar to the kaon–proton study, none of the variations could be assigned to the uncertainties. However, in the three deuteron studies the strategy is more conservative and effects of the analysis settings are included into the final calculations. For each experimental point, the maximum and minimum values are obtained through comparison of all variations of the correlation

function calculated by applying one change from Tab. 6.1. As the distribution of values in each bin shows a fairly uniform behavior, the uncertainty of each point is calculated as the maximum - minimum value divided by the standard deviation of a uniform distribution ($2\sqrt{3}$). The distributions of the systematic uncertainty from the analysis settings used in the three deuteron studies are shown in Figs. 6.2- 6.4. These figures are presented together with the exponential fit performed to smooth the uncertainties that is later applied to the data point.

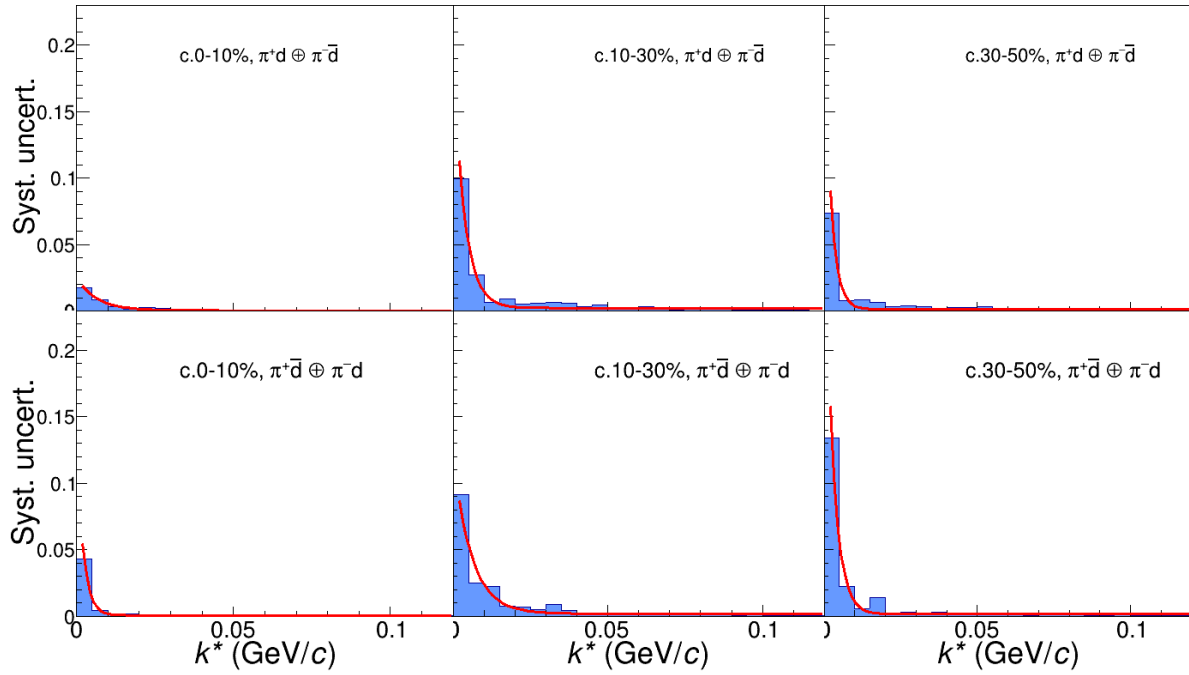


FIGURE 6.2: Distribution of relative error as a function of k^* together with $[0]+\exp([1]*k^*)$ fit obtained in pion–deuteron study. Top: pairs of the same charge sign, bottom: pairs of opposite charge signs. From left to right: 0-10%, 10-30%, 30-50%.

6.2 Systematic uncertainties of corrections and the fit

The systematic uncertainty of the corrections includes variations of the correction factor values and non-femtoscopic background estimation to account for their potential over- or underestimation. The fit uncertainty covers such effects as smearing of the theoretical function due to limited momentum resolution effects as well as the check of wider and narrower fit ranges. Additionally, the impact of the normalisation range of the correlation function is also checked. The kaon–proton study takes into

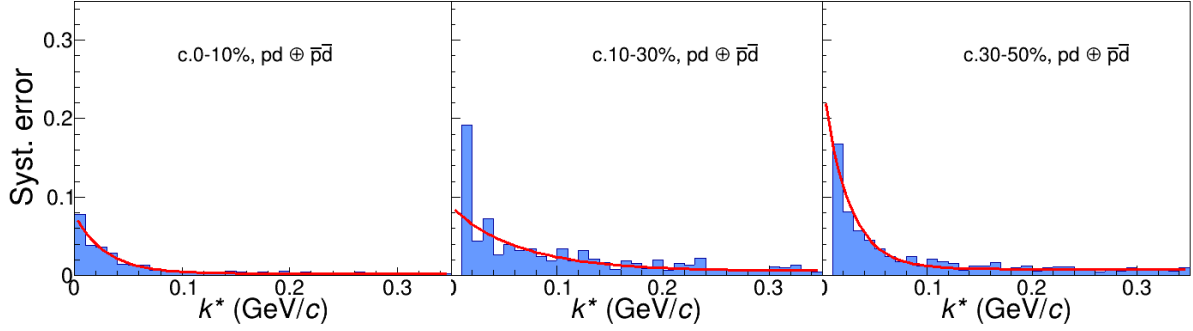


FIGURE 6.3: Distribution of relative error as a function of k^* together with $[0]+\exp([1]*k^*)$ fit obtained in proton–deuteron study. From left to right: 0-10%, 10-30%, 30-50%.

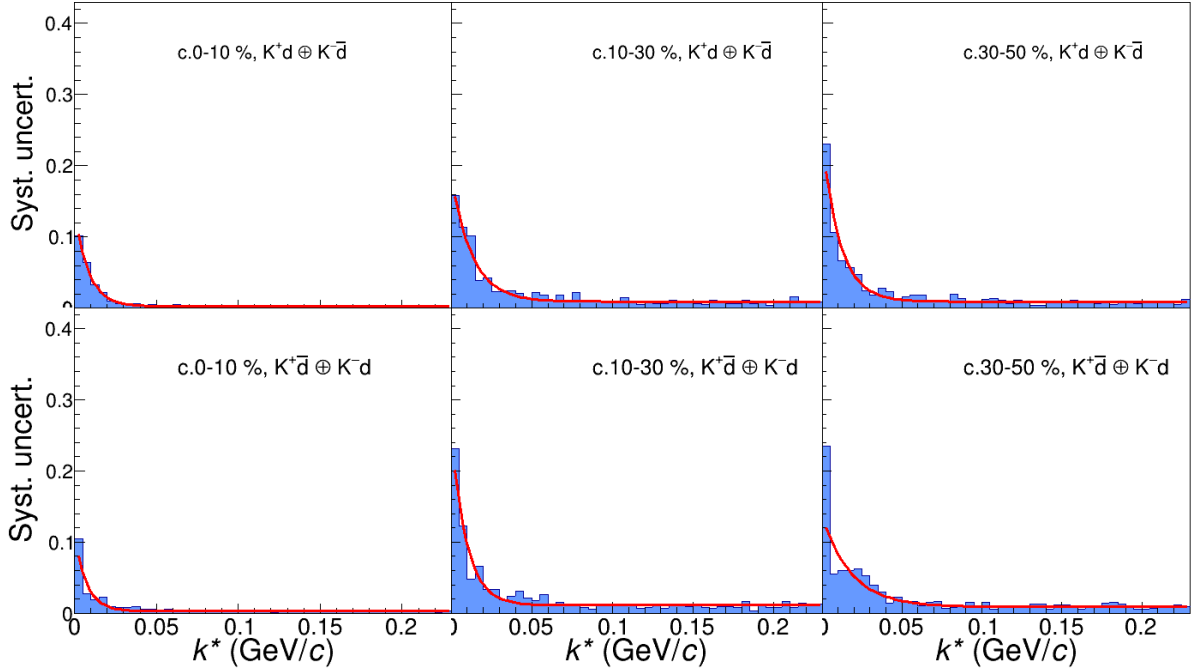


FIGURE 6.4: Distribution of relative error as a function of k^* together with $[0]+\exp([1]*k^*)$ fit obtained in kaon–deuteron study. Top: pairs of the same charge sign, bottom: pairs of opposite charge signs. From left to right: 0-10%, 10-30%, 30-50%.

account in addition the simultaneous and separate fitting with the second sample of data that cover higher momentum kaons ($p_T = (0.5 - 1.5)$ GeV/c). Such second kaon sample corresponds to different $\langle p_T \rangle$ and therefore different source sizes. However, the nature of the strong interaction should persist the same. That is why, in the simultaneous fit it is included in the search for the best scattering parameters values without sharing the source sizes. Similarly, in a separate fit, only the scattering

parameter values are included into the comparison. The summary of all the variations considered in the four studies is presented in Tab. 6.2. In the table the squared parenthesis corresponds to the selection of all possible values from the indicated range with step equal its precision.

TABLE 6.2: The systematic variations of the analysis corrections, background estimation and fit settings used in kaon–proton, pion–deuteron, proton–deuteron and kaon–deuteron studies.

	kaon–proton	pion–deuteron	proton–deuteron	kaon–deuteron
Setting name	Variation value			
Pair-purity value	-3%;3%	[-5%;5%]	[-5%;5%]	[-5%;5%]
Smearing	Gaussian Resolutions Matrix	Gaussian	Gaussian	Gaussian
Normalisation range		0.1-0.3 GeV/c		
Fit range	0.005-0.16 GeV/c 0.0-0.175 GeV/c 0.0-0.20 GeV/c	0.0-0.1 GeV/c 0.0-0.12 GeV/c 0.0-0.15 GeV/c	0.0-0.15 GeV/c 0.0-0.25 GeV/c	0.0-0.15 GeV/c 0.0-0.20 GeV/c 0.0-0.25 GeV/c
Non-femtoscopic background	As summarised in Tab. 4.4			
Different sample	yes	-	-	-

In the kaon–proton study, the fit is repeated after applying one variation at a time. Also fitting of correlation functions of the variations on DCA and track reconstruction are included. Next, the uncertainty is constrained as a maximum and minimum deviation from the default solution. In the three deuteron studies, all possible combinations of the settings from the Tab. 6.2 are checked applying one or more changes at a time and the uncertainty is obtained as one standard deviation of the distribution of obtained values. In the case of the kaon–deuteron study, the uncertainty of the scattering parameters of the K^-d scattering length used for plotting are additionally calculated by the ellipse of the uncertainty, which indicates the 1 sigma range of the 2D distribution. An example, of the kaon–proton and kaon–deuteron uncertainties is shown in Tab. 6.3 and Fig. 6.5, respectively. All the values of uncertainties are given next to the measured values in results sections of the corresponding analyses.

Systematic uncertainties of (anti)deuterons from pion and proton calculations

As shown in Fig. 5.6, the prediction of the pion source itself has some uncertainty, the main component of which is the uncertainty of previous pion measurements, which may have an impact on the deuteron prediction in this study. In order to estimate the systematic uncertainty of the (anti)deuteron femtoscopic sizes originating from the pion m_T scaling plot, the bootstrap is done, but this time resampling only the

TABLE 6.3: Radii (fm), real and imaginary part of the scattering parameter for kaon–proton analysis obtained for different variations of the fit. The colours indicate the lowest blue and the highest red values.

R c(%)	Default	gauss+lapl smearing	bkg 1 variation	bkg 2 variation	Purity -0.03	Purity +0.03	fit range wider	fit range narrower	DCA_Z strict cut	FB96&128 comb.	low&high K comb.	kaons 0.5-1.5
0-5	8.88	7.63	9.23	9.18	8.61	9.39	9.31	8.61	8.21	8.97	7.91	
5-10	8.09	7.00	8.13	8.33	7.77	8.39	8.26	7.87	7.59	8.15	7.47	
10-20	6.89	6.30	6.90	7.19	6.72	7.39	6.84	6.31	6.61	6.86	6.33	
20-30	6.43	5.73	6.44	6.64	6.24	6.66	6.37	6.42	6.06	6.29	5.57	
30-40	5.24	4.72	5.25	5.27	5.08	5.43	5.23	5.22	5.21	5.22	4.98	
40-50	4.95	4.47	4.96	5.10	4.82	5.17	4.92	4.94	4.59	4.64	4.76	
re	-0.91	-0.74	-0.94	-0.86	-0.91	-0.94	-0.93	-0.88	-0.90	-0.90	-0.77	-0.74
im	0.92	0.68	0.93	1.05	0.88	1.03	0.92	0.93	0.88	0.89	0.84	0.60

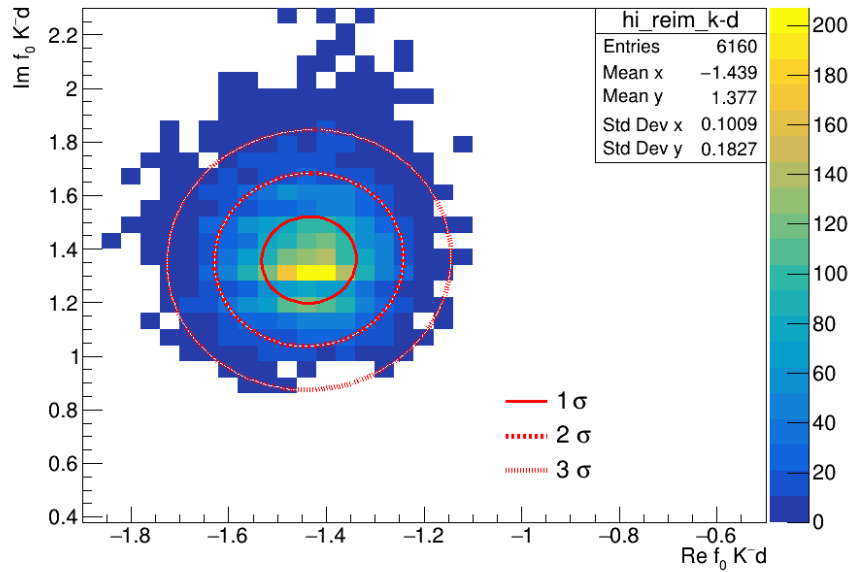


FIGURE 6.5: Distribution of fit results of the K^-d scattering length obtained for variations listed in Tab. 6.2 as described in the text.

pion sizes in the final fit. This is done in a way that the pion size is not fixed to a certain value, but is randomly set each time following a Gaussian distribution, where the mean of the Gaussian for resampling is the value of the extrapolated pion radii, the sigma value is the uncertainty of the pion prediction. Similarly, the the same is done for the proton–deuterons study but there the uncertainty from protons m_T scaling is much smaller as the proton femtoscopic radii are measured with lower systematic uncertainties. Therefore, it is not calculated separately but is included in the systematic variations of the fit.

6.3 Statistical uncertainties of the fit

The statistical uncertainties of the measured radii and scattering length parameters have been calculated based on the statistical bootstrap method. The experimental correlation function is re-sampled in a way where each of the points acquired a new value based on the default experimental observation and its statistical error which is considered to follow the normal distribution. The re-sampled correlation function is then re-fitted and new parameters are obtained. The procedure has been repeated 1500 times so the measured values form a distribution for a given parameter. The statistical uncertainty of the measured parameter is then the standard deviation of the fitted Gaussian distribution. An example of such distribution for measurement of $R_{\pi d}$ is presented in Fig. 6.6. All the values of uncertainties are given next to the measured values in results sections of corresponding analyses.

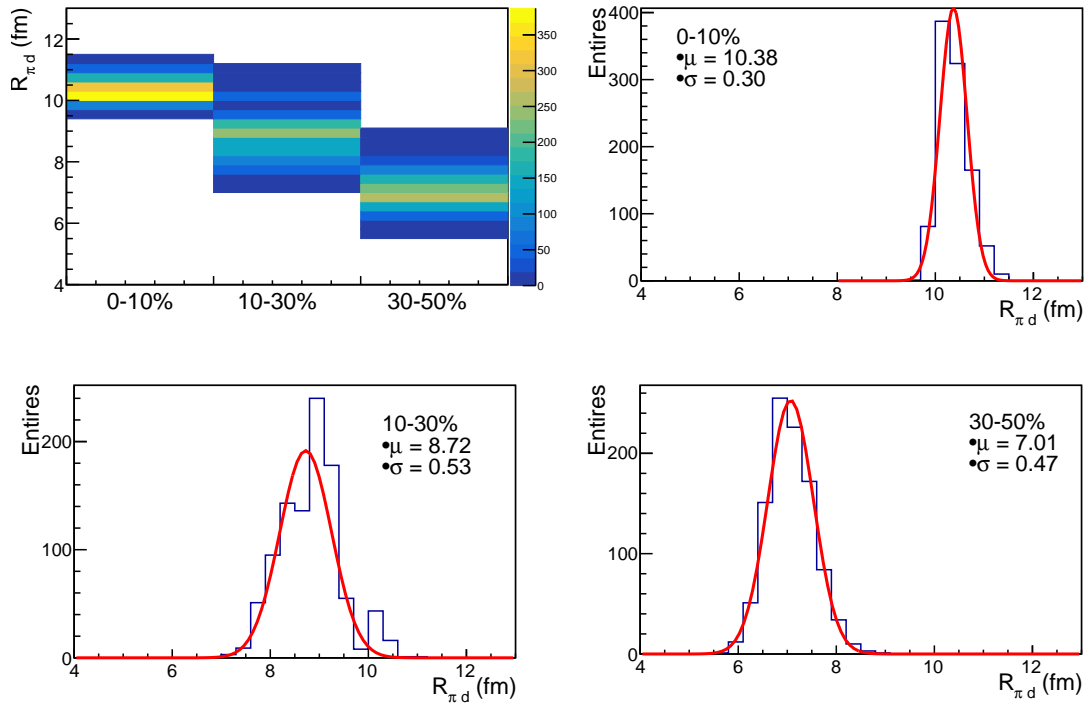


FIGURE 6.6: Distribution of fit results for 1500 bootstrapped pion-deuteron correlation function sets for the pion-deuteron radii obtained from fits as a function of event centrality and separately each centrality.

Chapter 7

Summary

*Wiedza jest nieodwracalna,
nie może cofnąć się w mrok słodkiej ignorancji.*
Stanisław Lem, Głos Pana ¹

This thesis presents femtoscopic analyses of pion–deuteron, proton–deuteron, kaon–proton, and kaon–deuteron pairs. The four studies are based on data from relativistic heavy-ion collisions at $\sqrt{s_{\text{NN}}} = 5.02$ TeV collected by the ALICE experiment at the LHC in the *Run – 2* period of data-taking. The studies have the following main objectives: to determine the scattering parameters of the KN strong interaction, which is challenging to probe experimentally; to improve our understanding of the formation of light ions, such as deuterons, in collisions involving the QGP state, which is a puzzle in heavy-ion research; to improve our understanding of particle interactions in heavy-ion collisions where the femtoscopic source sizes are relatively large, focusing on our ability to describe the interaction, the dynamics of many-body systems, and the effects of coupled channels.

The investigations encompass the measurement of momentum correlations between various particle species, as well as the study of experimental effects that could impact the results, such as those expressed by corrections or non-femtoscopic correlations. As the studies cover particles that were not widely investigated with femtoscopic technique before and many input values and assumptions were derived specifically for this work, e.g., studies on non-Gaussianity, the behavior of ultra-soft pions, and simulations of the elliptic flow effect involving deuterons. The performed calculations are compared with several theoretical descriptions that incorporate different techniques for determining the interactions between particles. Many of the

¹"Knowledge is irreversible, you cannot go back into the darkness of sweet ignorance." – Stanisław Lem, His Master's voice

studies included in this thesis, particularly those involving deuterons, are still not well understood theoretically. Therefore, to provide a robust theoretical descriptions presented in this thesis, the development of new tools and the use of resources created for very recent femtoscopic studies were required. This has been achieved through collaboration with numerous theorists and research groups from around the world.

The first part of this thesis concerns the correlation studies of pion–deuteron pairs performed in three centrality intervals: 0–10%, 10–30%, and 30–50% of Pb–Pb collisions. This study, which had never been investigated using the femtoscopia techniques before, is a feasibility research project to determine if we can efficiently study pairs of particles with a large mass difference and if our understanding of pion–deuteron interaction is sufficient to describe the measured data. In particular, the main motivation for this study was to determine if we can access the properties of the source of rare particle species through non-identical particle femtoscopia studies by pairing them with particles that appear abundantly after collisions.

The study demonstrates the feasibility of investigating interactions in pion–deuteron systems by examining the momentum correlation between pion and deuteron pairs. Specifically, the pion–deuteron correlation functions were analyzed in heavy-ion collisions, where the femtoscopic source sizes are relatively large. The measured pion–deuteron correlation functions exhibit a repulsive interaction for same-charge pairs and an attractive interaction for opposite-charge pairs. The functions are primarily dominated by the Coulomb force, with minimal sensitivity to the strong interaction. The Coulomb and Coulomb plus strong interactions modelled using Lednický-Lyuboshits formalism describe the measured data with very good agreement. The measured femtoscopic source sizes for pion–deuteron pairs being a subject of this study range from ~ 7 fm in 30 – 50% collisions to ~ 10.5 fm in 0 – 10% collisions.

Additionally, by employing previous measurements of pion sources in heavy-ion collisions, the study accessed the size properties of the deuteron source. The measured deuteron source size range from ~ 2.5 fm in 30 – 50% collisions to ~ 3.5 fm in 0 – 10% collisions. This represents the first measurement of the deuteron source properties in relativistic heavy-ion data, where the QGP state is present. It is important to emphasize that such an analysis would not be possible with deuteron–deuteron pairs due to insufficient statistics, and the performed analysis does not introduce any bias in the model description of deuteron production. These values are in very

good agreement with the m_T scaling dependence of hadrons in heavy-ion collisions, showing that for high m_T , the m_T scaling remains valid. This indicates that composite objects such as deuterons may obey the same rules of collective expansion and temperature of emission as other particles.

The study shows that it is possible to build statistically significant correlation functions of pion–deuteron pairs using *Run* – 2 data. However, it would be highly beneficial to repeat this study in *Run* – 3 with larger statistics and improved measurements of pion source sizes to obtain more precise measurements of deuteron source sizes. Additionally, it would be very interesting to extend the study in *Run* – 3 on measurements of the asymmetry in emission time and space between very light pions and heavy deuterons. This could provide further insights into scenarios of deuteron production.

The second part of this thesis focuses on the correlation studies of proton–deuteron pairs performed in three centrality intervals: 0–10%, 10–30%, and 30–50% of Pb–Pb collisions. While this study has previously been conducted using femtoscopy techniques in pp collisions [175], the environment and nature of interactions in pp collisions differ significantly from those in relativistic heavy-ion data. Therefore, this research aimed to study the dynamics of the proton–deuteron system in larger sources, assess the feasibility of determining deuteron properties through very precise measurements of proton–proton pairs that are relatively close in m_T space.

The recent proton–deuteron study in pp collisions has shown that the three-body interactions and higher-order partial waves play a significant role in determination of the correlation function in small collision systems. However, since this study focuses on heavy-ion data, the situation can differ because the emitted particles can originate from relatively large sources, greater than the nucleon separation in conventional nuclei, unlike in pp collisions. Therefore, this analysis investigates interactions in proton–deuteron systems using two- and three-body descriptions of the underlying dynamic.

The measured same-charge proton–deuteron pairs exhibited a repulsive interaction across the entire range of relative momentum space. Their interaction was described using three approaches:

- Two-body approach based on the Lednický-Lyuboshits formalism: This method describe the Coulomb and strong interactions for different sets of scattering parameters provided by the literature. Although such approach has been questioned for small

source sizes due to unrealistic peaks in small k^* not observed in any data, in the source sizes typical of heavy-ion data, the peak was not observed, and the data aligned well with expectations.

- Two-body approach based on the Schrödinger solution: This method also incorporates the Coulomb and strong interactions but additionally considers higher-order partial waves in the calculations. The calculations have been derived addressing concerns that approximations of asymptotic behavior used in Lednický-Lyuboshits approach may not be valid for small sizes. This approach is still under development but already it is able to describe data qualitatively well, with no significant differences observed between the two two-body approaches in the source sizes present in this thesis.

- Three-body approach: In addition to Coulomb plus strong interactions and higher order partial waves this method includes effects such as the antisymmetrization of interactions between two protons. The method is based on solution of the Schrödinger equation. Similarly to other two approaches also this one describe the experimental data well.

One of the main conclusions from the proton–deuteron study performed in heavy-ion data is that in large source sizes, three-body effects do not play a significant role, as both two- and three-body approaches can describe the data with comparable precision. This study represents the first experimental confirmation of such an effect.

Another crucial result from this study is the measurement of proton–deuteron and deuteron femtoscopic source sizes using proton–deuteron correlation functions and recently measured very precise proton m_T -scaling in the energy and collision system of this thesis. The measured proton–deuteron values reach ~ 4.5 fm in 30 – 50% collisions to ~ 7.0 fm in 0 – 10% collisions. The measured deuteron values reach ~ 2.5 fm in 30 – 50% collisions to ~ 4.5 fm in 0 – 10% collisions and follow the source scaling of protons within uncertainties. This study marks the first measurement of deuteron source sizes based on precise measurements of baryons in Pb–Pb collisions. The deuteron’s sizes of femtoscopic radii follow those of single nucleons. It shows that composite objects share the same flow field as single nucleons.

This study demonstrates that we can accurately determine the deuteron source size with a robust description of the correlation function. Similar to the pion–deuteron study, it would be highly beneficial to repeat this analysis in *Run – 3* with increased statistical precision. Also, extending the study to measure the asymmetry in emission time and space between protons and deuterons could significantly enhance our

understanding of deuteron production scenarios.

The third part of this thesis focuses on the correlation studies of kaon–proton pairs conducted in six centrality intervals: 0–5%, 5–10%, 10–20%, 20–30%, 30–40%, and 40–50% of Pb–Pb collisions. The femtoscopy techniques have been previously applied to study the kaon–proton correlations in pp collisions [182]. However, similarly to the proton–deuteron case the environment and dynamic in small collision systems are expected to differ significantly from those in relativistic heavy-ion data. Therefore the coupled channels observed in pp collisions, highlighted a key objective of this thesis to investigate the behavior of the kaon–proton system within large sources. Another crucial aim of kaon–proton pairs is to explore the properties of the strong interaction between the lightest strange meson and nucleons using femtoscopy and is a preliminary step towards the investigation of the more challenging kaon–deuteron system.

The measured same-charge kaon–proton pairs exhibited a repulsive interaction across the entire range of relative momentum space. The same-charge particle pairs were described with Coulomb plus strong interaction using Lednický-Lyuboshitz formalism that incorporated the precise measurements of the scattering length [202]. The opposite-charge pairs exhibited an attractive interaction with a repulsive part. As theoretically expected, no evidence was found for the opening of coupled channel which is characterised by cusp structures in the opposite-charge particles. This type of correlations were determined using the Coulomb plus strong interaction and two approaches, namely the Lednický-Lyuboshitz and Kyoto models. All the theoretical descriptions show a very good agreement with the measured data in all centrality intervals.

The study provides parameters describing six femtoscopic kaon–proton source sizes and the scattering parameters of the K^-p strong interaction. The measured kaon–proton femtoscopic sizes are in agreement to expectations from other measurements of the m_T scaling dependence, with values that reaches ~ 5.0 fm in 40 – 50% collisions to ~ 8.5 fm in 0 – 5% collisions. The measured scattering length of the K^-p strong interaction equals $\Re f_0 = -0.91 \pm 0.03(\text{stat})_{-0.03}^{+0.17}(\text{syst})$ fm, $\Im f_0 = 0.92 \pm 0.05(\text{stat})_{-0.33}^{+0.12}(\text{syst})$ fm. The values of the measured scattering parameters are consistent with other measurements and theoretical expectations. It is the first measurement of this scattering parameters using femtoscopy technique.

This study demonstrates the negligible effects of coupled channels in big

femtoscopic source sizes. Subsequently, further femtoscopic analysis of kaon–proton pairs was conducted in peripheral collisions to precisely examine the moment when coupled channels effects vanish experimentally [203].

The fourth part of this thesis concerns the correlation studies of kaon–deuteron pairs performed in three centrality intervals: 0–10%, 10–30%, and 30–50% of Pb–Pb collisions. This pair has previously been investigated using the femtoscopy technique in pp collisions [175], but only with same-sign charge pairs and mostly in the context of investigating three-body interactions. The goal of this study is to provide the first-ever measurements of the scattering parameters of the strong interaction for both K^-d and K^+d pairs, which have not been accessible in any prior experiments.

The measured same-charge kaon–deuteron pairs exhibited a repulsive interaction across the entire range of relative momentum space. Conversely, opposite-charge pairs exhibited an attractive interaction with a repulsive component similar to the one observed in kaon–proton system. These two types of correlations have been investigated using the Lednický-Lyuboshits formalism incorporating Coulomb plus strong interaction. The model description faces no issues to describe the measured data in all centrality intervals.

The three femtoscopic kaon–deuteron source sizes that cover values from ~ 5.0 fm in 30 – 50% collisions to ~ 8.5 fm in 0 – 10% collisions. Simultaneously, this analysis derives first ever experimental measurements of the K^-d and K^+d scattering lengths of the strong interaction. The K^-d scattering length has been established on $\Re f_0 = -1.44 \pm 0.15(\text{stat})^{+0.10}_{-0.10}(\text{syst})$, $\Im f_0 = 1.34 \pm 0.33(\text{stat})^{+0.21}_{-0.15}(\text{syst})$. The K^+d scattering length has been established on $\Re f_0 = -0.68 \pm 0.16(\text{stat})^{+0.09}_{-0.09}(\text{syst})$. The obtained values of scattering parameters are consistent with most of theoretical expectations.

The two scattering parameters measured in this thesis, K^-d and K^-p , are the key insights to future determination of the K^-n scattering parameters that is not accessible with present experimental techniques.

In conclusion, the work presented in this thesis marks the first milestones in the femtoscopic studies with deuterons in heavy-ion collisions providing their first measurements of interaction, source properties and dynamic of the system. The thesis provides several new techniques of describing the correlation function that can be used further in more precise data as those of *Run – 3*, e.g. theoretical approaches of calculating correlation functions or assessing the source parameters

of the non-identical system. Also this thesis provides first measurements of the interaction scattering parameters of the lightest strange meson and single and bound nucleons using the femtoscopic technique and verifies experimentally the sensitivity on various effects in heavy-ion data such as coupled channels or the three-body dynamics.

The author has contributed to the following publications and proceedings during the Ph.D.:

- ALICE Collaboration (2021) "Kaon–proton strong interaction at low relative momentum via femtoscopy in Pb–Pb collisions at the LHC", published in Physics Letters B, vol. 822
- W. Rzesza, G. Kornakov, A. R. Kisiel, Yu. M. Sinyukov, and V. M. Shapoval (2024) "Femtoscopy analysis of ultra-soft pion trap at LHC energies", Published in Physics Review C, vol. 110
- W. Rzesza, M. Stefaniak, S. Pratt (2025) "Theoretical description of proton-deuteron interactions using exact two-body dynamics of the femtoscopic correlation method" Published in Physics Review C, vol. 111
- proceedings: Wioleta Rzesza on behalf of ALICE Collaboration (2020) "Kaon–proton femtoscopy in Pb–Pb collisions with ALICE at the LHC", published in Photonics Applications in Astronomy, Communications, Industry, and High Energy Physics Experiments, vol.11581
- proceedings: Wioleta Rzesza on behalf of ALICE Collaboration (2023) "A study of K^-d and K^+d interactions via femtoscopy technique", published in IL NUOVO CIMENTO 47 C vol. 195
- ALICE Collaboration "Accessing the deuteron source with pion–deuteron femtoscopy in Pb–Pb collisions at $\sqrt{s_{NN}} = 5.02$ TeV", the manuscript is currently under collaboration review rounds.
- ALICE Collaboration "Femtoscopic study of the proton–proton and proton–deuteron systems in Heavy-Ion Collisions at the LHC", the manuscript is currently under collaboration review rounds.
- ALICE Collaboration "Probing Strong Interaction Parameters of the K^-d and K^+d Pairs Using Femtoscopy in Pb–Pb Collisions", the manuscript is currently under collaboration review rounds.
- K. M. Nałecz-Charkiewicz, J. Meles, W. Rzesza et al, "Current Advances in Information Quantum Technologies -Critical Issues" (2021), published in International Journal of Electronics and Telecommunications, vol. 67.

The author has received the following grants and awards during the Ph.D.:

- Grant PRELUDIUM NCN (2023) "L-ions in the QGP - Experimental studies towards a better understanding of the production mechanism of light ions and their interactions using femtoscopic correlations in momentum space in the

ALICE experiment at the LHC" - won with the highest note in Poland in section basic elements of matter,

- Grant IDUB YOUNG PW (2023) for femtoscopy studies of pion–deuteron and proton–deuteron pairs in Pb–Pb collisions,
- Travel grant Mobility PW (2023) for summer stay at CERN,
- Grant from the scientific council of the discipline (2023) "Badanie modelowe charakterystyki funkcji emisji par identycznych pionów w funkcji masy transversalnej",
- Grant from the scientific council of the discipline (2022) "Femtoskopowa analiza funkcji korelacyjnych par cząstek pion-deuteron na potrzeby badań korelacji par cząstek zawierających (anty)deuteron w zderzeniach Pb–Pb"
- A team award of the main rector of Warsaw University of Technology (2022) for work in 2020-2021.

The author has presented the results at the following conferences during the Ph.D.:

- XVII Workshop on Particle Correlations and Femtoscopy (WPCF 2024), Toulouse, France, presentation: *Femtoscopy analysis of ultrasoft pion trap at energies available at the CERN Large Hadron Collider* (**invited talk**)
- XVI Quark Confinement and the Hadron Spectrum Conference (QCHSC 2024), Cairns, Australia, presentation: *Non-identical particle femtoscopy of pairs containing (anti)deuteron in relativistic heavy-ion collisions with ALICE at the LHC* (**invited talk**).
- Mini Workshop of ALICE Correlations and Flow Physics, Shanghai, China, presentation: *Femtoscopic sources in relativistic heavy-ion collisions* (**invited talk**).
- Quark Matter (QM 2023), Houston, USA, poster: *First measurement of properties of strong interaction between deuterons and light hadrons in Pb–Pb collisions with ALICE*, in addition the results were a part of the talk: *Accessing strong interaction in three-hadron systems with ALICE*.
- XVI Workshop on Particle Correlations and Femtoscopy & IV Resonance Workshop 2023 WPCF 2023, Catania, Italy, presentation: *First measurement of properties of strong interaction between (anti-)deuterons and charged kaons in Pb–Pb collisions with ALICE* (**invited talk**).
- XVII International Workshop on Meson Physics (MESON 2023), Kraków, Poland, presentation: *A study of K-d and K+d interactions via femtoscopy technique*.

- XX International Conference on Hadron Spectroscopy and Structure (HADRON 2023) Genua, Italy, presentation: *A study of K - d and K + d interactions via femtoscopy technique.*
- XV Workshop on Particle Correlations and Femtoscopy (WPCF 2022), East Lansing, USA, presentation: *A study of the (anti)deuteron source in Pb-Pb collisions with ALICE at the LHC.*
- XIV International Conference on Hypernuclear and Strange Particle Physics (HYP 2022), Prague, Czech Republic, poster: *A study of the (anti)deuteron source in Pb-Pb collisions.*
- International Conference on Exotic Atoms and Related Topics (EXA 2021) (Vienna, Austria), presentation: *The study of K p interactions with the ALICE at the LHC.*

Bibliography

- [1] M. D. Schwartz. “Quantum Field Theory and the Standard Model”. In: *Cambridge University Press* (2013). DOI: doi.org/10.1017/9781139540940.
- [2] Wikipedia. *Standard Model*. [Online; accessed: 1st Oct 2024]. URL: https://en.wikipedia.org/wiki/Standard_Model.
- [3] J. Greensite. “An Introduction to the Confinement Problem”. In: *Springer Berlin, Heidelberg* 821 (2011). DOI: [10.1007/978-3-642-14382-3](https://doi.org/10.1007/978-3-642-14382-3).
- [4] H. D. Politzer. “Reliable Perturbative Results for Strong Interactions”. In: *Phys. Rev. Lett.* 30 (1973), pp. 1346–1349. DOI: [10.1103/PhysRevLett.30.1346](https://doi.org/10.1103/PhysRevLett.30.1346).
- [5] D. J. Gross and F. Wilczek. “Ultraviolet Behavior of Non-Abelian Gauge Theories”. In: *Phys. Rev. Lett.* 30 (1973), pp. 1343–1346. DOI: [10.1103/PhysRevLett.30.1343](https://doi.org/10.1103/PhysRevLett.30.1343).
- [6] Particle Data Group, R. L. Workman, V. D. Burkert, et al. “Review of Particle Physics”. In: *Progress of Theoretical and Experimental Physics* 2022.8 (2022), p. 083C01. DOI: [10.1093/ptep/ptac097](https://doi.org/10.1093/ptep/ptac097).
- [7] J. Ashman et al. “An Investigation of the Spin Structure of the Proton in Deep Inelastic Scattering of Polarised Muons on Polarised Protons”. In: *Nuclear Physics B* 328.1 (1989), pp. 1–35. DOI: [10.1016/0550-3213\(89\)90089-8](https://doi.org/10.1016/0550-3213(89)90089-8).
- [8] K. Schweda et al. “ $D\bar{D}$ Correlations Probing Thermalization in High-Energy Nuclear Collisions”. In: *arXiv: Nuclear Experiment* (2006). URL: <https://api.semanticscholar.org/CorpusID:261970836>.
- [9] P. W. Higgs. “Broken Symmetries and the Masses of Gauge Bosons”. In: *Phys. Rev. Lett.* 13 (1964). Ed. by J. C. Taylor, pp. 508–509. DOI: [10.1103/PhysRevLett.13.508](https://doi.org/10.1103/PhysRevLett.13.508).
- [10] F. Englert and R. Brout. “Broken Symmetry and the Mass of Gauge Vector Mesons”. In: *Phys. Rev. Lett.* 13 (1964), pp. 321–323. DOI: [10.1103/PhysRevLett.13.321](https://doi.org/10.1103/PhysRevLett.13.321).

- [11] G. S. Guralnik, C. R. Hagen, and T. W. B. Kibble. “Global Conservation Laws and Massless Particles”. In: *Phys. Rev. Lett.* 13 (1964), pp. 585–587. DOI: 10.1103/PhysRevLett.13.585.
- [12] H. Wiedemann. “Particle Accelerator Physics”. In: *Springer Nature* (2015). DOI: 10.1007/978-3-319-18317-6.
- [13] C. Curceanu et al. “The Modern Era of Light Kaonic Atom Experiments”. In: *Rev. Mod. Phys.* 91 (2019), p. 025006. DOI: 10.1103/RevModPhys.91.025006.
- [14] J. Gasser, V. Lyubovitskij, and A. Rusetsky. “Hadronic Atoms”. In: *Annual Review of Nuclear and Particle Science* 59 (2009). DOI: 10.1146/annurev.nucl.010909.083806.
- [15] “Centrality Dependence of the Charged-Particle Multiplicity Density at Midrapidity in Pb-Pb Collisions at $\sqrt{s_{NN}} = 5.02$ TeV”. In: *Phys. Rev. Lett.* 116 (2016), p. 222302. DOI: 10.1103/PhysRevLett.116.222302.
- [16] H. Yukawa. “On the Interaction of Elementary Particles. I”. In: *Progress of Theoretical Physics Supplement* 1 (1955), pp. 1–10. DOI: 10.1143/PTPS.1.1.
- [17] V. G. J. Stoks et al. “Construction of High-Quality NN Potential Models”. In: *Phys. Rev. C* 49 (1994), pp. 2950–2962. DOI: 10.1103/PhysRevC.49.2950.
- [18] R. Machleidt, F. Sammarruca, and Y. Song. “Nonlocal Nature of the Nuclear Force and its Impact on Nuclear Structure”. In: *Phys. Rev. C* 53 (1996), R1483–R1487. DOI: 10.1103/PhysRevC.53.R1483.
- [19] R. B. Wiringa, V. G. J. Stoks, and R. Schiavilla. “Accurate Nucleon-Nucleon Potential with Charge-Independence Breaking”. In: *Phys. Rev. C* 51 (1995), pp. 38–51. DOI: 10.1103/PhysRevC.51.38.
- [20] S. Weinberg. “Effective Chiral Lagrangians for Nucleon-Pion Interactions and Nuclear Forces”. In: *Nuclear Physics B* 363.1 (1991), pp. 3–18. DOI: 10.1016/0550-3213(91)90231-L.
- [21] S. Weinberg. “Nuclear Forces from Chiral Lagrangians”. In: *Physics Letters B* 251.2 (1990), pp. 288–292. DOI: 10.1016/0370-2693(90)90938-3.
- [22] M. Naghdi. “Nucleon-Nucleon Interaction: A Typical/Concise Review”. In: *Physics of Particles and Nuclei* 45 (2014), p. 924. DOI: 10.1134/S1063779614050050.

- [23] T. Hatsuda. “Lattice Quantum Chromodynamics and Baryon-Baryon Interactions”. In: *Frontiers of Physics* 13 (2018). DOI: 10 . 1007 / s11467 - 018-0829-4.
- [24] G. Comitini. “Perturbative Methods in Non-Perturbative Quantum Chromodynamics”. In: *arXiv* (2023). eprint: 2306 . 13624 (hep-th).
- [25] F. J. Dyson. “The S Matrix in Quantum Electrodynamics”. In: *Phys. Rev.* 75 (1949), pp. 1736–1755. DOI: 10 . 1103/PhysRev . 75 . 1736.
- [26] J. Schwinger. “On the Green’s Functions of Quantized Fields. I”. In: *Proceedings of the National Academy of Sciences* 37.7 (1951), pp. 452–455. DOI: 10 . 1073/pnas . 37 . 7 . 452.
- [27] K. G. Wilson. “Non-Lagrangian Models of Current Algebra”. In: *Phys. Rev.* 179 (1969), pp. 1499–1512. DOI: 10 . 1103/PhysRev . 179 . 1499.
- [28] V.N. Gribov. “Quantization of Non-Abelian Gauge Theories”. In: *Nuclear Physics B* 139.1 (1978), pp. 1–19. DOI: 10 . 1016/0550-3213(78)90175-X.
- [29] D. Zwanziger. “Local and Renormalizable Action from the Gribov Horizon”. In: *Nuclear Physics B* 323.3 (1989), pp. 513–544. DOI: 10 . 1016/0550-3213(89)90122-3.
- [30] B. Betz. “Jet Propagation and Mach-Cone Formation in (3+1)-dimensional Ideal Hydrodynamics”. In: *arXiv* (2009). eprint: 0910 . 4114 (nucl-th).
- [31] BNL - Brookhaven National Lab. [Online; accessed: 2nd Oct 2024]. URL: <https://www.bnl.gov/science/facilities.php>.
- [32] CERN - The European Organization for Nuclear Research. [Online; accessed: 2nd Oct 2024]. URL: <https://home.cern/>.
- [33] FAIR - Facility for Antiproton and Ion Research in Europe. [Online; accessed: 2nd Oct 2024]. URL: <https://fair-center.eu/>.
- [34] NICA - Nuclotron-based Ion Collider fAcility. [Online; accessed: 2nd Oct 2024]. URL: <https://nica.jinr.ru/megaproject.php>.
- [35] A. Bazavov et al. “Equation of State in $(2 + 1)$ -flavor QCD”. In: *Phys. Rev. D* 90 (2014), p. 094503. DOI: 10 . 1103/PhysRevD . 90 . 094503.
- [36] A. Andronic et al. “Decoding the Phase Structure of QCD via Particle Production at High Energy”. In: *Nature* 561.7723 (2018), pp. 321–330. DOI: 10 . 1038/s41586-018-0491-6.

- [37] F. Becattini et al. “Hadron Formation in Relativistic Nuclear Collisions and the QCD Phase Diagram”. In: *Physical Review Letters* 111 (2012). DOI: 10.1103/PhysRevLett.111.082302.
- [38] W. Busza, K. Rajagopal, and W. van der Schee. “Heavy Ion Collisions: The Big Picture and the Big Questions”. In: *Annual Review of Nuclear and Particle Science* 68.1 (2018), pp. 339–376. DOI: 10.1146/annurev-nucl-101917-020852.
- [39] S. A. Bass et al. “Hadronic Freeze-out Following a First Order Hadronization Phase Transition in Ultrarelativistic Heavy Ion Collisions”. In: *Phys. Rev. C* 60 (1999), p. 021902. DOI: 10.1103/PhysRevC.60.021902.
- [40] M. Bleicher and J. Aichelin. “Strange Resonance Production: Probing Chemical and Thermal Freeze-out in Relativistic Heavy Ion Collisions”. In: *Physics Letters B* 530.1 (2002), pp. 81–87. DOI: 10.1016/S0370-2693(02)01334-5.
- [41] J. W. Harris and B. Müller. “QGP Signatures- Revisited”. In: *arXiv* (2023). eprint: 2308.05743 (hep-ph).
- [42] J. Rafelski. “Discovery of Quark-Gluon Plasma: Strangeness Diaries”. In: *The European Physical Journal Special Topics* 229 (2020), pp. 1–140. DOI: 10.1140/epjst/e2019-900263-x.
- [43] B. I. Abelev et al. “Enhanced Strange Baryon Production in Au+Au Collisions Compared to $p + p$ at $\sqrt{s_{NN}} = 200$ GeV”. In: *Phys. Rev. C* 77 (2008), p. 044908. DOI: 10.1103/PhysRevC.77.044908.
- [44] J. Adam et al. “Enhanced Production of Multi-Strange Hadrons in High-Multiplicity Proton-Proton Collisions”. In: *Nature Phys.* 13 (2017), pp. 535–539. DOI: 10.1038/nphys4111.
- [45] A. Adare et al. “Centrality Dependence of Low-Momentum Direct-Photon Production in Au + Au Collisions at $\sqrt{s_{NN}} = 200$ GeV”. In: *Phys. Rev. C* 91 (2015), p. 064904. DOI: 10.1103/PhysRevC.91.064904.
- [46] J. Adam et al. “Direct Photon Production in Pb–Pb Collisions at $\sqrt{s_{NN}}=2.76$ TeV”. In: *Physics Letters B* 754 (2016), 235–248. DOI: 10.1016/j.physletb.2016.01.020.
- [47] B. Aboona et al. “Observation of Sequential Y Suppression in Au+Au Collisions at $\sqrt{s_{NN}} = 200$ GeV with the STAR Experiment”. In: *Phys. Rev. Lett.* 130.11 (2023), p. 112301. DOI: 10.1103/PhysRevLett.130.112301.

- [48] S. Acharya et al. “ $\psi(2S)$ Suppression in Pb-Pb Collisions at the LHC”. In: *Phys. Rev. Lett.* 132 (2024), p. 042301. DOI: 10.1103/PhysRevLett.132.042301.
- [49] J. Adam et al. “Measurement of Jet Quenching with Semi-Inclusive Hadron-Jet Distributions in Central Pb-Pb Collisions at $\sqrt{s_{NN}} = 2.76$ TeV”. In: *Journal of High Energy Physics* 2015 (2015). DOI: 10.1007/JHEP09(2015)170.
- [50] L. Adamczyk et al. “Measurements of Jet Quenching with Semi-Inclusive Hadron+Jet Distributions in Au+Au Collisions at $\sqrt{s_{NN}} = 200$ GeV”. In: *Phys. Rev. C* 96.2 (2017), p. 024905. DOI: 10.1103/PhysRevC.96.024905.
- [51] A. M. Poskanzer and S. A. Voloshin. “Methods for Analyzing Anisotropic Flow in Relativistic Nuclear Collisions”. In: *Phys. Rev. C* 58 (1998), pp. 1671–1678. DOI: 10.1103/PhysRevC.58.1671.
- [52] J.-Y. Ollitrault. “Collective Dynamics in Heavy Ion Collisions”. In: *QCD Perspectives on Hot and Dense Matter*. Ed. by J.-P. Blaizot and E. Iancu. Dordrecht: Springer Netherlands, 2002, pp. 237–256. DOI: 10.1007/978-94-010-0267-7_7.
- [53] S. A. Voloshin, A. M. Poskanzer, and R. Snellings. “Collective Phenomena in Non-Central Nuclear Collisions”. In: *Landolt-Bornstein* 23 (2010). Ed. by R. Stock, pp. 293–333. DOI: 10.1007/978-3-642-01539-7_10.
- [54] C. M. Hung and E. Shuryak. “Equation of State, Radial Flow, and Freeze-out in High Energy Heavy Ion Collisions”. In: *Phys. Rev. C* 57 (1998), pp. 1891–1906. DOI: 10.1103/PhysRevC.57.1891.
- [55] T. Hirano and K. Tsuda. “Collective Flow and Two-Pion Correlations from a Relativistic Hydrodynamic Model with Early Chemical Freeze-out”. In: *Physical Review C* 66.5 (2002). DOI: 10.1103/physrevc.66.054905.
- [56] P. Huovinen et al. “Radial and Elliptic Flow at RHIC: Further Predictions”. In: *Physics Letters B* 503 (2001), pp. 58–64. DOI: 10.1016/S0370-2693(01)00219-2.
- [57] R. Hanbury Brown and R.Q. Twiss. “LXXIV. A New Type of Interferometer for Use in Radio Astronomy”. In: *The London, Edinburgh, and Dublin Philosophical Magazine and Journal of Science* 45.366 (1954), pp. 663–682. DOI: 10.1080/14786440708520475.
- [58] R. Q. Twiss, A. G. Little, and R. Hanbury Brown. “Correlation Between Photons, in Coherent Beams of Light, Detected by a Coincidence Counting Technique”. In: *Nature* (1957), pp. 27–29. DOI: 10.1038/177027a0.

- [59] G. Goldhaber et al. "Influence of Bose-Einstein Statistics on the Antiproton-Proton Annihilation Process". In: *Phys. Rev.* 120 (1960), pp. 300–312. DOI: 10.1103/PhysRev.120.300.
- [60] V.G. Grishin, G.I. Kopylov, and M.I. Podgoretsky. "Correlations of Identical Particles Emitted by Highly Excited Nuclei". In: *Sov. J. Nucl. Phys.* (1972).
- [61] G.I. Kopylov. "Like Particle Correlations as a Tool to Study the Multiple Production Mechanism". In: *Physics Letters B* 50.4 (1974), pp. 472–474. DOI: 10.1016/0370-2693(74)90263-9.
- [62] S.V. Akkelin and Yu.M. Sinyukov. "The HBT-Interferometry of Expanding Sources". In: *Physics Letters B* 356.4 (1995), pp. 525–530. DOI: 10.1016/0370-2693(95)00765-D.
- [63] Yu. M. Sinyukov. "Spectra and Correlations in Locally Equilibrium Hadron and Quark-Gluon Systems". In: *Nucl. Phys. A* 566 (1994), p. 589.
- [64] S. E. Koonin. "Proton Pictures of High-Energy Nuclear Collisions". In: *Phys. Lett. B* 70 (1977), pp. 43–47. DOI: 10.1016/0370-2693(77)90340-9.
- [65] M. Gyulassy, S. K. Kauffmann, and Lance W. Wilson. "Pion Interferometry of Nuclear Collisions. I. Theory". In: *Phys. Rev. C* 20 (1979), pp. 2267–2292. DOI: 10.1103/PhysRevC.20.2267.
- [66] W. A. Zajc et al. "Two-Pion Correlations in Heavy Ion Collisions". In: *Phys. Rev. C* 29 (1984), pp. 2173–2187. DOI: 10.1103/PhysRevC.29.2173.
- [67] A. N. Makhlin and Yu. M. Sinyukov. "The Pion Interferometry Theory for the Hydrodynamic Stage of Multiple Processes". In: *Sov. J. Nucl. Phys* 46 (1987), p. 345.
- [68] A. N. Makhlin and Yu. M. Sinyukov. "Hydrodynamics of Hadron Matter Under Pion Interferometric Microscope". In: *Z. Phys. C* 39 (1988), p. 69.
- [69] H. U. Gersch. "Coulomb Final State Interaction in Identical Boson Interferometry". In: *Zeitschrift für Physik A Atomic Nuclei* 327 (1987), pp. 115–117. DOI: 10.1007/BF01295257.
- [70] M. A. Lisa et al. "Femtосcopy in Relativistic Heavy Ion Collisions: Two Decades of Progress". In: *Annual Review of Nuclear and Particle Science* 55.1 (2005), pp. 357–402. DOI: 10.1146/annurev.nucl.55.090704.151533.

- [71] S. Pratt. “Pion Interferometry of Quark-Gluon Plasma”. In: *Phys. Rev. D* 33 (1986), pp. 1314–1327. DOI: 10.1103/PhysRevD.33.1314.
- [72] A. Kisiel. “Non-identical Particle Femtoscopy at $\sqrt{s_{NN}} = 200$ -AGeV in Hydrodynamics with Statistical Hadronization”. In: *Phys. Rev. C* 81 (2010), p. 064906. DOI: 10.1103/PhysRevC.81.064906.
- [73] Yu. M. Sinyukov and V. M. Shapoval. “Correlation Femtoscopy of Small Systems”. In: *Phys. Rev. D* 87 (2013), p. 094024.
- [74] J. Adam et al. “Two-Pion Femtoscopy in p-Pb Collisions at $\sqrt{s_{NN}} = 5.02$ TeV”. In: *Phys. Rev. C* 91 (2015), p. 034906. DOI: 10.1103/PhysRevC.91.034906.
- [75] S. Acharya et al. “Kaon Femtoscopy in Pb-Pb Collisions at $\sqrt{s_{NN}} = 2.76$ TeV”. In: *Phys. Rev. C* 96 (2017), p. 064613. DOI: 10.1103/PhysRevC.96.064613.
- [76] K. Aamodt et al. “Two-Pion Bose-Einstein Correlations in Central Pb-Pb Collisions at $\sqrt{s_{NN}}=2.76$ TeV”. In: *Phys. Lett. B* 696 (2011), pp. 328–337. DOI: 10.1016/j.physletb.2010.12.053.
- [77] J. Adam et al. “One-Dimensional Pion, Kaon, and Proton Femtoscopy in Pb-Pb Collisions at $\sqrt{s_{NN}} = 2.76$ TeV”. In: *Phys. Rev. C* 92 (2015), p. 054908. DOI: 10.1103/PhysRevC.92.054908.
- [78] K. Aamodt et al. “Two-pion Bose-Einstein Correlations in pp Collisions at $\sqrt{s} = 900$ GeV”. In: *Phys. Rev. D* 82 (2010), p. 052001. DOI: 10.1103/PhysRevD.82.052001.
- [79] K. Aamodt et al. “Femtoscopy of pp Collisions at $\sqrt{s} = 0.9$ and 7 TeV at the LHC with Two-pion Bose-Einstein Correlations”. In: *Phys. Rev. D* 84 (2011), p. 112004. DOI: 10.1103/PhysRevD.84.112004.
- [80] J. Adam et al. “Centrality Dependence of Pion Freeze-out Radii in Pb-Pb Collisions at $\sqrt{s_{NN}} = 2.76$ TeV”. In: *Phys. Rev. C* 93.2 (2016), p. 024905. DOI: 10.1103/PhysRevC.93.024905.
- [81] S. Acharya et al. “Pion-Kaon Femtoscopy and the Lifetime of the Hadronic Phase in Pb–Pb Collisions at $\sqrt{s_{NN}} = 2.76$ TeV”. In: *Phys. Lett. B* 813 (2021), p. 136030. DOI: 10.1016/j.physletb.2020.136030.
- [82] C. Adler et al. “Pion Interferometry of $\sqrt{s_{NN}} = 130$ -GeV Au+Au Collisions at RHIC”. In: *Phys. Rev. Lett.* 87 (2001), p. 082301. DOI: 10.1103/PhysRevLett.87.082301.

- [83] S. S. Adler et al. "Bose-Einstein Correlations of Charged Pion Pairs in Au + Au Collisions at $\sqrt{s_{NN}} = 200$ GeV". In: *Phys. Rev. Lett.* 93 (2004), p. 152302. DOI: 10.1103/PhysRevLett.93.152302.
- [84] J. Adams et al. "Pion Interferometry in Au+Au Collisions at $\sqrt{s_{NN}} = 200$ -GeV". In: *Phys. Rev. C* 71 (2005), p. 044906. DOI: 10.1103/PhysRevC.71.044906.
- [85] B. Abelev et al. "Pion Interferometry in Au+Au and Cu+Cu Collisions at $\sqrt{s_{NN}} = 62.4$ and 200 GeV". In: *Phys. Rev. C* 80 (2009). DOI: 10.1103/PhysRevC.80.024905.
- [86] S. Acharya et al. "Search for a Common Baryon Source in High-Multiplicity pp Collisions at the LHC". In: *Physics Letters B* 811 (2020), p. 135849. DOI: 10.1016/j.physletb.2020.135849.
- [87] A. Kisiel, M. Gałazyn, and P. Bożek. "Pion, Kaon, and Proton Femtoscopy in Pb-Pb Collisions at $\sqrt{s_{NN}} = 2.76$ TeV Modeled in (3+1)D Hydrodynamics". In: *Phys. Rev. C* 90 (2014), p. 064914. DOI: 10.1103/PhysRevC.90.064914.
- [88] A. Kisiel. "Pion-Kaon Femtoscopy in Pb–Pb Collisions at $\sqrt{s_{NN}} = 2.76$ TeV Modeled in (3+1)D Hydrodynamics Coupled to Therminator 2 and the Effect of Delayed Kaon Emission". In: *Phys. Rev. C* 98 (2018), p. 044909. DOI: 10.1103/PhysRevC.98.044909.
- [89] V. M. Shapoval and Yu. M. Sinyukov. "Bulk Observables in Pb + Pb Collisions at $\sqrt{s_{NN}} = 5.02$ TeV at the CERN Large Hadron Collider within the Integrated Hydrokinetic Model". In: *Phys. Rev. C* 100 (2019), p. 044905. DOI: 10.1103/PhysRevC.100.044905.
- [90] H. P. Zbroszczyk. "Studies of Baryon–Baryon Correlations in Relativistic Nuclear Collisions Registered at the STARExperiment". In: *PhD thesis* (2008).
- [91] L. Fabbietti, V. Mantovani Sarti, and O. Vazquez Doce. "Study of the Strong Interaction Among Hadrons with Correlations at the LHC". In: *Ann. Rev. Nucl. Part. Sci.* 71 (2021), pp. 377–402. DOI: 10.1146/annurev-nucl-102419-034438.
- [92] D. J. Griffiths and D. F. Schroeter. "Introduction to Quantum Mechanics". In: (2018).
- [93] J. J. Sakurai and Jim Napolitano. *Modern Quantum Mechanics*. 2014.
- [94] D. Griffiths. *Introduction to Quantum Mechanics*. 2004.

- [95] S. Deser et al. "Energy Level Displacements in Pi-Mesonic Atoms". In: *Phys. Rev.* 96 (1954), pp. 774–776. DOI: 10.1103/PhysRev.96.774.
- [96] U. G. Meissner, U. Raha, and A. Rusetsky. "Spectrum and Decays of Kaonic Hydrogen". In: *Eur. Phys. J. C* 35 (2004), pp. 349–357. DOI: 10.1140/epjc/s2004-01859-4.
- [97] R. Lednicky and V. L. Lyuboshits. "Final State Interaction Effect on Pairing Correlations Between Particles with Small Relative Momenta". In: *Yad. Fiz.* 35 (1981), pp. 1316–1330.
- [98] R. Lednicky, S. Panitkin, and N. Xu. "Search for Delays Between Unlike Particle Emissions in Relativistic Heavy Ion Collisions". In: (2003).
- [99] R. Lednický. "Finite-size Effect on Two-Particle Production in Continuous and Discrete Spectrum". In: *Physics of Particles and Nuclei* 40 (2009). DOI: 10.1134/S1063779609030034.
- [100] E. G. Kessler Jr. "The Deuteron Binding Energy and the Neutron Mass". In: *Phys. Lett. A* 255 (1999), p. 221. DOI: 10.1016/S0375-9601(99)00078-X.
- [101] Peter Braun-Munzinger, Benjamin Dönigus, and Nicole Löhner. "ALICE investigates 'snowballs in hell'". In: *CERN Courier* 55.7 (2015), pp. 26–30.
- [102] Z. Lin et al. "Multiphase Transport Model for Relativistic Heavy Ion Collisions". In: *Phys. Rev. C* 72 (2005), p. 064901. DOI: 10.1103/PhysRevC.72.064901.
- [103] C. Adler et al. "Anti-deuteron and anti-He-3 production in $s(NN)^{1/2} = 130$ -GeV Au+Au collisions". In: *Phys. Rev. Lett.* 87 (2001). [Erratum: *Phys.Rev.Lett.* 87, 279902 (2001)], p. 262301. DOI: 10.1103/PhysRevLett.87.262301.
- [104] S. S. Adler and others. "Deuteron and Antideuteron Production in Au + Au Collisions at $\sqrt{s_{NN}} = 200$ GeV". In: *Phys. Rev. Lett.* 94 (2005), p. 122302. DOI: 10.1103/PhysRevLett.94.122302.
- [105] J. Adam et al. "Production of Light Nuclei and Anti-nuclei in pp and Pb-Pb Collisions at Energies Available at the CERN Large Hadron Collider". In: *Phys. Rev. C* 93 (2016), p. 024917. DOI: 10.1103/PhysRevC.93.024917.

- [106] F. Bellini. “Testing the System Size Dependence of Hydrodynamical Expansion and Thermal Particle Production with π , K, p, And ϕ in Xe–Xe and Pb–Pb Collisions with ALICE”. In: *Nuclear Physics A* 982 (2019), pp. 427–430. DOI: 10.1016/j.nuclphysa.2018.09.082.
- [107] “Performance of the ALICE Experiment at the CERN LHC”. In: *International Journal of Modern Physics A* 29.24 (2014), p. 1430044. DOI: 10.1142/S0217751X14300440.
- [108] S. Acharya et al. “Measurement of Deuteron Spectra and Elliptic Flow in Pb–Pb Collisions at $\sqrt{s_{NN}} = 2.76$ TeV at the LHC”. In: *Eur. Phys. J. C* 77.10 (2017), p. 658. DOI: 10.1140/epjc/s10052-017-5222-x.
- [109] S. Acharya et al. “Elliptic and Triangular Flow of (Anti)deuterons in Pb–Pb Collisions at $\sqrt{s_{NN}} = 5.02$ TeV”. In: *Phys. Rev. C* 102 (2020), p. 055203. DOI: 10.1103/PhysRevC.102.055203.
- [110] S. Acharya et al. “First Measurement of Antideuteron Number Fluctuations at Energies Available at the Large Hadron Collider”. In: *Phys. Rev. Lett.* 131 (2023), p. 041901. DOI: 10.1103/PhysRevLett.131.041901.
- [111] Dmytro O. “Overview of Light Nuclei Production in Relativistic Heavy-Ion Collisions”. In: *Nuclear Physics A* 1005 (2021). The 28th International Conference on Ultra-relativistic Nucleus-Nucleus Collisions: Quark Matter 2019, p. 121754. DOI: 10.1016/j.nuclphysa.2020.121754.
- [112] S. Acharya et al. “Multiplicity Dependence of (Anti-)deuteron Production in pp Collisions at $\sqrt{s} = 7$ TeV”. In: *Phys. Lett. B* 794 (2019), pp. 50–63. DOI: 10.1016/j.physletb.2019.05.028.
- [113] S. Acharya et al. “Measurement of the Production of (Anti)nuclei in p–Pb Collisions at $s_{NN}=8.16$ TeV”. In: *Phys. Lett. B* 846 (2023), p. 137795. DOI: 10.1016/j.physletb.2023.137795.
- [114] E. Schnedermann, J. Sollfrank, and U. Heinz. “Thermal Phenomenology of Hadrons from 200A GeV S+S Collisions”. In: *Phys. Rev. C* 48 (1993), pp. 2462–2475. DOI: 10.1103/PhysRevC.48.2462.
- [115] P. J. Siemens and J. O. Rasmussen. “Evidence for a Blast Wave from Compressed Nuclear Matter”. In: *Phys. Rev. Lett.* 42 (1979), pp. 880–883. DOI: 10.1103/PhysRevLett.42.880.

- [116] S. Acharya et al. "Measurement of the (anti-)3He Elliptic Flow in Pb–Pb Collisions at $\sqrt{s_{\text{NN}}}=5.02\text{TeV}$ ". In: *Physics Letters B* 805 (2020), p. 135414. DOI: 10.1016/j.physletb.2020.135414.
- [117] F. Karsch and K. Redlich. "Probing Freeze-out Conditions in Heavy Ion Collisions with Moments of Charge Fluctuations". In: *Physics Letters B* 695.1 (2011), pp. 136–142. DOI: 10.1016/j.physletb.2010.10.046.
- [118] S. Borsanyi et al. "Freeze-Out Parameters from Electric Charge and Baryon Number Fluctuations: Is There Consistency?" In: *Phys. Rev. Lett.* 113 (2014), p. 052301. DOI: 10.1103/PhysRevLett.113.052301.
- [119] S. Gupta et al. "Limits of Thermalization in Relativistic Heavy Ion Collisions". In: *Physics Letters B* 829 (2022), p. 137021. DOI: 10.1016/j.physletb.2022.137021.
- [120] Z. Fecková et al. "Formation of Deuterons by Coalescence: Consequences for Deuteron Number Fluctuations". In: *Phys. Rev. C* 93 (2016), p. 054906. DOI: 10.1103/PhysRevC.93.054906.
- [121] S. Mrówczyński and P. Słoń. "Hadron–Deuteron Correlations and Production of Light Nuclei in Relativistic Heavy-ion Collisions". In: *Acta Phys. Polon. B* 51.8 (2020), pp. 1739–1755. DOI: 10.5506/APhysPolB.51.1739.
- [122] S. Bazak and S. Mrówczyński. "Production of ^4Li and $p-^3\text{He}$ Correlation Function in Relativistic Heavy Ion Collisions". In: *Eur. Phys. J. A* 56.7 (2020), p. 193. DOI: 10.1140/epja/s10050-020-00198-6.
- [123] S. Mrówczyński and P. Słoń. "Deuteron-Deuteron Correlation Function in Nucleus-Nucleus Collisions". In: *Phys. Rev. C* 104.2 (2021), p. 024909. DOI: 10.1103/PhysRevC.104.024909.
- [124] S. Mrówczyński. "Production of Light Nuclei at Colliders – Coalescence vs. Thermal Model". In: *Eur. Phys. J. ST* 229.22-23 (2020), pp. 3559–3583. DOI: 10.1140/epjst/e2020-000067-0.
- [125] E. Mobs. "The CERN Accelerator Complex - August 2018. Complexe des accélérateurs du CERN - Août 2018". In: (2018). General Photo.
- [126] Lyndon E. and Philip B. "LHC Machine". In: *Journal of Instrumentation* 3.08 (2008), S08001. DOI: 10.1088/1748-0221/3/08/S08001.

- [127] K. Aamodt et al. “The ALICE Experiment at the CERN LHC”. In: *JINST* 3 (2008), S08002. DOI: 10.1088/1748-0221/3/08/S08002.
- [128] G Aad et al. “The ATLAS Experiment at the CERN Large Hadron Collider”. In: *Journal of Instrumentation* 3 (2008), S08003. DOI: 10.1088/1748-0221/3/08/S08003.
- [129] A. Augusto Alves Jr. et al. “The LHCb Detector at the LHC”. In: *JINST* 3 (2008), S08005. DOI: 10.1088/1748-0221/3/08/S08005.
- [130] S. Chatrchyan et al. “The CMS Experiment at the CERN LHC”. In: *JINST* 3 (2008), S08004. DOI: 10.1088/1748-0221/3/08/S08004.
- [131] L. Palomo. “The ALICE Experiment Upgrades for LHC Run 3 and Beyond: Contributions from Mexican Groups”. In: *Journal of Physics: Conference Series* 912 (2017), p. 012023. DOI: 10.1088/1742-6596/912/1/012023.
- [132] B. Abelev et al. “Centrality Determination of Pb–Pb Collisions at $\sqrt{s_{NN}} = 2.76$ TeV with ALICE”. In: *Phys. Rev. C* 88.4 (2013), p. 044909. DOI: 10.1103/PhysRevC.88.044909.
- [133] Juha Ä. et al. “Alignment of the ALICE Inner Tracking System with Cosmic-Ray Tracks”. English. In: *Journal of Instrumentation* 5.3 (2010). 37 pages, 15 figures, revised version, accepted by JINST, P03003. DOI: 10.1088/1748-0221/5/03/P03003.
- [134] J. Alme et al. “The ALICE TPC, a Large 3-dimensional Tracking Device with Fast Readout for Ultra-High Multiplicity Events”. In: *Nuclear Instruments and Methods in Physics Research Section A: Accelerators, Spectrometers, Detectors and Associated Equipment* 622.1 (2010), pp. 316–367. DOI: 10.1016/j.nima.2010.04.042.
- [135] “Real-time Data Processing in the ALICE High Level Trigger at the LHC”. In: *Computer Physics Communications* 242 (2019), pp. 25–48. DOI: 10.1016/j.cpc.2019.04.011.
- [136] R. Schicker. “Overview of ALICE Results in pp, pA and AA Collisions”. In: *EPJ Web of Conferences* 138 (2016). DOI: 10.1051/epjconf/201713801021.
- [137] A. Akindinov et al. “Performance of the ALICE Time-Of-Flight Detector at the LHC”. In: *Eur. Phys. J. Plus* 128 (2013), p. 44. DOI: 10.1140/epjp/i2013-13044-x.

- [138] J. Adam et al. "The ALICE Transition Radiation Detector: Construction, operation, and performance". In: *Nuclear Instruments and Methods in Physics Research Section A: Accelerators, Spectrometers, Detectors and Associated Equipment* 881 (2018), pp. 88–127. DOI: 10.1016/j.nima.2017.09.028.
- [139] J. Adam et al. "The High Momentum Particle Identification (HMPID) Detector PID Performance and its Contribution to the ALICE Physics Program". In: *Nuclear Instruments and Methods in Physics Research Section A: Accelerators, Spectrometers, Detectors and Associated Equipment* 876 (2017), pp. 133–136. DOI: 10.1016/j.nima.2017.02.037.
- [140] "Performance of the ALICE Photon Spectrometer PHOS". In: *Nuclear Instruments and Methods in Physics Research Section A: Accelerators, Spectrometers, Detectors and Associated Equipment* 537.1 (2005), pp. 363–367. DOI: 10.1016/j.nima.2004.08.044.
- [141] P. Cortese et al. "ALICE Electromagnetic Calorimeter Technical Design Report". In: *CERN-LHCC-2008-014, CERN-ALICE-TDR-014* (2008).
- [142] G. Dellacasa et al. "ALICE Technical Design Report: Photon Multiplicity Detector (PMD)". In: *CERN-LHCC-99-32, CERN-OPEN-2000-184* (1999).
- [143] C. Holm Christensen et al. "The ALICE Forward Multiplicity Detector". In: *Int. J. Mod. Phys. E* 16 (2007). Ed. by Y. Ma et al., pp. 2432–2437. DOI: 10.1142/S0218301307008057.
- [144] G. Puddu et al. "The Zero Degree Calorimeters for the ALICE Experiment". In: *Nuclear Instruments and Methods in Physics Research Section A: Accelerators, Spectrometers, Detectors and Associated Equipment* 581.1 (2007). VCI 2007, pp. 397–401. DOI: 10.1016/j.nima.2007.08.013.
- [145] P. Rosnet. "The Muon Spectrometer of the ALICE Experiment at LHC". In: *2005 IEEE Nuclear Science Symposium (NSS)*. présenté par P. Rosnet, à paraître dans les proceedings. San Juan, Puerto Rico, 2005, pp. 1–5.
- [146] A. Fernández et al. "ACORDE a Cosmic Ray Detector for ALICE". In: *Nuclear Instruments and Methods in Physics Research Section A: Accelerators, Spectrometers, Detectors and Associated Equipment* 572.1 (2007), pp. 102–103. DOI: 10.1016/j.nima.2006.10.336.
- [147] V Grigoriev et al. "ALICE T0 Detector". In: vol. 52. 2004, 605–608 Vol. 1. DOI: 10.1109/NSSMIC.2004.1462267.

- [148] A. Villatoro T. “AD, the ALICE Diffractive Detector”. In: *AIP Conf. Proc.* 1819.1 (2017). Ed. by M. Capua et al., p. 040020. DOI: 10.1063/1.4977150.
- [149] R. Brun and F. Rademakers. “ROOT: An Object Oriented Data Analysis Framework”. In: *Nucl. Instrum. Meth. A* 389 (1997). Ed. by M. Werlen and D. Perret-Gallix, pp. 81–86. DOI: 10.1016/S0168-9002(97)00048-X.
- [150] P. Saiz et al. “AliEn—ALICE Environment on the GRID”. In: *Nuclear Instruments and Methods in Physics Research Section A: Accelerators, Spectrometers, Detectors and Associated Equipment* 502.2 (2003), pp. 437–440. DOI: 10.1016/S0168-9002(03)00462-5.
- [151] X. Wang and M. Gyulassy. “HIJING: A Monte Carlo Model for Multiple Jet Production in p p, p A and A A Collisions”. In: *Phys. Rev. D* 44 (1991), pp. 3501–3516. DOI: 10.1103/PhysRevD.44.3501.
- [152] R. Brun et al. “GEANT Detector Description and Simulation Tool”. In: (1994). DOI: 10.17181/CERN.MUHF.DMJ1.
- [153] A. Kisiel, W. Florkowski, and W. Broniowski. “Femtосcopy in Hydro-Inspired Models with Resonances”. In: *Phys. Rev. C* 73 (2006), p. 064902. DOI: 10.1103/PhysRevC.73.064902.
- [154] And I. Wykiel-Piekarska. “Particle Spectra in Pb-Pb Collisions at $\sqrt{s_{NN}} = 2.76$ TeV”. In: *Phys. Rev. C* 85 (2012), p. 064915. DOI: 10.1103/PhysRevC.85.064915.
- [155] M. Chojnacki et al. “THERMINATOR 2: THERMal heavy IoN generATOR 2”. In: *Comput. Phys. Commun.* 183.3 (2012), pp. 746–773. DOI: 10.1016/j.cpc.2011.11.018.
- [156] S. Acharya et al. “Anisotropic Flow of Identified Particles in Pb-Pb Collisions at $\sqrt{s_{NN}} = 5.02$ TeV”. In: *Journal of High Energy Physics* 2018 (2018), p. 064915. DOI: 10.1007/jhep09(2018)006.
- [157] W. Rzesza et al. “Femtосcopy Analysis of Ultrasoft Pion Trap at Energies Available at the CERN Large Hadron Collider”. In: *Phys. Rev. C* 110 (2024), p. 034904. DOI: 10.1103/PhysRevC.110.034904.
- [158] J. Bailey et al. “The d Scattering Length from K X-rays”. In: *Physics Letters B* 50.3 (1974), pp. 403–406. DOI: 10.1016/0370-2693(74)90700-X.

- [159] A. Forster et al. "Determination of the $2p - 1s$ Transition Energy and Strong Interaction Shift in Pionic Hydrogen Using Crystal Diffraction". In: *Phys. Rev. C* 28 (1983), pp. 2374–2379. DOI: 10.1103/PhysRevC.28.2374.
- [160] E. Bovet et al. "A New Determination of the H and D $2P$ - $1s$ Strong Interaction Shifts Using Crystal Diffraction". In: *Physics Letters B* 153.4 (1985), pp. 231–234. DOI: 10.1016/0370-2693(85)90537-4.
- [161] D. Chatellard et al. "X-ray Spectroscopy of the Pionic Deuterium Atom". In: *Nuclear Physics A* 625.4 (1997), pp. 855–872. DOI: 10.1016/S0375-9474(97)00466-1.
- [162] P. Hauser et al. "New Precision Measurement of the Pionic Deuterium s -wave Strong Interaction Parameters". In: *Phys. Rev. C* 58 (1998), R1869–R1872. DOI: 10.1103/PhysRevC.58.R1869.
- [163] U. Meissner, U. Raha, and A. Rusetsky. "The Pion-Nucleon Scattering Lengths from Pionic Deuterium". In: *Eur. Phys. J. C* 41 (2005). [Erratum: *Eur.Phys.J.C* 45, 545 (2006)], pp. 213–232. DOI: 10.1140/epjc/s2005-02182-4.
- [164] V. Baru et al. "Precision Calculation of Threshold πd Scattering, πN Scattering Lengths, and the GMO Sum Rule". In: *Nuclear Physics* 872 (2011), pp. 69–116. DOI: 10.1103/PhysRevC.85.064915.
- [165] K. Aamodt et al. "Centrality Dependence of the Charged-Particle Multiplicity Density at Midrapidity in Pb-Pb Collisions at $\sqrt{s_{NN}} = 2.76$ TeV". In: *Physical review letters* 106 (2011), p. 032301. DOI: 10.1103/PhysRevLett.106.032301.
- [166] V. Yu. Naboka et al. "Initialization of Hydrodynamics in Relativistic Heavy Ion Collisions with an Energy-Momentum Transport Model". In: *Phys. Rev. C* 91 (2015), p. 014906. DOI: 10.1103/PhysRevC.91.014906.
- [167] W T.H. Van Oers and K W Brockman Jr. "Phase-Shift Analysis of Elastic Nucleon–Deuteron Scattering." In: *Phys. Rev. C* 85 (2012), p. 064915. DOI: 10.1016/0375-9474(67)90633-1.
- [168] J. Arvieux. "Phase-Shift Analysis of Elastic Proton-Deuteron Scattering Cross Sections and ^3He Excited States". In: *Nuclear Physics A* 221.2 (1974), pp. 253–268. DOI: 10.1016/0375-9474(74)90317-0.
- [169] E. Huttel et al. "Phase-Shift Analysis of pd Elastic Scattering Below Break-up Threshold". In: *Nuclear Physics A* 406.3 (1983), pp. 443–455. DOI: 10.1016/0375-9474(83)90369-X.

- [170] A. Kievsky et al. “The Three-Nucleon System Near the N-d Threshold”. In: *Physics Letters B* 406.4 (1997), pp. 292–296. DOI: 10.1016/S0370-2693(97)00691-6.
- [171] T.C. Black et al. “Determination of Proton-Deuteron Scattering Lengths”. In: *Physics Letters B* 471.2 (1999), pp. 103–107. DOI: 10.1016/S0370-2693(99)01366-0.
- [172] W. Tornow, A. Kievsky, and H. Witała. “Improved Proton-Deuteron Phase-Shift Analysis Above the Deuteron Breakup Threshold and the Three-Nucleon Analyzing-Power Puzzle”. In: *Few-Body Systems* 32.9 (2002), p. 064915. DOI: 10.1007/s00601-002-0112-6.
- [173] D. L. Mihaylov et al. “A Femtoscopic Correlation Analysis Tool Using the Schrödinger Equation (CATS)”. In: *European Physical Journal C* 78.5 (2018), p. 064915. DOI: 10.1140/epjc/s10052-018-5859-0.
- [174] Bhawani S. “Study of the Strong Interaction in p-d System and of Deuteron Production in pp Collisions”. In: *PhD thesis, Technical University of Munich, 2023* 85 (2012), p. 064915. DOI: 10.1103/PhysRevC.85.064915.
- [175] ALICE. “Exploring the Strong Interaction of Three-Body Systems at the LHC”. In: *arXiv* 85 (2023), p. 064915. DOI: 10.1103/PhysRevC.85.064915. eprint: 2308.16120 (nucl-ex).
- [176] D. A. Brown et al. “Imaging three dimensional two-particle correlations for heavy-ion reaction studies”. In: *Phys. Rev. C* 72 (2005), p. 054902. DOI: 10.1103/PhysRevC.72.054902.
- [177] M. Viviani et al. “Role of three-body dynamics in nucleon-deuteron correlation functions”. In: *Phys. Rev. C* 108 (2023), p. 064002. DOI: 10.1103/PhysRevC.108.064002.
- [178] R. Del Grande et al. “A Method to Remove Lower Order Contributions in Multi-Particle Femtoscopic Correlation Functions”. In: *Eur. Phys. J. C* 82.3 (2022), p. 244. DOI: 10.1140/epjc/s10052-022-10209-z.
- [179] S. Acharya et al. “Towards the Understanding of the Genuine Three-body Interaction for p-p-p and p-p- Λ ”. In: *Eur. Phys. J. A* 59.7 (2023), p. 145. DOI: 10.1140/epja/s10050-023-00998-6.
- [180] B. S. Pudliner et al. “Quantum Monte Carlo Calculations of $A \leq 6$ Nuclei”. In: *Phys. Rev. Lett.* 74 (1995), pp. 4396–4399. DOI: 10.1103/PhysRevLett.74.4396.

- [181] S. Acharya et al. "Kaon-Proton Strong Interaction at Low Relative Momentum via Femtoscopy in Pb-Pb Collisions at the LHC". In: *Physics Letters B* 822 (2021), p. 136708. DOI: 10.1016/j.physletb.2021.136708.
- [182] S. Acharya et al. "Scattering Studies with Low-Energy Kaon-Proton Femtoscopy in Proton-Proton Collisions at the LHC". In: *Phys. Rev. Lett.* 124.9 (2020), p. 092301. DOI: 10.1103/PhysRevLett.124.092301.
- [183] W. E. Humphrey and R. R. Ross. "Low-Energy Interactions of K^- Mesons in Hydrogen". In: *Phys. Rev.* 127 (1962), pp. 1305–1323. DOI: 10.1103/PhysRev.127.1305.
- [184] M. Sakitt et al. "Low-Energy K^- -Meson Interactions in Hydrogen". In: *Phys. Rev.* 139 (1965), B719–B728. DOI: 10.1103/PhysRev.139.B719.
- [185] J.K. Kim. "Low Energy $K^- - p$ Interaction and Interpretation of the 1405-MeV Y_0^* Resonance as a $\bar{K}N$ Bound State". In: *Phys. Rev. Lett.* 14 (1965), p. 29. DOI: 10.1103/PhysRevLett.14.29.
- [186] J.K. Kim. "Multichannel Phase-Shift Analysis of $\bar{K}N$ Interaction in the Region 0 to 550 MeV/c". In: *Phys. Rev. Lett.* 19 (1967), p. 1074. DOI: 10.1103/PhysRevLett.19.1074.
- [187] W. Kittel, G. Otter, and I. Wacek. "The K^-p Charge Exchange Interactions at Low Energies and Scattering Lengths Determination". In: *Phys. Lett.* 21 (1966), pp. 349–351. DOI: 10.1016/0031-9163(66)90845-6.
- [188] D. Evans et al. "Charge Exchange Scattering in K- P Interactions Below 300 MeV/c". In: *J. Phys. G* 9 (1983), pp. 885–894. DOI: 10.1088/0305-4616/9/8/011.
- [189] J. Ciborowski et al. "Kaon Scattering and Charged Sigma Hyperon Production in K- P Interactions below 300 MeV/c". In: *J. Phys. G* 8 (1982), pp. 13–32. DOI: 10.1088/0305-4616/8/1/005.
- [190] A. D. Martin. "Kaon - Nucleon Parameters". In: *Nucl. Phys. B* 179 (1981), pp. 33–48. DOI: 10.1016/0550-3213(81)90247-9.
- [191] G. Beer et al. "Measurement of the Kaonic Hydrogen X-Ray Spectrum". In: *Phys. Rev. Lett.* 94 (2005), p. 212302. DOI: 10.1103/PhysRevLett.94.212302.
- [192] M. Iwasaki et al. "Observation of Kaonic Hydrogen K_α X Rays". In: *Phys. Rev. Lett.* 78 (1997), pp. 3067–3069. DOI: 10.1103/PhysRevLett.78.3067.

- [193] J. Zmeskal et al. "Kaonic Atoms at DAFNE: The SIDDHARTA Experiment". In: *Int. J. Mod. Phys. A* 24 (2009). Ed. by S. Kistryn et al., pp. 190–197. DOI: 10.1142/S0217751X0904347X.
- [194] A. Ghigo et al. "Commissioning of the DAFNE Beam Test Facility". In: *Nucl. Instrum. Meth. A* 515 (2003), pp. 524–542. DOI: 10.1016/j.nima.2003.07.017.
- [195] T.M. Ito et al. "Observation of Kaonic Hydrogen Atom X Rays". In: *Phys. Rev. C* 58 (1998), pp. 2366–2382. DOI: 10.1103/PhysRevC.58.2366.
- [196] T. Hoshino et al. "Constraining the $\bar{K}N$ Interaction from the 1S Level Shift of Kaonic Deuterium". In: *Phys. Rev. C* 96.4 (2017), p. 045204. DOI: 10.1103/PhysRevC.96.045204.
- [197] Y. Ikeda, T. Hyodo, and W. Weise. "Improved Constraints on Chiral SU(3) Dynamics from Kaonic Hydrogen". In: *Phys. Lett. B* 706 (2011), pp. 63–67. DOI: 10.1016/j.physletb.2011.10.068.
- [198] Y. Ikeda, T. Hyodo, and W. Weise. "Chiral SU(3) Theory of Antikaon-Nucleon Interactions with Improved Threshold Constraints". In: *Nucl. Phys. A* 881 (2012), pp. 98–114. DOI: 10.1016/j.nuclphysa.2012.01.029.
- [199] B. Borasoy, U.-G. Meissner, and R. Nissler. " K^-p Scattering Length from Scattering Experiments". In: *Phys. Rev. C* 74 (2006), p. 055201. DOI: 10.1103/PhysRevC.74.055201.
- [200] Zhan-Wei L. et al. "Kaonic Hydrogen and Deuterium in Hamiltonian Effective Field Theory". In: *Physics Letters B* 808 (2020), p. 135652. DOI: 10.1016/j.physletb.2020.135652.
- [201] Yukihide K. et al. " K^-p Correlation Function from High-Energy Nuclear Collisions and Chiral SU(3) Dynamics." In: *Physical review letters* 124 13 (2019), p. 132501. DOI: 10.1103/PhysRevC.85.064915.
- [202] R.H. Dalitz and S.F. Tuan. "The Phenomenological Description of K^- -nucleon Reaction Processes". In: *Annals Phys.* 10 (1960), pp. 307–351. DOI: 10.1016/0003-4916(60)90001-4.
- [203] S. Acharya et al. "Constraining the $\bar{K}N$ Coupled Channel Dynamics Using Femtoscopic Correlations at the LHC". In: *The European Physical Journal C* 83 (2023), S08005. DOI: 10.1140/epjc/s10052-023-11476-0.

- [204] R. H. Dalitz et al. "Theory of Low-Energy Kaon - Nucleon Scattering". In: *Hypernuclear and Kaon Physics*. Vol. 85. 1982, pp. 201–214. DOI: 10 . 1103 / PhysRevC.85.064915.
- [205] A. Sibirtsev et al. "Kaon-Deuteron Scattering at Low Energies". In: *J. Phys. G* 32 (2006), R395–R416. DOI: 10 . 1088/0954-3899/32/11/R02.
- [206] F. Sgaramella et al. "Characterization of the SIDDHARTA-2 Setup via the Kaonic Helium Measurement". In: *Condensed Matter* 9.1 (2024), p. 064915. DOI: 10.3390/condmat9010016.
- [207] T. Mizutani et al. "Faddeev-Chiral Unitary Approach to the K^-d Scattering Length". In: *Phys. Rev. C* 87 (2013), p. 035201. DOI: 10 . 1103 / PhysRevC . 87 . 035201.
- [208] J. Révai. "Signature of the (1405) Resonance in Neutron Spectra from the $K^- + d$ Reaction". In: *Few-Body Systems* 54 (2013), p. 135652. DOI: doi . org / 10 . 1007 / s00601-013-0619-z.
- [209] N. V. Shevchenko. "Faddeev Treatment of the Quasi-Bound and Scattering States in the $\bar{K}NN - \pi\Sigma N$ System". In: *Few-Body Systems* 54 (2013), pp. 1187–1189. DOI: 10 . 1007 / s00601-012-0543-7.
- [210] M. Döring et al. "Kaon-Nucleon Scattering Lengths from Kaonic Deuterium Experiments Revisited". In: *Physics Letters B* 704.5 (2011), pp. 663–666. DOI: doi . org / 10 . 1016 / j . physletb . 2011 . 09 . 099.
- [211] S. S. Kamalov, E. Oset, and A. Ramos. "Chiral Unitary Approach to the K-Deuteron Scattering Length". In: *Nucl. Phys. A* 690 (2001), pp. 494–508. DOI: 10.1016/S0375-9474(00)00709-0.
- [212] T. Takaki. "Optical Potential Approach to K^+d Scattering at Low Energies". In: *Phys. Rev. C* 81 (2010), p. 055204. DOI: 10 . 1103 / PhysRevC . 81 . 055204.